Kinetic Theory for Anisotropic Thermalization and Transport of Vibrated Granular Materials

by

Jayant Vijay Khambekar

A Dissertation

Submitted to the Faculty

of

Worcester Polytechnic Institute

In partial fulfillment of the requirements for the

Degree of Doctor of Philosophy

in

Mechanical Engineering

by

April 2007

APPROVED:

Prof. Mark W. Richman, Advisor

Prof. Nikolaos A. Gatsonis, Committee Member

Prof. David J. Olinger, Committee Member

Prof. Arshad Kudrolli, Committee Member

Prof. Michael A. Demetriou, Graduate Committee Representative

ABSTRACT

The purpose of this work is to develop a continuum theory that may be used to predict the effects of anisotropic boundary vibrations on loose granular assemblies. In order to do so, we extend statistical averaging techniques employed in the kinetic theory to derive an anisotropic flow theory for rapid, dense flows of identical, inelastic spheres. The theory is anisotropic in the sense that it treats the full second moment of velocity fluctuations, rather than only its isotropic piece, as a mean field to be determined. In this manner, the theory can, for example, predict granular temperatures that are different in different directions. The flow theory consists of balance equations for mass, momentum, and full second moment of velocity fluctuations, as well as constitutive relations for the pressure tensor, the flux of second moment, and the source of second moment. The averaging procedure employed in deriving the constitutive relations is based on a Maxwellian that is perturbed due to the presence of a deviatoric second and full third moment of velocity fluctuations. Because the theory is anisotropic, it can predict the normal stress differences observed in granular shear flows, as well as the evolution to isotropy in an assembly with granular temperatures that are initially highly anisotropic.

In order to complement the theory, we employ similar statistical techniques to derive boundary conditions that ensure that the flux of momentum as well as the flux of second moment are balanced at the vibrating boundary. The bumps are hemispheres arranged in regular arrays, and the fluctuating boundary motion is described by an anisotropic Maxwellian distribution function. The bumpiness of the surface may be adjusted by changing the size of the hemispheres, the spacing between the hemispheres in two separate array-directions, and the angle between the two directions. Statistical

averaging consistent with the constitutive theory yields the rates at which momentum and full second moment are transferred to the flow. In order to present results in a form that is easy to interpret physically, the statistical parameters that describe the boundary fluctuations are related in a plausible manner to amplitudes and frequencies of sinusoidal vibrations that may differ in three mutually perpendicular directions, and to phase angles that may be adjusted between the three directions of vibration.

The focus of the results presented here is on the steady response of unconfined granular assemblies that are thermalized and driven by horizontal bumpy vibrating boundaries. In a first detailed study of the effects of the boundary geometry and boundary motion on the overall response of the assemblies, the anisotropic theory is reduced to a more familiar isotropic form. The resulting theory predicts the manner in which the profiles of isotropic granular temperature and solid volume fraction as well as the uniform velocity and corresponding flow rate vary with spacings between the bumps, angle of the bump-array, energy of vibration, direction of vibration, and phase angles of the vibration.

In a second study, we solve the corresponding, but more elaborate, boundary value problem for anisotropic flows induced by anisotropic boundary vibrations. The main focus in presenting these results is on the differences between granular temperatures in three perpendicular directions normal and tangential to the vibrating surface, and how each is affected by the bumpiness of the boundary and the direction of the vibration. In each case, we calculate the corresponding nonuniform velocity profile, solid volume fraction profile, and mass flow rate.

ACKNOWLEDGEMENTS

I would like to thank members of my dissertation committee, Prof. Gatsonis, Prof. Kudrolli, Prof. Olinger and Prof. Demetriou, for reading my dissertation. Especially I am very thankful to my advisor, Prof. Richman, for giving me a challenging project and guiding me to complete it successfully. His mathematical insights helped me many times throughout this work. I have learnt a lot from him and I feel fortunate that I got the opportunity to work with him.

All of my friends have helped me in one way or another. Although it is not possible to mention all of them, I have to mention two names, Ganapathi Raman Balasubramanian and Sauvik Biswas. I am thankful to them for all their help, encouragement and for many enjoyable technical discussions.

I am also very thankful for all the help I got from department secretaries, Barbara E., Barbara F. and Janice. Special thanks go to Sia for all his support and help.

How can one thank his parents enough? My parents, Pappa and Mammi, are the reasons behind all my accomplishments. I am also thankful to my brother Nilesh, and Snehal for all their support. Finally, none of this would have been possible without the amazing patience and support of my wife, Aparna. She is as much responsible for this work as I am.

TABLE OF CONTENTS

LIST OF FIGURES

Chapter 2

CHAPTER 1

Introduction

Granular materials or bulk solids is the term given to an assembly of discrete solid particles, which are in contact or near contact with each other. For example, sand, rice, nuts, ball bearings, powders are all granular materials. Raw materials or final products in many industries are in granular form. For example, at DuPont, more than 60% of their products are found to be powders, crystalline solids, granules, flakes, dispersions, slurries and pastes. (Studt, 1995). It is estimated that about 10% of the world's energy consumption is spent on transporting or processing granular materials. Flows of such materials are termed *granular flows* and occur in many industrial applications commonly encountered in the abrasives, mining, food, pharmaceutical, plastic and chemical industries.

Granular materials can demonstrate both solid-like and fluid-like behaviors. When the motion of granular materials is slow, the particles keep in contact with each other during the movement, and the inter-particle friction force becomes dominant factor. As a result, granular materials demonstrate solid-like behavior and can withstand certain amount of deformation without starting to flow. On the other hand, when motion of granular particles is fast, flow particles interact with each other through abrupt collisions and granular materials demonstrate fluid-like behavior. Many variables influence the motion of granular materials including size, shape, density, surface roughness and contact stiffness of particles, flow depth and most importantly, interaction of particles with confining boundaries.

Granular flows include gravity driven or vibrationally enhanced chute flows, vibrationally driven flows in spiral elevators and "linear" conveyors. In such granular flows, interaction of particles with themselves and with boundaries that contain them are typically complex and not very well understood. Consequently, these flows have been the subject of much recent research. In past few years, several researchers have conducted experiments, performed numerical simulations and developed theories to try to better understand the behavior of granular materials.

1.1 Review of Previous Work

One of the earliest scientific study of granular materials was done by Sir Osbourne Reynolds (1885). He put forth principles of granular dilatancy which explained drying of wet beach sand around one's foot, when stepped on. Modern granular flow research began with the classic work of Bagnold (1954) on the flow behavior of granular materials. He suspended wax spheres in a glycerin-water-alcohol mixture and sheared them in a coaxial cylinder rheometer which measured both shear and normal forces on the walls. From his experiments he demonstrated that both, shear stress and normal stress, are proportional to the square of mean shear rate. He argued that this was because both, momentum exchanged in a collision and frequency of collisions, are proportional to the mean rate of shear. The work demonstrated importance of granular collisions in explaining non-Newtonian characteristics of rapid granular flows. Bagnold's findings stirred a lot of interest in scientific community and after that many attempts were made to write a mathematical theory to describe behavior of granular materials, including Mandl and Fernadez (1970), Goodman and Cowin (1971), Cowin

(1974), Ackermann and Shen (1978), Blinowski (1978), Cowin (1978), McTigue (1978), Ogawa (1978), Jenkins and Cowin (1979), Savage (1979), Ogawa et. al. (1980), Jenkins and Savage (1981), Savage and Jeffrey (1981), Ackermann and Shen (1982) and Haff (1983). At the same time, experimental investigations done by Toyama (1970), Arthur and Menzies (1972), Savage (1978), Savage and McKeown (1983), Hanes and Inman (1985) and Savage and Sayed (1984) helped to better understand the behavior of granular materials.

Theoretical analysis of granular flows demands intricate mathematical models because of the complexities involved. However these models will not admit analytical solutions. In order to reveal major physical mechanisms and be able to make future predictions, good mathematical approximations must be employed. Kinetic theory method is one such approach based upon the analogy between motion of granular particles and motion of gas molecules. It accounts for the effects that fluctuations of particles' velocities have on the transfer of momentum, energy and higher order quantities within the flow. However, inelasticity of granular collisions makes major difference between gas and granular materials. Kinetic energy is lost in collisions between pairs of grains and hence those results in kinetic theory, obtained using the reversibility of collisions, must be re-derived. Jenkins and Savage (1983) took such an approach and applied methods of averaging employed in the kinetic theory to a dense system of identical, smooth, nearly elastic spheres experiencing a rapid flow. Their calculations were based on a physically plausible but ad hoc characterization of the probability of collision between two particles. These calculations were improved by Lun et. al. (1984) and, Jenkins and Richman (1985 a). Jenkins and Richman extended method

of moments used by Grad (1949) for determining single particle velocity distribution function in *dense* system of *inelastic* particles whereas Lun et. al. used simpler but cruder moment method described, for example, by Reif (1965). Lun et. al. and Jenkins and Richman applied these theories to shear flows of granular materials with prescribed shear rate. The theories successfully predicted the shear behavior of granular materials.

A dissipative mechanism for exchange between translational and rotational energies of colliding bodies was proposed by Richman (1984). He also studied evolution of the roughness coefficient. Jenkins and Richman (1985 b) formulated kinetic theory for plane dense flows of identical, rough, inelastic circular discs, in which they introduced an additional temperature to measure kinetic energy of particle rotation.

To apply the kinetic theory to flows other than shear flows with prescribed shear rate, required development of consistent boundary conditions. Jenkins and Richman (1986) developed a set of boundary conditions for two-dimensional smooth, identical, circular disk flows in the neighborhood of a bumpy wall. Later this work was extended to flows of spherical particles by Richman (1988) who used an improved Maxwellian velocity distribution function and calculated the rates at which momentum and energy are transferred across bumpy boundaries and obtained conditions that ensured the balance of momentum and energy at such boundaries. He also applied these boundary conditions to shear flow of granular material driven by bumpy boundaries and obtained explicit dependence of slip velocity and resulting stresses on boundary roughness. Richman and Marciniec (1990) applied these more formal boundary conditions to inclined flows. Richman and Chou (1988) derived boundary conditions for granular shear flows of smooth disks by incorporating a more accurate velocity distribution function. Richman

and Chou (1989) derived a kinetic theory for homogeneous granular shear flows of identical spheres in which collisions between particles result in small fractures on their peripheries and, over time, effectively reduce their average diameter. Richman (1992) developed boundary conditions that ensured momentum and energy balance at isotropically vibrating bumpy boundaries. Richman and Martin (1992, 1993) improved upon this work by considering boundaries whose fluctuating motion was anisotropic, but restricted their attention on assemblies with uniform velocity. Martin (1993) further extended the work to include effects of spatial variation of mean velocity. Richman and Martin (1992) provided a continuum description of a vibro-fluidized system where the constitutive relations were adapted from Jenkins and Richman (1985 a). Kumaran (1998 a) further investigated the problem and theoretically calculated velocity distribution function for a two-dimensional vibro-fluidized bed of particles using asymptotic analysis for nearly elastic assemblies with small density gradients. He also studied the anisotropy of granular temperature due to vibro-fluidization. Kumaran (1998 b) examined scaling of temperature of a granular material fluidized by external vibrations. Richman and Wang (1995, 1996) derived the boundary conditions for granular flows that passed through the vibrating sieves. Jenkins and Askari (1991) calculated stress and energy flux in amorphous solid of nearly elastic spheres and used their continuity at the interface with a dense granular flow to obtain boundary conditions for the flow. Jenkins (1992) determined boundary conditions for a flat, frictional wall by employing coulomb friction and both, tangential and normal restitution. Jenkins and Hanes (1993) derived the boundary condition for the balance of momentum and energy at an interface between colliding and freely flying grains in an inclined, rapid granular flow. Jenkins and Louge

(1997) considered a flow of colliding spheres that interacts with a flat, frictional wall and calculated the flux of fluctuation energy. Jenkins and La Ragione (2001) demonstrated the necessity of distinguishing the average rotation of the spheres about their centers from average rotation of the aggregate. Yoon and Jenkins (2005) developed kinetic theory for flows of slightly friction and nearly elastic discs. Jenkins et. al. (2006) derived a stress-strain relation for static deformations of a random array of identical discs that interact through elastic, frictional contacts.

Computer simulations of rapidly flowing granular material are used as research tools to investigate the macromechanics and micromechanics. Campbell and Brennen (1984) implemented numerical schemes and studied flows of granular materials. Campbell (1989) studied in detail the complete stress tensor for assembly of spheres and Campbell (1993) discussed the effect of boundary roughness on granular flows. Walton and Broun (1986 a, 1986 b) and Walton (1989) studied the effect of highly dissipative interactions of particles on pressures and velocity distribution in assemblies undergoing uniform shear. The simulations predicted that the normal stresses in the direction of flow and perpendicular to it are not even close. This indicated that the granular temperatures in those directions must also be different. This was theoretically established by Jenkins and Richman (1988) and Richman (1989) who demonstrated that the differences increase with inelasticity. Campbell (1994) performed discrete particle simulations to measure the impulses that particles experience while undergoing rapid shear. Potapov and Campbell (1996) described two-dimensional simulations of hopper flows. Sadjadpour and Campbell (1999) analyzed cohesionless granular flows in inclined open channels to give insight into effect of chute geometry on clogging of chutes. Campbell (2002)

performed simulations to study dense granular materials where particles are in persistent contact with their neighbours. Campbell (2005) examined stress controlled granular flows and found that they behave very differently from flows at fixed concentration. Rosato and Kim (1994) performed particle dynamics simulations to characterize the effects of boundary geometry on the flow of dry granular materials composed of smooth, inelastic spheres between parallel, bumpy walls in the absence of gravity. Lan and Rosato (1995) performed three-dimensional, granular dynamics simulations to investigate macroscopic behavior of assembly of smooth inelastic, uniform spheres subjected to vibrations through sinusoidally oscillating boundary. Lan and Rosato (1997) performed 3d discrete element simulations to investigate behavior of shallow bed of inelastic, frictional spheres which are energized by floor oscillations. Rosato and Yacoub (2000) modeled densification of frictional, inelastic spheres under the action of floor oscillations. Rosato et. al. (2002) performed simulations and proposed that "void-filling" beneath large particles promotes segregation while convection helps mixing in a non-uniform particle size mixture. Liu and Rosato (2003) carried out 3d, steady discrete element simulations of a single large spherical intruder in a gravity-free granular Couette flow and studied the effect of high pressure near the wall on intruder particle's motion.

Development of theoretical models needs quantitative experiments which investigate properties of granular materials. Several such experiments were performed by Kudrolli and his co-workers. Kudrolli and Henry (2000) showed that velocity distribution in a system of steel spheres rolling on a tilted rectangular two dimensional surface and excited by periodic forcing of one of the side walls, is far from Gaussian. Blair and Kudrolli (2001) studied the correlations of particle velocities over long

distances whereas Blair and Kudrolli (2003 a) obtained collision properties including path length, collision time, distributions of particles and the inelasticity parameter. Experiments of Samadani and Kudrolli (2000) reported one of the first systematic studies of segregation transition of bidisperse granular mixtures in the presence of liquids. Samadani and Kudrolli (2001) showed the importance of viscosity of the liquid in determining the angle of repose of the pile formed after pouring the wet granular mixture. Blair and Kudrolli (2003 b, 2004) studied the effects of long range interactions on the phases observed in cohesive granular materials. Blair, Neicu and Kudrolli (2003) investigated the effect of anisotropy of the constituent particles on the packing and dynamics of granular matter. Nowak, Samadani and Kudrolli (2005) developed a new liquid bridge model which takes into account the nature of the grain contacts and the cohesive force due to liquid bridges.

During recent years, vibro-fluidization of granular materials has received a lot of attention from researchers and several experiments have been carried out bringing into light a plethora of unusual phenomenon. For example, in the low magnitude regime, the vibrations constitute sound propagation as investigated by Liu and Nagel (1994). As the amplitude of vibration increases heaping and convection rolls are observed, as reported by Evesque et. al. (1989) and Ehrichs et. al. (1995). At larger vibration amplitudes, Douady et. al. (1989) observed period doubling instabilities leading to standing waves, whereas Pak and Behringer (1993) observed traveling waves. Goldshtein et. al. (1995), Clement et. al. (1993) and Luding et. al. (1994) studied the transition of granular flows from liquid-like condensed state to gas-like fluidized state.

Measuring granular temperatures inside granular flows is a difficult task. Ahn et. al. (1991) and Hsiau and Hunt (1993) employed fibre-optic probe technology to measure velocity fluctuations and calculated granular temperature in steamwise direction. Drake (1991) employed high speed photography and image technology to measure the two-dimensional fluctuations in gravity driven chute flows. Natarajan, Hunt and Taylor (1996) employed image technology to measure the two-dimensional fluctuations in vertical channel granular flows. Warr et. al. (1994, 1995) used high speed photography to obtain experimental information on the velocity distribution functions for a two dimensional array of spheres. These experiments yielded information on the moments of the velocity distribution and spatial pair correlation function in these materials. Hunt (1997) performed a study of effective thermal conductivity and self-diffusivity for granular flows. Zenit, Hunt and Brennen (1997) carried out experiments to measure the collisional particle pressure in cocurrent and countercurrent flows of liquid and particulate mixtures. Karion and Hunt (2000) studied granular shear flows where the upper and lower bounding walls are flat and frictional, with the focus on wall stresses. Wassgren et. al. (2002) experimentally investigated the discharge of granular material from a hopper subjected to vertical oscillations. Muite, Hunt and Joseph (2004) carried out experiments to investigate the effects of interstitial fluid on the discharge of granular material within an hourglass.

Many experiments to investigate in detail the transmission of stress in granular materials were performed by Behringer and his co-workers. Howell, Behringer and Veje (1999) performed experiments on a slowly sheared granular material and found that there is a critical value of packing fraction around which network of stress chains changes

structure. Behringer (2002) discussed about the possibility to tie granular temperature to grain mobility and diffusion. Hartley and Behringer (2003) experimentally investigated the rate dependence of stress in a slowly sheared system of photoelastic disks and determined forces on the granular scale. Peidong and Behringer (2005) characterized the effect of loading on a model soil-like system to find statistical and mean properties of model soil response. Majmudar and Behringer (2005) reported measurements of the normal and tangential grain-scale forces inside a system of photoelastic disks that are subject to pure shear and isotropic compression. Daniels and Behringer (2006) carried out experiments on monodisperse spherical particles in an annular cell geometry, vibrated from below and sheared from above.

A number of studies have been done on mean velocity in granular flows which have revealed many unusual and baffling phenomenon, and a clear understanding of flow properties is still far from achieved. Gallas et. al. (1992) simulated transport of particles on a belt having vertical and horizontal vibrations. Using molecular dynamics, they calculated velocity profiles in assembly of uniform spheres and found that velocity increased away from boundary. Derenyi et. al. (1998) experimentally investigated horizontal transport of an assembly of granular particles in a vertically vibrated system that has a sawtooth-shaped base. They observed that the direction of flow depended on the shape of sawtooth and increasing the mass hold-up reversed the direction of flow. Farkas et. al. (1999) performed event driven molecular dynamics simulations which agreed with the results of Derenyi et. al. (1998) and further showed that the direction of flow also reverses with driving frequency of vibrations. Levanon and Rapaport (2001) performed discrete particle simulations of vibration-induced flow of granular material

and found that the transport velocity varied as a function of height and could even change directions with height. Contrary to Gallas et. al. (1992), molecular dynamics simulations of Wambaugh et. al. (2002) showed that the transport velocity monotonically decreased away from the boundary. Grochowski et. al. (2004) used an annular, flat base conveyor, instead of sawtooth-shaped base, and subjected it to both vertical and circular oscillations and observed that the flow direction reversed with increasing vibration frequency. El hor et. al. (2005) performed similar experiments for straight, linear conveyor subjected to both vertical and horizontal vibrations and noticed reversal of flow direction with increasing vibration frequency.

Such studies of slip velocity have also been done for inclined granular flows. For example, Hanes and Walton (2000) experimentally measured velocity profiles for flows down inclines. Poschel (1993) and Zheng and Hill (1996, 1998) studied velocity and density profiles for flows down inclines, using molecular dynamics simulation. Baldassarri et. al. (2001) carried out simulations of inclined flows enhanced by boundary vibrations and studied temperature, density and velocity profiles.

Most recently, several new areas are being explored by researchers and the study of granular materials is getting broader every day. Forterre and Pouliquen (2001) reported a new instability observed in rapid granular flows down inclined planes that leads to the spontaneous formation of longitudinal vortices, and Forterre and Pouliquen (2002) showed that the kinetic theory is able to capture the formation of longitudinal vortices. Chehata et. al. (2003) experimentally studied dense granular flow around a cylinder and found that the mean drag force acting on the cylinder is independent of the mean flow velocity, contrary to what is expected from any ordinary fluid. Silbert et. al.

(2002) uncovered strong analogies between the jamming of the grains and the liquid-glass transition based on large-scale, three-dimensional chute flow simulations of granular systems. Corwin et. al. (2005) investigated whether there is a structural signature of the jammed granular state that distinguishes it from its flowing counterpart and found that there is a qualitative change in the force distribution at the onset of jamming. Hsiau and Lu (2005) studied numerically the effect of electrostatic force on granular assembly by defining electrostatic number Es as the ratio of the electrostatic force to the particle weight. The simulation results demonstrate that the granular temperatures increase linearly with the increasing Es. Mayor et. al. (2005) developed a non-equilibrium version of the classical Brownian motion experiment by observing the motion of a torsion oscillator immersed in an externally vibrated granular medium and found the motion to be Brownian-like. Huang et. al. (2006) experimentally studied the formation of shockwave and its propagation in vertically vibrated quasi-2d granular material. Pohlman et. al. (2006) carried out experiments to show that nanoscale surface roughness can affect the flowability and angle of repose of granular matter without driving de-mixing of bulk granular material.

Wildman and Parker (2002) showed that two granular temperatures can coexist in binary systems and the dissipative and non-equilibrium nature of granular flows does not allow the interdispersed granular gases to relax towards a single temperature. Montanero and Garzo (2002) studied steady, simple shear flow of a low-density binary mixture of inelastic smooth hard spheres and showed that the partial temperatures of each species are different even in the weak dissipation limit. Galvin et. al. (2005) numerically simulated rapid granular flows undergoing segregation and revealed that the more

massive particle may exhibit a lower species temperature than its lighter counterpart, contrary to-previous observations in non-segregating systems.

Makse and Kurchan (2002) numerical modeled slow, enduring contact flows, by considering particles of different sizes in a slowly sheared dense granular system and extracted an effective temperature from a relation connecting their diffusivity and mobility. Santos et. al. (2004) studied the rheology of granular fluids under a uniform shear flow with uniform temperature and density, and observed that the temperature in the unsteady state increased depending on whether the viscous heating of the initial state was larger than the collisional cooling. Bose and Kumaran (2004) analyzed the velocity distribution for the shear flow of a granular material using an event driven simulation for a wide variation in the coefficients of restitution and the Knudsen number. Montanero and Garzo (2003) numerically studied energy non-equipartition in a sheared granular mixture. Liu and Rosato (2005) reported on the behavior of uniform granular particles undergoing a gravity-free shear flow induced through parallel bumpy boundaries that move in opposite directions at constant velocity and found that a non-uniform local shear rate produces an imbalance in the contact distribution of particles in the vicinity of the walls so that they drift toward the geometric centre of the flow. Cordero et. al. (2005) used Newtonian molecular dynamics to study a gas of inelastic hard disks subject to shear between two planar parallel thermal walls and observed significant non-Newtonian behavior as non linear viscosity, shear thinning and normal stress differences. Xu et. al. (2005) performed molecular dynamics simulations of frictionless granular systems undergoing boundary driven planar shear flow and determined the conditions under which they will have linear velocity profiles and when they will develop highly localized

velocity profiles. Khain and Meerson (2006) theoretically investigated steady, plane and very dense Couette flow of inelastic hard spheres under constant pressure and studied shear-induced crystallization,i.e. formation of solid-like crystals of spheres.

Strumendo and Canu (2002) developed a method of moments for the dilute granular flow of inelastic spheres. Zhang and Rosato (2004) numerically examined the dynamic states of granular material vibrated vertically with special consideration of particle roughness, inelasticity and structure of assembly before vibrations started. Changfu et. al. (2004) presented the directly measured experimental data of collision rate in vertical two-phase flow and claimed that the theoretical correlations based on kinetic theory overestimate the collision rate in the gas-particle flows. Massoudi and Anand (2004) have presented the governing equations for the flow of granular materials down an incline, taking into account the heat transfer mechanism. Massoudi (2006) emphasized that for complex non-linear materials it is the heat flux vector which should be studied rather than proposing generalized form of the thermal conductivity. He showed that the heat flux vector in addition to being proportional to the temperature gradient (the Fourier's law), could also depend on the gradient of density and the symmetric part of the velocity gradient. Kumaran (2006) derived the constitutive relations for granular flow of rough spheres in the limit where the energy dissipation in a collision is small compared to the energy of particle.

1.2 Summary of Approach

The theoretical work described in this dissertation makes two major contributions. It derives a constitutive theory for flows of granular materials that can have anisotropic

temperatures in different directions, and it gives boundary conditions for anisotropically vibrating bumpy boundaries that ensure balance of not only momentum and energy, but also the complete second moment. This anisotropic theory together with the boundary conditions can make very detail predictions of effect of surface roughness and boundary motion on assemblies of granular material.

The constitutive theory for flow is an extension of the pioneering work of Jenkins and Richman (1985 a). They had derived a very detailed constitutive theory using an isotropic Maxwellian distribution function. Here, we extend that work using a distribution function that is anisotropic and includes perturbations in Maxwellian distribution due to the presence of deviatoric second moment and complete third moment. We extend the work of Richman and Martin (1993) who derived boundary conditions for randomly fluctuating bumpy boundaries with random array of boundary particles. Here, we derive boundary conditions where the array pattern of boundary particles is fixed and can be adjusted. Also, we derive relations for change of momentum as well as complete second moment at these vibrating, bumpy boundaries.

In Chapter 2, we derive the general constitutive theory for rapid, dense flows of identical, inelastic, smooth spheres. First, we write down the balance laws. In order to predict the anisotropy of temperatures, we use a velocity distribution function that includes corrections to Maxwellian distribution due to presence of second moment and third moment. Using such a distribution, we carry out statistical averaging over all possible collisions to calculate the change of properties in collisions and we also calculate change in property due to transport of particles between the collisions. We make assumptions that are consistent with the constitutive theory of Jenkins and Richman

(1985 a). Particularly, we assume that the gradients of second moment, velocity and density are small. After deriving the constitutive relations, we study the relaxation behavior to equipartition of second moment. We also look at simple homogenous shearing of granular particles. In the end, we also derive the individual velocity distributions.

Chapter 3 is devoted to formulating the effects of a randomly fluctuating, bumpy boundary on an assembly of granular particles. Here, we first write down the momentum and full second moment boundary conditions, in their most general form. Then, we analyze a bumpy boundary, determine the limits in which the analysis is valid and study the characteristics of such boundary, particularly the accessible area of boundary bumps. Then, we write down the expressions for transfer rates by statistically averaging the changes in a collision over all possible collisions between boundary particles and flow particles. We also make approximations consistent to the constitutive theory used in the flow and simplify the expressions for constitutive relations to the extent possible. We also write down the boundary conditions at free surface.

In Chapter 4, we write down the general non-dimensional boundary value for free surface flows of granular materials over vibrating, bumpy boundaries. We focus on flows that are steady, parallel and fully-developed. Also, the mean fields in these flows are functions of only normal direction. We use balance laws and constitutive theory derived in Chapter 2 and boundary conditions and transfer rates derived in Chapter 3, consistent with the approximations made in Chapter 2 and Chapter 3.

Chapter 5 discusses the boundary value problem when the flow is isotropic and the boundary vibrations are anisotropic. In this case, the induced mean motion is uniform

the individual temperatures are equal. Here, we primarily focus on the effects of boundary roughness and boundary vibration on the thermalization and induced mean motion in the flow. We look at the profiles of granular temperature and solid volume fractions. We study the variation of temperature, solid volume fraction and flow heights. We also look at the effects of this on mean motion of the assembly.

Chapter 6 describes a very detail study of anisotropic flows of granular materials. First we show that the velocity distribution functions can differ significantly from Maxwellian distribution. Then we study thermalization of assemblies by looking at the cases where no mean motion is induced and later we look at mean motion. We look at profiles of not only the total temperature and solid volume fractions but also the profiles of the individual temperatures, for different values of mass hold-ups, restitution coefficients and distribution of total vibrational energy. Further, we look at the variation of total temperature as well as all individual temperatures, flow heights, solid volume fractions at base for different distributions of vibrational energy. We look at the effects of changes in array spacings, array angle, mass hold-up, coefficients of restitution, total boundary energy on the thermalization of the assembly. In the second part, we look at the profiles of mean velocity under different mass hold-ups, restitution coefficients and distribution of energy. We study the effects of distribution of vibrational energy, phase angles, array spacings, array angle, total vibrational energy, ratio of flow particle size and boundary bump size, mass hold-ups, restitution coefficients on mean motion.

CHAPTER 2

Flow Statistics and Collision Integrals

Following techniques employed in the kinetic theory of gases, we introduce a single particle distribution function f defined such that, at time t, the probable number of particles located at position $\boldsymbol{r}$ within volume element $d\boldsymbol{r} \equiv d\boldsymbol{r}_1 d\boldsymbol{r}_2 d\boldsymbol{r}_3$ with velocities $\boldsymbol{c}$ within the range $d\boldsymbol{c} \equiv d\boldsymbol{c}_1 d\boldsymbol{c}_2 d\boldsymbol{c}_3$ is given by $f(\boldsymbol{c},\boldsymbol{r},t)d\boldsymbol{c}d\boldsymbol{r}$. The number density n of particles within the flow is then

$$n(\boldsymbol{r},t) = \int f(\boldsymbol{c},\boldsymbol{r},t)d\boldsymbol{c} \quad , \tag{2.1}$$

where the integration is carried out over all velocities. If each sphere is of mass m, diameter σ, and mass density ρ_p, then the solid volume fraction ν is $n\pi\sigma^3/6$ and the mass density ρ of the flow is either mn or $\rho_p \nu$.

The mean value of any particle property $\phi(\boldsymbol{c})$ is the weighted average,

$$\langle \phi \rangle \equiv \frac{1}{n}\int \phi(\boldsymbol{c}) f(\boldsymbol{c},\boldsymbol{r},t)d\boldsymbol{c} \quad , \tag{2.2}$$

where the integration is over all velocities. The mean velocity $\boldsymbol{u}(\boldsymbol{r},t)$ is simply $\langle \boldsymbol{c} \rangle$, the fluctuation velocity $\boldsymbol{C}$ is the difference $\boldsymbol{c} - \boldsymbol{u}$, and the full second moment $\boldsymbol{K}$ of fluctuation velocity is $\langle \boldsymbol{C} \otimes \boldsymbol{C} \rangle$. The granular temperature $T \equiv \langle \boldsymbol{C} \cdot \boldsymbol{C} \rangle / 3 = tr(\boldsymbol{K})/3$ is proportional to the kinetic energy associated with the velocity fluctuations, and is the isotropic part of $\boldsymbol{K}$.

A pair distribution function $f^{(2)}$ is defined such that $f^{(2)}(\boldsymbol{c}_1,\boldsymbol{r}_1,\boldsymbol{c}_2,\boldsymbol{r}_2,t)d\boldsymbol{c}_1 d\boldsymbol{c}_2 d\boldsymbol{r}_1 d\boldsymbol{r}_2$ gives the number of pairs of particles with velocities $\boldsymbol{c}_1$ and $\boldsymbol{c}_2$ within the ranges $d\boldsymbol{c}_1$ and $d\boldsymbol{c}_2$ that are located at $\boldsymbol{r}_1$ and $\boldsymbol{r}_2$ within the ranges $d\boldsymbol{r}_1$ and $d\boldsymbol{r}_2$ at time t. An integral

expression for the collisional rate of production $\mathsf{C}(\phi)$ of any particle property $\phi(\boldsymbol{c})$ is obtained by averaging over all binary collisions in which ϕ_1 and ϕ_1' are the pre- and post-collisional amounts of ϕ possessed by particle 1, ϕ_2 and ϕ_2' are the pre- and post-collisional amounts of ϕ possessed by particle 2, and $\Delta\phi \equiv \phi_1' + \phi_2' - \phi_1 - \phi_2$ is the total change in ϕ per collision. Jenkins and Savage [1983] have shown that the collisional production may be decomposed into the sum,

$$\mathsf{C}(\phi) = X(\phi) - \nabla \cdot \boldsymbol{\Omega}(\phi) \quad . \tag{2.3}$$

If ϕ is given as a function $\phi(\boldsymbol{C})$ of fluctuation velocity $\boldsymbol{C}$ rather than absolute velocity $\boldsymbol{c}$, then equation (2.3) must be modified by adding an extra term, which in component form is given by $-(\partial u_i / \partial r_j)\Omega_j(\partial\phi / \partial C_i)$. If at impact, $\boldsymbol{k}$ is the unit vector directed from particle 1 to particle 2, $d\boldsymbol{k}$ is an element of solid angle centered about $\boldsymbol{k}$, and $\boldsymbol{g}$ is the relative velocity $\boldsymbol{c}_1 - \boldsymbol{c}_2$, then the collisional contribution $X(\phi)$ is given by the integral,

$$X(\phi) = \frac{\sigma^2}{2}\int \Delta\phi\, f^{(2)}(\boldsymbol{c}_1, \boldsymbol{r} - \sigma\boldsymbol{k}, \boldsymbol{c}_2, \boldsymbol{r})(\boldsymbol{g}\cdot\boldsymbol{k})\, d\boldsymbol{k} d\boldsymbol{c}_1 d\boldsymbol{c}_2 \quad , \tag{2.4}$$

and the collisional term $\boldsymbol{\Omega}(\phi)$ is given by the integral,

$$\boldsymbol{\Omega}(\phi) = \frac{-\sigma^3}{2}\int (\phi_1' - \phi_1)\boldsymbol{k} \sum_{n=0}^{\infty} \frac{(-\sigma)^n}{(n+1)!}(\boldsymbol{k}\cdot\nabla)^n f^{(2)}(\boldsymbol{c}_1, \boldsymbol{r}, \boldsymbol{c}_2, \boldsymbol{r} + \sigma\boldsymbol{k})(\boldsymbol{g}\cdot\boldsymbol{k})\, d\boldsymbol{k} d\boldsymbol{c}_1 d\boldsymbol{c}_2 \quad , \tag{2.5}$$

where the integration is carried out over all velocities $(\boldsymbol{g}\cdot\boldsymbol{k} > 0)$ for which a collision is impending. Equations (2.4) and (2.5) are exact expressions for the collisional terms $X(\phi)$ and $\boldsymbol{\Omega}(\phi)$.

Here we follow the kinetic theory for dense gases and adopt a modified statement of molecular chaos. In this manner, the pair distribution function for two particles at impact is given in terms of single particle distribution functions by,

$$f^{(2)}(\boldsymbol{c}_1,\boldsymbol{r},\boldsymbol{c}_2,\boldsymbol{r}+\sigma\boldsymbol{k}) = g_0(\boldsymbol{r}+\sigma\boldsymbol{k}/2) f(\boldsymbol{c}_1,\boldsymbol{r}) f(\boldsymbol{c}_2,\boldsymbol{r}+\sigma\boldsymbol{k}) \quad , \tag{2.6}$$

where g_0 is the radial distribution function that depends entirely on the solid volume fraction ν. Equation (2.6) may be employed in the collisional integrals (2.4) and (2.5). Approximations for the resulting integrals are based on the Taylor series for the single particle distribution function,

$$f(\boldsymbol{c},\boldsymbol{r}\pm\sigma\boldsymbol{k}) = \sum_{n=0}^{\infty} \frac{(\pm\sigma)^n}{n!} (\boldsymbol{k}\cdot\nabla)^n f(\boldsymbol{c},\boldsymbol{r}) \quad , \tag{2.7}$$

and for the radial distribution function,

$$g_o\left(\boldsymbol{r}\pm\frac{\sigma}{2}\boldsymbol{k}\right) = \sum_{n=0}^{\infty} \frac{(\pm\sigma)^n}{n!\,2^n} (\boldsymbol{k}\cdot\nabla)^n g_o(\boldsymbol{r}) \quad . \tag{2.8}$$

In order to retain the three lowest order terms in C (ϕ), it is necessary to retain the three lowest order terms in $X(\phi)$ and the two lowest order terms in $\Omega(\phi)$. In fact, some of the third order terms in $X(\phi)$ may be written as the divergence of second order terms, which for consistency with $\Omega(\phi)$ must be included in the collisional flux. To this order of the approximation, $X(\phi)$ may be written as,

$$X(\phi) = \chi(\phi) - \nabla\cdot\left[\boldsymbol{E}(\phi) + \tilde{\boldsymbol{E}}(\phi)\right] \quad , \tag{2.9}$$

where $\chi(\phi)$ is the integral given by

$$\chi(\phi) = \frac{\sigma^2 g_0}{2}\int \Delta\phi \left\{1 + \frac{\sigma}{2}\boldsymbol{k}\cdot\nabla\left[\ell n\left(\frac{f_2}{f_1}\right)\right] - \frac{\sigma^2}{2}\left[\boldsymbol{k}\cdot\nabla\ell n(f_1)\right]\left[\boldsymbol{k}\cdot\nabla\ell n(f_2)\right]\right\} f_1 f_2 (\boldsymbol{g}\cdot\boldsymbol{k}) d\boldsymbol{k} d\boldsymbol{c}_1 d\boldsymbol{c}_2 + \frac{1}{2g_o}\frac{dg_o}{d\nu}\boldsymbol{E}(\phi)\cdot\nabla\nu \quad , \tag{2.10}$$

$\boldsymbol{E}(\phi)$ is,

$$\boldsymbol{E}(\phi) = -\frac{\sigma^4 g_0}{8}\int \Delta\phi\, \boldsymbol{k}\left[\boldsymbol{k}\cdot\nabla\ell n(f_1 f_2)\right] f_1 f_2 (\boldsymbol{g}\cdot\boldsymbol{k}) d\boldsymbol{k} d\boldsymbol{c}_1 d\boldsymbol{c}_2 \quad , \tag{2.11}$$

and $\tilde{E}(\phi)$ is,

$$\tilde{E}(\phi) = -\frac{\sigma^4}{16}\frac{dg_o}{d\nu}\nabla\nu\cdot\int\Delta\phi\,\boldsymbol{k}\otimes\boldsymbol{k}\,f_1 f_2(\boldsymbol{g}\cdot\boldsymbol{k})d\boldsymbol{k}d\boldsymbol{c}_1 d\boldsymbol{c}_2 \quad . \tag{2.12}$$

where the integrations in equations (2.10) and (2.11) are (2.12) are carried out over all impending collisions $(\boldsymbol{g}\cdot\boldsymbol{k}>0)$. The corresponding approximation $\boldsymbol{\omega}(\phi)$ for $\boldsymbol{\Omega}(\phi)$ is given by,

$$\boldsymbol{\omega}(\phi) = -\frac{\sigma^3 g_0}{2}\int(\phi_1' - \phi_1)\boldsymbol{k}\left\{1+\frac{\sigma}{2}\boldsymbol{k}\cdot\nabla\left[\ell n\left(\frac{f_2}{f_1}\right)\right]\right\}f_1 f_2(\boldsymbol{g}\cdot\boldsymbol{k})d\boldsymbol{k}d\boldsymbol{c}_1 d\boldsymbol{c}_2 \quad , \tag{2.13}$$

where the limits of integration are $\boldsymbol{g}\cdot\boldsymbol{k}>0$. The expression for the collisional production C (ϕ) that contains the three lowest order terms may therefore be decomposed into the sum,

$$\mathrm{C}\ (\phi) = \chi(\phi) - \nabla\cdot\boldsymbol{\theta}(\phi) \quad , \tag{2.14}$$

where $\chi(\phi)$ is the approximate collisional source given by equation (2.10) and $\boldsymbol{\theta}(\phi)$ is the corresponding approximation for the collisional flux is equal to the sum,

$$\boldsymbol{\theta}(\phi) \equiv \boldsymbol{\omega}(\phi) + \boldsymbol{E}(\phi) + \tilde{\boldsymbol{E}}(\phi) \quad , \tag{2.15}$$

where $\boldsymbol{\omega}(\phi)$, $\boldsymbol{E}(\phi)$, and $\tilde{\boldsymbol{E}}(\phi)$ are given by integrals (2.13), (2.11), and (2.12), respectively. If ϕ is given as a function $\phi(\boldsymbol{C})$ of fluctuation velocity $\boldsymbol{C}$ rather than absolute velocity $\boldsymbol{c}$, then equation (2.14) must be modified by adding an extra term, which in component form is given by $-(\partial u_i/\partial r_j)\theta_j(\partial\phi/\partial C_i)$.

The collisional source employed by Jenkins and Savage [1983], Jenkins and Richman [1985 a], and Richman and Chou [1989], for example, did not include the terms on the right-hand-side of equation (2.10) involving the product of spatial gradients. However, because the only source term in each of their constitutive theories was the

energy dissipation and because their theories were developed for nearly elastic particles, the added terms will make contributions to C (ϕ) that are of higher order than those retained. The collisional flux employed by Jenkins and Savage [1983] and by Jenkins and Richman [1985 a] did not include the extra terms $E(\phi)+\tilde{E}(\phi)$. However, the only flux terms in their constitutive theories were for stress and energy flux. In the case of collisional stress, the extra terms will vanish because momentum is conserved in each collision. In the case of collisional energy flux, the extra term will contribute terms that are of an order higher than those retained because the theories were restricted to nearly elastic particles. The collisional flux derived by Richman and Chou [1989] did not include the extra term $\tilde{E}(\phi)$ because their application was to homogeneous shear flows.

2.1 Balance Equations and Constitutive Quantities

The theory presented here is more elaborate than the standard kinetic theories for granular flows because the mean fields to be determined are the density ρ, the mean velocity $\boldsymbol{u}$, and the full second moment of velocity fluctuations $\boldsymbol{K}$. Standard kinetic theories are concerned with ρ, $\boldsymbol{u}$, and only the isotropic piece T of $\boldsymbol{K}$. The equations that determine these mean fields are balance of mass,

$$\dot{\rho}+\rho\frac{\partial u_i}{\partial x_i}=0 \quad , \tag{2.16}$$

where an overdot denotes the material time derivative; the balance of momentum,

$$\rho\dot{u}_i=-\frac{\partial P_{ij}}{\partial x_j}+\rho g_i \quad , \tag{2.17}$$

where $\boldsymbol{P}$ is the pressure tensor and $\boldsymbol{g}$ is the body force per unit mass; and the balance of the full second moment,

$$\rho \dot{K}_{ij} = -\frac{\partial Q_{kij}}{\partial x_k} - P_{ik}\frac{\partial u_j}{\partial x_k} - P_{jk}\frac{\partial u_i}{\partial x_k} + \Gamma_{ij} \quad , \tag{2.18}$$

where the third order tensor $\boldsymbol{Q}$ is the flux of second moment, and the second order tensor $\boldsymbol{\Gamma}$ is the collisional source of second moment. Alternatively, the balance of second moment (2.18) may be decomposed into its isotropic piece,

$$3\rho \dot{T} = -\frac{\partial Q_{kii}}{\partial x_k} - 2P_{ik}\frac{\partial u_i}{\partial x_k} + \Gamma_{ii} \quad , \tag{2.19}$$

which is the energy equation, and its remaining deviatoric piece,

$$\rho \dot{\hat{K}}_{ij} = -\frac{\partial}{\partial x_k}\left(Q_{kij} - \frac{1}{3}Q_{kmm}\delta_{ij}\right) - P_{ik}\frac{\partial u_j}{\partial x_k} - P_{jk}\frac{\partial u_i}{\partial x_k} + \frac{2}{3}P_{mk}\frac{\partial u_m}{\partial x_k}\delta_{ij} + \hat{\Gamma}_{ij} \quad , \tag{2.20}$$

which are the five additional equations required to treat $\hat{K}_{ij}$ as mean fields.

The constitutive quantities of interest here are the pressure tensor $\boldsymbol{P}$, the flux of second moment $\boldsymbol{Q}$, and the source of second moment $\boldsymbol{\Gamma}$. The quantities $\boldsymbol{P}$ and $\boldsymbol{Q}$ are fluxes of momentum and second moment, respectively, given by the sums,

$$\boldsymbol{P} = \langle \rho \boldsymbol{C} \otimes \boldsymbol{C} \rangle + \boldsymbol{\theta}(m\boldsymbol{C}) \quad , \tag{2.21}$$

and

$$\boldsymbol{Q} = \langle \rho \boldsymbol{C} \otimes \boldsymbol{C} \otimes \boldsymbol{C} \rangle + \boldsymbol{\theta}(m\boldsymbol{C} \otimes \boldsymbol{C}) \quad . \tag{2.22}$$

The first term on the right-hand-sides of equations (2.21) and (2.22) are the transport contributions to these constitutive quantities, and the second term corresponds to the collisional contributions evaluated according to sum (2.15) and integrals (2.13), (2.11), and (2.12). The source of second moment is a purely collisional quantity given by,

$$\boldsymbol{\Gamma} = \chi(m\boldsymbol{C} \otimes \boldsymbol{C}) \quad , \tag{2.23}$$

calculated according to integral (2.10).

2.2 Constitutive Relations

In order to derive the constitutive relations for the pressure tensor $\boldsymbol{P}$, the flux of second moment $\boldsymbol{Q}$, and the source of second moment $\boldsymbol{\Gamma}$, it is necessary to evaluate the integrals on the right-hand-sides of equations (2.21), (2.22), and (2.23). These integrals involve the single particle distribution function $f(\boldsymbol{c},\boldsymbol{r})$, which we take to be the perturbed Maxwellian,

$$f(\boldsymbol{c},\boldsymbol{r}) = \left\{1 + \frac{\hat{K}_{ij}}{2T^2} C_i C_j + \frac{K_{ijk}}{6T^3}\left[C_i C_j C_k - T(C_i \delta_{jk} + C_j \delta_{ki} + C_k \delta_{ij})\right]\right\} f_o(\boldsymbol{c},\boldsymbol{r}) \quad , \qquad (2.24)$$

where $\hat{K}_{ij}$ are the components of the deviatoric part of the second moment $\boldsymbol{K} \equiv \langle \boldsymbol{C} \otimes \boldsymbol{C} \rangle$, K_{ijk} are the components of the third moment $\langle \boldsymbol{C} \otimes \boldsymbol{C} \otimes \boldsymbol{C} \rangle$, and $f_o(\boldsymbol{c},\boldsymbol{r})$ is the Maxwellian distribution given by,

$$f_o(\boldsymbol{c},\boldsymbol{r}) = \frac{n}{(2\pi T)^{3/2}} \exp\left(-\frac{\boldsymbol{C}\cdot\boldsymbol{C}}{2T}\right) \quad . \qquad (2.25)$$

With the distribution function given by equation (2.24), the components $< \rho C_i C_j >$ of the transport part of the pressure tensor are $\rho(T\delta_{ij} + \hat{K}_{ij})$, and the components $< \rho C_i C_j C_k >$ of the transport part of the flux of second moment are K_{ijk}. Strictly, the perturbed Maxwellian given by equation (2.24) is valid only if the perturbations $\hat{K}_{ij}$ are small compared to T, and the perturbations K_{ijk} are small compared to $T^{3/2}$.

In order to compute the collisional contributions to the constitutive quantities, we need the changes per collision in the appropriate particle properties. For a collision between hard spheres of mass m, with fluctuation velocities $\boldsymbol{C}_1$ and $\boldsymbol{C}_2$ before collision, and velocities $\boldsymbol{C}_1'$ and $\boldsymbol{C}_2'$ after collision, the change in velocity of the first particle is,

$$\boldsymbol{C}_1' - \boldsymbol{C}_1 = -\frac{1}{2}(1+e)(\boldsymbol{g}\cdot\boldsymbol{k})\boldsymbol{k} \quad , \tag{2.26}$$

where e is the coefficient of restitution between the particles, $\boldsymbol{k}$ is the unit vector directed from the center of the first particle to the center of the second at impact, and $\boldsymbol{g} \equiv \boldsymbol{C}_1 - \boldsymbol{C}_2$. The change in the second moment of the first particle is,

$$\boldsymbol{C}_1' \otimes \boldsymbol{C}_1' - \boldsymbol{C}_1 \otimes \boldsymbol{C}_1 = (1+e)(\boldsymbol{g}\cdot\boldsymbol{k})\left[-\boldsymbol{C}_1 \otimes \boldsymbol{k} + \frac{(1+e)}{4}(\boldsymbol{g}\cdot\boldsymbol{k})\boldsymbol{k}\otimes\boldsymbol{k}\right] \quad , \tag{2.27}$$

and the total change in the second moment is,

$$\begin{aligned}\boldsymbol{C}_1' \otimes \boldsymbol{C}_1' + \boldsymbol{C}_2' \otimes \boldsymbol{C}_2' - \boldsymbol{C}_1 \otimes \boldsymbol{C}_1 - \boldsymbol{C}_2 \otimes \boldsymbol{C}_2 = \\ -\frac{(1+e)}{2}(\boldsymbol{g}\cdot\boldsymbol{k})\{(1-e)(\boldsymbol{g}\cdot\boldsymbol{k})\boldsymbol{k}\otimes\boldsymbol{k} + [\boldsymbol{g} - (\boldsymbol{g}\cdot\boldsymbol{k})\boldsymbol{k}]\otimes\boldsymbol{k} + \boldsymbol{k}\otimes[\boldsymbol{g} - (\boldsymbol{g}\cdot\boldsymbol{k})\boldsymbol{k}]\}\,.\end{aligned} \tag{2.28}$$

In the collisonal part $\boldsymbol{\theta}(m\boldsymbol{C})$ of the pressure tensor, both $\boldsymbol{E}(m\boldsymbol{C})$ and $\tilde{\boldsymbol{E}}(m\boldsymbol{C})$ vanish because momentum is conserved in every collision. According to the sum (2.15), the only nonzero contribution is from $\boldsymbol{\omega}(m\boldsymbol{C})$ in which the change $\phi_1' - \phi_1$ is given by equation (2.26). Here we retain terms up to those that are linear in velocity gradients and second moments. Implicitly then, we ignore terms nonlinear in the second moment, terms nonlinear in the third moment, gradients of the third moment, and products of temperature gradients and third moments. In this manner we obtain the components of the collisional pressure tensor,

$$\theta_i(mC_j) = 2(1+e)\rho G T\left\{\left[1 - \frac{2\sigma}{3(\pi T)^{1/2}}D_{kk}\right]\delta_{ij} - \frac{4\sigma}{5(\pi T)^{1/2}}\hat{D}_{ij} + \frac{2}{5T}\hat{K}_{ij}\right\} \quad , \tag{2.29}$$

where D_{ij} are the components of the strain tensor $\boldsymbol{D} \equiv (\nabla\boldsymbol{u} + \nabla\boldsymbol{u}^T)/2$, an overhat denotes the deviatoric part of a tensor, and $G \equiv \nu g_o(\nu)$. According to the sum (2.21), the components of the full pressure tensor are then,

$$P_{ij} = 2(1+e)\rho GT\left\{\left[F - \frac{2\sigma}{3(\pi T)^{1/2}} D_{kk}\right]\delta_{ij} - \frac{4\sigma}{5(\pi T)^{1/2}}\hat{D}_{ij} + \frac{H}{T}\hat{K}_{ij}\right\} \quad , \tag{2.30}$$

where $F(\nu,e)$ and $H(\nu,e)$ are functions of solid fraction and coefficient of restitution defined by,

$$F(\nu,e) \equiv 1 + \frac{1}{2(1+e)G} \quad , \tag{2.31}$$

and

$$H(\nu,e) \equiv \frac{2}{5}\left[1 + \frac{5}{4(1+e)G}\right] \quad . \tag{2.32}$$

In the collisional contributions $\theta_i(mC_jC_k)$ to the components Q_{ijk} of flux of second moment, we retain terms linear in the gradients of temperature T, solid volume fraction ν, and deviatoric second moment $\hat{K}_{jk}$, as well as those linear in third moment K_{ijk}. According to decomposition (15), contributions to $\theta_i(mC_jC_k)$ come from $\omega_i(mC_jC_k)$ with the change in second moment of the first particle given by expression (2.27), and from $E_i(mC_jC_k)$ and $\tilde{E}_i(mC_jC_k)$ with the total change in second moment given by expression (2.28). Interestingly, the terms proportional to gradients of temperature and solid volume fraction from $E_i(mC_jC_k)$ and $\tilde{E}_i(mC_jC_k)$ are also proportional to $(1-e)$, and may be neglected as second order effects for the nearly elastic particles of interest here. In fact, the only terms from $E_i(mC_jC_k)$ and $\tilde{E}_i(mC_jC_k)$ that we retain here are those contributed by $E_i(mC_jC_k)$ that are proportional to gradients of K_{ij}. The flux $\omega_i(mC_jC_k)$ gives rise to terms proportional to K_{ijk} as well as terms proportional to gradients of T and $\hat{K}_{jk}$. Strictly the gradients of $\hat{K}_{jk}$ are of higher order than those of

T, but they must be retained if the components $\hat{K}_{jk}$ are to be treated as mean fields with corresponding boundary conditions.

In writing down the results of these integrations, we employ the approximate expression obtained by Jenkins and Richman [1985 a] for the components of the third moment,

$$K_{ijk} = -\frac{3\pi^{1/2}(1+e)(2e-1)\sigma T^{1/2}}{2(49-33e)}\left[1+\frac{5}{3(1+e)^2(2e-1)G}\right]\left(\frac{\partial T}{\partial r_i}\delta_{jk}+\frac{\partial T}{\partial r_j}\delta_{ki}+\frac{\partial T}{\partial r_k}\delta_{ij}\right), \qquad (2.33)$$

where, for consistency with the considerations above, we have neglected terms proportional to products of density gradients and $(1-e)$. According to equation (2.22) and the considerations for approximating the integrations outlined above, the components Q_{ijk} of the flux of second moment (equal to the sum of the transport contributions ρK_{ijk} and the collisional contributions $\theta_i(mC_jC_k)$), are

$$Q_{ijk} = -\frac{4(1+e)\rho G\sigma T^{1/2}}{5\pi^{1/2}}\left\{\alpha(\nu,e)\frac{\partial T}{\partial r_i}\delta_{jk}+\beta(\nu,e)\left(\frac{\partial T}{\partial r_j}\delta_{ki}+\frac{\partial T}{\partial r_k}\delta_{ij}\right)+\right.$$
$$\left.+\frac{(1+3e)}{7}\left[\left(\frac{\partial \hat{K}_{jk}}{\partial r_i}+\frac{\partial \hat{K}_{ki}}{\partial r_j}+\frac{\partial \hat{K}_{ij}}{\partial r_k}\right)+\left(\frac{\partial \hat{K}_{im}}{\partial r_m}\delta_{jk}+\frac{\partial \hat{K}_{jm}}{\partial r_m}\delta_{ki}+\frac{\partial \hat{K}_{km}}{\partial r_m}\delta_{ij}\right)\right]\right\}, \qquad (2.34)$$

in which $\alpha(\nu,e)$ and $\beta(\nu,e)$ are functions of solid fraction and coefficient of restitution defined by,

$$\alpha(\nu,e) \equiv 1+\frac{3\pi(1+e)(2e-1)}{2(49-33e)}\left[1+\frac{5}{3(1+e)^2(2e-1)G}\right]\left[1+\frac{5}{4(1+e)G}\right], \qquad (2.35)$$

and

$$\beta(\nu,e) \equiv 1+\frac{27\pi(1+e)(2e-1)}{8(49-33e)}\left[1+\frac{5}{3(1+e)^2(2e-1)G}\right]\left[1+\frac{5}{9(1+e)G}\right]. \qquad (2.36)$$

If the flows are dense, then the transport part ρK_{ijk} of Q_{ijk} may be neglected compared to the collisional part $\theta_i(mC_jC_k)$. In fact, if K_{ijk} is simply set equal to zero, then the resulting expression for the components of the flux of second moment is given by equation (2.34) with $\alpha(\nu,e)=\beta(\nu,e)=1$. Such a simple expression would apply to dense flows only.

In order to derive an appropriate constitutive relation for the source of second moment $\Gamma \equiv \chi(m\boldsymbol{C}\otimes\boldsymbol{C})$, we employ expression (2.28) for the total change in the second moment in equation (10) for $\chi(m\boldsymbol{C}\otimes\boldsymbol{C})$. We retain all terms that are linear in second moment and in gradients of velocity. Furthermore, according to the second moment equation (2.18), there are circumstances (such as in homogeneous shearing) in which the source of second moment Γ must balance products $\boldsymbol{P}\cdot\nabla\boldsymbol{u}+(\boldsymbol{P}\cdot\nabla\boldsymbol{u})^{\mathrm{T}}$ of the pressure tensor and the velocity gradient. Because, according to equation (2.30), $\boldsymbol{P}$ includes terms up to those linear in $\boldsymbol{K}$ and $\boldsymbol{D}$, the simplest constitutive relation for Γ that is consistent with constitutive relation (2.30) for $\boldsymbol{P}$ must include terms proportional to $\boldsymbol{K}\cdot\nabla\boldsymbol{u}$ and $\nabla\boldsymbol{u}\cdot\nabla\boldsymbol{u}$. In addition, the ordering scheme used by Jenkins and Richman [1985 a] showed that in homogeneous shearing, for example, both $\hat{\boldsymbol{K}}$ and $\nabla\boldsymbol{u}$ are of the same order. Consequently, the constitutive relation for Γ must also include terms proportional to $\hat{\boldsymbol{K}}\cdot\hat{\boldsymbol{K}}$. On the other hand, equation (2.18) also demonstrates the there may be circumstances (such as in a steady thermalized granular assembly undergoing no mean motion) in which the source of second moment Γ must balance the divergence of $\boldsymbol{Q}$. The types of terms in the divergence of $\boldsymbol{Q}$ that will also arise in $\Gamma\equiv\chi(m\boldsymbol{C}\otimes\boldsymbol{C})$ are products of the temperature gradient with itself, products of the temperature gradient with

the density gradient, products of the temperature gradient with the gradient of $\hat{\boldsymbol{K}}$, and products of the density gradient with the gradient of $\hat{\boldsymbol{K}}$. Because the latter two are of higher order than the former two, they will be neglected in Γ and whenever they arise from the divergence of $\boldsymbol{Q}$ in the second moment equation (2.18). On the other hand, there are terms in $\Gamma \equiv \chi(mC \otimes C)$ from the Maxwellian contribution to the single particle distribution function (2.24) that are products of the temperature gradient with itself, and products of the temperature gradient with the density gradient. Interestingly however, each of these products is proportional to (1-*e*) and may be neglected for the nearly elastic particles of interest here. In principle, the correction to the Maxwellian involving K_{ijk} would give terms in $\Gamma \equiv \chi(mC \otimes C)$ proportional to products of K_{ijk} and gradients of T, products of K_{ijk} and gradients of ν, products of K_{ijk} with itself, as well as terms proportional to the gradient of K_{ijk} itself. With K_{ijk} approximated by (2.33), these terms in turn give rise to terms like those arising from the divergence of $\boldsymbol{Q}$, and strictly should be retained. We neglect them here only because our goal is to write down the *simplest* constitutive theory in which the components $\hat{K}_{ij}$ may be treated as mean fields. Neglecting terms in $\Gamma \equiv \chi(mC \otimes C)$ that are proportional to products of both the temperature gradient with itself, and the temperature gradient with the density gradient does not actually affect the mathematical structure of the resulting theory because terms of the same type appear in the second moment equation from the divergence of $\boldsymbol{Q}$.

By carrying out the integration $\chi(mC \otimes C)$ for Γ according to these considerations and by extracting those terms proportional to the spin tensor

$\boldsymbol{W} \equiv (\nabla \boldsymbol{u}^{\mathrm{T}} - \nabla \boldsymbol{u})/2$, we find that the (components of the) source of second moment can be decomposed into the sum,

$$\Gamma_{ij} = \gamma_{ij} + \theta_i(mC_k)W_{jk} + \theta_j(mC_k)W_{ik} \quad . \tag{2.37}$$

Here the components γ_{ij} (of $\boldsymbol{\gamma}$) may be written in terms of the tensor components D_{ij}, $\hat{K}_{ij}$, $d_{ij} \equiv D_{ik}D_{kj}$, $A_{ij} \equiv (\hat{K}_{ik}D_{kj} + D_{ik}\hat{K}_{kj})/2$, and $b_{ij} \equiv \hat{K}_{ik}\hat{K}_{kj}$ as

$$\begin{aligned}\gamma_{ij} = \frac{6(1+e)\rho G T^{3/2}}{\sigma\pi^{1/2}}\Bigg\{ & \frac{(1-e)}{3}\left[-4 + \frac{\sigma\pi^{1/2}}{T^{1/2}}D_{kk} - \frac{\sigma^2}{5T}D_{kk}D_{mm} - \frac{2\sigma^2}{5T}d_{kk} + \frac{2\sigma\pi^{1/2}}{5T^{3/2}}A_{kk} - \frac{1}{5T^2}b_{kk}\right]\delta_{ij} \\ & + \frac{2(2-e)\sigma}{5T^{1/2}}\left[\pi^{1/2} - \frac{2\sigma}{7T^{1/2}}D_{kk}\right]\hat{D}_{ij} + \frac{2(3-e)}{5T}\left[-2 + \frac{\sigma\pi^{1/2}}{3T^{1/2}}D_{kk}\right]\hat{K}_{ij} \\ & - \frac{8(2-e)\sigma^2}{35T}\hat{d}_{ij} + \frac{4\pi^{1/2}(5-2e)\sigma}{35T^{3/2}}\hat{A}_{ij} - \frac{4(3-e)}{35T^2}\hat{b}_{ij}\Bigg\} \quad ,\end{aligned} \tag{2.38}$$

where overhats denote the deviatoric part of a tensor.

The set of equations that determine the solid fraction ν, components u_i of the mean velocity, granular temperature T, and the components $\hat{K}_{ij}$ of the deviatoric second moment are the balance of mass (2.16), the balance of momentum (2.17), and either the balance of full second moment (2.18) or both the energy equation (2.19) and the deviatoric second moment equation (2.20). Constitutive relation (2.37) may be employed to eliminate Γ_{ij} from equation (2.20). With the velocity gradient $\partial u_i/\partial x_j$ written as the sum of the strain rate $D_{ij} \equiv (\partial u_i/\partial x_j + \partial u_j/\partial x_i)/2$ and the spin tensor $W_{ij} \equiv (\partial u_i/\partial x_j - \partial u_j/\partial x_i)/2$, and the pressure tensor P_{ij} written as the sum $\rho K_{ij} + \theta_i(mC_j)$ wherever it multiplies the spin tensor, the deviatoric second moment equation becomes,

$$\rho\overset{\circ}{\hat{K}}_{ij} = -\frac{\partial}{\partial x_k}\left(Q_{kij} - \frac{1}{3}Q_{kmm}\delta_{ij}\right) - \rho K_{ik}W_{jk} - \rho K_{jk}W_{ik} - P_{ik}D_{jk} - P_{jk}D_{ik} + \frac{2}{3}P_{km}D_{km}\delta_{ij} + \hat{\gamma}_{ij} \quad . \tag{2.39}$$

2.3 Constitutive Relations for Nearly Elastic Particles

When the particles are nearly elastic and there is no external source, such as a vibrating boundary, that induces significantly anisotropic velocity fluctuations, the deviatoric components $\hat{K}_{ij}$ may be treated in the following approximate manner. Following Jenkins and Richman [1985 a], the deviatoric second moment equation (2.20) is approximated to lowest order by,

$$0 = -P_{ik}\frac{\partial u_j}{\partial x_k} - P_{jk}\frac{\partial u_i}{\partial x_k} + \frac{2}{3}P_{mk}\frac{\partial u_m}{\partial x_k}\delta_{ij} + \hat{\Gamma}_{ij} \quad . \tag{2.40}$$

in which, according to equations (2.30), (2.37), and (2.38), the components P_{ik} and $\hat{\Gamma}_{ij}$ are given to lowest order by,

$$P_{ij} = 2(1+e)\rho GFT\delta_{ij} \quad , \tag{2.41}$$

and

$$\hat{\Gamma}_{ij} = \frac{12(1+e)\rho GT^{3/2}}{5\sigma}\left[\frac{(2-e)\sigma}{T^{1/2}}\hat{D}_{ij} - \frac{2(3-e)}{\pi^{1/2}T}\hat{K}_{ij}\right] \quad . \tag{2.42}$$

Employing equations (2.41) and (2.42) in (2.40), we find that to this order of approximation $\hat{K}_{ij}$ are given in terms of $\hat{D}_{ij}$ by,

$$\frac{\hat{K}_{ij}}{T} = -\frac{\pi^{1/2}(3e-1)}{6(3-e)}\left[1 + \frac{5}{2(3e-1)(1+e)G}\right]\frac{\sigma\hat{D}_{ij}}{T^{1/2}} \quad . \tag{2.43}$$

In the theory for nearly elastic particles, this constitutive relation replaces the exact balance equation (2.20), and may be used to eliminate the components $\hat{K}_{ij}$ from the constitutive theory. In this manner, we find from equation (2.30) that the approximation for P_{ij} that is linear in $\hat{D}_{ij}$ may be written as,

$$P_{ij} = 2(1+e)\rho G T\left[F - \frac{2\sigma}{3(\pi T)^{1/2}} D_{kk}\right]\delta_{ij} - 2\mu E\hat{D}_{ij} \quad , \tag{2.44}$$

in which,

$$\mu \equiv \frac{4(1+e)\sigma\rho G T^{1/2}}{5\pi^{1/2}} \quad , \tag{2.45}$$

and

$$E \equiv 1 + \frac{\pi(3e-1)}{12(3-e)}\left[1 + \frac{5}{4(1+e)G}\right]\left[1 + \frac{5}{2(3e-1)(1+e)G}\right] \quad . \tag{2.46}$$

The remaining constitutive quantities are the energy flux Q_{ijj} and the energy dissipation Γ_{ii}. If the deviatoric components $\hat{K}_{ij}$ are ignored compared to the isotropic temperature T, then equation (34) gives the energy flux,

$$Q_{ijj} = -5\mu M \frac{\partial T}{\partial x_i} \quad , \tag{2.47}$$

where

$$M \equiv 1 + \frac{9\pi(1+e)(2e-1)}{4(49-33e)}\left[1 + \frac{5}{3(1+e)^2(2e-1)G}\right]\left[1 + \frac{5}{6(1+e)G}\right] \quad . \tag{2.48}$$

If only terms up to those linear in $\hat{D}_{ij}$ are retained in equation (2.38), then the dissipation is given by,

$$\Gamma_{ii} = -\frac{30(1-e)\mu T}{\sigma^2}\left[1 - \frac{\pi^{1/2}\sigma}{4T^{1/2}} D_{kk}\right] \quad . \tag{2.49}$$

With appropriate boundary conditions, the balance of mass (2.16), the balance of linear momentum (2.17), the balance of energy (2.19), and constitutive relations (2.44) for the pressure tensor P_{ij}, (2.47) for the energy flux Q_{ijj}, and (2.49) for the energy dissipation Γ_{ii} form a complete set of equations for the solid fraction ν, the mean velocity u, and the granular temperature T.

An even simpler set of constitutive relations for nearly elastic particles is obtained by setting the coefficient of restitution e equal to 1 everywhere except in the factor of $(1-e)$ in the energy dissipation Γ_{ii}, and by neglecting terms proportional to D_{kk} in both the pressure tensor P_{ij} and the dissipation Γ_{ii}. The balance of mass, momentum, and energy are again given by equations (2.16), (2.17), and (2.19).

2.4 Equipartition and Relaxation of the Components of the Second Moment

Here we consider an unbounded space (with no body force $\boldsymbol{g}$) in which the solid fraction ν is uniform throughout, the mean velocity $\boldsymbol{u}$ vanishes everywhere, and the second moment $\boldsymbol{K}$ varies with time t but not with position. In this case, the velocity gradients and flux of second moment both vanish, and the pressure tensor is a function of time only. Under these circumstances, the balance of mass and the balance of momentum are satisfied identically.

In order to write the down the balance of second moment, we introduce an initial temperature T_o, a dimensionless time $s \equiv (GT_o^{1/2}/\sigma\pi^{1/2})t$, a dimensionless temperature $\tau \equiv T/T_o$, and dimensionless components of the second moment $\kappa_{ij} \equiv K_{ij}/T_o$. The function $G(\nu)$ $(=\nu g_o(\nu))$ that appears as a numerical factor in the dimensionless time increases monotonically from zero when $\nu = 0$, and becomes unbounded as ν approaches its maximum value. Consequently, the dimensional time t that corresponds to any prescribed value of s varies monotonically from large values in very dilute flows to very small values as the assembly approaches its maximum density.

With the components Γ_{ij} $(=\gamma_{ij})$ of the source of second moment given by equation (2.38), the energy equation (2.19) becomes,

$$\frac{d\tau}{ds} = -8(1-e^2)\left[1+\frac{1}{20\tau^2}\left(\hat{\kappa}_{11}^2+\hat{\kappa}_{22}^2+\hat{\kappa}_{33}^2+2\hat{\kappa}_{12}^2+2\hat{\kappa}_{23}^2+2\hat{\kappa}_{31}^2\right)\right]\tau^{3/2} \quad . \tag{2.50}$$

Similarly, the diagonal components of the deviatoric second moment equation (2.20) become,

$$\frac{d\hat{\kappa}_{11}}{ds} = -\frac{24(1+e)(3-e)\tau^{3/2}}{5}\left[\frac{\hat{\kappa}_{11}}{\tau}+\frac{1}{21\tau^2}\left(2\hat{\kappa}_{11}^2-\hat{\kappa}_{22}^2-\hat{\kappa}_{33}^2+\hat{\kappa}_{12}^2+\hat{\kappa}_{13}^2-2\hat{\kappa}_{23}^2\right)\right] \quad , \tag{2.51}$$

$$\frac{d\hat{\kappa}_{22}}{ds} = -\frac{24(1+e)(3-e)\tau^{3/2}}{5}\left[\frac{\hat{\kappa}_{22}}{\tau}+\frac{1}{21\tau^2}\left(2\hat{\kappa}_{22}^2-\hat{\kappa}_{33}^2-\hat{\kappa}_{11}^2+\hat{\kappa}_{12}^2+\hat{\kappa}_{23}^2-2\hat{\kappa}_{13}^2\right)\right] \quad , \tag{2.52}$$

and,

$$\frac{d\hat{\kappa}_{33}}{ds} = -\frac{24(1+e)(3-e)\tau^{3/2}}{5}\left[\frac{\hat{\kappa}_{33}}{\tau}+\frac{1}{21\tau^2}\left(2\hat{\kappa}_{33}^2-\hat{\kappa}_{11}^2-\hat{\kappa}_{22}^2+\hat{\kappa}_{13}^2+\hat{\kappa}_{23}^2-2\hat{\kappa}_{12}^2\right)\right] \quad . \tag{2.53}$$

The off-diagonal components of the deviatoric second moment equation are,

$$\frac{d\hat{\kappa}_{12}}{ds} = -\frac{24(1+e)(3-e)\tau^{3/2}}{5}\left[\frac{\hat{\kappa}_{12}}{\tau}+\frac{1}{7\tau^2}\left(\hat{\kappa}_{11}\hat{\kappa}_{12}+\hat{\kappa}_{12}\hat{\kappa}_{22}+\hat{\kappa}_{13}\hat{\kappa}_{32}\right)\right] \quad , \tag{2.54}$$

$$\frac{d\hat{\kappa}_{13}}{ds} = -\frac{24(1+e)(3-e)\tau^{3/2}}{5}\left[\frac{\hat{\kappa}_{13}}{\tau}+\frac{1}{7\tau^2}\left(\hat{\kappa}_{11}\hat{\kappa}_{13}+\hat{\kappa}_{12}\hat{\kappa}_{23}+\hat{\kappa}_{13}\hat{\kappa}_{33}\right)\right] \quad , \tag{2.55}$$

and,

$$\frac{d\hat{\kappa}_{23}}{ds} = -\frac{24(1+e)(3-e)\tau^{3/2}}{5}\left[\frac{\hat{\kappa}_{23}}{\tau}+\frac{1}{7\tau^2}\left(\hat{\kappa}_{21}\hat{\kappa}_{13}+\hat{\kappa}_{22}\hat{\kappa}_{23}+\hat{\kappa}_{23}\hat{\kappa}_{33}\right)\right] \quad . \tag{2.56}$$

The lowest order relaxation behavior of the second moment is obtained by ignoring the terms in equations (2.50) through (2.56) that are nonlinear in the components of the second moment. In this manner, we find from the approximation of equation (2.50) that the temperature decays according to,

$$\tau = \frac{1}{\left[1+4(1-e^2)s\right]^2} \quad , \tag{2.57}$$

which satisifies the initial condition $\tau(0)=1$. As expected, the granular temperature remains unchanged when the coefficient of restitution $e=1$, and decays to zero at a rate that increases as the coefficient of restitution e decreases from unity. With $\tau(s)$ given by equation (2.57), the corresponding linear approximations to equations (2.51) through (2.56) demonstrate that when $e\neq 1$ the deviatoric components of the second moment evolve according to,

$$\hat{\kappa}_{ij}=\hat{\kappa}_{ij}(0)\left[1+4(1-e^2)s\right]^{\frac{-6(3-e)}{5(1-e)}} \quad , \tag{2.58}$$

and when $e=1$

$$\hat{\kappa}_{ij}=\hat{\kappa}_{ij}(0)\exp\left(-\frac{96s}{5}\right) \quad . \tag{2.59}$$

Equation (2.57) demonstrates the tendency of the temperature to decay when the particles are inelastic, and shows how the decay occurs more rapidly as the particles become more inelastic. Equations (2.58) and (2.59), on the other hand, demonstrate that regardless of the extent of the anisotropy initially imposed, as a result of repeated collisions between particles the velocity fluctuations tend to become isotropic as time increases. In particular, the decay of the diagonal components of $\hat{\boldsymbol{\kappa}}$ demonstrate the trend toward equipartition of energy among the three degrees of translational freedom. In direct contrast with the decay of the temperature, the anisotropies in the velocity fluctuations actually decay more *slowly* as the particles become more *inelastic*. This is because, while repeated collisions promote isotropy, the frequency of collisions decreases as the particles become more inelastic.

The nonlinear terms in equations (2.51) through (2.56) demonstrate that anisotropy in the diagonal components of the second moment can be induced by the

presence of off-diagonal components of the second moment, but that off-diagonal components of the second moment can not be induced by the presence of anisotropies in the diagonal components alone. Interestingly, the nonlinear terms in equations (2.54) through (2.56) demonstrate that the off-diagonal component of the second moment in a given plane will be induced by two off-diagonal components when the two occur simultaneously in mutually perpendicular planes that are normal to the given plane.

As a numerical example to demonstrate the equipartition tendency of the diagonal components of second moment to equilibrate, we consider the extreme case in which initially the fluctuation energy is entirely in the x_1-direction ($\tau(0)=1$, $\kappa_{11}(0)=3$, and $\kappa_{22}(0)=\kappa_{33}(0)=0$) and the off-diagonal components of the second moment all vanish ($\kappa_{12}(0)=\kappa_{23}(0)=\kappa_{13}(0)=0$). With $\kappa_{11}=\tau+\hat{\kappa}_{11}$, $\kappa_{22}=\tau+\hat{\kappa}_{22}$, and $\kappa_{33}=\tau+\hat{\kappa}_{33}$, this corresponds to assigning the initial values $\hat{\kappa}_{11}(0)=2$, and $\hat{\kappa}_{22}(0)=\hat{\kappa}_{33}(0)=-1$ to the diagonal components of the deviatoric second moment. In Figures 2.1, 2.2, 2.3 and 2.4 we show for four values of coefficient of restitution ($e=1$, .8, .5 and 0) the evolution in time (s) of the granular temperature $\tau(s)$ and the separate diagonal components $\kappa_{11}(s)$ and $\kappa_{22}(s)=\kappa_{33}(s)$ of the second moment. The off-diagonal components remain zero for all time. In these figures, the solid curves correspond to the solutions of the full set of equations (2.50), (2.51), and (2.52), and the dashed curves correspond to the approximate solutions given by equations (2.57), (2.58), and (2.59). The granular temperature $\tau=(\kappa_{11}+\kappa_{22}+\kappa_{33})/3$ remains constant when the particles are perfectly elastic, and decays to zero at rates that increase as the particles become increasingly inelastic. In all cases, the velocity fluctuations become increasingly isotropic with time, although the approach to isotropy becomes slower as the particles become more inelastic. Figures 2.1, 2.2, 2.3

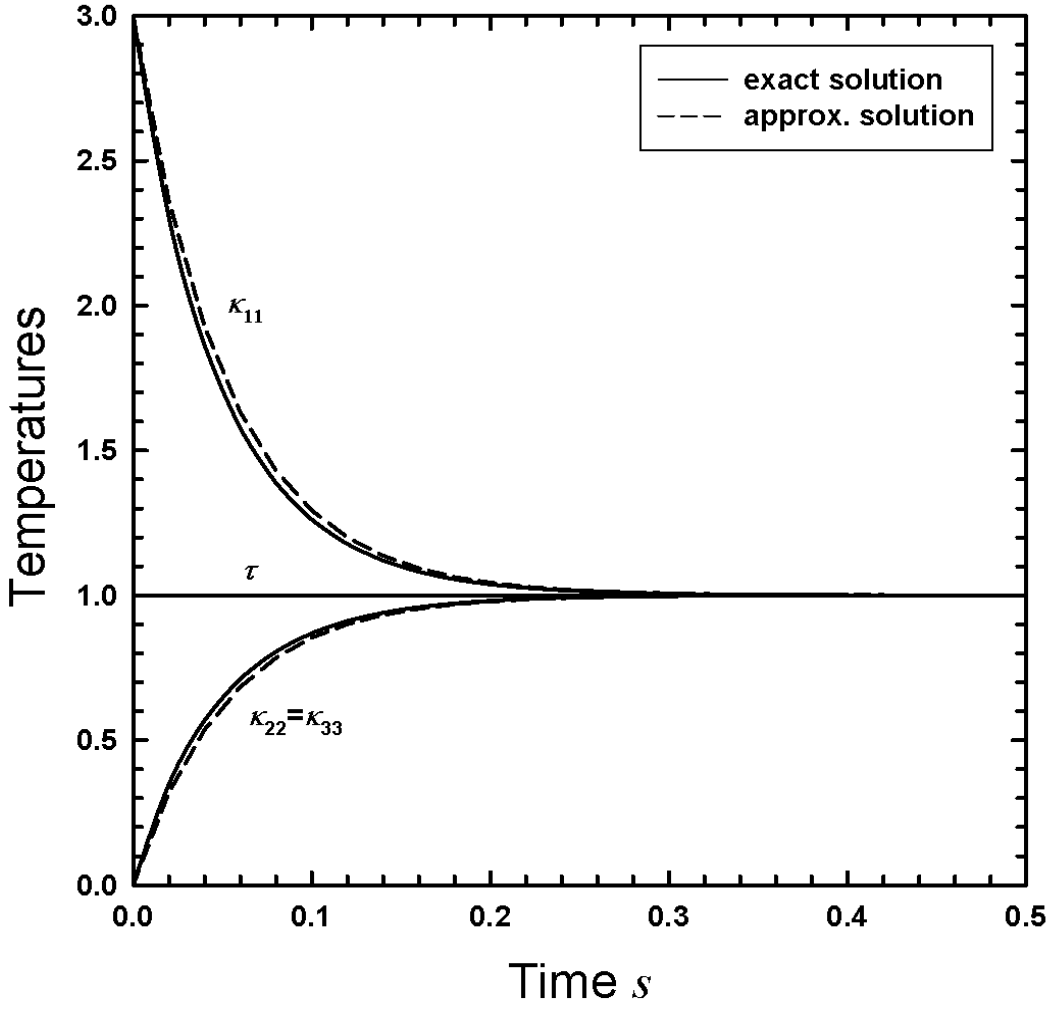

Figure 2.1: The variations of τ, κ_{11}, κ_{22}, κ_{33} with s when e=1 and $\tau(0)$=1, $\kappa_{11}(0)$=3, $\kappa_{22}(0)$=0, $\kappa_{33}(0)$=0, $\kappa_{12}(0)$=0, $\kappa_{23}(0)$=0, $\kappa_{13}(0)$=0. Solid (dashed) lines indicate exact (approximate) solutions.

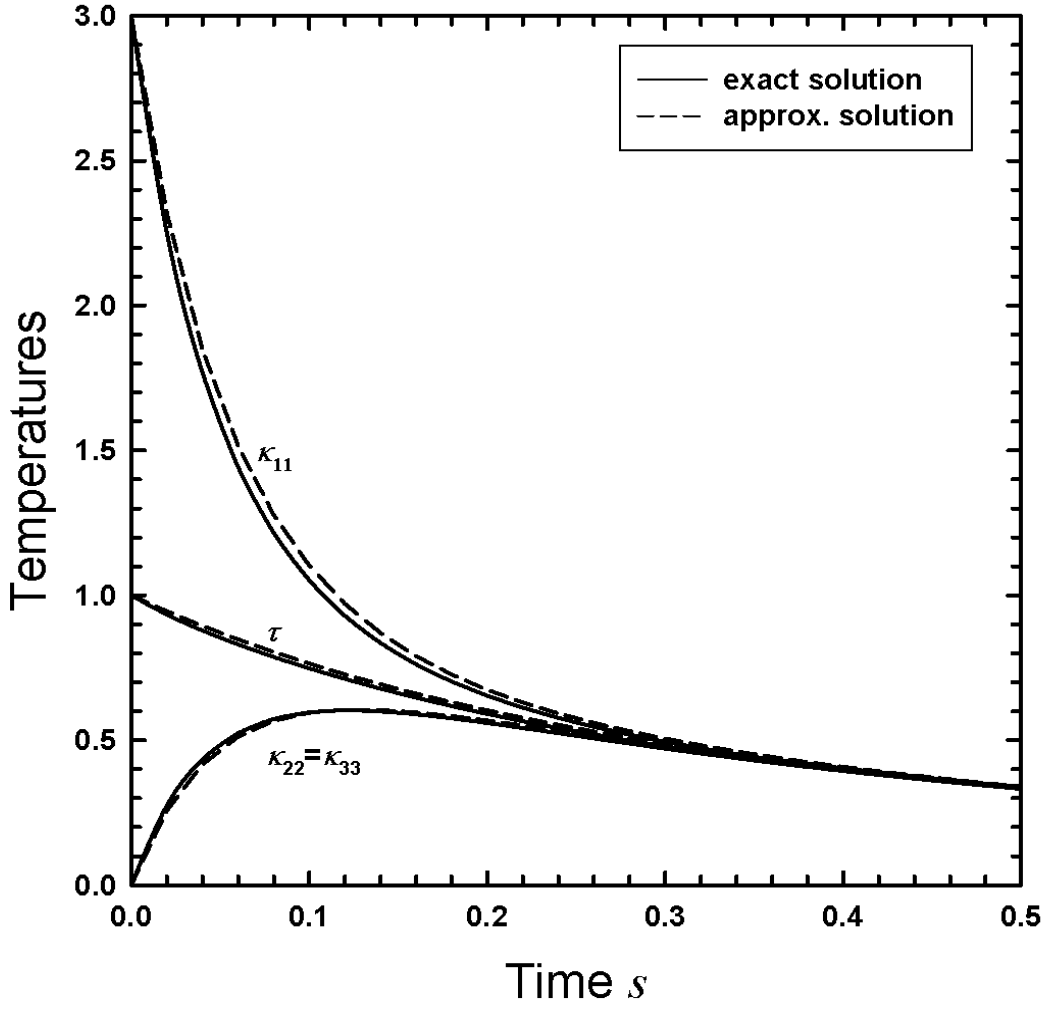

Figure 2.2: The variations of τ, κ_{11}, κ_{22}, κ_{33} with s when e=.8 and $\tau(0)$=1, $\kappa_{11}(0)$=3, $\kappa_{22}(0)$=0, $\kappa_{33}(0)$=0, $\kappa_{12}(0)$=0, $\kappa_{23}(0)$=0, $\kappa_{13}(0)$=0. Solid (dashed) lines indicate exact (approximate) solutions.

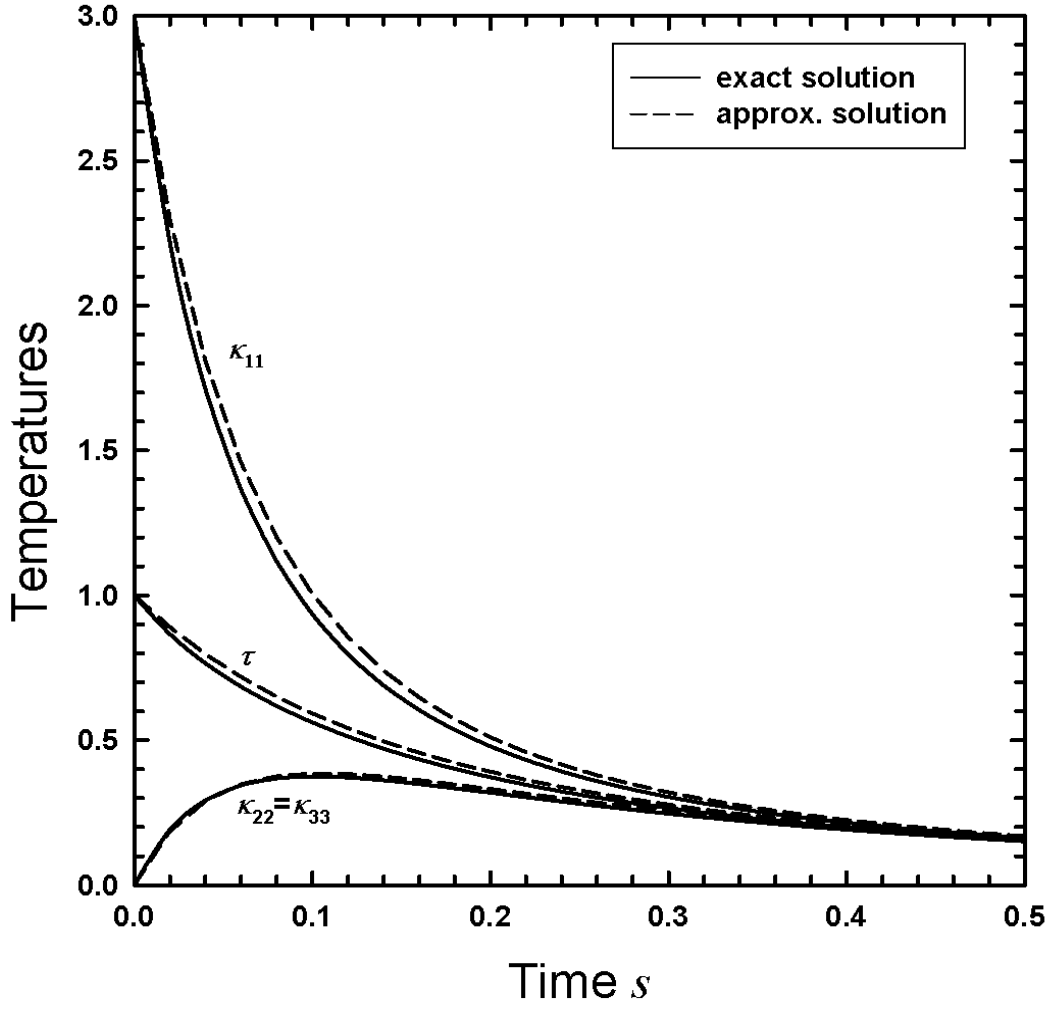

Figure 2.3: The variations of τ, κ_{11}, κ_{22}, κ_{33} with s when e=.5 and τ (0)=1, $\kappa_{11}(0)$=3, $\kappa_{22}(0)$=0, $\kappa_{33}(0)$=0, $\kappa_{12}(0)$=0, $\kappa_{23}(0)$=0, $\kappa_{13}(0)$=0. Solid (dashed) lines indicate exact (approximate) solutions.

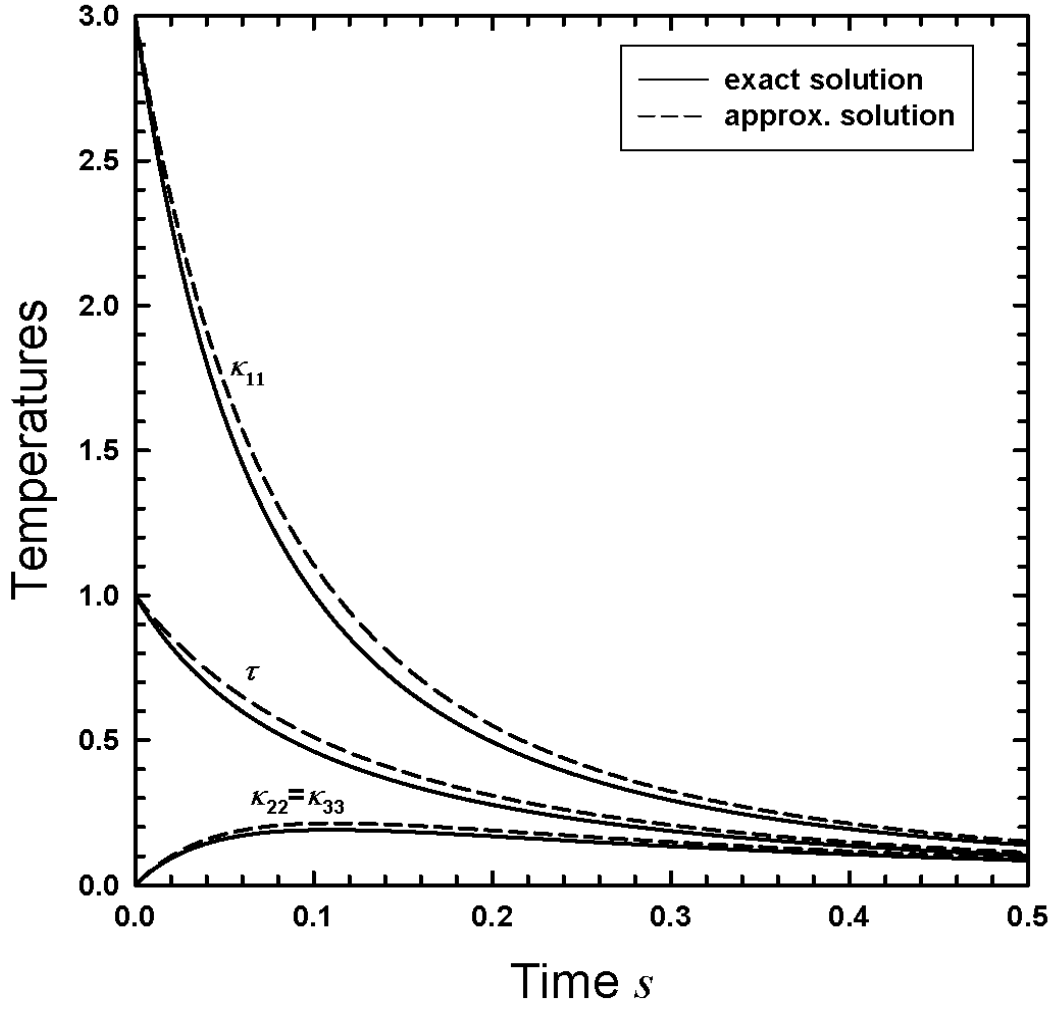

Figure 2.4: The variations of τ, κ_{11}, κ_{22}, κ_{33} with s when e=0 and $\tau(0)$=1, $\kappa_{11}(0)$=3, $\kappa_{22}(0)$=0, $\kappa_{33}(0)$=0, $\kappa_{12}(0)$=0, $\kappa_{23}(0)$=0, $\kappa_{13}(0)$=0. Solid (dashed) lines indicate exact (approximate) solutions.

and 2.4 also demonstrate excellent agreement between the exact numerical solutions and the approximate closed form solutions (2.57), (2.58), and (2.59).

As a numerical example to demonstrate the extent to which the presence of off-diagonal components of the second moment can induce anisotropy in the diagonal components, we consider the case in which the diagonal components are initially all equal ($\kappa_{11}(0)=\kappa_{22}(0)=\kappa_{33}(0)=\tau(0)=1$, so that $\hat{\kappa}_{11}(0)=\hat{\kappa}_{22}(0)=\hat{\kappa}_{33}(0)=0$), and only the x_1-x_2 off-diagonal component is non-zero ($\kappa_{12}(0)=1$ and $\kappa_{23}(0)=\kappa_{13}(0)=0$). The induced anisotropy is not captured by the approximate solutions (2.58) and (2.59). In this case, equations (2.55) and (2.56) show that κ_{13} and κ_{23} remain zero for all time. In Figures 2.5 and 2.6, we show the variation with time of τ and κ_{12} for $e=1$, .8, .5 and 0. The solid curves give the exact numerical solution. The dashed curves are the corresponding linear approximations given by equation (2.57) for τ, by equation (2.59) for κ_{12} when e=1, and by equation (2.58) for κ_{12} when $e=.8$, .5 and 0. The granular temperature behaves much like it did in the previous case. The behavior of the off-diagonal component is captured quite well by the approximate solutions. Figures 2.7 and 2.8 show the corresponding variations with time of the deviatoric diagonal components $\hat{\kappa}_{11}=\hat{\kappa}_{22}$, and $\hat{\kappa}_{33}$. According to these two figures, anisotropies in the diagonal components grow with time initially due to the presence of κ_{12}, and eventually decay with time as κ_{12} itself decays. Because the anisotropies in the diagonal components is due to the nonlinear terms in equations (2.51), (2.52), and (2.53), at all times their magnitudes are much smaller than the granular temperature itself.

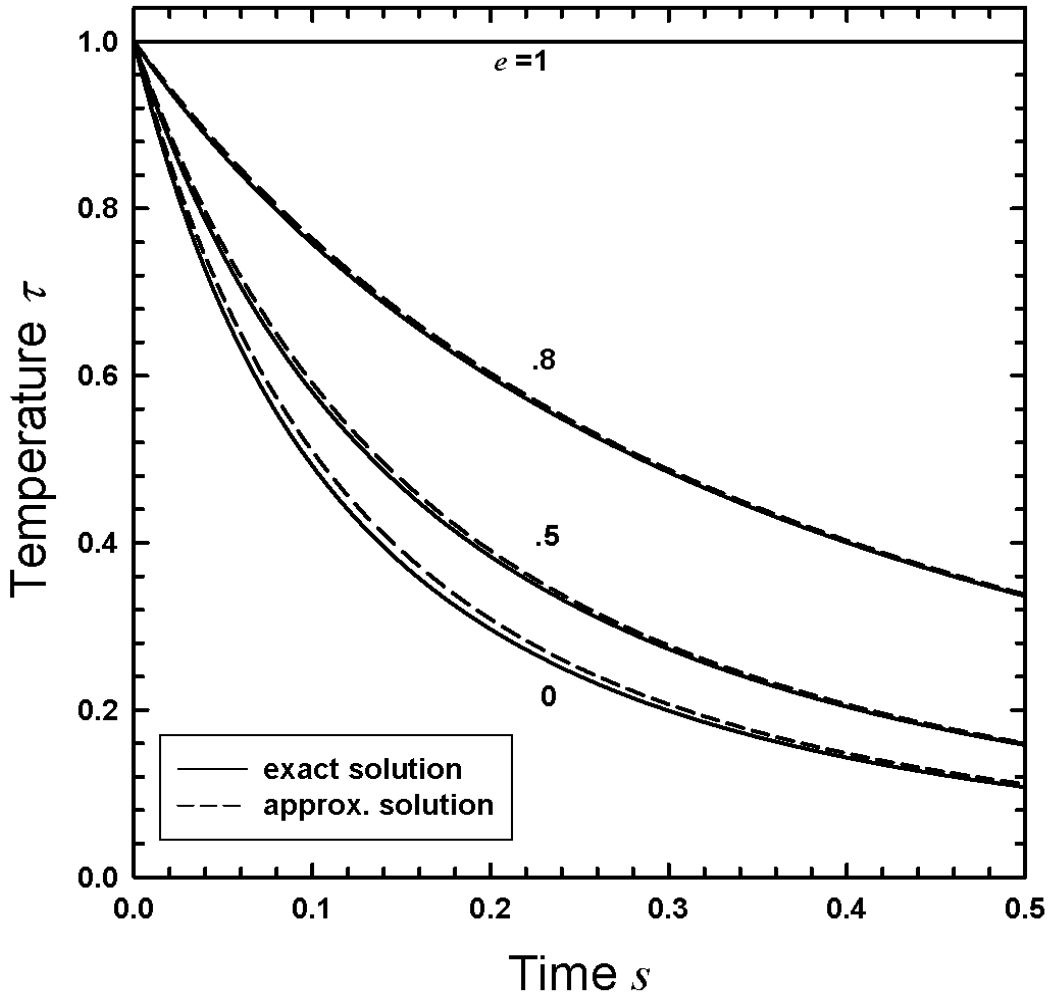

Figure 2.5: The variations of τ with s when e=1, .8, .5 and 0, and $\tau(0)$=1, $\kappa_{11}(0)$=1, $\kappa_{22}(0)$=1, $\kappa_{33}(0)$=1, $\kappa_{12}(0)$=1, $\kappa_{23}(0)$=0, $\kappa_{13}(0)$=0. Solid (dashed) lines indicate exact (approximate) solutions.

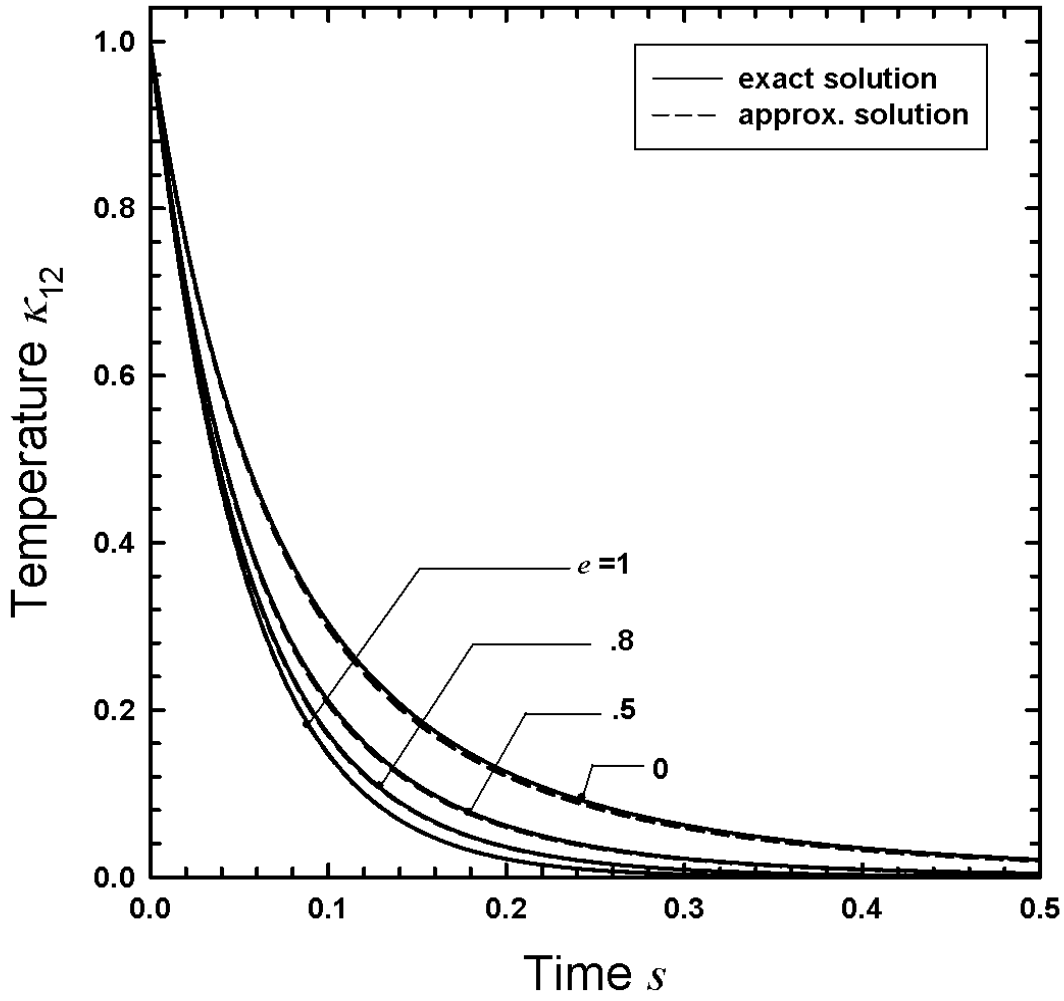

Figure 2.6: The variations of κ_{12} with s when e=1, .8, .5 and 0, and $\tau(0)$=1, $\kappa_{11}(0)$=1, $\kappa_{22}(0)$=1, $\kappa_{33}(0)$=1, $\kappa_{12}(0)$=1, $\kappa_{23}(0)$=0, $\kappa_{13}(0)$=0. Solid (dashed) lines indicate exact (approximate) solutions.

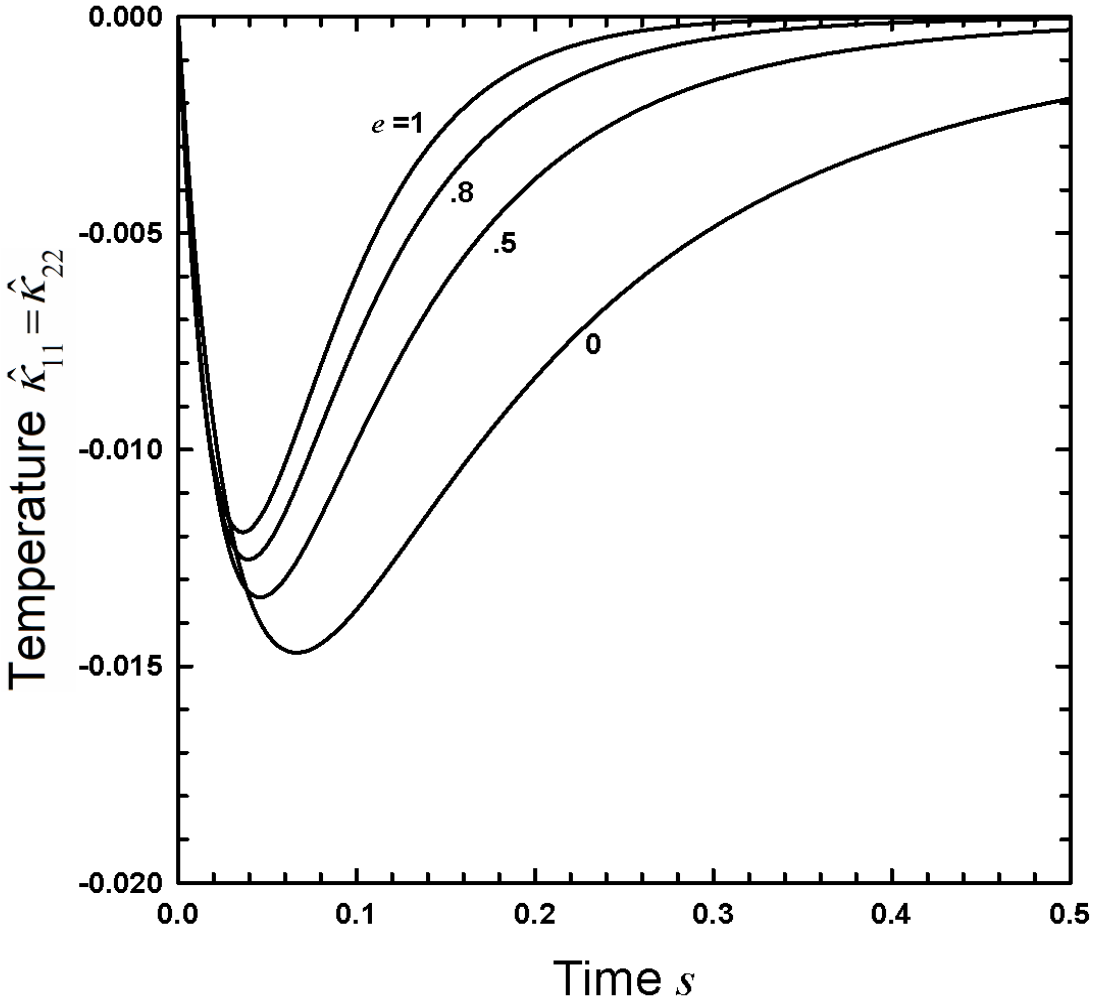

Figure 2.7: The variations of $\hat{\kappa}_{11} = \hat{\kappa}_{22}$ with s when e=1, .8, .5 and 0, and $\tau(0)$=1, $\kappa_{11}(0)$=1, $\kappa_{22}(0)$=1, $\kappa_{33}(0)$=1, $\kappa_{12}(0)$=1, $\kappa_{23}(0)$=0, $\kappa_{13}(0)$=0.

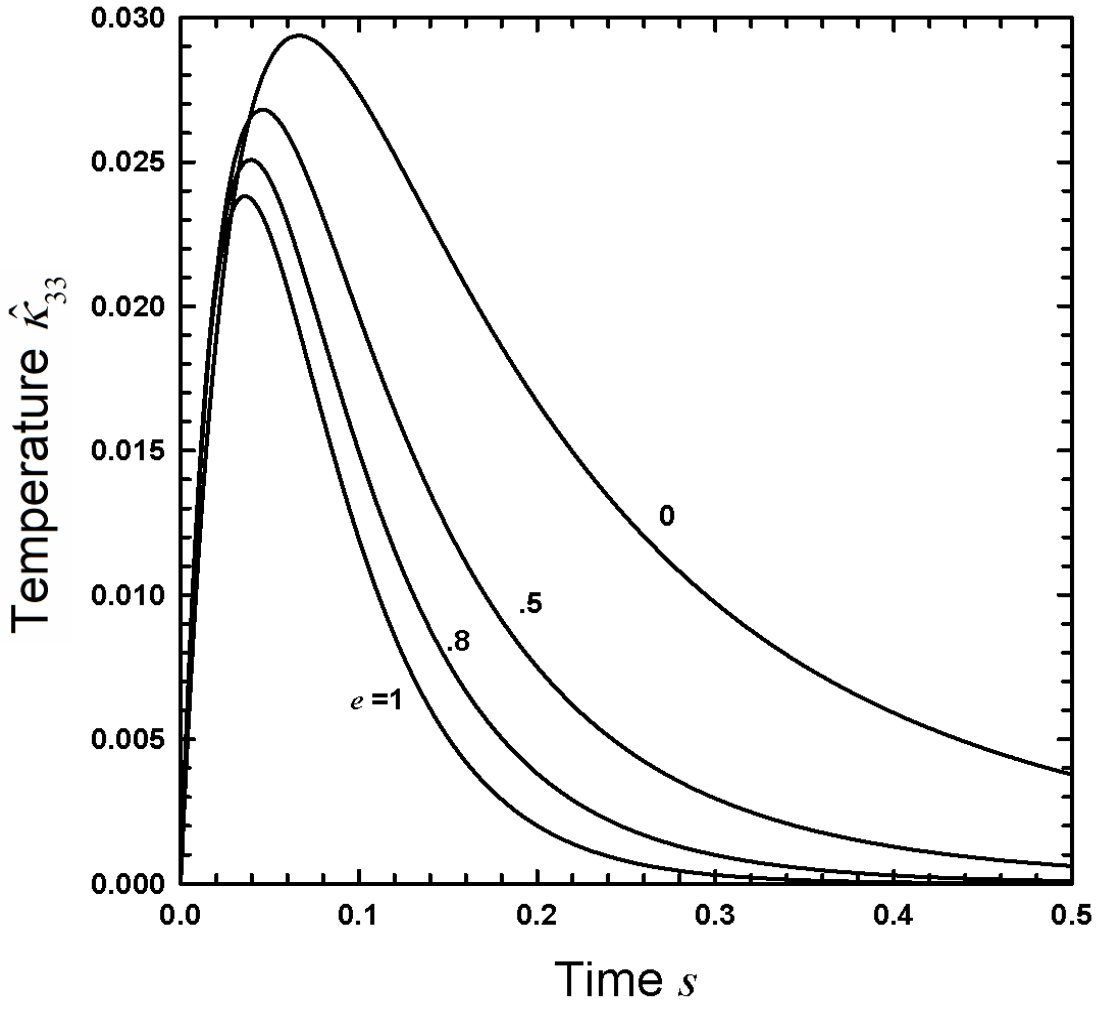

Figure 2.8: The variations of $\hat{\kappa}_{33}$ with s when e=1, .8, .5 and 0, and τ (0)=1, $\kappa_{11}(0)$=1, $\kappa_{22}(0)$=1, $\kappa_{33}(0)$=1, $\kappa_{12}(0)$=1, $\kappa_{23}(0)$=0, $\kappa_{13}(0)$=0.

2.5 Homogenous Shearing Flow

Here we apply the balance equations for mass, momentum, and energy, as well as the constitutive relations for pressure tensor and source of second moment to a steady, homogeneous, rectilinear shear flow of identical particles with diameters σ. In this flow, the solid fraction ν, the velocity gradient u', and the second moment $\boldsymbol{K}$ are uniform throughout. An $x_1 - x_2 - x_3$ Cartesian coordinate system is defined such that x_1 is the direction of flow and x_2 is the direction of the velocity gradient. The only nonzero components of the strain rate are $D_{12} = D_{21} = u'/2$, and the only nonzero components of the spin tensor are $W_{12} = -W_{21} = u'/2$.

Under these circumstances, the balance of mass (2.16) and the balance of momentum (2.17) are identically satisfied. The components $\dot{K}_{ij}$ and Q_{ijk} all vanish, so the energy equation (2.19) (with $\Gamma_{ii} = \gamma_{ii}$ from equation (2.37)) reduces to,

$$2P_{12}u' = \gamma_{ii} \quad . \tag{2.60}$$

Similarly, the deviatoric second moment equation (2.39) simplifies to,

$$\rho K_{ik}W_{jk} + \rho K_{jk}W_{ik} + P_{ik}D_{jk} + P_{jk}D_{ik} - \frac{2}{3}P_{12}u'\delta_{ij} = \hat{\gamma}_{ij} \quad . \tag{2.61}$$

For a prescribed velocity gradient u', equations (2.60) and (2.61) are six scalar equations that, when combined with constitutive relations (2.30) and (2.38) for P_{ij} and γ_{ij}, determine the variations of the components K_{ij} of the second moment with solid fraction ν and coefficient of restitution e. The $x_1 - x_3$ and $x_2 - x_3$ equations are satisfied for all values of ν if and only if the components K_{13} and K_{23} both vanish. This is because, in this simple flow, the $x_1 - x_3$ and $x_2 - x_3$ components of the shear stresses are equal to zero. The remaining unknowns ($T, \hat{K}_{11}, \hat{K}_{22}$, and K_{12}) are determined by the energy

equation (2.60) and the $x_1 - x_1$, $x_2 - x_2$, and $x_1 - x_2$ components of the deviatoric second moment equation (2.61).

The dimensionless parameter $R \equiv \sigma u' / T^{1/2}$ is an inverse measure of the fluctuation speed of the particles relative to the spatial variation in mean velocity. Dimensionless measures k_{ij} of the nonzero components of the second moment are defined by K_{ij}/T, while the corresponding sum and difference of the diagonal terms are $2\xi \equiv \hat{k}_{11} + \hat{k}_{22}$ and $2\eta \equiv \hat{k}_{11} - \hat{k}_{22}$ With P_{ij} given by equation (2.30) and γ_{ij} given by equation (2.38), the energy equation (2.60) becomes,

$$-4R^2 + 10\pi^{1/2} H k_{12} R = 3(1-e)\left[-20 - R^2 + 2\pi^{1/2} k_{12} R - 2(3\xi^2 + \eta^2 + k_{12}^2)\right] \quad , \tag{2.62}$$

where $H = H(\nu, e)$ is defined by equation (2.32). Similarly, the $x_1 - x_2$ component of the deviatoric second moment equation (2.61) becomes,

$$-\frac{35\pi^{1/2} R\eta}{G} + 70\pi^{1/2}(1+e)\left[F + H\xi\right]R = 6(1+e)\left[7\pi^{1/2}(2-e)R - 28(3-e)k_{12} + \right. \\ \left. + 2\pi^{1/2}(5-2e)R\xi - 8(3-e)k_{12}\xi\right] \quad , \tag{2.63}$$

where $F = F(\nu, e)$ is defined by equation (2.31). Rather than the individual diagonal components, it is more convenient to write down the sum and difference of the $x_1 - x_1$ and $x_2 - x_2$ components of equation (2.61). The sum is given by,

$$-14R^2 + 35\pi^{1/2} H k_{12} R = -252(3-e)\xi - 6(2-e)R^2 + 6\pi^{1/2}(5-2e)k_{12}R + \\ + 12(3-e)(3\xi^2 - \eta^2 - 2k_{12}^2) \quad , \tag{2.64}$$

and the difference is given by,

$$\frac{35\pi^{1/2} k_{12} R}{G} = -24(1+e)(3-e)(7+2\xi)\eta \quad . \tag{2.65}$$

With the values of solid fraction ν and coefficient of restitution e prescribed, equations (2.62) through (2.65) may be solved numerically for the corresponding values of $R, k_{12}, \xi,$ and η. Alternatively, it is possible to obtain approximate closed form solutions to equations (2.62) through (2.65) for $R, k_{12}, \xi,$ and η that are valid up to the order of approximation employed in deriving the constitutive relations. To this end, we expand $R, k_{12}, \xi,$ and η in powers of the parameter $\varepsilon \equiv (1-e)^{1/2}$. The forms of equations (2.62) through (2.65) dictate that there are no even powers of ε in either R or k_{12}, and no odd powers of ε in either ξ or η. Consequently, the appropriate expansions are

$$R = R_1\varepsilon + R_3\varepsilon^3 \tag{2.66}$$

$$k_{12} = k_1\varepsilon + k_3\varepsilon^3 \quad , \tag{2.67}$$

$$\xi = \xi_2\varepsilon^2 + \xi_4\varepsilon^4 \quad , \tag{2.68}$$

and

$$\eta = \eta_2\varepsilon^2 + \eta_4\varepsilon^4 \quad , \tag{2.69}$$

where we have truncated the series after the two lowest order terms in each. The corresponding expansions for the functions $F(G,\varepsilon)$ and $H(G,\varepsilon)$ defined by equations (2.31) and (2.32), respectively, are given by,

$$F = F_0 + \frac{\varepsilon^2}{8G} \quad \text{and} \quad H = H_0 + \frac{\varepsilon^2}{8G} \quad , \tag{2.70}$$

where $F_0 \equiv F(G, \varepsilon = 0)$ and $H_0 \equiv H(G, \varepsilon = 0)$ are the expressions (2.31) and (2.32) for F and H evaluated when the particles are perfectly elastic (i.e. when $e = 1$). Approximations (2.66) through (2.70) may be employed in equations (2.62), (2.63), (2.64), and (2.65). Equating coefficients of the terms proportional to ε in equations (2.62) and (2.63), for example, yields

$$-R_1^2 + 5\pi^{1/2} H_0 k_1 R_1 = -30 \quad , \tag{2.71}$$

and

$$k_1 = \frac{-\pi^{1/2}}{8}\left[1 - \frac{5F_0}{3}\right] R_1 \quad . \tag{2.72}$$

By using the second of these to eliminate k_1 from the first, and by employing the expressions for F_0 and H_0 in terms of G, we find that

$$R_1 = \sqrt{15}\left[1 + \frac{\pi}{12}\left(1 + \frac{5}{8G}\right)^2\right]^{-1/2} \quad , \tag{2.73}$$

which may be employed in equation (2.72) to determine k_1. Similarly, equating the coefficients of terms proportional to ε^2 in equations (2.64) and (2.65) yields, respectively,

$$\xi_2 = \frac{1}{63} R_1^2 + \frac{\pi^{1/2}}{504}[18 - 35H_0] k_1 R_1 - \frac{2}{21} k_1^2 \quad , \tag{2.74}$$

and

$$\eta_2 = \frac{-5\pi^{1/2}}{96G} k_1 R_1 \quad . \tag{2.75}$$

At the next order, equating the coefficients of the terms proportional to ε^3 in equations (2.62) and (2.63) yields,

$$2(5\pi^{1/2} H_0 k_1 - 4R_1) R_3 + (10\pi^{1/2} H_0 R_1) k_3 = -3R_1^2 + \pi^{1/2}(6 - \frac{5}{4G}) k_1 R_1 - 6k_1^2 \quad , \tag{2.76}$$

and

$$28\pi^{1/2}(5F_0 - 3) R_3 + 672 k_3 = \pi^{1/2}\left[42 + 70F_0 - \frac{35}{2G} + 4(18 - 35H_0)\xi_2 + \frac{35}{G}\eta_2\right] R_1 - 192 k_1 \xi_2 \quad . \tag{2.77}$$

These are two simultaneous linear algebraic equations that easily determine R_3 and k_3. Finally, by equating coefficients of the terms proportional to ε^4 in equations (2.64) and (2.65) yield, we find,

$$\xi_4 = \frac{-\xi_2}{2} - \frac{1}{84}(2R_1R_3 + R_1^2) + \frac{\pi^{1/2}}{84}(3k_1R_3 + 3k_3R_1 + 2k_1R_1) + \frac{1}{21}(3\xi_2^2 - \eta_2^2 - 4k_1k_3) - \frac{1}{21}k_1^2 + \\ + \frac{1}{18}R_1R_3 - \frac{5\pi^{1/2}}{72}\left[H_0(k_1R_3 + k_3R_1) + \frac{1}{8G}k_1R_1\right] \quad , \tag{2.78}$$

and

$$\eta_4 = \frac{-5\pi^{1/2}}{96G}(k_1R_3 + k_3R_1) - \frac{2}{7}\xi_2\eta_2 \quad . \tag{2.79}$$

The coefficients $R_1, R_3, k_1, k_3, \xi_2, \xi_4, \eta_2$, and η_4 are determined as functions of ν by equations (2.72) through (2.79). The dependence of R, k_{12}, ξ, and η on ν and e are then approximated by the truncated series (2.66) through (2.69). With ξ and η determined in this manner, the diagonal components of $\hat{k}_{ij}$ are fixed according to $\hat{k}_{11} = \xi + \eta$, $\hat{k}_{22} = \xi - \eta$, and $\hat{k}_{33} = -(\hat{k}_{11} + \hat{k}_{22})$.

A dimensionless measure of the velocity fluctuations is $\mathcal{K}_{ij} \equiv K_{ij}/(\sigma u')^2 = k_{ij}/R^2$. The diagonal components, in particular, are given by,

$$\mathcal{K}_{11} = \frac{1}{R^2}(1 + \hat{k}_{11}) \quad , \qquad \mathcal{K}_{22} = \frac{1}{R^2}(1 + \hat{k}_{22}) \quad , \qquad \text{and} \qquad \mathcal{K}_{33} = \frac{1}{R^2}(1 + \hat{k}_{33}) \quad . \tag{2.80}$$

The dimensionless components p_{ij} of the pressure tensor are defined in terms of their dimensional counterparts P_{ij} by $p_{ij} \equiv P_{ij}/\rho_p(\sigma u')^2$, in which ρ_p is the mass density of each particle. In the case of homogeneous shearing, equation (2.30) yields the normal pressures,

$$p_{11} = \frac{2(1+e)\nu G}{R^2}\left(F + H\hat{k}_{11}\right) \quad , \tag{2.81}$$

$$p_{22} = \frac{2(1+e)\nu G}{R^2}\left(F + H\hat{k}_{22}\right) \quad , \tag{2.82}$$

and

$$p_{33} = \frac{2(1+e)\nu G}{R^2}\left(F + H\hat{k}_{33}\right) \quad , \tag{2.83}$$

while the average normal pressure is given by $p = 2(1+e)\nu GF/R^2$. Similarly, the dimensionless shear stress is

$$p_{12} = \frac{2(1+e)\nu G}{R^2}\left[\frac{-2R}{5\pi^{1/2}} + H\hat{k}_{12}\right] \quad . \tag{2.84}$$

In Figure 2.9, we show the variation of the parameter $R \equiv \sigma u'/T^{1/2}$ with solid fraction ν for e=.95, .8, .6, and .4. The exact solutions for R obtained by numerically solving equations (2.62) through (2.65) are shown as solid curves. The approximate solutions given by truncated series (2.66) (in which R_1 is given by equation (2.73) and R_3 is obtained from equations (2.76) and (2.77)) are shown as dashed curves. In this flow, the balance is between the rate at which energy is supplied to the flow by the imposed shear rate and the rate at which energy is dissipated due to inelastic collisions. For a fixed rate of energy supply, the frequency of collisions and therefore the granular temperature must increase as either the flow becomes less dense or the particles become less dissipative. Consequently, R decreases with decreasing ν or increasing e. In fact, equations (2.66) through (2.77) demonstrate that in the dilute limit both R_1, R_3 and R itself are proportional to ν. By contrast, equations (2.66) through (2.79) demonstrate that $\hat{k}_{11}(=\xi+\eta)$, $\hat{k}_{22}(=\xi-\eta)$, $\hat{k}_{33}$, and k_{12} approach finite non-zero values in the same limit. Figure 2.9 also demonstrates that the accuracy of the approximate solution

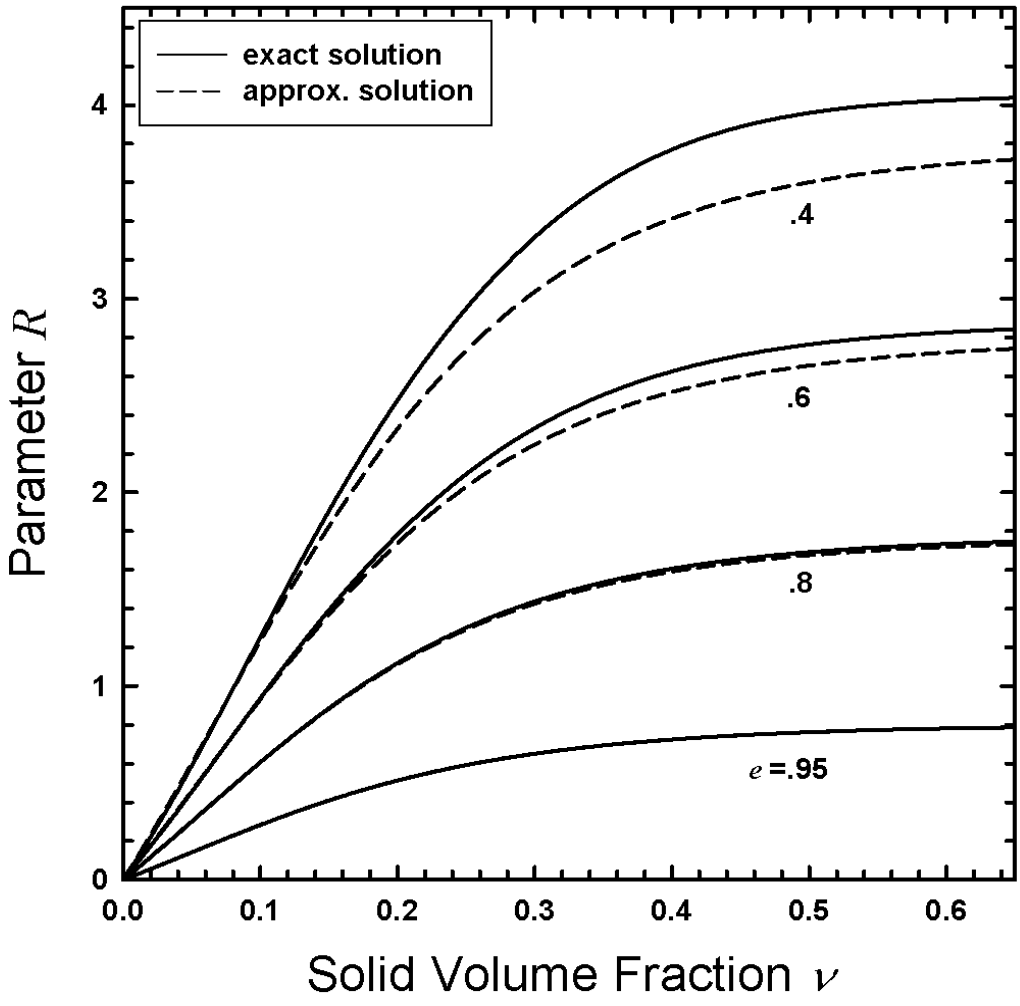

Figure 2.9: The variations of R with ν when e=.95, .8, .6 and .4. Solid (dashed) lines indicate exact (approximate) solutions.

diminishes as e decreases. This is to be expected because the approximation is a truncated series in powers of $\varepsilon \equiv (1-e)^{1/2}$. Figures 2.10, 2.11, 2.12 and 2.13 show the variations of the normal pressures p_{11}, p_{22}, and p_{33} and the shear stress $-p_{12}$ with ν for e=.95, .8, .6, and .4. Solid curves are based on the exact values of R, $\hat{k}_{11}$, $\hat{k}_{22}$, $\hat{k}_{33}$, and $\hat{k}_{12}$, whereas the dashed curves are based on the truncated series for these same quantities. If the granular temperature were fixed as the density varied, the pressures and shear stress would each decrease monotonically with decreasing solid fraction. However, Figure 2.9 showed that as the solid fraction decreases, the granular temperature increases. Decreases in solid fraction tend to decrease the pressures and the shear stress, while increases in temperatures have the opposite effect. Figures 2.10, 2.11, 2.12 and 2.13 indicate that for relatively dense flows (i.e. ν greater than about .25) the effect of varying solid fraction dominates over the corresponding effect of varying granular temperature, so that the pressures and shear stress decrease with decreasing solid fraction. However, in relatively dilute flows (i.e. ν less than about .25) the pressures and shear stress actually increase as the solid fraction continues to decrease. This indicates that in this range of ν, the effect of varying temperature dominates over that of varying solid fraction. In fact, this is because as ν becomes small, T becomes unbounded (with $1/\nu^2$) faster than ν approaches zero.

Figures 2.14 and 2.15 show the variations of ratios of normal pressures p_{11}/p_{22} and p_{33}/p_{22} with ν for e=.95, .8, .6, and .4. Solid curves are based on the exact values of R, $\hat{k}_{11}$, $\hat{k}_{22}$, $\hat{k}_{33}$, and $\hat{k}_{12}$, and the dashed curves are based on the truncated series for above mentioned quantities. The ratio p_{11}/p_{22} deviates strongly from 1, when the flows

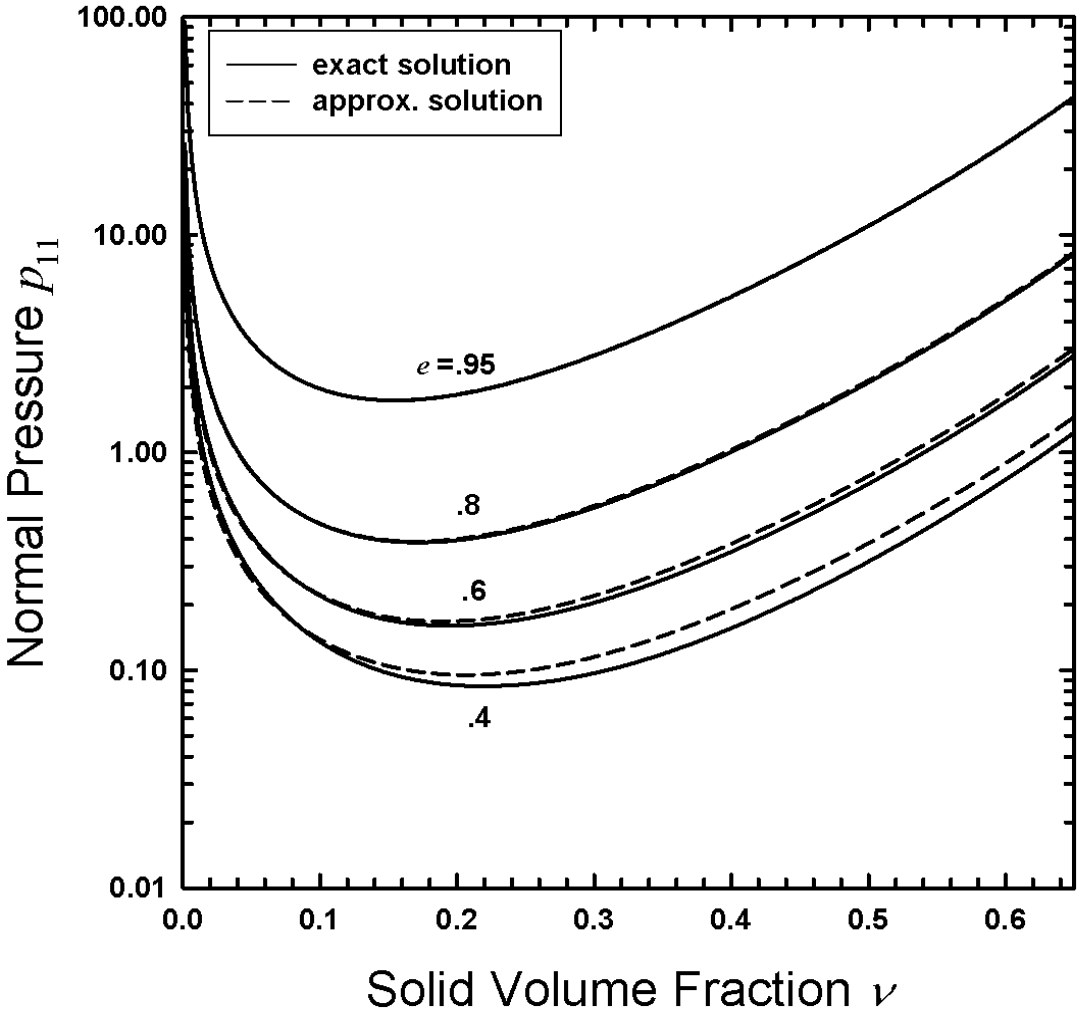

Figure 2.10: The variations of p_{11} with ν when e=.95, .8, .6 and .4. Solid (dashed) lines indicate exact (approximate) solutions.

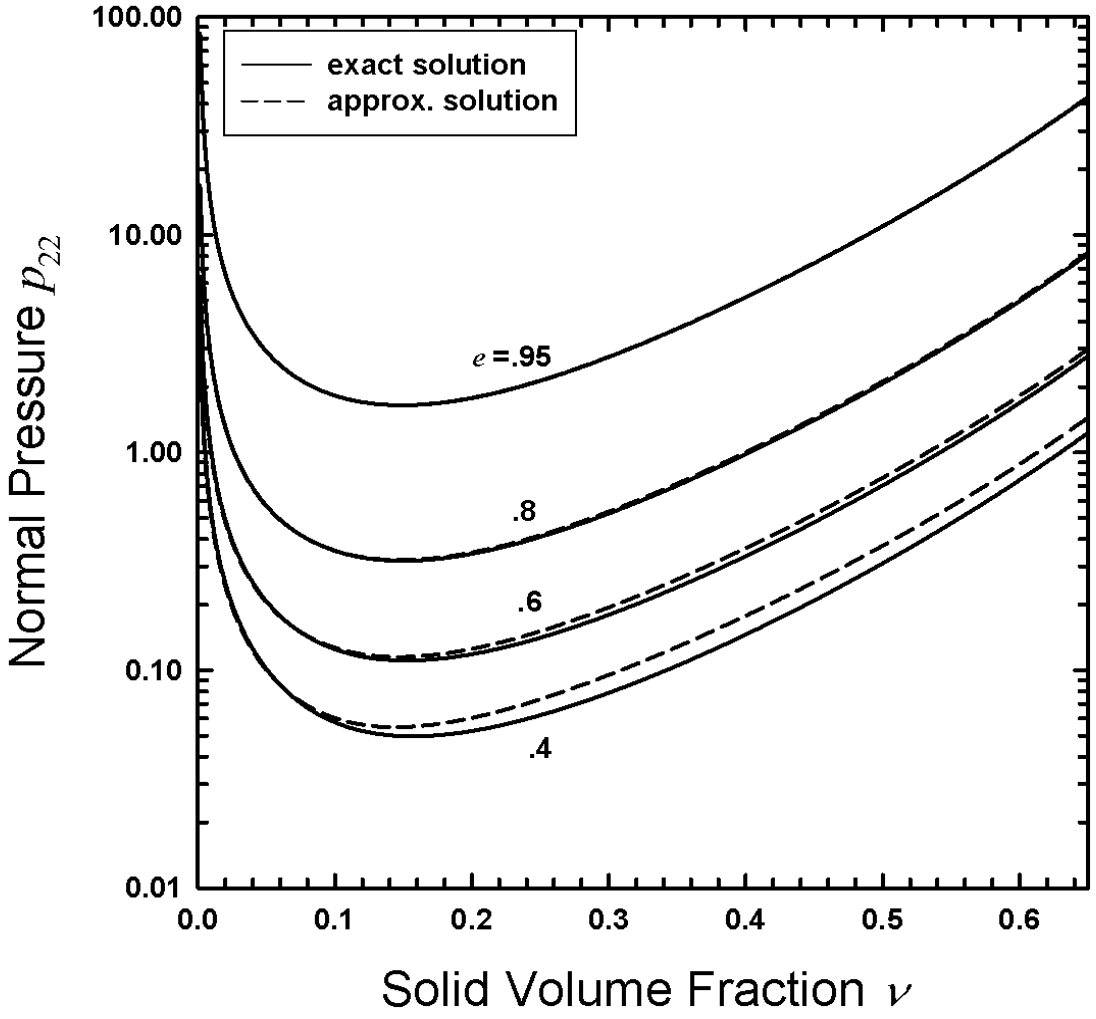

Figure 2.11: The variations of p_{22} with ν when e=.95, .8, .6 and .4. Solid (dashed) lines indicate exact (approximate) solutions.

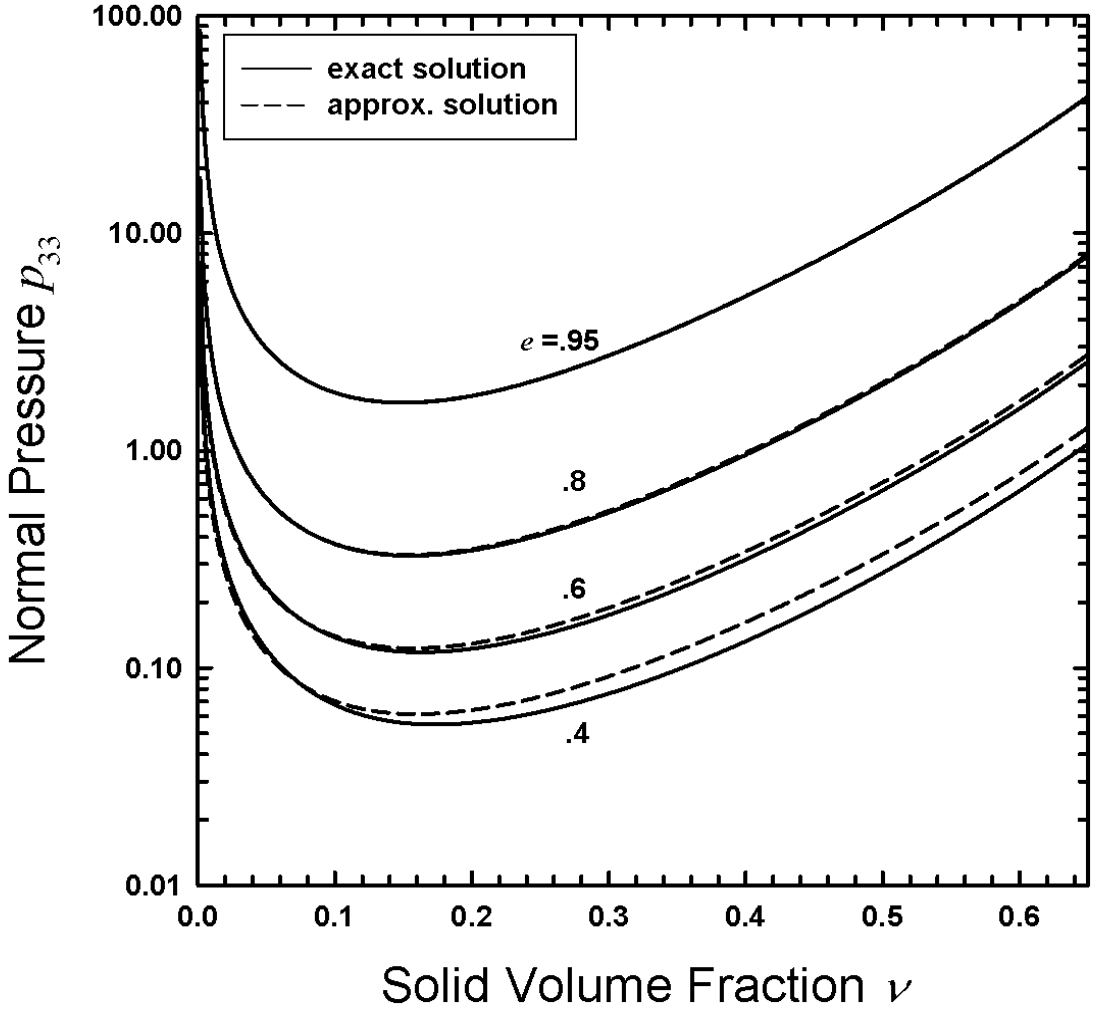

Figure 2.12: The variations of p_{33} with ν when e=.95, .8, .6 and .4. Solid (dashed) lines indicate exact (approximate) solutions.

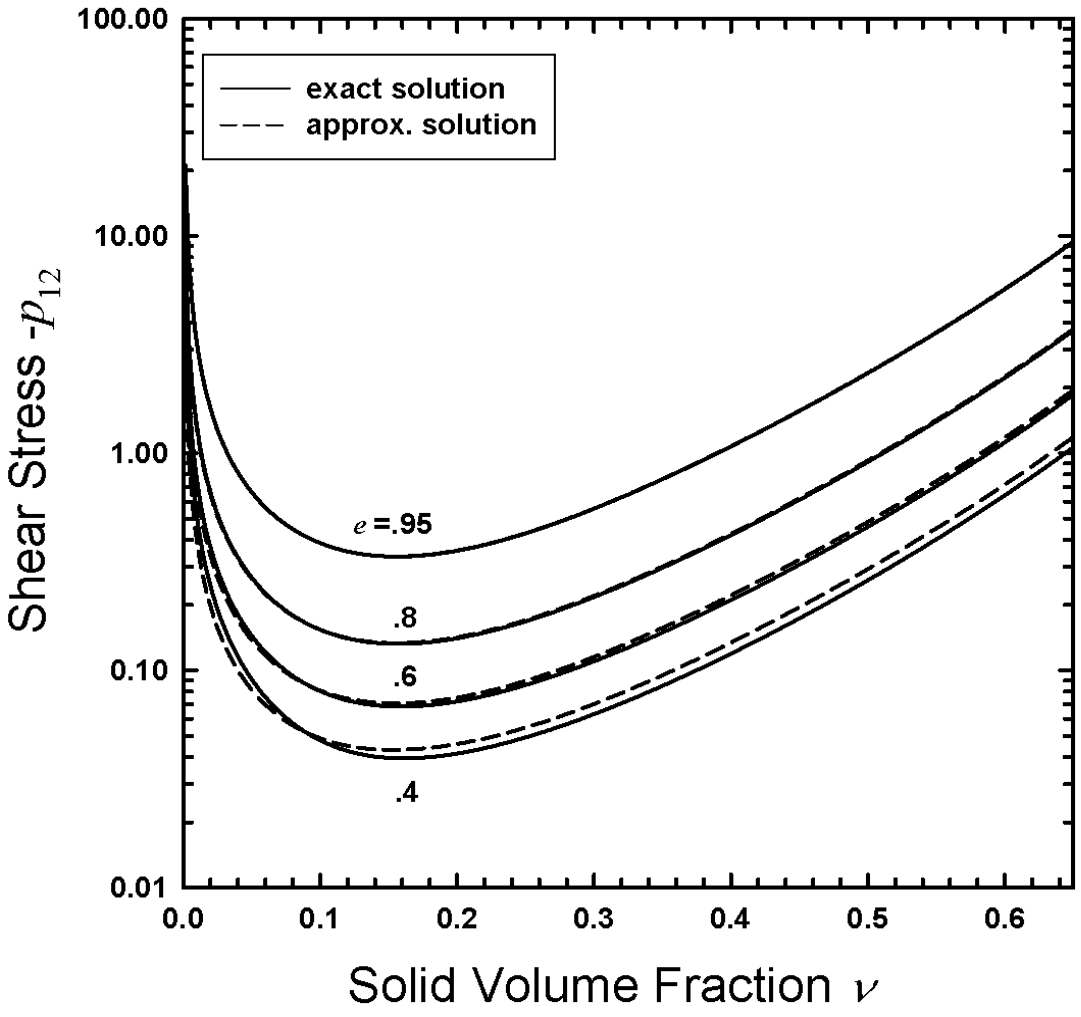

Figure 2.13: The variations of $-p_{12}$ with ν when e=.95, .8, .6 and .4. Solid (dashed) lines indicate exact (approximate) solutions.

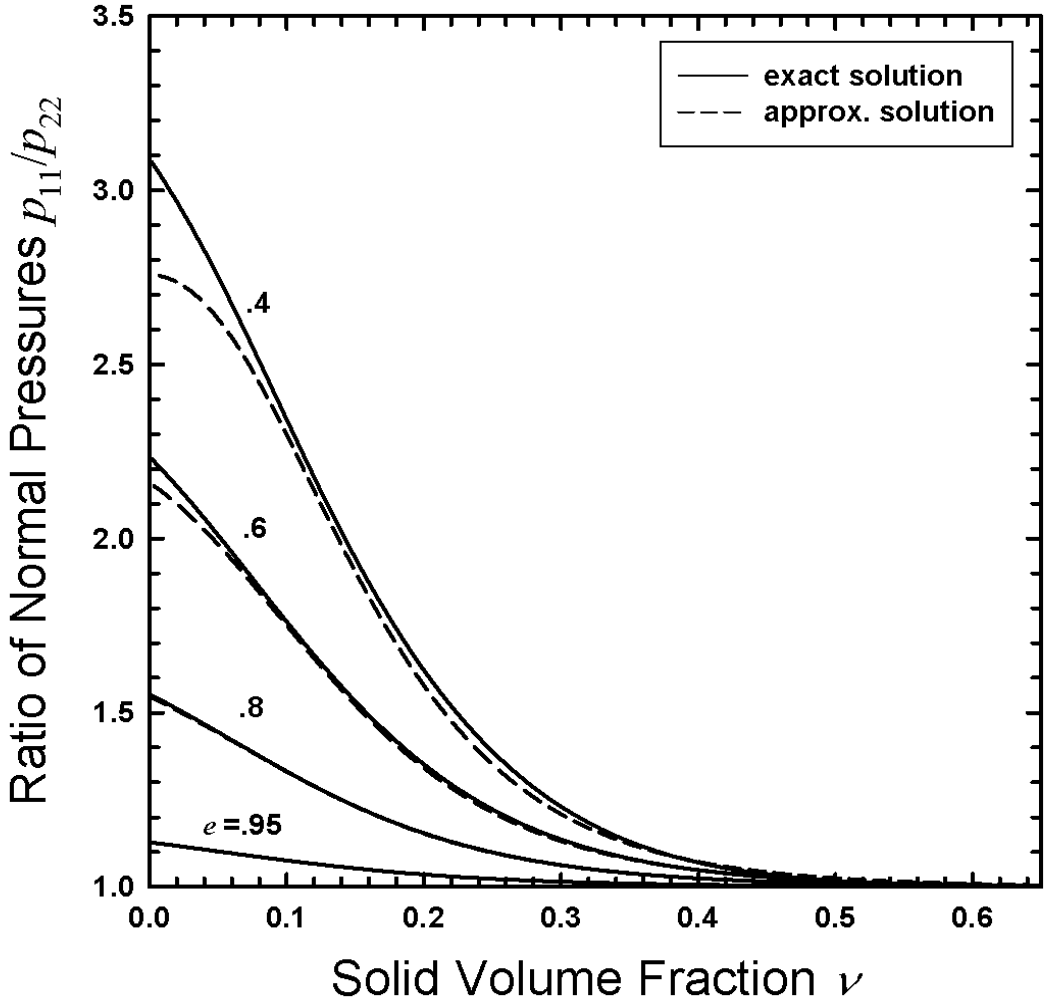

Figure 2.14: The variations of $p_{11}/\ p_{22}$ with ν when e=.95, .8, .6 and .4. Solid (dashed) lines indicate exact (approximate) solutions. Also shown are numerical data from Walton (1989) for e=.95 (solid circles) and e=.8 (triangles) and Walton and Broun (1986 b) for e=.6(hollow circles).

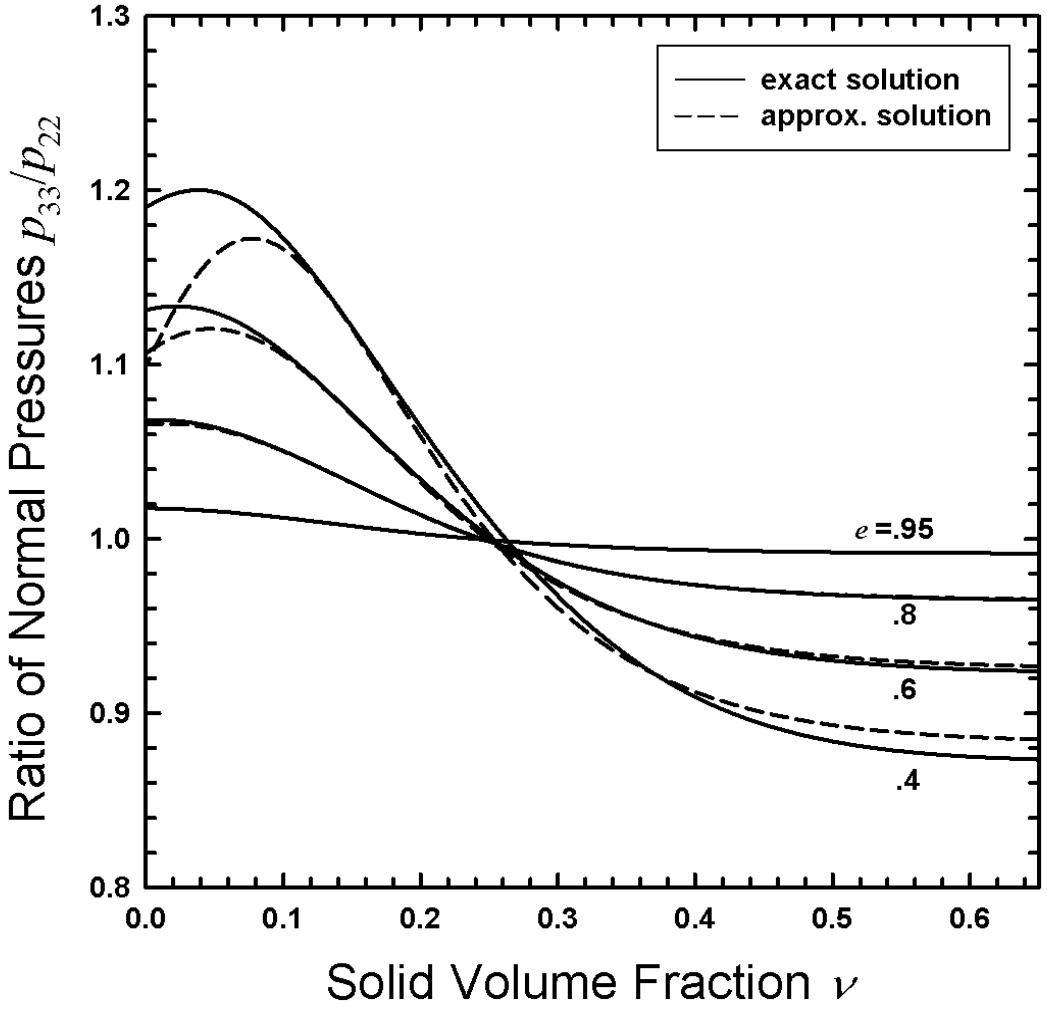

Figure 2.15: The variations of $p_{33}/\ p_{22}$ with ν when e=.95, .8, .6 and .4. Solid (dashed) lines indicate exact (approximate) solutions. Also shown are numerical data from Walton (1989) for e=.95 (solid circles) and e=.8 (triangles) and Walton and Broun (1986 b) for e=.6(hollow circles).

are highly dilute and inelastic. As the solid volume fraction increases to its maximum value, the ratio becomes equal to 1. This can be explained by analyzing the motion of particles between collisions and the associated effect on their fluctuation velocities. Particles at any vertical location can be thought to have reached there from some position above or below. Then, their total velocity is unchanged but because of different mean velocity at the new vertical location, the particles acquire additional fluctuation velocity in x_1-direction but no additional fluctuation velocity in x_2-direction. So, particles have greater $\hat{k}_{11}$ than $\hat{k}_{22}$, and hence larger p_{11} than p_{22}, and this difference in $\hat{k}_{11}$ than $\hat{k}_{22}$ is proportional to the product of vertical distance particle travels between the collisions and R^2. As ν increases, the vertical distance that the particles could travel between collisions reduces and hence p_{22} approaches p_{11}. Also as inelasticity increases R increases and hence the differences increase. As regards the variation of pressure ratio p_{33}/p_{22}, for relatively dilute flows (i.e. ν less than about .25), the ratio p_{33}/p_{22} is greater than 1. As ν increases, the ratio decreases and for relatively dense flows (i.e. ν greater than about .25) the ratio decreases to values less than 1. Although it is not precisely clear why the ratio p_{33}/p_{22} varies the way it does, similar qualitative variation is observed in numerical simulations of Campbell (1989) for rough spheres. Figures 2.16 and 2.17 show the simulation results of Campbell for the variation of pressure ratios p_{11}/p_{22} and p_{33}/p_{22}, for e=.4, .6, .8 and 1.

2.6 Probability Distribution Function for Velocities

In an earlier section of this chapter, we discussed the single particle distribution function $f(\boldsymbol{c},\boldsymbol{r})$, which was taken to be the perturbed Maxwellian, given by

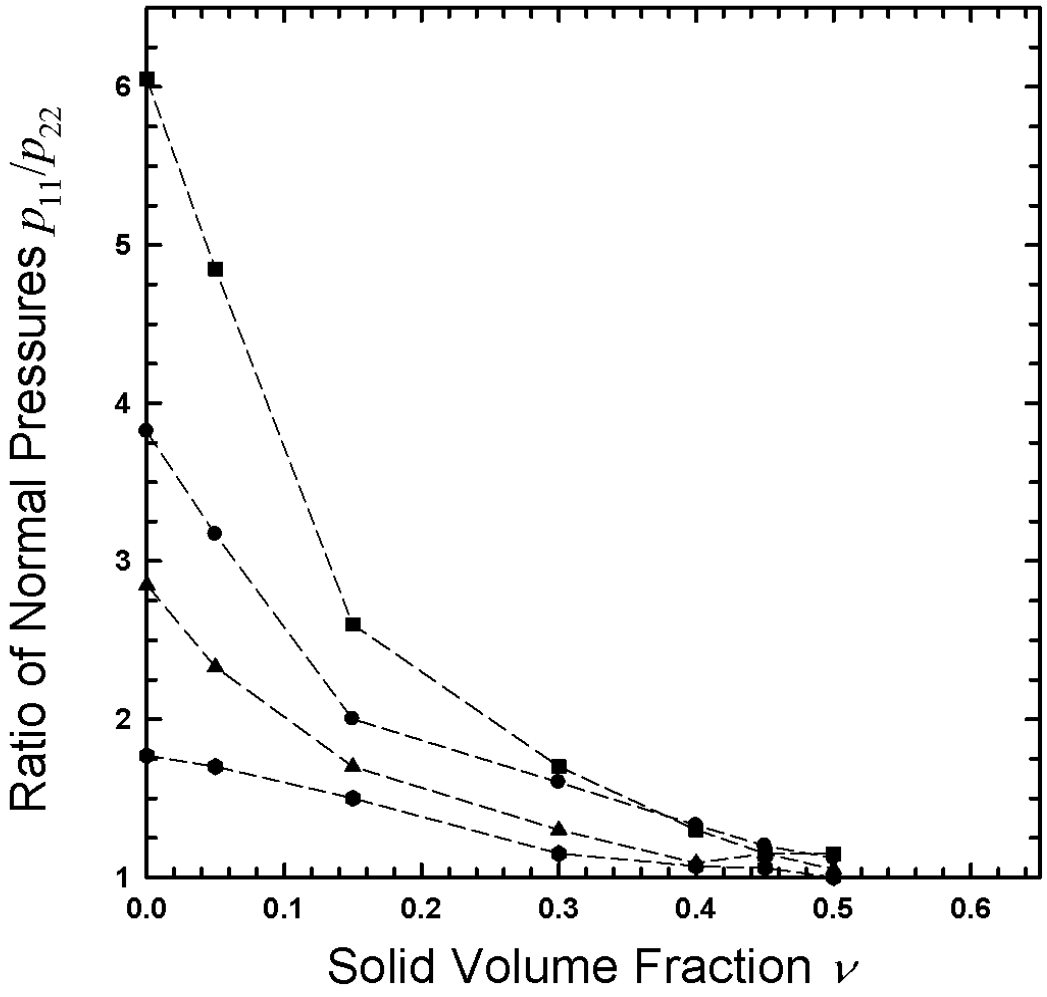

Figure 2.16: The simulations results of Campbell (1989) showing variations of $p_{11}/\ p_{22}$ with ν. Squares, circles, triangles and hexagons represent e=.4, .6, 8, and 1 respectively.

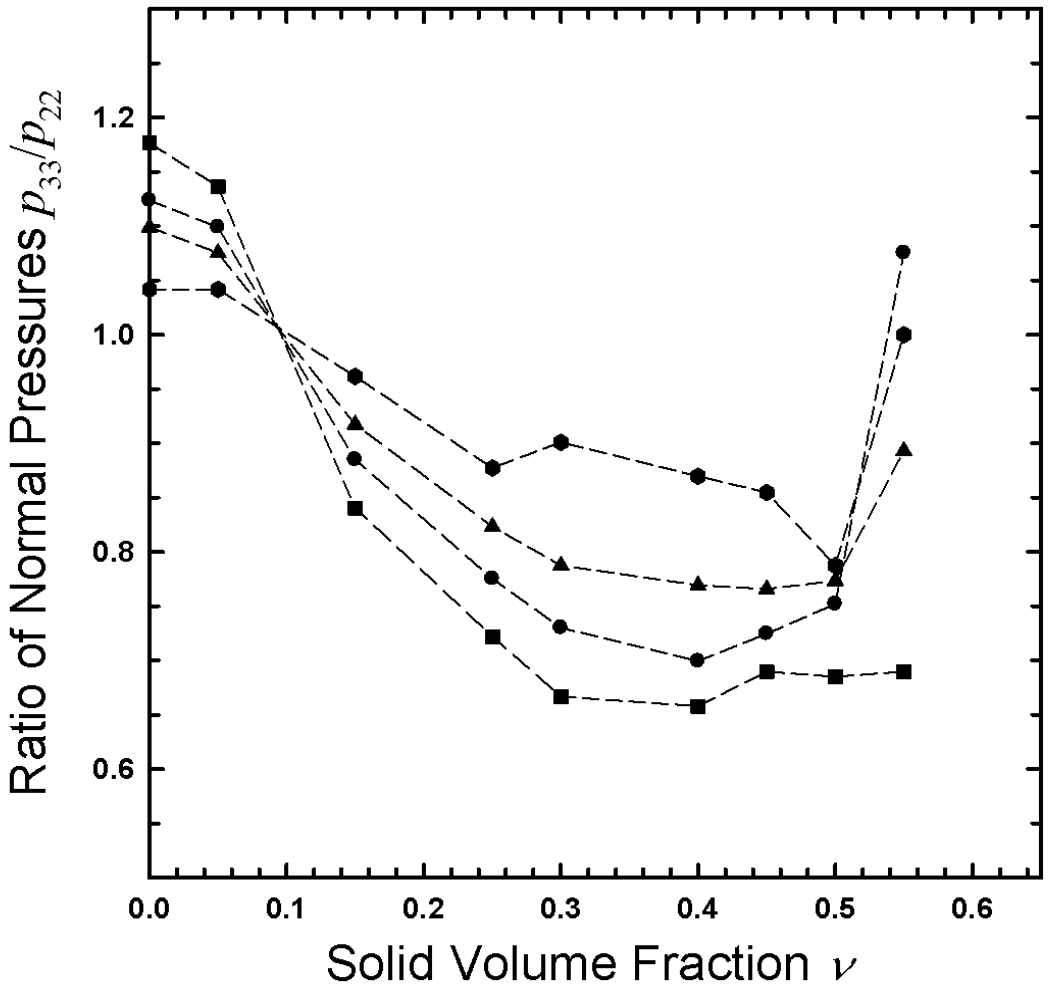

Figure 2.17: The simulations results of Campbell (1989) showing variations of $p_{33}/\ p_{22}$ with ν for rough spheres. Squares, circles, triangles and hexagons represent e=.4, .6, 8, and 1 respectively.

Equation (2.24). To obtain the individual velocity distribution functions, we need to integrate the single particle distribution function $f(\boldsymbol{c},\boldsymbol{r})$ with respect to the remaining two velocities, in the limits -∞ to ∞. In a general $x_1 - x_2 - x_3$ Cartesian coordinate system the individual velocity distribution functions, scaled by number density n to give probability, are thus obtained as:

$$P(C_1) = \frac{1}{n}\int_{-\infty}^{\infty}\int_{-\infty}^{\infty} f(\boldsymbol{c},\boldsymbol{r})dc_2 dc_3 \ , \tag{2.85}$$

$$P(C_2) = \frac{1}{n}\int_{-\infty}^{\infty}\int_{-\infty}^{\infty} f(\boldsymbol{c},\boldsymbol{r})dc_1 dc_3 \ , \tag{2.86}$$

$$P(C_3) = \frac{1}{n}\int_{-\infty}^{\infty}\int_{-\infty}^{\infty} f(\boldsymbol{c},\boldsymbol{r})dc_1 dc_2 \ , \tag{2.87}$$

where, $P(C_1)$, $P(C_2)$ and $P(C_3)$ are individual velocity distribution functions in x_1-, x_2- and x_3-directions respectively. Substituting expression (2.24) for $f(\boldsymbol{c},\boldsymbol{r})$ and carrying out the integrations, we get,

$$P(C_1) = \frac{1}{\sqrt{2\pi T}}\exp\left(-\frac{C_1^{\,2}}{2T}\right)\left[1+\frac{C_1^{\,2}}{T}\frac{\hat{K}_{11}}{2T}+\frac{\hat{K}_{22}}{2T}+\frac{\hat{K}_{33}}{2T} + \frac{3\sqrt{\pi}(1+e)(2e-1)}{4(49-33e)}\left(1+\frac{5}{3(1+e)^2(2e-1)G}\right)\frac{\sigma}{T}\frac{\partial T}{\partial x_1}\left(3-\frac{C_1^{\,2}}{T}\right)\frac{C_1}{\sqrt{T}}\right] \ , \tag{2.88}$$

$$P(C_2) = \frac{1}{\sqrt{2\pi T}}\exp\left(-\frac{C_2^{\,2}}{2T}\right)\left[1+\frac{\hat{K}_{11}}{2T}+\frac{C_2^{\,2}}{T}\frac{\hat{K}_{22}}{2T}+\frac{\hat{K}_{33}}{2T} + \frac{3\sqrt{\pi}(1+e)(2e-1)}{4(49-33e)}\left(1+\frac{5}{3(1+e)^2(2e-1)G}\right)\frac{\sigma}{T}\frac{\partial T}{\partial x_2}\left(3-\frac{C_2^{\,2}}{T}\right)\frac{C_2}{\sqrt{T}}\right] \tag{2.89}$$

and,

$$P(C_3)=\frac{1}{\sqrt{2\pi T}}\exp\left(-\frac{C_3^{\,2}}{2T}\right)\left[1+\frac{\hat{K}_{11}}{2T}+\frac{\hat{K}_{22}}{2T}+\frac{C_3^{\,2}}{T}\frac{\hat{K}_{33}}{2T}\right.$$
$$\left.+\frac{3\sqrt{\pi}(1+e)(2e-1)}{4(49-33e)}\left(1+\frac{5}{3(1+e)^2(2e-1)G}\right)\frac{\sigma}{T}\frac{\partial T}{\partial x_3}\left(3-\frac{C_3^{\,2}}{T}\right)\frac{C_3}{\sqrt{T}}\right] \tag{2.90}$$

Note that $P(C_1)$, $P(C_2)$ and $P(C_3)$ in general depend on ν, T, $\hat{K}_{11}$, $\hat{K}_{22}$, $\hat{K}_{33}$, $\partial T/\partial x_1$, $\partial T/\partial x_2$ and $\partial T/\partial x_3$ which are functions of position $\boldsymbol{x}$, and parameters σ and e. So, we can not plot $P(C_1)$, $P(C_2)$ and $P(C_3)$ unless we solve boundary value problem to obtain above mentioned fields. Hence we defer the plots of $P(C_1)$, $P(C_2)$ and $P(C_3)$ until Chapter 6.

CHAPTER 3

Boundary Conditions

We consider the interaction of a three-dimensional granular flow with an impenetrable boundary that randomly fluctuates about mean velocity $\boldsymbol{U}$. The velocity of the flow at the boundary is $\boldsymbol{u}$. Of particular interest are the mechanisms by which the balance of momentum and the balance full second moment are satisfied at the flow/boundary surface. We focus attention on a parallelepiped in the flow with two opposite faces of unit area, as shown in Figure 3.1. One face is coincident with the boundary, and the opposite parallel face protrudes by a differential distance into the flow. In the limit as the four lateral sides of the parallelepiped shrink to zero, the balance of momentum within the parallelepiped requires in component form that

$$M_i = P_{ij} n_j \ , \tag{3.1}$$

where $\boldsymbol{M}$ is the rate per unit area (of the boundary) at which momentum is transferred to the flow through collisions with the boundary, and $\boldsymbol{n}$ is the unit normal directed into the flow.

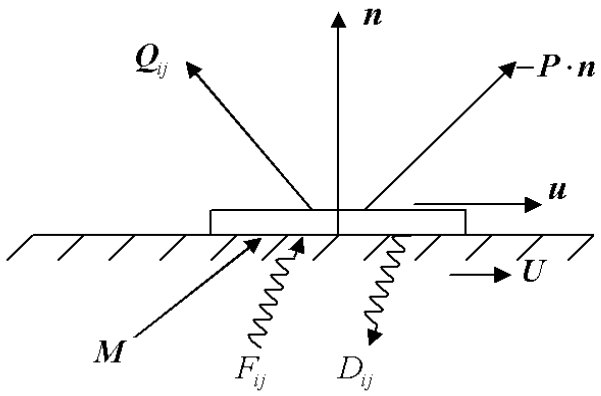

Figure 3.1: A fixed control volume at the boundary

Furthermore, if F_{ij} is one-half the rate per unit area at which the full second moment of velocity fluctuation is supplied by the boundary to the flow due to its random motion about the mean velocity $\boldsymbol{U}$, and if D_{ij} is the corresponding rate at which it would be removed from the flow if the boundary were not fluctuating about its mean velocity, then in the limit as the lateral sides shrink to zero, the balance of the full second moment requires that

$$\frac{1}{2}(M_i v_j + M_j v_i) + F_{ij} - D_{ij} = \frac{1}{2} Q_{kij} n_k \ , \tag{3.2}$$

where $\boldsymbol{v}$ is the slip velocity defined as the difference $\boldsymbol{U} - \boldsymbol{u}$ between the mean velocity of the boundary and the mean velocity of the flow at the boundary.

The isotropic piece of boundary condition (3.2) yields the energy balance,

$$M_i v_i + F_{ii} - D_{ii} = \frac{1}{2} Q_{kii} n_k \ , \tag{3.3}$$

where F_{ii} corresponds to the energy supplied by boundary due to its fluctuating motion, D_{ii} corresponds to the energy dissipated through inelastic collisions at boundary, and Q_{kii} are the components of the flux $\boldsymbol{Q}_{ii}$ of energy at the boundary. The slip work term, $\boldsymbol{M} \cdot \boldsymbol{v}$ is the rate at which work is done by equal tractions acting on opposite sides of the parallelepiped through velocities that differ by $\boldsymbol{v}$. Thus the boundary can either supply or absorb fluctuation energy depending on the relative sizes of the slip work $\boldsymbol{M} \cdot \boldsymbol{v}$, the supply rate F_{ii} and the dissipation rate D_{ii}. In fact, even when the boundary does not vibrate (i.e., $F_{ii} = 0$) and when all the interactions between the boundary and the flow particles are dissipative (i.e., $D_{ii} > 0$), the boundary may actually supply energy to the

flow provided that $\boldsymbol{M}\cdot\boldsymbol{v}$ is greater than D_{ii}. The deviatoric piece of the second moment balance (3.2) at the boundary is,

$$\frac{1}{2}(M_i v_j + M_j v_i) - \frac{1}{3}(M_k v_k)\delta_{ij} + (F_{ij} - D_{ij}) - \frac{1}{3}(F_{kk} - D_{kk})\delta_{ij} = \frac{1}{2}\left[Q_{kij}n_k - \frac{1}{3}Q_{kmm}n_k\delta_{ij}\right]. \quad (3.4)$$

Mean fields (of density ρ, velocity u_i, and second moment K_{ij}) that satisfy the balance of mass (2.16), the balance of momentum (2.17) and either the balance of second moment (2.18) or the balance of both energy (2.19) and deviatoric second moment (2.20) throughout the flow, must also satisfy conditions (3.1) and either equation (3.2) or both equations (3.3) and (3.4) at the boundary.

In the Equations (3.1) through (3.4), the rates M_i, F_{ij} and D_{ij} are not known and must be determined. To calculate the rates M_i, F_{ij} and D_{ij}, we need to calculate in each collision between a flow particle and the boundary, the momentum transferred by the boundary, second moment transferred due to fluctuation motion of boundary and second moment removed at the boundary, respectively. Then, these single collision contributions are multiplied by the frequency of those collisions and integrated over all possible collisions. To do so, we need to specify the geometry of the boundary and the vibratory motion of the boundary. In the next section, we describe the geometry of the boundary.

3.1 Description of Boundary

We consider flat surfaces to which identical, smooth, hemispherical particles of diameter d are fixed in a regular pattern that repeats indefinitely in two perpendicular

directions within the plane of the flat surface. The fundamental element of the pattern is a straight row of hemispheres in which the centers of adjacent particles are a fixed distance apart. Particles are attached to the boundary in identical parallel rows. The pattern is set by both the perpendicular distance between any two adjacent rows and the parallel distance by which any one row is shifted relative to its neighbor. A rectangular array results when there is no parallel shift. If, in addition, the distance between particle centers within a row is equal to the perpendicular between rows, then the array is square. The maximum parallel shift between rows is equal to the spacing between the centers of the particles in any one row.

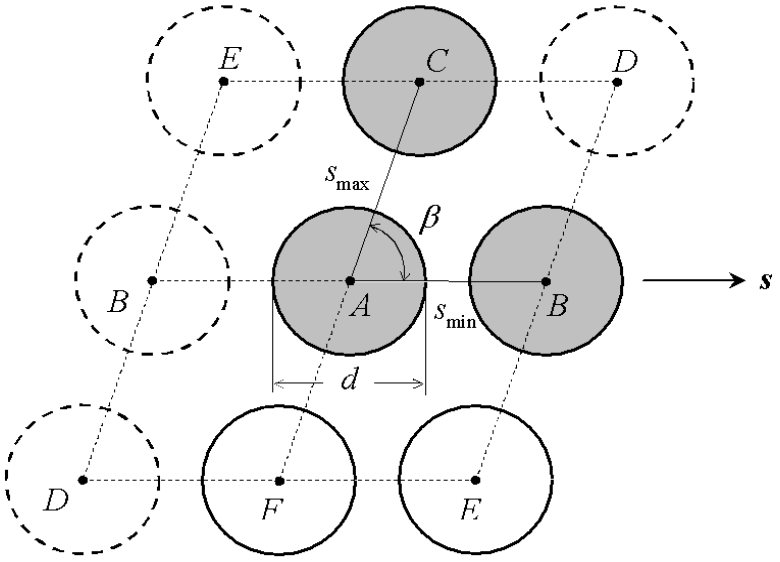

Figure 3.2: Top-view of an array of boundary particles

The boundary pattern is shown in Figure 3.2. The basic pattern is described by a central shaded boundary particle (labeled A), two shaded neighbors (labeled B and C), as well as the solid lines that connect the centers of particle A to the centers of B and C. The pattern can be constructed in such a way that the angle β formed by the solid lines is

always less than or equal to $\pi/2$. Rectangular arrays are those for which $\beta = \pi/2$. Without loss of generality, we assume that particle B is closer than particle C to particle A. The distances along the lines from the edge of any particle A to its two neighbors B and C are s_{min} and s_{max}, where $s_{min} \le s_{max}$. Dimensionless measures of these spacings are defined as $\delta_{min} \equiv s_{min}/d$ and $\delta_{max} \equiv s_{max}/d$. By adjusting the values of array angle β and spacings $\delta_{\min}$ and $\delta_{\max}$, the bumpiness of the boundary can be changed. Square arrays are rectangular arrays ($\beta = \pi/2$) for which $\delta_{\min} = \delta_{\max}$. All boundary patterns constructed from the rows of particles described above are characterized by angles β that satisfy the condition,

$$\cos\beta \le \frac{1+\delta_{\min}}{1+\delta_{\max}} \quad , \tag{3.5}$$

so that $\cos^{-1}[(1+\delta_{\min})/(1+\delta_{\max})] \le \beta \le \pi/2$. The unit vector $\boldsymbol{s}$, which describes the orientation of the array, is directed from the center of the central particle to the center of the *closest* particle (i.e. along the line of spacing $\delta_{\min}$) as shown in Figure 3.2.

For completeness we make the following observations concerning the pattern of bumps shown in Figure 3.2. First, because angle β is less than $\pi/2$, particle D can never be closer than either particles B or C to particle A. Furthermore, when

$$\cos\beta \le \frac{1+\delta_{\min}}{2(1+\delta_{\max})} \quad , \tag{3.6}$$

the nearest neighbors to particle A are particles B and C. This is because under these circumstances, the distance from A to E is greater than the distance from A to C. In this case, B is nearer than C to A because $\delta_{\min} < \delta_{\max}$. On the other hand, when

$$\cos\beta \geq \frac{1+\delta_{\min}}{2(1+\delta_{\max})} \quad , \tag{3.7}$$

the nearest neighbors to particle A are particles B and E. Under these circumstances, the distance from A to E is less than the distance from A to C. In this case, B is nearer than E to A when

$$\frac{1+\delta_{\min}}{2(1+\delta_{\max})} \leq \cos\beta \leq \frac{1+\delta_{\max}}{2(1+\delta_{\min})} \quad , \tag{3.8}$$

whereas E is nearer to A when

$$\cos\beta \geq \frac{1+\delta_{\max}}{2(1+\delta_{\min})} \quad . \tag{3.9}$$

In fact, there are no angles β that can satisfy both conditions (3.5) and (3.9) unless

$$\frac{1+\delta_{\min}}{1+\delta_{\max}} \geq \frac{1}{\sqrt{2}} \quad . \tag{3.10}$$

Particles E and F can never be the two nearest neighbors to particle A because the distance $\delta_{\max}$ from A to F is always greater than the distance $\delta_{\min}$ from A to B.

We restrict our attention to spacings $\delta_{\min}$ and $\delta_{\max}$ between the particles that, for any angle β, are never so large as to allow a flow particle to collide with the flat surface of the boundary.

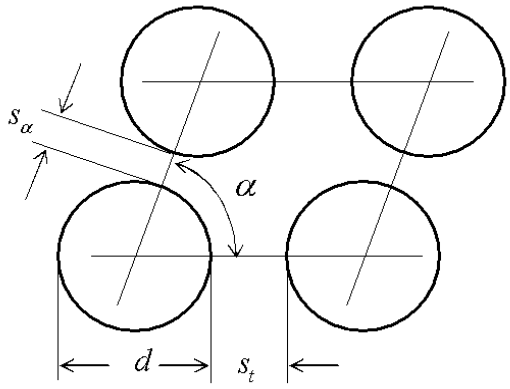

Figure 3.3: Top-view of an array of boundary particles and associated coordinate system

If the pattern is instead described (as shown in Figure 3.3) by the angle α, between 0 and $\pi/2$, the spacings s_t, s_α, and their dimensionless counterparts $\Delta_t \equiv s_t / d$ and $\Delta_\alpha \equiv s_\alpha / d$ such that

$$\cos\alpha > \frac{1+\min(\Delta_t, \Delta_\alpha)}{1+\max(\Delta_t, \Delta_\alpha)} \quad , \tag{3.11}$$

then α, Δ_t, and Δ_α may be transformed into a corresponding set of β, $\delta_{\min}$, and $\delta_{\max}$ in the following manner. We decompose the quotient,

$$\frac{1+\max(\Delta_t, \Delta_\alpha)\cos\alpha}{1+\min(\Delta_t, \Delta_\alpha)} = n + \lambda \quad , \tag{3.12}$$

where n is an integer and $0 < \lambda < 1$. Then the corresponding value of β is determined by,

$$\tan\beta = \frac{[1+\max(\Delta_t, \Delta_\alpha)]\sin\alpha}{\lambda} \quad . \tag{3.13}$$

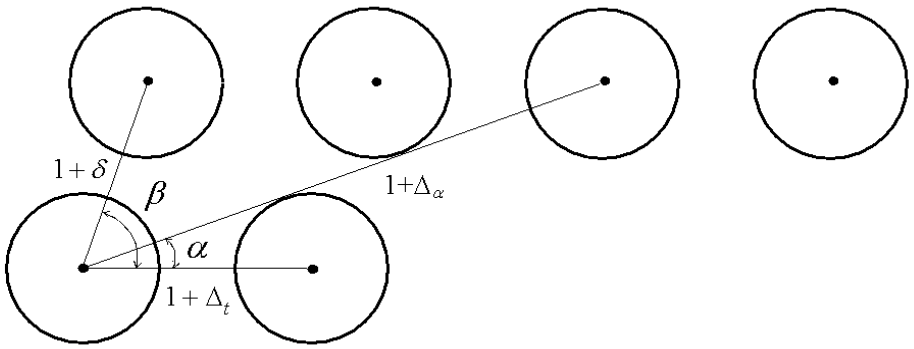

Figure 3.4 : Transformation of Array from α, Δ_t and Δ_α to β, $\delta_{\min}$ and $\delta_{\max}$ (Here n=2)

Furthermore, the dimensionless length δ, shown in Figure 3.4, is fixed by the relation,

$$1+\delta = \sqrt{[1+\max(\Delta_t, \Delta_\alpha)]^2 \sin^2\alpha + \lambda^2} \quad . \tag{3.14}$$

The corresponding values of $\delta_{\min}$ and $\delta_{\max}$ are then given simply by,

$$\delta_{\min} = \min[\min(\Delta_t, \Delta_\alpha), \delta] \quad \text{and} \quad \delta_{\max} = \max[\min(\Delta_t, \Delta_\alpha), \delta] \quad . \tag{3.15}$$

Finally, the orientation of the transformed array is described by the unit vector $\boldsymbol{s}$, which must be directed along the line of spacing $\delta_{\min}$. Explicitly, this means that $\boldsymbol{s}$ is directed along the line of spacing $\min(\Delta_t, \Delta_\alpha)$ if $\min(\Delta_t, \Delta_\alpha) < \delta$, or along the line of spacing δ if $\delta < \min(\Delta_t, \Delta_\alpha)$.

3.2 Transfer Rates

The transfer rates M_i, F_{ij} and D_{ij} depend on boundary geometry and motion as well as motion of particles in flow. Here, we will calculate the transfer rates when the boundaries fluctuate anisotropically and when the flow is undergoing anisotropic motion and experiences gradients of mean velocity at the boundary. Consequently, we will calculate M_i, F_{ij} and D_{ij} based on an anisotropic Maxwellian boundary velocity distribution and an anisotropic Maxwellian flow particle velocity distribution.

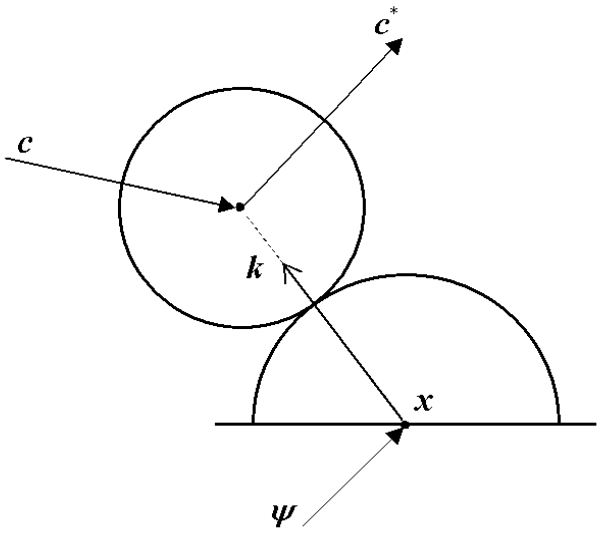

Figure 3.5: A typical boundary collision

The dynamics of a collision at the boundary are described in terms of the pre-collisional velocities $\boldsymbol{c}$ of the flow particle and $\boldsymbol{\psi}$ of the boundary particle, the unit vector $\boldsymbol{k}$ directed from the center of the boundary particle to the center of the flow particle at impact and the coefficient of restitution e_w which characterizes the energy dissipated when smooth particles collide. If the velocity of the boundary particle is unaffected by the collision, then in terms of the relative velocity $\boldsymbol{g} \equiv \boldsymbol{\psi} - \boldsymbol{c}$, the change in linear momentum experienced by the flow particle is

$$m(c_i^* - c_i) = m(1+e_w)(\boldsymbol{g}\cdot\boldsymbol{k})k_i \ , \tag{3.16}$$

where $\boldsymbol{c}^*$ is the post-collisional velocity of the flow particle. The corresponding change in the full second moment is

$$\frac{m}{2}(c_i^* c_j^* - c_i c_j) = \frac{m}{2}(1+e_w)(\boldsymbol{g}\cdot\boldsymbol{k})\Big[(U_i k_j + U_j k_i) + (\Psi_i k_j + \Psi_j k_i) - (1-e_w)(\boldsymbol{g}\cdot\boldsymbol{k})k_i k_j - (g_i k_j + g_j k_i - 2(\boldsymbol{g}\cdot\boldsymbol{k})k_i k_j)\Big] \ , \tag{3.17}$$

where $\Psi \equiv \boldsymbol{\psi} - \boldsymbol{U}$ is the fluctuation velocity of the boundary particle.

The statistics associated with collisions between boundary and flow particles are governed by two velocity distribution functions: $f(\boldsymbol{c}, \boldsymbol{r})$ which describes the flow particles' velocities and $p(\boldsymbol{\psi})$ which gives the probability per unit volume $d\boldsymbol{\psi} \equiv d\psi_1 d\psi_2 d\psi_3$ in velocity space that any boundary particle will have velocity $\boldsymbol{\psi}$ within range $d\boldsymbol{\psi}$.

The motion of the boundary particle is described by its mean velocity $\boldsymbol{U}$ and full second moment of boundary fluctuation velocity $\boldsymbol{B}$. These quantities are analogous to $\boldsymbol{u}$ and $\boldsymbol{K}$ within the flow and are calculated according to

$$\boldsymbol{U_i} = \int \psi_i \, p(\boldsymbol{\psi}) \, d\boldsymbol{\psi} \ , \tag{3.18}$$

and

$$\boldsymbol{B_{ij}} = \int (\psi_i \psi_j)\, p(\boldsymbol{\psi}) d\boldsymbol{\psi} \ , \tag{3.19}$$

in which integrations are over all velocities.

At the instant of impact, the center of boundary particle is located at $\boldsymbol{x}$ and the distance between the centers of the two particles is $\overline{\sigma} \equiv (\sigma + d)/2$. The frequency of collisions per unit area of flat boundary surface that involve flow particles with velocities $\boldsymbol{c}$ in the range $d\boldsymbol{c}$ and boundary particles with velocities $\boldsymbol{\psi}$ in the range $d\boldsymbol{\psi}$ and occur within an element of solid angle $d\boldsymbol{k}$ centered about $\boldsymbol{k}$ on the surface of the boundary particle is

$$\frac{(d+\sigma)^2}{4A} \chi\, f(\boldsymbol{c}, \boldsymbol{x} + \overline{\sigma}\boldsymbol{k})\, p(\boldsymbol{\psi})(\boldsymbol{g} \cdot \boldsymbol{k})\, d\boldsymbol{k} d\boldsymbol{c} d\boldsymbol{\psi} \ , \tag{3.20}$$

Here, $(\boldsymbol{g} \cdot \boldsymbol{k}) > 0$ for a collision to occur and A is the flat surface area inaccessible to flow particles due to the presence of any one boundary particle and its neighbours. In the next section, we derive an expression for A. The factor χ accounts for the effects of excluded volume and the shielding of flow particles from boundary particles by other flow particles. Excluded volume effects account for the space occupied by both the flow particles and boundary particles. Furthermore, the extent of shielding depends on the motion of the flow particles, the motion of the boundary particles and the arrangement of boundary particles. Consequently, we anticipate that χ will at least depend on ν and K_{ij} at the boundary, as well as B_{ij} and the geometry of boundary.

The transfer rates M_i, F_{ij} and D_{ij} are statistical averages of the appropriate changes per collision weighted by collision frequency (3.20). According to equation

(3.16), M_i is the weighted average of $m(1+e_w)(\boldsymbol{g}\cdot\boldsymbol{k})k_i$. According to Equation (3.17), F_{ij} and D_{ij} are the corresponding averages of $\frac{m}{2}(1+e_w)(\boldsymbol{g}\cdot\boldsymbol{k})(\Psi_i k_j+\Psi_j k_i)$ and $\frac{m}{2}(1+e_w)(\boldsymbol{g}\cdot\boldsymbol{k})\left[(1-e_w)(\boldsymbol{g}\cdot\boldsymbol{k})k_i k_j+(g_i k_j+g_j k_i-2(\boldsymbol{g}\cdot\boldsymbol{k})k_i k_j)\right]$. These may be written in the integral form:

$$M_i=\frac{m(1+e_w)}{4A/(d+\sigma)^2}\int\left[(\boldsymbol{g}\cdot\boldsymbol{k})k_i\right]\chi(\boldsymbol{g}\cdot\boldsymbol{k})f(\boldsymbol{c},\boldsymbol{x}+\bar{\sigma}\boldsymbol{k})p(\boldsymbol{\psi})d\boldsymbol{k}d\boldsymbol{c}d\boldsymbol{\psi}\ , \tag{3.21}$$

$$F_{ij}=\frac{m(1+e_w)}{4A/(d+\sigma)^2}\int\left[\frac{1}{2}(\boldsymbol{g}\cdot\boldsymbol{k})(\Psi_i k_j+\Psi_j k_i)\right]\chi(\boldsymbol{g}\cdot\boldsymbol{k})f(\boldsymbol{c},\boldsymbol{x}+\bar{\sigma}\boldsymbol{k})p(\boldsymbol{\psi})d\boldsymbol{k}d\boldsymbol{c}d\boldsymbol{\psi} \tag{3.22}$$

and,

$$D_{ij}=\frac{m(1+e_w)}{4A/(d+\sigma)^2}\int\left[\frac{1}{2}(\boldsymbol{g}\cdot\boldsymbol{k})\left((1-e_w)(\boldsymbol{g}\cdot\boldsymbol{k})k_i k_j+(g_i k_j+g_j k_i-2(\boldsymbol{g}\cdot\boldsymbol{k})k_i k_j)\right)\right] \times\chi(\boldsymbol{g}\cdot\boldsymbol{k})f(\boldsymbol{c},\boldsymbol{x}+\bar{\sigma}\boldsymbol{k})p(\boldsymbol{\psi})d\boldsymbol{k}d\boldsymbol{c}d\boldsymbol{\psi} \tag{3.23}$$

where the velocity integrations are carried out over all velocities such that $(\boldsymbol{g}.\boldsymbol{k})>0$ and the $\boldsymbol{k}-$integration is surface integral over the area of a boundary particle that is accessible to colliding flow particles.

In order to carry out averaging procedure, we must first write down the distribution functions $f(\boldsymbol{c},\boldsymbol{r})$ and $p(\boldsymbol{\psi})$. Here, we take $f(\boldsymbol{c},\boldsymbol{r})$ to be the anisotropic Maxwellian given by Equation (2.24). In addition, we take $p(\boldsymbol{\psi})$ as the anisotropic Maxwellian:

$$p(\boldsymbol{\psi})=\frac{1}{\sqrt{8\pi^3\det(\boldsymbol{B})}}\exp\left\{-\frac{1}{2}\boldsymbol{\Psi}\cdot\boldsymbol{B}^{-1}\cdot\boldsymbol{\Psi}\right\}\ . \tag{3.24}$$

If the integrations over velocities $\boldsymbol{c}$ and $\boldsymbol{\psi}$ in averages (3.21), (3.22) and (3.23) are carried out first, then the intermediate results can be written compactly in terms of the quantity

$$\Phi = \frac{\boldsymbol{v}\cdot\boldsymbol{k}}{\sqrt{2\left(\boldsymbol{k}\cdot(\boldsymbol{K}+\boldsymbol{B})\cdot\boldsymbol{k}\right)}}\ , \tag{3.25}$$

where both $\boldsymbol{v}$ and $\boldsymbol{K}$ are evaluated at $\boldsymbol{x}+\overline{\sigma}\boldsymbol{k}$. The resulting integral expression for the rate at which momentum is supplied to the flow is

$$M_i = \frac{(1+e_w)(d+\sigma)^2}{4\sqrt{\pi}A}\int \rho\chi\left(\boldsymbol{k}\cdot(\boldsymbol{K}+\boldsymbol{B})\cdot\boldsymbol{k}\right)k_i\left[\sqrt{\pi}\left(\frac{1}{2}+\Phi^2\right)\mathrm{erfc}(-\Phi) + \Phi\exp(-\Phi^2)\right]d\boldsymbol{k} \tag{3.26}$$

The corresponding expressions for F_{ij} and D_{ij} are

$$F_{ij} = \frac{(1+e_w)(d+\sigma)^2}{4\sqrt{2\pi}A}\int \rho\chi\left(\boldsymbol{k}\cdot(\boldsymbol{K}+\boldsymbol{B})\cdot\boldsymbol{k}\right)^{1/2}\left((\boldsymbol{k}\cdot\boldsymbol{B})_i k_j + (\boldsymbol{k}\cdot\boldsymbol{B})_j k_i\right) \times\left[\sqrt{\pi}\Phi\mathrm{erfc}(-\Phi)+\exp(-\Phi^2)\right]d\boldsymbol{k} \tag{3.27}$$

and

$$\begin{aligned} D_{ij} = \frac{(1+e_w)(d+\sigma)^2}{4\sqrt{2\pi}A}\int \rho\chi\Bigg\{ & \\ & [(1-e_w)-2]\left(\boldsymbol{k}\cdot(\boldsymbol{K}+\boldsymbol{B})\cdot\boldsymbol{k}\right)^{3/2}k_i k_j\left[\sqrt{\pi}\Phi\left(\frac{3}{2}+\Phi^2\right)\mathrm{erfc}(-\Phi)+(1+\Phi^2)\exp(-\Phi^2)\right] \\ & +\left(\boldsymbol{k}\cdot(\boldsymbol{K}+\boldsymbol{B})\cdot\boldsymbol{k}\right)^{1/2}\left([\boldsymbol{k}\cdot(\boldsymbol{K}+\boldsymbol{B})]_i k_j + [\boldsymbol{k}\cdot(\boldsymbol{K}+\boldsymbol{B})]_j k_i\right)\left[\sqrt{\pi}\Phi\mathrm{erfc}(-\Phi)+\exp(-\Phi^2)\right] \\ & +\frac{1}{\sqrt{2}}\left(\boldsymbol{k}\cdot(\boldsymbol{K}+\boldsymbol{B})\cdot\boldsymbol{k}\right)\left(v_i k_j + v_j k_i\right)\left[\sqrt{\pi}\left(\frac{1}{2}+\Phi^2\right)\mathrm{erfc}(-\Phi)+\Phi\exp(-\Phi^2)\right]\Bigg\}d\boldsymbol{k} \end{aligned} \tag{3.28}$$

where ρ, χ and $\boldsymbol{K}$ are evaluated at $\boldsymbol{x}+\overline{\sigma}\boldsymbol{k}$.

We make the following approximations in the above expressions. We assume that the deviatoric part of $\boldsymbol{K}$ is small compared to its isotropic part T, the velocity $\boldsymbol{v}$ is small compared to isotropic temperature $T^{1/2}$, and the change $\sigma\nabla\boldsymbol{u}$ in velocity is small

compared to $\sqrt{T}$. Also, we assume that the gradients of density are small. We then expand the integrands (3.26), (3.27) and (3.28) in Taylor series about $\boldsymbol{x}+\overline{\sigma}\boldsymbol{n}$ with respect to these quantities. Consistent to the approximations made in the constitutive theory, we retain up to first order terms in the expression for M_i, and only the lowest order terms in F_{ij} and D_{ij}.

In this manner, the resulting expression for M_i may be compactly written as:

$$M_i = \frac{(1+e_w)(d+\sigma)^2}{4\sqrt{\pi}A}\rho\chi\left[\frac{\sqrt{\pi}}{2}\left(T\delta_{jk}+B_{jk}+\hat{K}_{jk}\right)\mathscr{I}_{ijk}+\sqrt{2}\mathscr{I}_i+\sqrt{2}\sigma\mathscr{l}_i\right], \tag{3.29}$$

where, the integrals $\mathscr{I}_{ijk}$, $\mathscr{I}_i$ and $\mathscr{l}_i$, evaluated over the accessible area, are

$$\mathscr{I}_{ijk} = \int k_i k_j k_k \, d\boldsymbol{k} \quad , \tag{3.30}$$

$$\mathscr{I}_i = v_j \int \left(\boldsymbol{k}\cdot(T\boldsymbol{\delta}+\boldsymbol{B})\cdot\boldsymbol{k}\right)^{1/2} k_i k_j \, d\boldsymbol{k} \quad , \tag{3.31}$$

$$\mathscr{l}_i = \frac{\partial u_j}{\partial r_k}\int (k_k - N_k)k_j k_i \left(\boldsymbol{k}\cdot(T\boldsymbol{\delta}+\boldsymbol{B})\cdot\boldsymbol{k}\right)^{1/2} d\boldsymbol{k} \quad . \tag{3.32}$$

Similarly, the expressions for F_{ij} and D_{ij} can be written as:

$$F_{ij} = \frac{(1+e_w)(d+\sigma)^2}{4\sqrt{2\pi}A}\rho\chi\left[\mathscr{f}_{ij}\right] \quad , \tag{3.33}$$

$$D_{ij} = \frac{(1+e_w)(d+\sigma)^2}{4\sqrt{2\pi}A}\rho\chi\left[\left([1-e_w]-2\right)\mathscr{d}_{ij}^{(1)}+\mathscr{d}_{ij}^{(2)}\right] \tag{3.34}$$

where, the integrals $\mathscr{f}_{ij}$, $\mathscr{d}_{ij}^{(1)}$ and $\mathscr{d}_{ij}^{(2)}$, evaluated over the accessible area, are

$$\mathscr{f}_{ij} = \int \left(\boldsymbol{k}\cdot(T\boldsymbol{\delta}+\boldsymbol{B})\cdot\boldsymbol{k}\right)^{1/2}\left((\boldsymbol{k}\cdot\boldsymbol{B})_i k_j + (\boldsymbol{k}\cdot\boldsymbol{B})_j k_i\right)d\boldsymbol{k}\,, \tag{3.35}$$

$$\mathscr{d}_{ij}^{(1)} = \int \left(\boldsymbol{k}\cdot(T\boldsymbol{\delta}+\boldsymbol{B})\cdot\boldsymbol{k}\right)^{3/2} k_i k_j \, d\boldsymbol{k}\,, \tag{3.36}$$

$$\mathcal{d}_{ij}^{(2)} = \int \left(\boldsymbol{k}\cdot(T\boldsymbol{\delta}+\boldsymbol{B})\cdot\boldsymbol{k}\right)^{1/2} \left(\left(\boldsymbol{k}\cdot(T\boldsymbol{\delta}+\boldsymbol{B})\right)_i k_j + \left(\boldsymbol{k}\cdot(T\boldsymbol{\delta}+\boldsymbol{B})\right)_j k_i\right) d\boldsymbol{k}\,. \qquad (3.37)$$

Note that in the expressions (3.29) through (3.37), all mean fields are evaluated at $\boldsymbol{x}+\overline{\sigma}\boldsymbol{n}$.

Now, to calculate the transfer rates M_i, F_{ij} and D_{ij}, it remains only to carry out $\boldsymbol{k}-$integrations (3.29), (3.33) and (3.34) over the portion of a boundary particle's surface that is accessible to flow particles. Hence, we need to determine the accessible surface area of boundary particles.

3.3 Accessible Surface Area of Boundary Particle

At this point, we introduce an $x_1 - x_2 - x_3$ Cartesian coordinate system in which the x_3-direction is normal to the flat surface of boundary and, x_1- and x_2- directions are parallel to the flat surface of the boundary. We also introduce the right-handed orthonormal triad $\boldsymbol{n}-\boldsymbol{t}-\boldsymbol{\tau}$, in which the unit vector $\boldsymbol{n}$ points in $\pm x_3-$direction, the unit vector $\boldsymbol{t}$ points in $\pm x_1-$direction and the unit vector $\boldsymbol{\tau}$ points in x_2-direction. Arrays are fixed on the boundary such that the direction associated with the array spacing s_t, always coincides with the direction of unit vector $\boldsymbol{t}$, i.e., s_t is the array spacing in $\boldsymbol{t}-$direction. In the special case when $\alpha = 90^\circ$, s_α becomes array spacing in $\boldsymbol{\tau}-$direction.

As a result of fixing hemispheres in arrays to the boundary surface, not the entire surface of a hemispherical boundary particle is accessible for interaction with particles in the granular assembly. Furthermore, the accessible surface will change depending upon

the values of α, s_t and s_α. For the purpose of future surface integrations over this accessible area, we need to define and determine it.

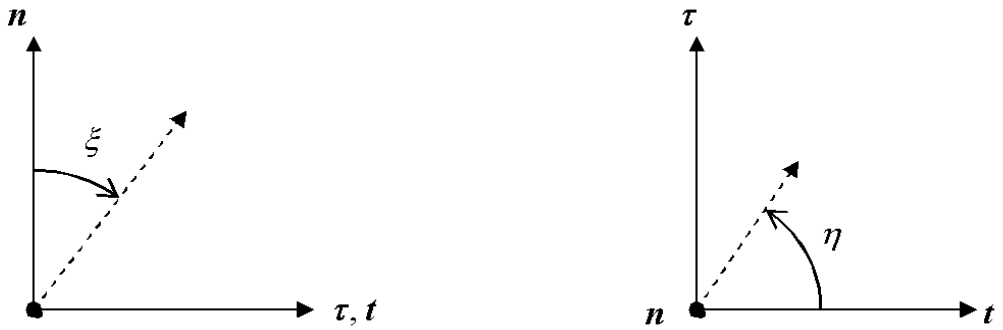

Figure 3.6: Angle-definition for integration over boundary particle surface

To that effect, we define angles ξ and η with respect to the orthonormal triad $\boldsymbol{n}-\boldsymbol{t}-\boldsymbol{\tau}$, as shown in Figure 3.6 (a) and (b). Figure 3.6 (a) shows a plane orthogonal to $\boldsymbol{t}-\boldsymbol{\tau}$ plane. In this plane, angle ξ measures the *positive* acute angle between vector $\boldsymbol{n}$ and the normal to the surface at any point on the surface of a boundary particle. Figure 3.6 (b) shows top-view of a plane parallel to the $\boldsymbol{t}-\boldsymbol{\tau}$ plane. In this plane, angle η measures the counter-clockwise angle from vector $\boldsymbol{t}$, made by the projection on $\boldsymbol{t}-\boldsymbol{\tau}$ plane, of the normal at any point on the surface. Then, ξ, η and the radius $d/2$ can together describe the position of any point on the surface of boundary particle, with respect to the center of the boundary particle. An elemental surface area of the boundary particle is given as $\left(d^2/4\right)\sin\xi d\xi d\eta$. Now, keeping the radial distance fixed at $d/2$, if we vary ξ from 0 to $\pi/2$ and η from 0 to 2π, we can cover the entire surface of

hemispherical boundary particle. However, the entire surface is not accessible and the accessible surface changes with η.

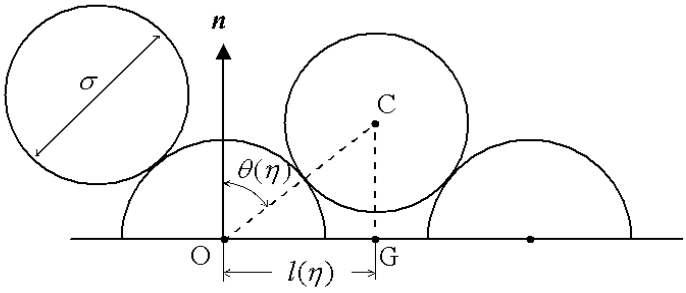

Figure 3.7: Determining the accessible area of a boundary particle

To determine this accessible surface, we look at a plane orthogonal to the $\boldsymbol{t}-\boldsymbol{\tau}$ plane and at an angle η from the vector $\boldsymbol{t}$. In this plane, as shown in Figure 3.7, angle $\theta=\theta(\eta)$ is the maximum possible angle between vector $\boldsymbol{n}$ and the line joining the centers of boundary particle and colliding flow particle. The angle $\theta(\eta)$ dictates the maximum value of ξ for which a flow particle can collide with the boundary particle, in this specific plane. It is defined as

$$\theta(\eta)\equiv\sin^{-1}\left[2l(\eta)/(d+\sigma)\right], \tag{3.38}$$

where $l(\eta)$ is the length OG, of projection of line OC on $\boldsymbol{t}-\boldsymbol{\tau}$ plane. Angle $\theta(\eta)$ is related to roughness of boundary. As the average value of $\theta(\eta)$ increases, boundary becomes more effective at transferring momentum in directions parallel to its flat surface and in that sense, becomes *rougher*.

From the definition (3.38), we see that $\theta(\eta)$ gets determined by calculating $l(\eta)$, which is the length OG as shown in Figure 3.7. While point O is fixed in space, position of point G changes as η changes. Figure 3.8 shows the locus of point G, i.e., the path

G_0-G_1-G_2-G_3-G_4-G_5-G_6, in the top view of array shown in Figure 3.2. Particularly, points G_0, G_2, G_4 and G_6 are the mid-points of lines joining the centers of particles A and B, A and C, A and E and, A and B in the Figure 3.2, respectively. Here, η_s is an angle similar to the angle η, but measured from vector $\boldsymbol{s}$ instead of vector $\boldsymbol{t}$ in counterclockwise direction.

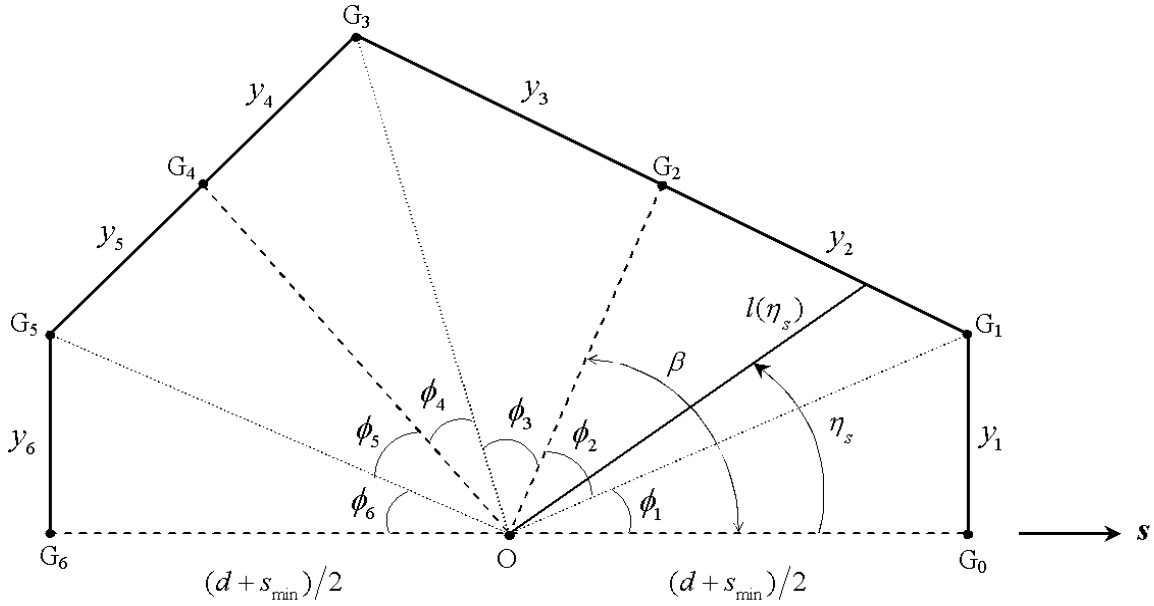

Figure 3.8: Path G_0-G_1-G_2-G_3-G_4-G_5-G_6 shows the locus of point G

The lengths y_1, y_2, y_3, y_4, y_5 and y_6, shown in the Figure 3.8, can be determined using the geometry of the array. Particularly, lengths y_1 and y_2 are simultaneously determined by the following two geometric conditions:

$$4y_1^2 - 4y_2^2 = (d+s_{\max})^2 - (d+s_{\min})^2 \quad , \tag{3.39}$$

and

$$2(d+s_{\max})y_1 + 2(d+s_{\min})y_2 + 4\tan(\beta)y_1y_2 = (d+s_{\min})(d+s_{\max})\tan(\beta) \, . \tag{3.40}$$

Similarly, lengths y_5 and y_6 are simultaneously determined by following two geometric conditions:

$$4y_5^2 - 4y_6^2 = (d + s_{\min})^2 - (d + s_{OG_4})^2 \tag{3.41}$$

and

$$2(d + s_{OG_4})y_6 + 2(d + s_{\min})y_5 + 4\tan(\zeta)y_5y_6 = (d + s_{\min})(d + s_{OG_4})\tan(\zeta) \tag{3.42}$$

where, the length s_{OG_4} and the angle ζ are defined as:

$$s_{OG_4} = \sqrt{(d + s_{\min})^2 + (d + s_{\max})^2 - 2(d + s_{\min})(d + s_{\max})\cos(\beta)} \; - \; d \tag{3.43}$$

$$\zeta = \sin^{-1}\left(\frac{d + s_{\max}}{d + s_{OG_4}}\sin(\beta)\right) \tag{3.44}$$

After lengths y_1, y_2, y_5 and y_6, are determined, lengths y_3 and y_4 get determined from the equality conditions:

$$y_3 = y_2 \tag{3.45}$$

$$y_4 = y_5 \tag{3.46}$$

The flat surface area A, inaccessible to flow particles due to the presence of any one boundary particle and its neighbours, can be obtained as

$$A = y_1(d + s_{\min}) + y_2(d + s_{\max}) + y_5(d + s_{OG_4}) \;, \tag{3.47}$$

and, $A^* = A/d^2$ gives the dimensionless measure of A.

After the lengths y_1, y_2, y_3, y_4, y_5 and y_6 are known, the angles ϕ_1, $\phi_2, \phi_3, \phi_4, \phi_5$ and ϕ_6 can be written down as :

$$\phi_1 = \phi_6 = \tan^{-1}\left(\frac{2y_1}{d + s_{\min}}\right) \tag{3.48}$$

$$\phi_2 = \phi_3 = \tan^{-1}\left(\frac{2y_3}{d + s_{\max}}\right) \tag{3.49}$$

$$\phi_4 = \phi_5 = \tan^{-1}\left(\frac{2y_5}{d + s_{OG_4}}\right) \tag{3.50}$$

Figure 3.8 shows, for $0 \le \eta_s \le \pi$, $l(\eta_s)$ will have four different expressions in the ranges $0 \le \eta_s \le \phi_1$, $\phi_1 \le \eta_s \le (\beta + \phi_3)$, $(\beta + \phi_3) \le \eta_s \le (\pi - \phi_6)$ and $(\pi - \phi_6) \le \eta_s \le \pi$. As a result, $\theta(\eta_s)$ also has four different piecewise expressions in the range $0 \le \eta_s \le \pi$. In terms of array angle β, particle diameter d, array spacings $s_{\min}$, $s_{\max}$, and the lengths y_1, y_2, y_3, y_4, y_5 and y_6, the piecewise expressions for $l(\eta_s)$ and $\theta(\eta_s)$ can be written as follows.

For $0 \le \eta_s \le \phi_1$,

$$l(\eta_s) = \frac{1}{2}\frac{d + s_{\min}}{\cos\eta_s} \text{ and } \theta(\eta_s) = \sin^{-1}\left[\frac{d + s_{\min}}{(d+\sigma)\cos\eta_s}\right]. \tag{3.51}$$

For $\phi_1 \le \eta_s \le (\beta + \phi_3)$,

$$l(\eta_s) = \frac{1}{2}\frac{d + s_{\max}}{\cos(\eta_s - \beta)} \text{ and } \theta(\eta_s) = \sin^{-1}\left[\frac{d + s_{\max}}{(d+\sigma)\cos(\eta_s - \beta)}\right]. \tag{3.52}$$

For $(\beta + \phi_3) \le \eta_s \le (\pi - \phi_6)$,

$$l(\eta_s) = \frac{1}{2}\frac{d + s_{OG_4}}{\cos(\eta_s - \beta - \phi_3 - \phi_4)} \text{ and } \theta(\eta_s) = \sin^{-1}\left[\frac{d + s_{OG_4}}{(d+\sigma)\cos(\eta_s - \beta - \phi_3 - \phi_4)}\right]. \tag{3.53}$$

For $(\pi - \phi_6) \le \eta_s \le \pi$,

$$l(\eta_s) = -\frac{1}{2}\frac{d + s_{\min}}{\cos\eta_s} \text{ and } \theta(\eta_s) = \sin^{-1}\left[\frac{d + s_{\min}}{-(d+\sigma)\cos\eta_s}\right]. \tag{3.54}$$

For the range, $\pi \le \eta_s \le 2\pi$, we can use the *symmetry* of the array to write

$$\theta(\eta_s) = \theta(\eta_s - \pi). \tag{3.55}$$

Expressions for $\theta(\eta)$ can be obtained by using $\theta(\eta_s)$, and relating the angles η and η_s, and hence relating orientations of unit vectors $\boldsymbol{t}$ and $\boldsymbol{s}$. As described previously, vector $\boldsymbol{t}$ is directed along the line of spacing Δ_t and vector $\boldsymbol{s}$ is directed along the line of spacing $\delta_{\min}$. As shown in Figure 3.4, this means that $\boldsymbol{s}$ is directed along the line of spacing $\min(\Delta_t, \Delta_\alpha)$ if $\min(\Delta_t, \Delta_\alpha) < \delta$, or along the line of spacing δ if $\delta < \min(\Delta_t, \Delta_\alpha)$. Hence, depending upon the values of α, Δ_t and Δ_α, η and η_s are related as follows:

If $\min(\Delta_t, \Delta_\alpha) < \delta$ and $\Delta_t \le \Delta_\alpha$,

$$\eta = \eta_s. \tag{3.56}$$

If $\min(\Delta_t, \Delta_\alpha) < \delta$ and $\Delta_\alpha < \Delta_t$,

$$\eta = \eta_s + \alpha. \tag{3.57}$$

Finally, if $\delta < \min(\Delta_t, \Delta_\alpha)$,

$$\eta = \eta_s + \beta \tag{3.58}$$

Hence, using the appropriate of Equations (3.56), (3.57) and (3.58), we can obtain $\theta(\eta)$ by using $\theta(\eta_s)$. Once $\theta(\eta)$ is determined, the accessible surface area of a boundary particle can be obtained by integrating the elemental surface area $\left(d^2/4\right)\sin\xi d\xi d\eta$ over angles ξ and η, in the limits 0 to $\theta(\eta)$ for angle ξ and 0 to 2π for angle η.

For the above analysis to be valid, the spacings between the boundary particles should never be so great that a flow particle could touch the flat surface of boundary. To find the restrictions this condition puts on array parameters α, Δ_t and Δ_α, lets analyze a case when a flow particle would just touch flat surface of boundary.

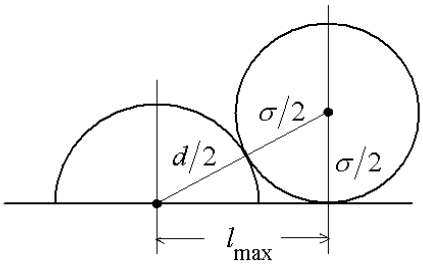

Figure 3.9: Extreme case when a flow particle just touches flat surface of boundary

As shown in Figure 3.9, under such condition, l would be equal to its maximum allowable value $l_{\max}$ given by

$$l_{\max} = \frac{1}{2}\sqrt{(d+\sigma)^2 - \sigma^2}\ . \tag{3.59}$$

If this situation is not to occur, $l(\eta)$ should always be less than $l_{\max}$. Referring to Figure 3.8, we can write down the maximum possible value of $l(\eta)$, $[l(\eta)]_{\max}$, in terms of parameters d, $s_{\min}$ and y_1 as,

$$[l(\eta)]_{\max} = \frac{1}{2}\sqrt{(d+s_{\min})^2 + 4y_1^{\,2}} \tag{3.60}$$

So, the condition that α, Δ_t and Δ_α must satisfy so that no flow particle can touch the flat part of boundary is

$$[(d+s_{\min})^2 + 4y_1^{\,2}] \ < \ [(d+\sigma)^2 - \sigma^2] \tag{3.61}$$

Figure 3.10 shows the curves that put limit on values of Δ_t and Δ_α, for α=45°, 60°, 75° and 90°, when $\sigma = d$. The region below each curve indicates the permissible values of Δ_t and Δ_α, for that particular value of α. As α decreases, permissible range of Δ_t and Δ_α increases. Also, we note that the maximum possible value of $\Delta_t = \Delta_\alpha$ that can be used for any array angle α is 0.2247.

In this Chapter, we have written down the boundary conditions and calculated the integral expressions of the transfer rates M_i, F_{ij} and D_{ij}. The general formulation for the flow has already been derived in Chapter 2. So, in the next Chapter, we can look at the general boundary value problem for vibrated granular flows.

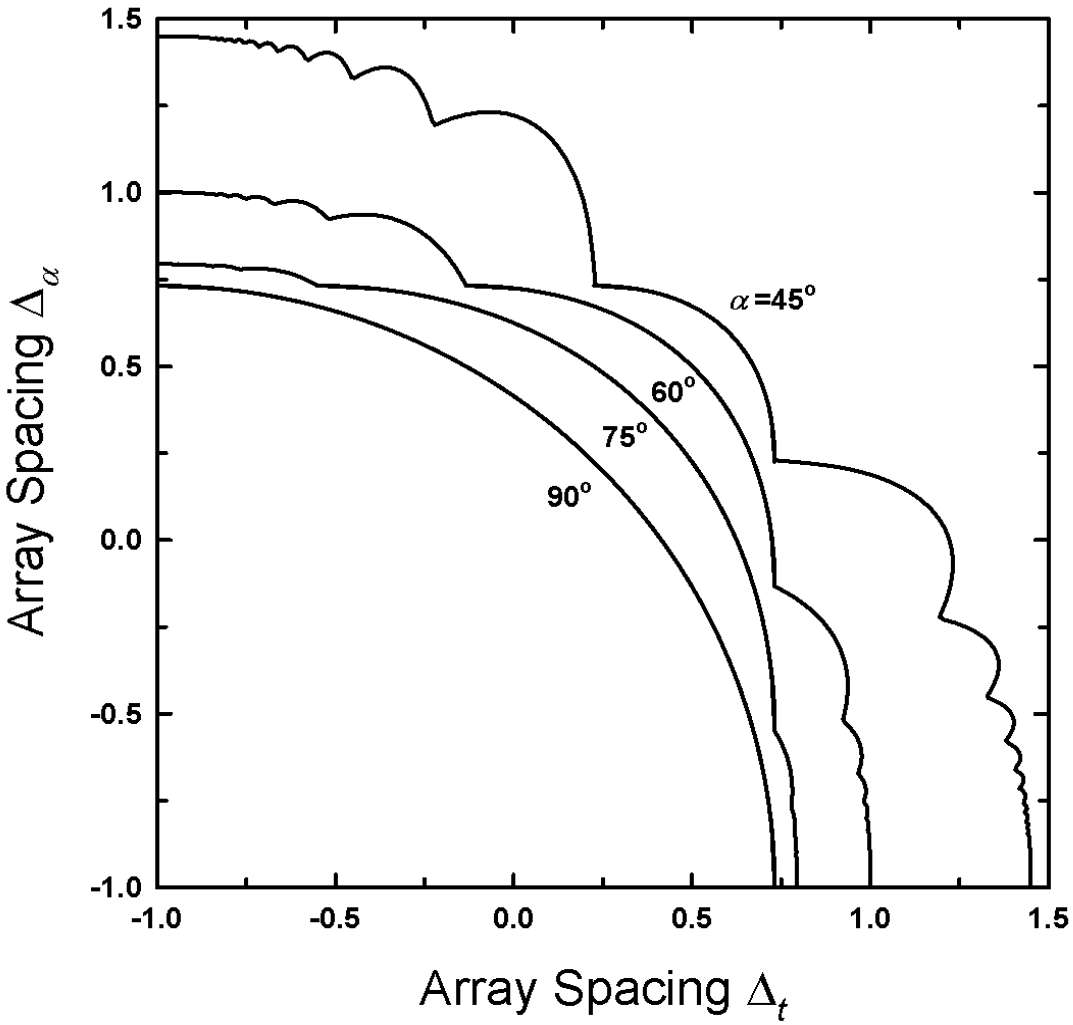

Figure 3.10: Limiting values of Δ_α and Δ_t for α=45°, 60°, 75° and 90°, when $\sigma = d$. The region below each curve indicates the permissible values of Δ_α and Δ_t, for that particular value of α.

CHAPTER 4

Steady, Fully Developed, Parallel Flows: Boundary Value Problem

In the chapters that follow we will examine steady, fully developed granular flows in which the mean velocity is parallel to the flat surface of boundary and where spatial variations of mean fields occur only in the direction perpendicular to that of the mean flow. In this chapter, we write down the general boundary value problem, in non-dimensional form, for these flows.

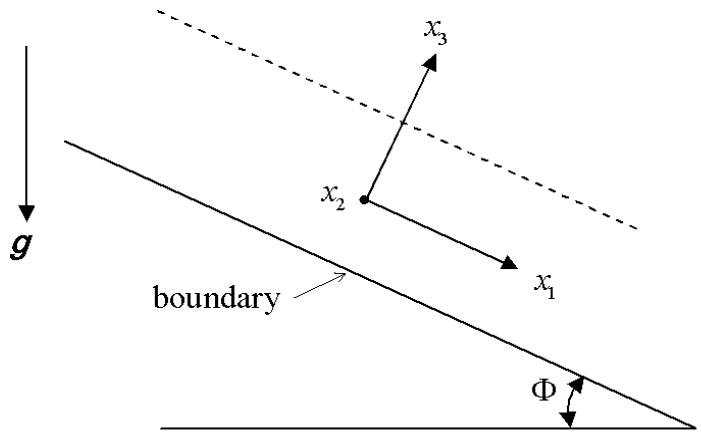

Figure 4.1: The coordinate system

We employ the same Cartesian coordinate system introduced to write down the boundary conditions. Here, x_3- defines the direction upon which the mean fields depend. The flows are infinite in x_1- and x_2- directions. The vertical acceleration due to gravity is g and the angle between the boundary and horizontal is Φ.

4.1 Balance Equations

For purposes of non-dimensionalization, we introduce the characteristic velocity a. Then, the dimensionless mean fields are defined as follows. The dimensionless

coordinate $z \equiv x_3/\sigma$. The solid volume fraction ν has already been defined. The non-dimensional velocities u_t and u_τ are defined as $u_t \equiv u_1/a$ and $u_\tau \equiv u_2/a$. The full second moment for granular flow is $\kappa_{ij} \equiv K_{ij}/a^2$. The isotropic measure of temperature and the temperatures in individual directions can be written in non-dimensional form as $w^2 = \mathcal{T} \equiv T/a^2$, $\mathcal{T}_t \equiv K_{11}/a^2$, $\mathcal{T}_\tau \equiv K_{22}/a^2$ and $\mathcal{T}_n \equiv K_{33}/a^2$. The dimensionless versions of pressures are defined as $P_{nn} \equiv P_{33}/\rho_p a^2$, $S_{nt} \equiv P_{31}/\rho_p a^2$ and $S_{n\tau} \equiv P_{32}/\rho_p a^2$. The mean fields depend only on z.

In these flows, balance of mass (2.16) is identically satisfied. The simplified, appropriate forms of equation (2.17) yield momentum balance. The x_1-component of the momentum balance is

$$\frac{dS_{nt}}{dz} = \frac{\sigma g}{a^2}\nu\sin(\Phi)\,, \tag{4.1}$$

where, $S_{nt} = \nu\left(1+\frac{4(1+e)G}{5}\right)\kappa_{13} - \frac{4(1+e)\nu G w}{5\sqrt{\pi}}\frac{du_t}{dz}$. (4.2)

The x_2-component is given as

$$\frac{dS_{n\tau}}{dz} = 0\,, \tag{4.3}$$

where, $S_{n\tau} = \nu\left(1+\frac{4(1+e)G}{5}\right)\kappa_{23} - \frac{4(1+e)\nu G w}{5\sqrt{\pi}}\frac{du_\tau}{dz}$, (4.4)

and, the x_3-component is

$$\frac{dP_{nn}}{dz} = -\frac{\sigma g}{a^2}\nu\cos(\Phi)\,, \tag{4.5}$$

where, for P_{nn} we substitute $P_{nn} = \nu w^2\left(1+2(1+e)G\right) + \nu\hat{\kappa}_{33}\left(1+\frac{4(1+e)G}{5}\right)$. (4.6)

The balance of full second moment is decomposed into balance of energy and balance of the deviatoric part of second moment. In terms of non-dimensional flux of full second moment $q_{ij} \equiv Q_{3ij} / \rho_p a^3$ and collisional source of second moment $\Upsilon_{ij} \equiv \gamma_{ij} \sigma / \rho_p a^3$, the balance of energy (2.19) becomes,

$$\frac{1}{2}\frac{dq_{ii}}{dz} + S_{n\tau}\frac{du_\tau}{dz} + S_{nt}\frac{du_t}{dz} - \frac{1}{2}\Upsilon_{ii} = 0, \tag{4.7}$$

and the remaining independent components of the deviatoric second moment equation (2.20) can be written down as,

$$\frac{1}{2}\frac{d\hat{q}_{22}}{dz} + \frac{1}{3}\left(\frac{1}{2}S_{n\tau} + \frac{3}{2}\nu\kappa_{23}\right)\frac{du_\tau}{dz} - \frac{1}{3}S_{nt}\frac{du_t}{dz} - \frac{1}{2}\left(\Upsilon_{22} - \frac{1}{3}\Upsilon_{ii}\right) = 0, \tag{4.8}$$

$$\frac{1}{2}\frac{d\hat{q}_{33}}{dz} - \frac{1}{3}\left(-\frac{1}{2}S_{n\tau} + \frac{3}{2}\nu\kappa_{23}\right)\frac{du_\tau}{dz} - \frac{1}{3}\left(-\frac{1}{2}S_{nt} + \frac{3}{2}\nu\kappa_{13}\right)\frac{du_t}{dz} - \frac{1}{2}\left(\Upsilon_{33} - \frac{1}{3}\Upsilon_{ii}\right) = 0, \tag{4.9}$$

$$\begin{aligned}\frac{1}{2}\frac{dq_{23}}{dz} &+ \left(\frac{1}{2}\nu(w^2 + \hat{\kappa}_{33}) + (1+e)\nu G\left(w^2 + \frac{1}{5}(\hat{\kappa}_{22} + \hat{\kappa}_{33})\right)\right)\frac{du_\tau}{dz} \\ &+ \frac{1}{5}(1+e)\nu G\kappa_{12}\frac{du_t}{dz} - \frac{1}{2}\Upsilon_{23} = 0\end{aligned} \tag{4.10}$$

$$\begin{aligned}\frac{1}{2}\frac{dq_{13}}{dz} &+ \left(\frac{1}{2}\nu(w^2 + \hat{\kappa}_{33}) + (1+e)\nu G\left(w^2 - \frac{1}{5}\hat{\kappa}_{22}\right)\right)\frac{du_t}{dz} \\ &+ \frac{1}{5}(1+e)\nu G\kappa_{12}\frac{du_\tau}{dz} - \frac{1}{2}\Upsilon_{13} = 0\end{aligned} \tag{4.11}$$

and,

$$\frac{1}{2}\frac{dq_{12}}{dz} + \frac{1}{4}(S_{nt} + \nu\kappa_{13})\frac{du_\tau}{dz} + \frac{1}{4}(S_{n\tau} + \nu\kappa_{23})\frac{du_t}{dz} - \frac{1}{2}\Upsilon_{12} = 0, \tag{4.12}$$

where for the components of Υ, we substitute the following expressions:

$$\begin{aligned}\Upsilon_{ii} = \frac{6(1-e)(1+e)\nu G w^3}{\sqrt{\pi}}\Bigg[&-4 - \frac{1}{5w^2}\left(\left(\frac{du_t}{dz}\right)^2 + \left(\frac{du_\tau}{dz}\right)^2\right) + \frac{2\sqrt{\pi}}{5w^3}\left(\kappa_{23}\frac{du_\tau}{dz} + \kappa_{13}\frac{du_t}{dz}\right) \\ &- \frac{2}{5w^4}\left(\hat{\kappa}_{22}^{\,2} + \hat{\kappa}_{33}^{\,2} + \hat{\kappa}_{22}\hat{\kappa}_{33} + \kappa_{12}^{\,2} + \kappa_{23}^{\,2} + \kappa_{13}^{\,2}\right)\Bigg]\end{aligned} \tag{4.13}$$

$$\hat{\Upsilon}_{22} = \frac{6(1+e)\nu G w^3}{\sqrt{\pi}}\Bigg[-\frac{4(3-e)}{5w^2}\hat{\kappa}_{22} - \frac{2(2-e)}{105w^2}\left(\left(\frac{du_\tau}{dz}\right)^2 - 2\left(\frac{du_t}{dz}\right)^2\right) + \frac{2\sqrt{\pi}(5-2e)}{105w^3}\left(\kappa_{23}\frac{du_\tau}{dz} - 2\kappa_{13}\frac{du_t}{dz}\right) - \frac{4(3-e)}{105w^4}\left(\hat{\kappa}_{22}{}^2 - 2\hat{\kappa}_{33}{}^2 - 2\hat{\kappa}_{22}\hat{\kappa}_{33} + \kappa_{12}{}^2 + \kappa_{23}{}^2 - 2\kappa_{13}{}^2\right)\Bigg] \tag{4.14}$$

$$\hat{\Upsilon}_{33} = \frac{6(1+e)\nu G w^3}{\sqrt{\pi}}\Bigg[-\frac{4(3-e)}{5w^2}\hat{\kappa}_{33} - \frac{2(2-e)}{105w^2}\left(\left(\frac{du_\tau}{dz}\right)^2 + \left(\frac{du_t}{dz}\right)^2\right) + \frac{2\sqrt{\pi}(5-2e)}{105w^3}\left(\kappa_{23}\frac{du_\tau}{dz} + \kappa_{13}\frac{du_t}{dz}\right) - \frac{4(3-e)}{105w^4}\left(-2\hat{\kappa}_{22}{}^2 + \hat{\kappa}_{33}{}^2 - 2\hat{\kappa}_{22}\hat{\kappa}_{33} - 2\kappa_{12}{}^2 + \kappa_{23}{}^2 + \kappa_{13}{}^2\right)\Bigg] \tag{4.15}$$

$$\Upsilon_{23} = \frac{6(1+e)\nu G w^3}{\sqrt{\pi}}\Bigg[-\frac{4(3-e)}{5w^2}\kappa_{23} + \frac{\sqrt{\pi}(2-e)}{5w}\frac{du_\tau}{dz} + \frac{\sqrt{\pi}(5-2e)}{35w^3}\left((\hat{\kappa}_{22}+\hat{\kappa}_{33})\frac{du_\tau}{dz} + \kappa_{12}\frac{du_t}{dz}\right) - \frac{4(3-e)}{35w^4}\left((\hat{\kappa}_{22}+\hat{\kappa}_{33})\kappa_{23} + \kappa_{12}\kappa_{13}\right)\Bigg] \tag{4.16}$$

$$\Upsilon_{13} = \frac{6(1+e)\nu G w^3}{\sqrt{\pi}}\Bigg[-\frac{4(3-e)}{5w^2}\kappa_{13} + \frac{\sqrt{\pi}(2-e)}{5w}\frac{du_t}{dz} + \frac{\sqrt{\pi}(5-2e)}{35w^3}\left(\kappa_{12}\frac{du_\tau}{dz} - \hat{\kappa}_{22}\frac{du_t}{dz}\right) - \frac{4(3-e)}{35w^4}\left(-\hat{\kappa}_{22}\kappa_{13} + \kappa_{23}\kappa_{12}\right)\Bigg] \tag{4.17}$$

$$\Upsilon_{12} = \frac{6(1+e)\nu G w^3}{\sqrt{\pi}}\Bigg[-\frac{4(3-e)}{5w^2}\kappa_{12} - \frac{2(2-e)}{35w^2}\frac{du_t}{dz}\frac{du_\tau}{dz} + \frac{\sqrt{\pi}(5-2e)}{35w^3}\left(\kappa_{13}\frac{du_\tau}{dz} + \kappa_{23}\frac{du_t}{dz}\right) - \frac{4(3-e)}{35w^4}\left(-\hat{\kappa}_{33}\kappa_{12} + \kappa_{23}\kappa_{13}\right)\Bigg] \tag{4.18}$$

and, the constitutive relations for the components of flux of second moment appearing in above balance equations are given as :

$$q_{ii} = -\frac{4(1+e)\nu G w}{5\sqrt{\pi}}\left(2w\left(3\alpha(\nu,e) + 2\beta(\nu,e)\right)\frac{dw}{dz} + (1+3e)\frac{d\hat{\kappa}_{33}}{dz}\right) \tag{4.19}$$

$$\hat{q}_{22} = -\frac{4(1+e)\nu G w}{5\sqrt{\pi}}\left(-\frac{4}{3}w\beta(\nu,e)\frac{dw}{dz}+\frac{(1+3e)}{7}\frac{d\hat{\kappa}_{22}}{dz}-\frac{4(1+3e)}{21}\frac{d\hat{\kappa}_{33}}{dz}\right) \tag{4.20}$$

$$\hat{q}_{33} = -\frac{4(1+e)\nu G w}{5\sqrt{\pi}}\left(\frac{8}{3}w\beta(\nu,e)\frac{dw}{dz}+\frac{11(1+3e)}{21}\frac{d\hat{\kappa}_{33}}{dz}\right) \tag{4.21}$$

$$q_{23} = -\frac{12(1+e)(1+3e)\nu G w}{35\sqrt{\pi}}\left(\frac{d\kappa_{23}}{dz}\right) \tag{4.22}$$

$$q_{13} = -\frac{12(1+e)(1+3e)\nu G w}{35\sqrt{\pi}}\left(\frac{d\kappa_{13}}{dz}\right) \tag{4.23}$$

and,

$$q_{12} = -\frac{4(1+e)(1+3e)\nu G w}{35\sqrt{\pi}}\left(\frac{d\kappa_{12}}{dz}\right) \tag{4.24}$$

In general, the boundary value problem has 17 unknown mean fields which are ν, w, $\hat{\kappa}_{22}$, $\hat{\kappa}_{33}$, κ_{12}, κ_{23}, κ_{13}, u_t, u_τ, q_{ii}, $\hat{q}_{22}$, $\hat{q}_{33}$, q_{12}, q_{23}, q_{13}, S_{nt} and $S_{n\tau}$.

These 17 mean fields are solutions of 17 non-linear *O.D.E.*s formed by balance equations (4.1), (4.3), (4.5), (4.7), (4.8), (4.9), (4.10), (4.11), (4.12) together with the constitutive relations (4.2), (4.4), (4.19), (4.20), (4.21), (4.22), (4.23) and (4.24).

4.2 Boundary Conditions

In order to write conditions that express the balance of momentum and full second moment at a randomly fluctuating bumpy boundary in non-dimensional form, we introduce dimensionless full second moment of boundary velocity fluctuations, $\beta_{ij} = \frac{B_{ij}}{a^2}$.

The diagonal components of this second moment tensor β_{ij} correspond to fluctuation energies of the boundary in the 3 orthogonal directions. These can be written in non-

dimensional form as $V_t^2 = V_1^2/a^2$, $V_\tau^2 = V_2^2/a^2$ and $V_n^2 = V_3^2/a^2$. Also the mean square velocity of boundary fluctuations $V^2 = (B_{11}+B_{22}+B_{33})/3$ which represents the total energy associated with boundary fluctuations, can be non-dimensionalized as $E \equiv V^2/a^2$.

Then, the x_1 – component of momentum balance at the boundary can be written in non-dimensional form as :

$$S_{nt} = \frac{(1+e_w)(1+r)^2}{4\sqrt{\pi}A^*}\nu\chi\left[\sqrt{\pi}/2\left(w^2\delta_{lm}+\beta_{lm}+\hat{\kappa}_{lm}\right)I_{1lm} - \sqrt{2}\left(I_1 - I_1\right)\right] \quad (4.25)$$

where, the integrals I_{ijk}, I_i and I_i, which correspond to $\mathcal{I}_{ijk}$, $\mathcal{I}_i$ and $\mathcal{I}_i$ given by Equations (3.30), (3.31) and (3.32) when U=0, are defined as

$$I_{ijk} = \int_0^{2\pi}\int_0^{\theta(\eta)} k_i k_j k_k \sin\xi \, d\xi d\eta \ , \quad (4.26)$$

$$\begin{aligned} I_i = {} & u_t \int_0^{2\pi}\int_0^{\theta(\eta)} \left(\boldsymbol{k}\cdot(w^2\boldsymbol{\delta}+\boldsymbol{\beta})\cdot\boldsymbol{k}\right)^{1/2} k_i \sin^2\xi\cos\eta \, d\xi d\eta \\ & + u_\tau \int_0^{2\pi}\int_0^{\theta(\eta)} \left(\boldsymbol{k}\cdot(w^2\boldsymbol{\delta}+\boldsymbol{\beta})\cdot\boldsymbol{k}\right)^{1/2} k_i \sin^2\xi\sin\eta \, d\xi d\eta \end{aligned} \quad (4.27)$$

and,

$$\begin{aligned} I_i = {} & \frac{du_t}{dz}\int_0^{2\pi}\int_0^{\theta(\eta)} \left(\boldsymbol{k}\cdot(w^2\boldsymbol{\delta}+\boldsymbol{\beta})\cdot\boldsymbol{k}\right)^{1/2} k_i(1-\cos\xi)\sin^2\xi\cos\eta \, d\xi d\eta \\ & + \frac{du_\tau}{dz}\int_0^{2\pi}\int_0^{\theta(\eta)} \left(\boldsymbol{k}\cdot(w^2\boldsymbol{\delta}+\boldsymbol{\beta})\cdot\boldsymbol{k}\right)^{1/2} k_i(1-\cos\xi)\sin^2\xi\sin\eta \, d\xi d\eta \end{aligned} \ , \quad (4.28)$$

The x_2 – and x_3 – components of momentum balance are, respectively, given as

$$S_{n\tau} = \frac{(1+e_w)(1+r)^2}{4\sqrt{\pi}A^*}\nu\chi\left[\sqrt{\pi}/2\left(w^2\delta_{lm}+\beta_{lm}+\hat{\kappa}_{lm}\right)I_{3lm} - \sqrt{2}\left(I_3 - I_3\right)\right] \quad (4.29)$$

$$P_{nn} = \frac{(1+e_w)(1+r)^2}{4\sqrt{\pi}A^*}\nu\chi\left[\sqrt{\pi}/2\left(w^2\delta_{lm}+\beta_{lm}+\hat{\kappa}_{lm}\right)I_{2lm}-\sqrt{2}\left(I_2-I_2\right)\right] \tag{4.30}$$

where, for P_{nn}, we use expression given by equation (4.6).

The full second moment balance boundary condition can be decomposed into energy balance boundary condition and deviatoric second moment balance boundary condition. In terms of the non-dimensional integrals f_{ij}, $d_{ij}^{(1)}$ and $d_{ij}^{(2)}$, which correspond to $\mathcal{f}_{ij}$, $\mathcal{d}_{ij}^{(1)}$ and $\mathcal{d}_{ij}^{(2)}$ given by Equations (3.24) through (3.26), are

$$f_{ij} = \int_0^{2\pi}\int_0^{\theta(\eta)}\left(\boldsymbol{k}\cdot(w^2\boldsymbol{\delta}+\boldsymbol{\beta})\cdot\boldsymbol{k}\right)^{1/2}\left((\boldsymbol{k}\cdot\boldsymbol{\beta})_i k_j+(\boldsymbol{k}\cdot\boldsymbol{\beta})_j k_i\right)\sin\xi\, d\xi d\eta\,, \tag{4.31}$$

$$d_{ij}^{(1)} = \int_0^{2\pi}\int_0^{\theta(\eta)}\left(\boldsymbol{k}\cdot(w^2\boldsymbol{\delta}+\boldsymbol{\beta})\cdot\boldsymbol{k}\right)^{3/2} k_i k_j \sin\xi\, d\xi d\eta\,, \tag{4.32}$$

and,

$$d_{ij}^{(2)} = \int_0^{2\pi}\int_0^{\theta(\eta)}\left(\boldsymbol{k}\cdot(w^2\boldsymbol{\delta}+\boldsymbol{\beta})\cdot\boldsymbol{k}\right)^{1/2}\left(\left(\boldsymbol{k}\cdot(w^2\boldsymbol{\delta}+\boldsymbol{\beta})\right)_i k_j+\left(\boldsymbol{k}\cdot(w^2\boldsymbol{\delta}+\boldsymbol{\beta})\right)_j k_i\right)\sin\xi\, d\xi d\eta \tag{4.33}$$

the dimensionless form of energy balance boundary condition becomes:

$$0 = q_{ii}+S_{nt}u_t+S_{n\tau}u_\tau-\frac{(1+e_w)(1+r)^2}{4\sqrt{2\pi}A^*}\nu\chi\left\{f_{ii}-\left[((1-e_w)-2)d_{ii}^{(1)}+d_{ii}^{(2)}\right]\right\} \tag{4.35}$$

Then, the components of deviatoric second moment balance boundary condition can be written down as follows:

2-2 component of deviatoric second moment balance:

$$\begin{aligned}0 = q_{22}-\frac{1}{3}S_{nt}u_t+\frac{2}{3}S_{n\tau}u_\tau-\frac{(1+e_w)(1+r)^2}{4\sqrt{2\pi}A^*}\nu\chi\Bigg\{&\left(f_{22}-\frac{1}{3}f_{ii}\right)-\Bigg[((1-e_w)-2)\left(d_{22}^{(1)}-\frac{1}{3}d_{ii}^{(1)}\right)\\&+\left(d_{22}^{(2)}-\frac{1}{3}d_{ii}^{(2)}\right)\Bigg]\Bigg\}\end{aligned} \tag{4.36}$$

3-3 component of deviatoric second moment balance:

$$0 = q_{33} - \frac{1}{3}S_{nt}u_t - \frac{1}{3}S_{n\tau}u_\tau - \frac{(1+e_w)(1+r)^2}{4\sqrt{2\pi}A^*}\nu\chi\left\{\left(f_{33} - \frac{1}{3}f_{ii}\right) - \left[((1-e_w)-2)\left(d_{33}{}^{(1)} - \frac{1}{3}d_{ii}{}^{(1)}\right) + \left(d_{33}{}^{(2)} - \frac{1}{3}d_{ii}{}^{(2)}\right)\right]\right\} \tag{4.37}$$

1-2 component of deviatoric second moment balance:

$$0 = q_{12} + \frac{1}{2}S_{nt}u_\tau + \frac{1}{2}S_{n\tau}u_t - \frac{(1+e_w)(1+r)^2}{4\sqrt{2\pi}A^*}\nu\chi\left\{f_{12} - \left[((1-e_w)-2)d_{12}{}^{(1)} + d_{12}{}^{(2)}\right]\right\} \tag{4.38}$$

2-3 component of deviatoric second moment balance:

$$0 = q_{23} + \frac{1}{2}P_{nn}u_\tau - \frac{(1+e_w)(1+r)^2}{4\sqrt{2\pi}A^*}\nu\chi\left\{f_{23} - \left[((1-e_w)-2)d_{23}{}^{(1)} + d_{23}{}^{(2)}\right]\right\} \tag{4.39}$$

and,

1-3 component of deviatoric second moment balance:

$$0 = q_{13} + \frac{1}{2}P_{nn}u_t - \frac{(1+e_w)(1+r)^2}{4\sqrt{2\pi}A^*}\nu\chi\left\{f_{13} - \left[((1-e_w)-2)d_{13}{}^{(1)} + d_{13}{}^{(2)}\right]\right\} \tag{4.40}$$

The boundary conditions at the free surface dictate that normal stress, shear stress and flux of second moment vanish there. So, at the free surface we have:

$$P_{nn} = 0 \Rightarrow \nu = 0 \tag{4.41}$$

$$S_{nt} = 0 \tag{4.42}$$

$$S_{n\tau} = 0 \tag{4.43}$$

$$q = 0 \tag{4.44}$$

$$\hat{q}_{22} = 0 \tag{4.45}$$

$$\hat{q}_{33} = 0 \tag{4.46}$$

$$q_{12} = 0 \tag{4.47}$$

$$q_{23} = 0 \tag{4.48}$$

$$q_{13} = 0 \tag{4.49}$$

Equation (4.30) can be used to eliminate the unknown factor χ appearing in the boundary conditions. Then, Equations (4.25), (4.29) and (4.35) through (4.49) provide 17 non-linear boundary conditions for the 17 non-linear *O.D.E.*s described in previous section. Then the only parameter to be determined is the depth of flow, β. By prescribing the mass hold-up, m_t, defined as

$$m_t \equiv \int_0^{\beta} v dz \tag{4.50}$$

the flow height gets determined. With this, the boundary value problem for free surface flows gets completely described.

4.3 Deterministic Boundary Motion

The boundary conditions derived in Chapter 3 apply to boundaries whose vibrations are random and described in terms of velocity distribution function. Calculating similar boundary conditions for boundaries that vibrate harmonically would require carrying out averages that account for the dependence of the boundaries' velocities on time. To avoid this complication, we assume that the averages carried out based on a statistical description (i.e. anisotropic Maxwellian) of the boundaries' velocities adequately represent boundaries whose motion is harmonic provided that we relate the components of second moment tensor $\boldsymbol{B}$ that describe the random motion of fluctuating boundaries to the amplitudes and frequencies that describe the periodic motion of harmonic boundaries. To this end, we consider boundaries that vibrate periodically in the three coordinate directions about a position that is independent of time. The particles on the boundary have velocities in the three directions given by

$$\dot{x}_i = A_i d_i \omega \sin(d_i \omega t + \xi_i), \qquad (i=1,2, \text{ or } 3) \tag{4.51}$$

where d_3=1, and d_1 and d_2 are positive integers. The amplitudes A_i, phase angles ξ_i, integers d_1 and d_2, and frequency factor ω are all adjustable parameters that influence the rates at which momentum and energy are transferred to the flows. We restrict attention to boundaries with amplitudes of vibration that are of the same order as the mean free path within the flow, and with periods of oscillation that are of the same order as the time between collisions within the flow. For these boundaries, we interpret the components B_{ij} as the time averages of the products $\dot{x}_i \dot{x}_j$ over the longest period $(2\pi/\omega)$ of oscillation; i.e.

$$B_{ij} = \begin{cases} \frac{1}{2} A_i A_j d_i d_j \omega^2 \cos \xi_{ij} & d_i = d_j \\ 0 & d_i \neq d_j \end{cases} \tag{4.52}$$

where, $\xi_{ij} = \xi_i - \xi_j$.

According to this correspondence, any two diagonal components of $\boldsymbol{B}$ will be equal when the corresponding products, $A_1 d_1$, $A_2 d_2$, $A_3 d_3$ are equal; any off-diagonal component of $\boldsymbol{B}$ will vanish when the vibrations in the two corresponding orthogonal directions are either at the same frequency and $\pi/2$ radians out of phase, or at frequencies that are unequal integer multiples of same factor.

However, for purposes of conciseness, to describe boundary vibrations we will use the parameters θ and ϕ which are defined as

$$\theta \equiv \tan^{-1}\left(\sqrt{V_t^2 + V_\tau^2} \,/ V_n \right) \tag{4.53}$$

and,

$$\phi \equiv \tan^{-1}\left(V_\tau / V_t \right), \tag{4.54}$$

instead of using the boundary velocities V_n, V_t and V_τ which satisfy the constraint

$$V_n^2 + V_t^2 + V_\tau^2 = 3. \tag{4.55}$$

Particularly, when θ=0, the vibrations are purely in normal direction and when θ=90°, they are completely tangential and, θ=35.26° and 54.73° correspond respectively to the cases where 2/3rd and 1/3rd of the vibrational energy is distributed in the normal direction. When ϕ=0, there is no vibration in $\tau-$direction and when ϕ=90°, there is no vibration in $t-$direction.

CHAPTER 5

Thermalization and Mean Motion in Isotropic Assemblies

In this chapter, we examine steady, fully developed, nearly elastic and isotropic granular flows in which the boundary is horizontal, spatial variations of mean fields occur only in the direction perpendicular to the flat surface of boundary and the granular temperature is isotropic. The boundary vibrates anisotropically, i.e., the second moment of boundary velocity fluctuations, B_{ij}, is anisotropic. Although the shear stress vanishes everywhere within the assembly, the boundary may transmit tangential momentum to the assembly, which therefore may experience mean motion. In this chapter, we write down a particular boundary value problem for these flows to study effect of such boundaries on unconfined granular assemblies in the presence of gravity. Particularly, we examine dependence of thermalization and mean motion of assembly on direction of vibration, phase differences, total amount of vibrational energy and boundary bumpiness.

5.1 Boundary Value Problem for Isotropic Flows

We employ the same Cartesian coordinate system as introduced earlier and locate the origin of coordinate system at the boundary such that z increases from 0 at the boundary upwards (see Figure 4.1, with Φ=0). We also carry out non-dimensionalization in the same exact way. Here, we take the characteristic velocity a equal to $\sqrt{\sigma g}$. In addition, we take $G(\nu) = \nu/(1-\nu/\nu_m)^{5\nu_m/2}$, where the random close packed value ν_m=.65. Because the temperature is isotropic, we are only concerned with the following quantities: the dimensionless coordinate z, solid volume fraction ν, non-

dimensional velocities u_t and u_τ, isotropic granular temperature $\mathcal{T} = w^2$, dimensionless pressures P_{nn}, S_{nt} and $S_{n\tau}$, non-dimensional energy flux $q = q_{ii}$ and energy dissipation $\Upsilon = \gamma_{ii} / \rho_p g \sqrt{\sigma g}$. The mean fields depend only on z. The full second moment of boundary velocity fluctuations in dimensionless form is given by $\beta_{ij} = \dfrac{B_{ij}}{\sigma g}$ and the mean square velocity of boundary fluctuations, $V^2 = (B_{11} + B_{22} + B_{33})/3$, gets non-dimensionalized as $E = V^2 / \sigma g$. The diagonal components of this second moment tensor $\boldsymbol{B}$ correspond to fluctuation energies of the boundary in the 3 orthogonal directions. They can be written in non-dimensional form as $V_t^2 = V_1^2 / \sigma g$, $V_\tau^2 = V_2^2 / \sigma g$ and $V_n^2 = V_3^2 / \sigma g$.

In these flows, balance of mass (2.16) is identically satisfied. The x_1- and x_2-components of momentum balance (2.17), coupled with no shear stress boundary condition at free surface require that the shear stresses vanish everywhere in the assembly. The x_3-component of momentum balance is given as:

$$\frac{dP_{nn}}{dz} = -\nu, \tag{5.1}$$

in which, $P_{nn} = 4\nu GFw^2$, . (5.2)

where, $F = 1 + \dfrac{1}{4G}$. (5.3)

The balance of energy (2.19) becomes,

$$\frac{dq}{dz} - \Upsilon = 0, \tag{5.4}$$

where the constitutive relations for Υ and q are given as:

$$\Upsilon = -\frac{12(1-e)wP_{nn}}{\sqrt{\pi}F} \text{ and} \tag{5.5}$$

$$q = -\frac{4MP_{nn}}{\sqrt{\pi}F}\frac{dw}{dz}, \tag{5.6}$$

$$\text{where, } M = 1+\frac{9\pi}{32}\left[1+\frac{5}{12G}\right]^2 \tag{5.7}$$

This boundary value problem has 3 unknown mean fields ν, w and q. These 3 mean fields are solutions of 3 *O.D.E.*s formed by plugging constitutive relations (5.2) and (5.5) into balance equations (5.1) and (5.4) respectively, and using constitutive relation (5.6).

The boundary moves with velocities given by equation (4.51) for $\dot{x}_i$. According to relation (4.52), the boundary corresponds to randomly vibrating boundary whose velocity fluctuations are described by the second moment tensor,

$$\boldsymbol{B} = \begin{bmatrix} V_1^2 = \frac{A_1^2\omega^2}{2} & B_{12} = V_1V_2\cos\xi_{12} & B_{13} = V_1V_3\cos\xi_{13} \\ B_{21} = V_1V_2\cos\xi_{12} & V_2^2 = \frac{A_2^2\omega^2}{2} & B_{23} = V_2V_3\cos\xi_{23} \\ B_{31} = V_1V_3\cos\xi_{13} & B_{32} = V_2V_3\cos\xi_{23} & V_3^2 = \frac{A_3^2\omega^2}{2} \end{bmatrix} \tag{5.8}$$

To write down the boundary conditions which formulate the effect of such boundary on granular assembly, lets define some integrals which appear while carrying out averaging over all possible collisions of granular particles with the boundary.

$$I_i = \int_0^{2\pi}\int_0^{\theta(\eta)} \left(\boldsymbol{k}\cdot(w^2\boldsymbol{\delta}+\boldsymbol{\beta})\cdot\boldsymbol{k}\right)^{1/2} \left(u_t\sin\xi\cos\eta + u_\tau\sin\xi\sin\eta\right)k_i\sin\xi\, d\xi\, d\eta \tag{5.9}$$

$$I_{ijk} = \int_0^{2\pi}\int_0^{\theta(\eta)} k_ik_jk_k\sin\xi\, d\xi\, d\eta \tag{5.10}$$

Then, the x_1-, x_2- and x_3-components of momentum balance at the boundary can be written in non-dimensional form respectively as :

$$S_{nt} = \frac{(1+r)^2}{2\sqrt{\pi}A^*}\nu\chi\left[\sqrt{\pi}/2\left(w^2\delta_{lm}+\beta_{lm}\right)I_{1lm}-\sqrt{2}I_1\right] \tag{5.11}$$

$$S_{n\tau} = \frac{(1+r)^2}{2\sqrt{\pi}A^*}\nu\chi\left[\sqrt{\pi}/2\left(w^2\delta_{lm}+\beta_{lm}\right)I_{2lm}-\sqrt{2}I_2\right] \tag{5.12}$$

$$P_{nn} = \frac{(1+r)^2}{2\sqrt{\pi}A^*}\nu\chi\left[\sqrt{\pi}/2\left(w^2\delta_{lm}+\beta_{lm}\right)I_{3lm}-\sqrt{2}I_3\right] \tag{5.13}$$

where, for P_{nn}, we substitute expression (5.2).

The dimensionless form of energy balance boundary condition is:

$$0 = q_{ii}+S_{nt}u_t+S_{n\tau}u_\tau-\frac{(1+r)^2}{2\sqrt{2\pi}A^*}\nu\chi\left[f-d\right] \tag{5.14}$$

in which,

$$f = 2\int_0^{2\pi}\int_0^{\theta(\eta)}\left(k.(w^2\delta+\beta).k\right)^{1/2}(k.\beta.k)\sin\xi d\xi d\eta \tag{5.15}$$

$$d = \int_0^{2\pi}\int_0^{\theta(\eta)}\left(k.(w^2\delta+\beta).k\right)^{3/2}\sin\xi d\xi d\eta \tag{5.16}$$

Also, at the free surface, we require that,

$$P_{nn}=0 \Rightarrow \nu=0 \tag{5.17}$$

$$S_{nt}=0 \tag{5.18}$$

$$S_{n\tau}=0 \tag{5.19}$$

$$q=0 \tag{5.20}$$

As indicated earlier, conditions (5.18) and (5.19), together with the x_1- and x_2-components of momentum balance require that the shear stresses vanish everywhere in the assembly, which further implies that the transport velocity must be uniform. Equations (5.11) and (5.12) simultaneously determine the values of the uniform slip velocities u_t and u_τ. Equation (5.13) determines the unknown factor, χ. Equations (5.14), (5.17) and (5.20) serve as the 3 *B.C.*s for the 3 *O.D.E.*s for w, ν and q. The depth of the flow β gets determined from the prescribed mass hold-up m_t, as described in chapter 4.

For fixed values of m_t, V_n, V_t, ξ_{nt}, $\xi_{n\tau}$, E, e, e_w, α, Δ_α and Δ_t, we guess w which is the measure of granular temperature, at the free surface and using 4th order Runge-Kutta technique, numerically integrate the 3 *O.D.E.*s downward from the free surface where both ν and w' vanish to the depth at which mass holdup reaches its prescribed value, m_t. Condition (5.14) then, determines the value of E that sustains the thermalized state. Finally, we iterate on the guess for w until the value of E calculated in this manner, agrees with its prescribed value. The distance over which the final integration is carried out is the depth of the flow, β.

In practice, the solution procedure is somewhat more complicated. Whenever a free surface exists, ν', w' and q' each vanish at the free surface. Integrations initiated from the top of the flow therefore yield no spatial variations in ν, w and q. This implies that the theory predicts that the flow is infinitely deep and that the mean fields approach their free surface values asymptotically from the base. In order to overcome this difficulty, we initiate the integrations with a very small value of ν, e.g. 10^{-6}, at the "top" of the flow, which is equivalent to relaxing very slightly the normal stress condition there

and allows the integrations to proceed away from zero. We also have checked and made sure that the solution does not depend on this particular value of ν, by trying various values between 10^{-5} and 10^{-7} at the free surface.

5.2 Results and Discussion

Of primary interest are the effects of boundary's motion, bumpiness and vibrational energy on the thermalized states and mean motion that is induced by vibrations of boundary. Mean motion in a direction may occur if the phase angle between the vibrations in that direction and n-direction is not 90°. With this in mind, for the results presented here m_t=5, e=e_w=.9, r=1, and we have varied V_n, V_t, ξ_{nt}, $\xi_{n\tau}$, E, α, Δ_α and Δ_t. For the purpose of simplicity, we use angles θ and ϕ, defined by Equations (4.53) and (4.54), which together describe the direction of vibration of the boundary. Also, we use the non-dimensional temperature $\mathcal{T} = w^2$ for the purpose of presentation of results. Lets first look at cases where no mean motion occurs.

In Figures 5.1 and 5.2, we show the granular temperature $\mathcal{T}^{1/2}(z)$ and solid volume fraction profiles $\nu(z)$ for θ=0, 35.26°, 54.74° and 90° (V_n^2=3, 2, 1 and 0), when ϕ=0 ($V_\tau^2 = 0$), ξ_{nt}=$\xi_{n\tau}$=90°, E=4, α=90° and Δ_α=Δ_t=.22. For these parameters, as θ decreases from 90° to 0, vibrations have more and more normal component and hence boundary becomes more effective at thermalizing the assembly and the temperatures increase and flows become deeper and more dilute. Solid dots on the profiles indicate the value of z below which 99% of the mass m_t is contained. Temperature monotonically reduces as we go away from the vibrating boundary. Solid volume fraction, ν, is small near the vibrating boundary. It initially increases as we go away from boundary.

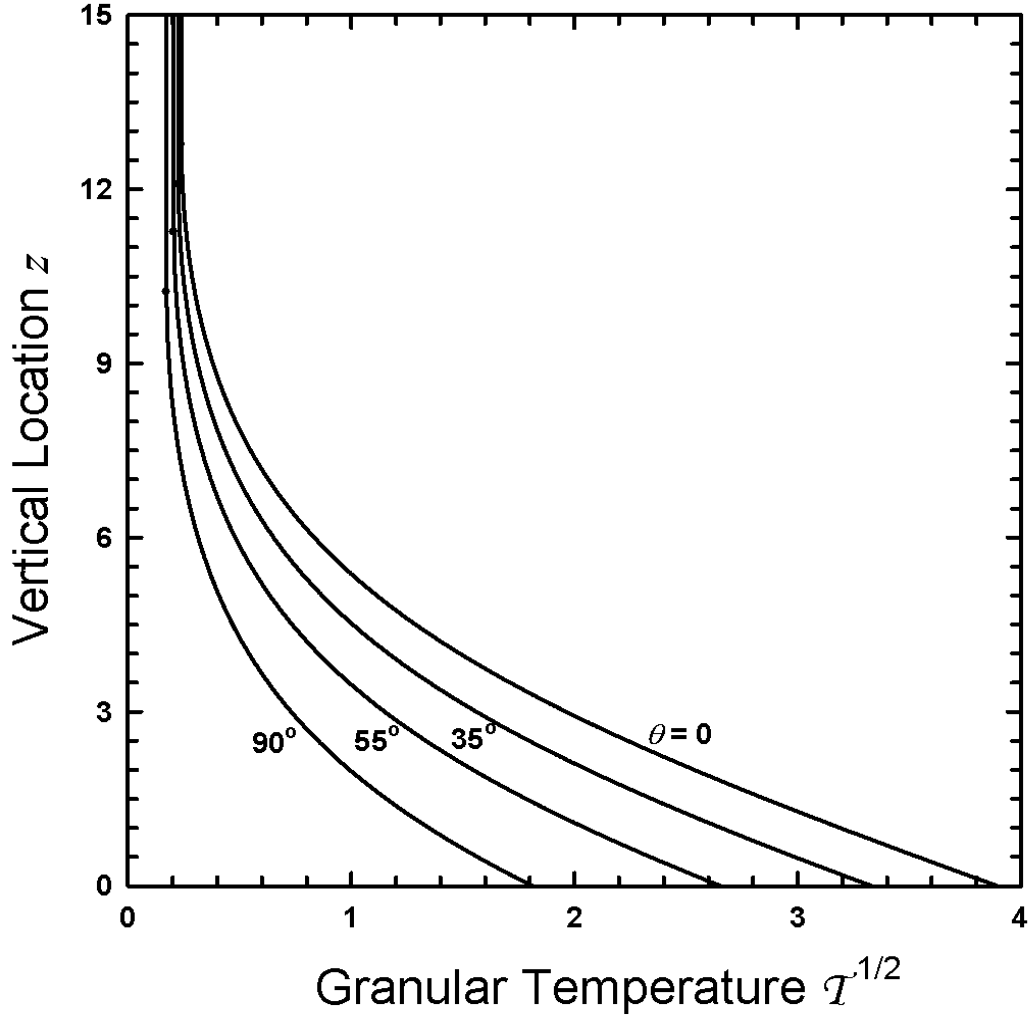

Figure 5.1: The variations of $\mathcal{T}^{1/2}$ with z for θ=90°, 54.74°, 35.26° and 0, when ϕ=0, $\xi_{nt} = \xi_{n\tau}$=90°, E=4, α=90° and $\Delta_\alpha = \Delta_t$ =.22. Solid dots on the profiles indicate the value of z below which 99% of the mass m_t is contained.

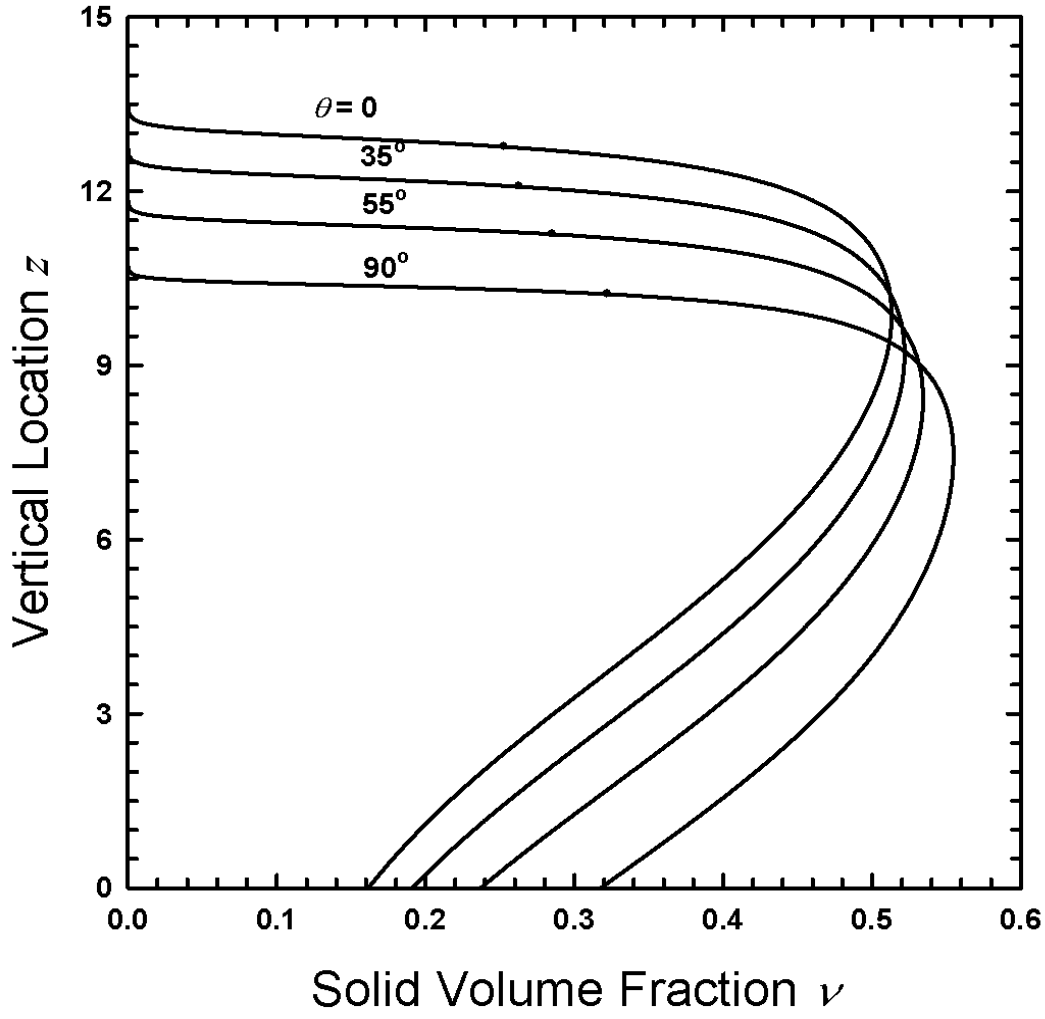

Figure 5.2: The variations of ν with z for θ=90°, 54.74°, 35.26° and 0, when ϕ=0, $\xi_{nt}=\xi_{n\tau}$=90°, E=4, α=90° and $\Delta_\alpha=\Delta_t$=.22. Solid dots on the profiles indicate the value of z below which 99% of the mass m_t is contained.

However, as we reach near the top surface, ν decreases and reaches zero value at the free surface. Qualitatively similar observations can be made for other fixed combinations of bumpiness and vibrational energy.

Figures 5.3 and 5.4 show comparison of predictions of our theory with numerical simulations of Lan and Rosato (1995), for profiles of $T^{1/2}(z)$ and $\nu(z)$. The discrete points are simulation results for flat boundary and for different values of vibrational energy E=.0625, 4 and 25, and the curves are predictions of theory for the same. Here, θ=54.74°, ϕ=45° ($V_n^2 = V_t^2 = V_\tau^2 = 1$) and $\xi_{nt} = \xi_{n\tau}$=90°. As E increases, boundary supplies more energy and hence assembly becomes more thermalized, more deep and more dilute. The predictions of theory match excellently with simulation results.

Figures 5.5, 5.6 and 5.7 show the effect of changing the direction of tangential vibration ϕ on the thermalization of the assembly, i.e., the granular temperature, the solid volume fraction, and the flow heights, for 3 different cases of bumpiness Δ_α=.22, -.5 and -1. Here, Δ_t=.22, θ=90° (V_n^2=0), α=90°, $\xi_{nt} = \xi_{n\tau}$=90° and E=4. The variations of granular temperature at the base, $T^{1/2}(0)$, height from base at which maximum density occurs β_d and the maximum solid volume fraction $\nu(\beta_d)$ are shown by solid curves whereas the variations of granular temperature at top, $T^{1/2}(h)$, ν at the base, $\nu(0)$, and flow height β are shown by dashed curves. In the first case, when $\Delta_\alpha = \Delta_t$=.22, as ϕ changes from 0 to 90° there is slight variation in the thermalization of the assembly because of the fact that orientation of the square array with respect to direction of tangential vibration changes. In the second case when Δ_α=-.5, the array is no longer square and there is a preferred direction of vibration. The boundary is more bumpy in

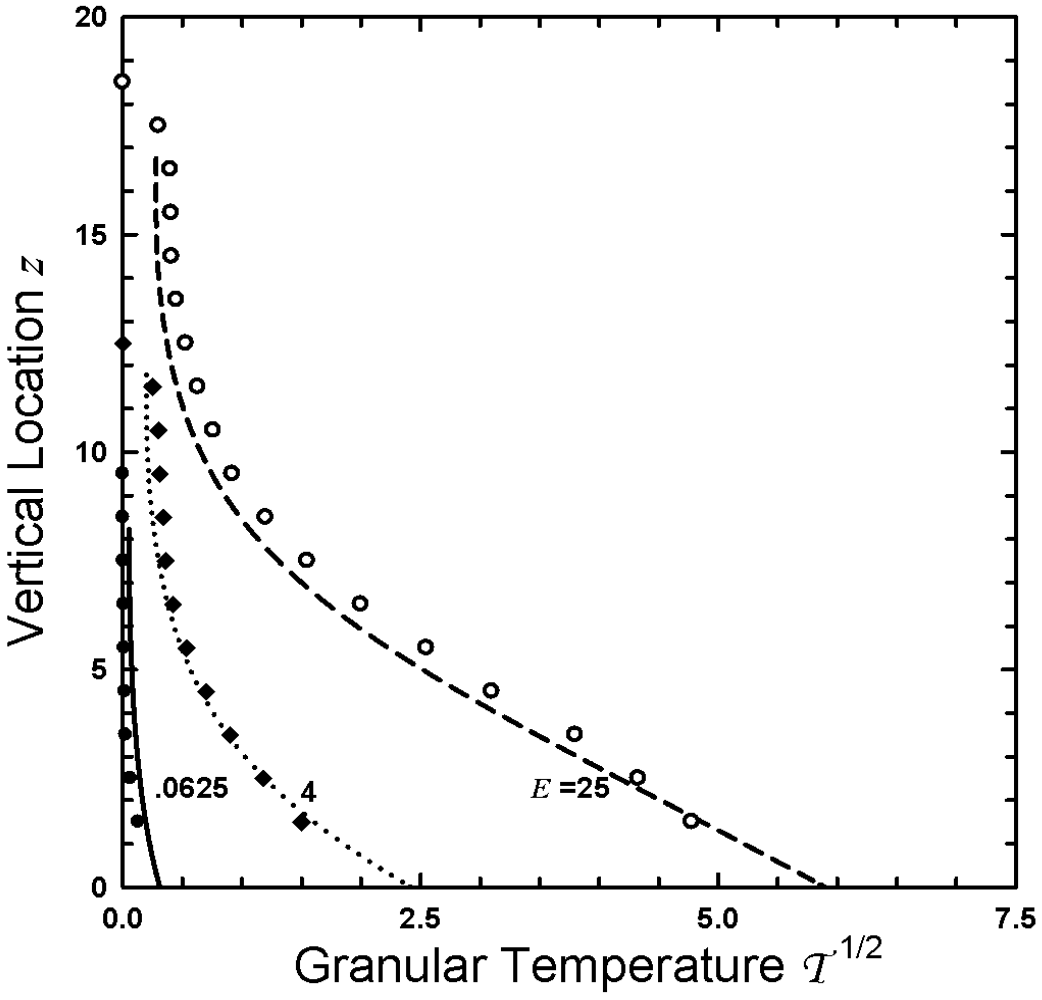

Figure 5.3: The variations of $\mathcal{T}^{1/2}$ with z for E=25, 4 and .0625, when θ=54.74°, ϕ=45° and $\xi_{nt}=\xi_{n\tau}$=90° for a flat boundary. Curves are the predictions of the theory and solid dots are simulation results of Lan and Rosato (1995).

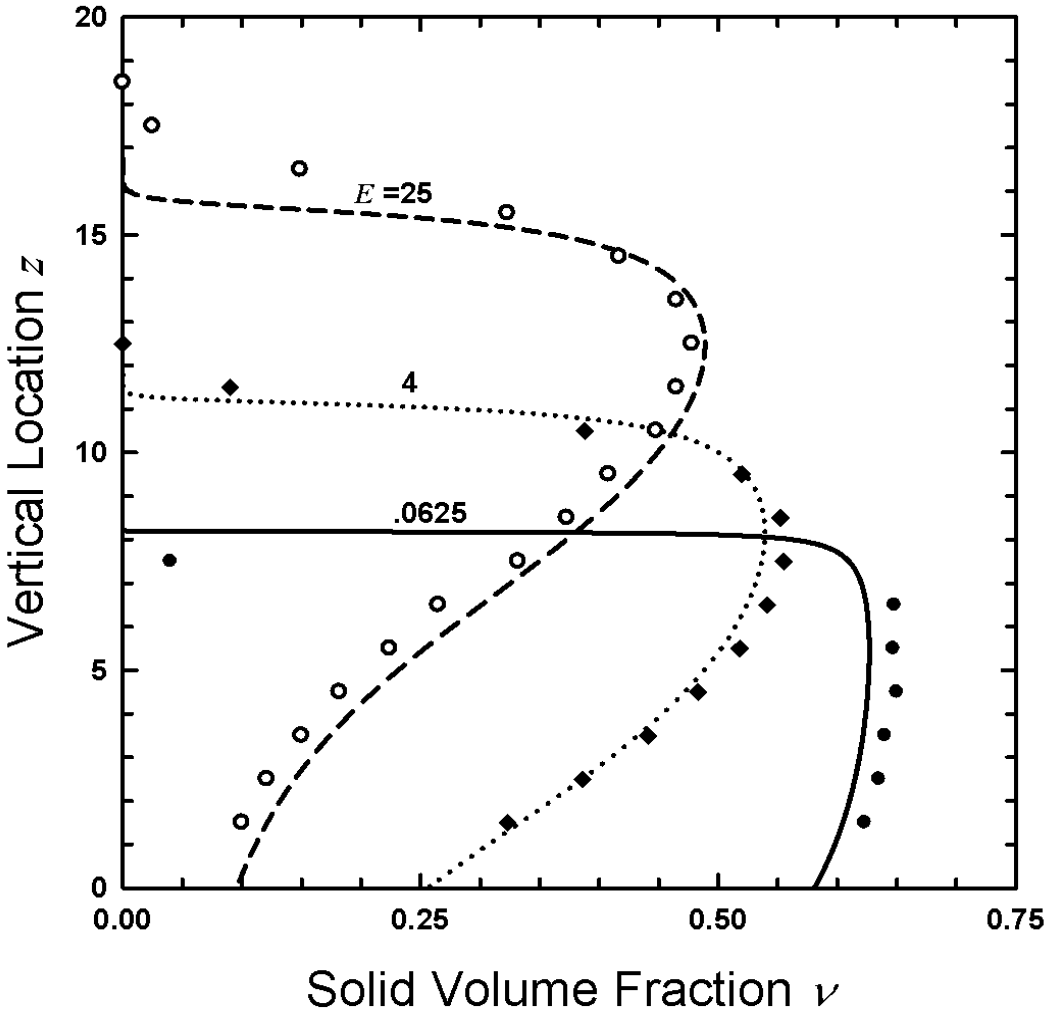

Figure 5.4: The variations of ν with z for E=25, 4 and .0625, when θ=54.74°, ϕ=45° and $\xi_{nt}=\xi_{n\tau}$=90° for a flat boundary. Curves are the predictions of the theory and solid dots are simulation results of Lan and Rosato (1995).

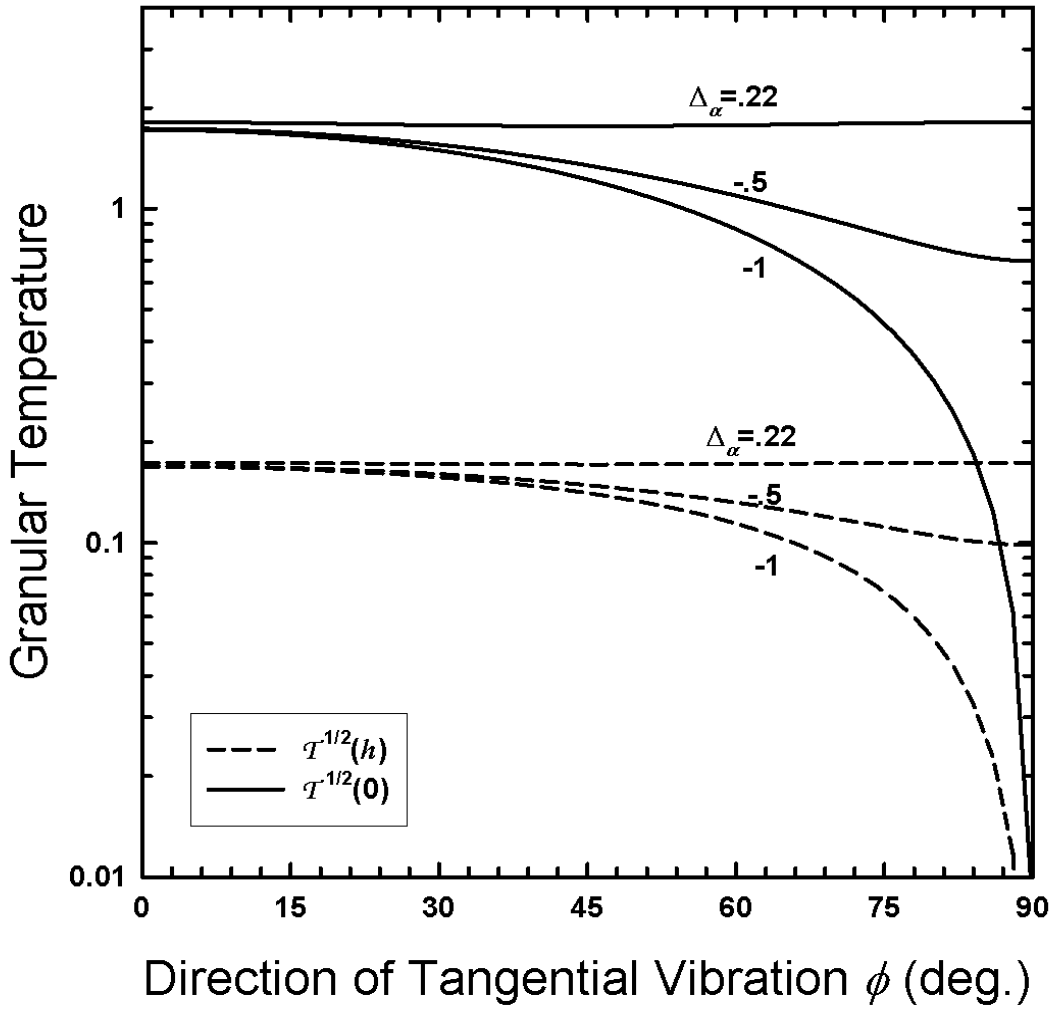

Figure 5.5: The variations of $\mathcal{T}^{1/2}$ at z=0 (shown by solid curves) and at z=h (shown by dashed curves), with ϕ for 3 different cases Δ_α=.22, -.5 and -1. Here, Δ_t=.22, θ=90°, α=90°, $\xi_{nt}=\xi_{n\tau}$=90° and E=4.

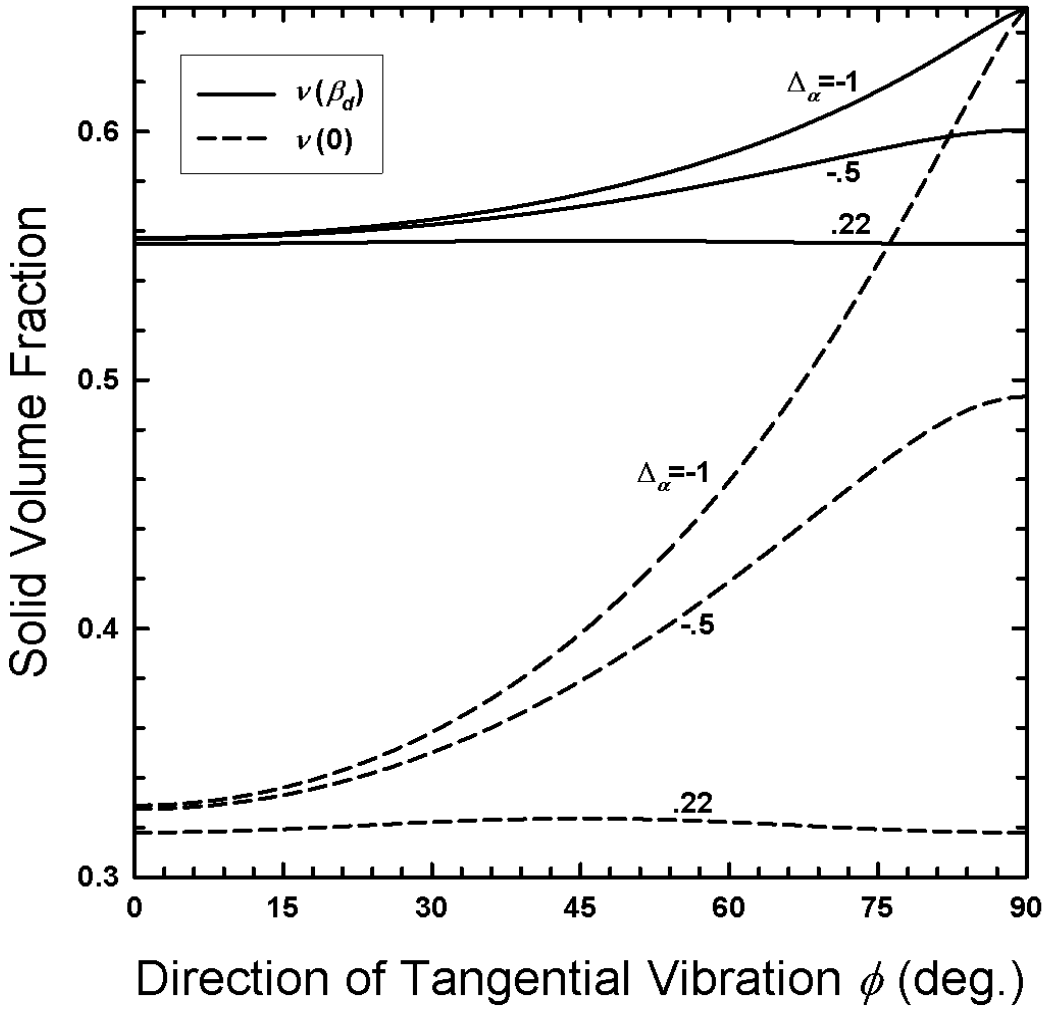

Figure 5.6: The variations of $\nu(\beta_d)$ and $\nu(0)$ with ϕ for 3 different cases Δ_α=.22, -.5 and -1. Here, Δ_t=.22, θ=90°, α=90°, $\xi_{nt}=\xi_{n\tau}$=90° and E=4.

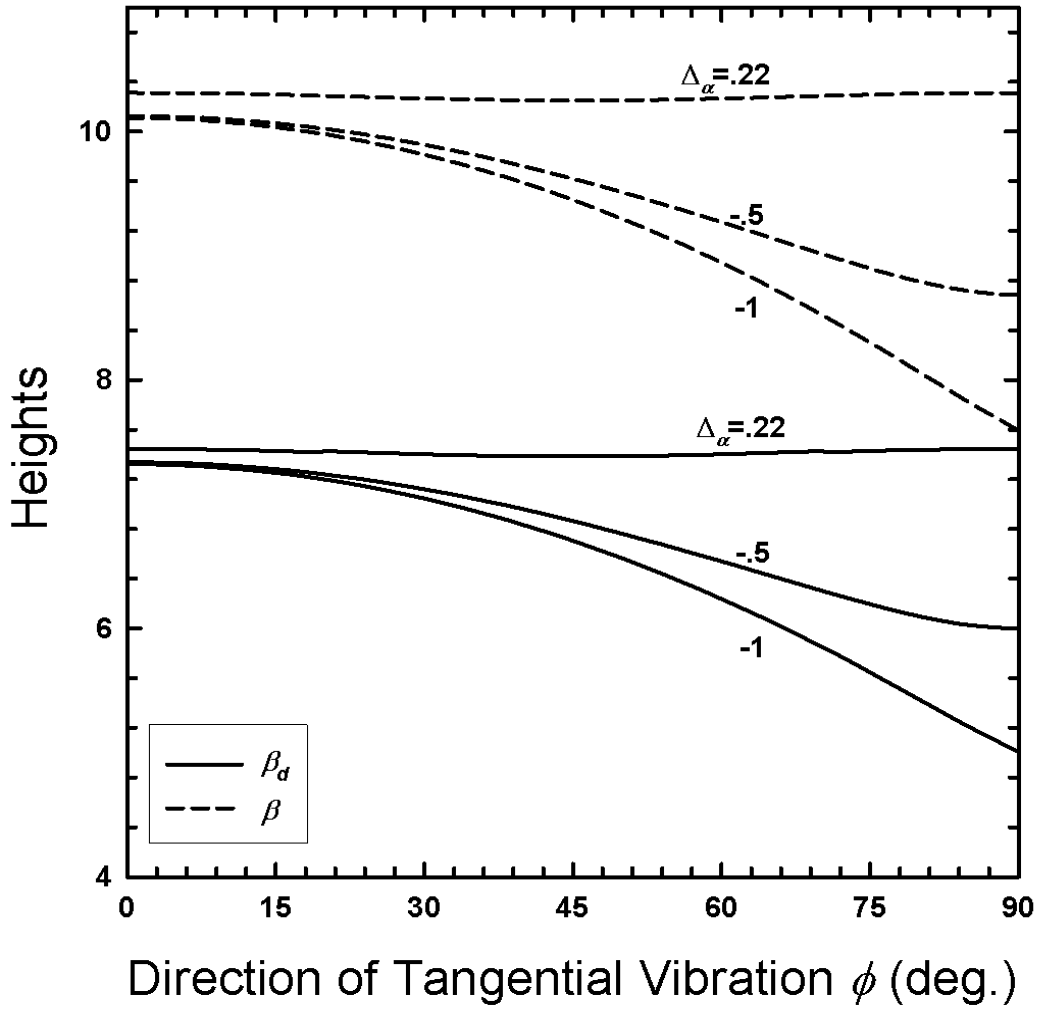

Figure 5.7: The variations of β and β_d with ϕ for 3 different cases Δ_α=.22, -.5 and -1. Here, Δ_t =.22, θ=90°, α =90°, $\xi_{nt} = \xi_{n\tau}$ =90° and E=4.

$t-$direction than in $\tau-$direction and hence as ϕ changes from 0 to 90°, thermalization of the assembly decreases, decreasing the flow heights β and β_d, and making flows more dense by increasing $\nu(0)$ and $\nu(\beta_d)$. Finally when Δ_α=-1, i.e., when boundary is perfectly smooth in $\tau-$direction while very bumpy in $t-$direction. In this case, we get these extreme situations where shaking in $\tau-$direction results in no thermalization, with zero granular temperature, solid volume fraction equals its maximum possible value .65 everywhere in the flow and flow heights are minimum, and shaking in $t-$direction results in highly thermalized assembly, with small values of $\nu(0)$ and $\nu(\beta_d)$, and taller flow heights β and β_d.

Now, lets look at the effect of θ, i.e. the effect of distribution of vibrational energy on mean motion of assembly, for three different cases E=1, 4 and 9, and when ϕ=0 ($V_\tau^2 = 0$), ξ_{nt}=90°, α=90° and $\Delta_\alpha = \Delta_t$ =.22. Figure 5.8 demonstrates that when θ is 0 or 90°, i.e., when boundary motion is entirely in normal or tangential direction then no mean motion is induced. However, away from these extreme cases, slip $u \equiv \sqrt{u_t^{\,2} + u_\tau^{\,2}}$ is induced in the assembly. In fact, there is an optimum value of θ at which slip is maximum and this optimum value changes as parameter values change. As E increases from 1 to 9, boundary supplies more energy to the flow and the slip also increases. Figure 5.9 shows the corresponding variations of granular temperatures $T^{1/2}$ at the base. Temperature increases as vibrations become more normal, i.e., as θ decreases and also as the energy E increases. It shows that more thermalization does not necessarily imply more induced slip.

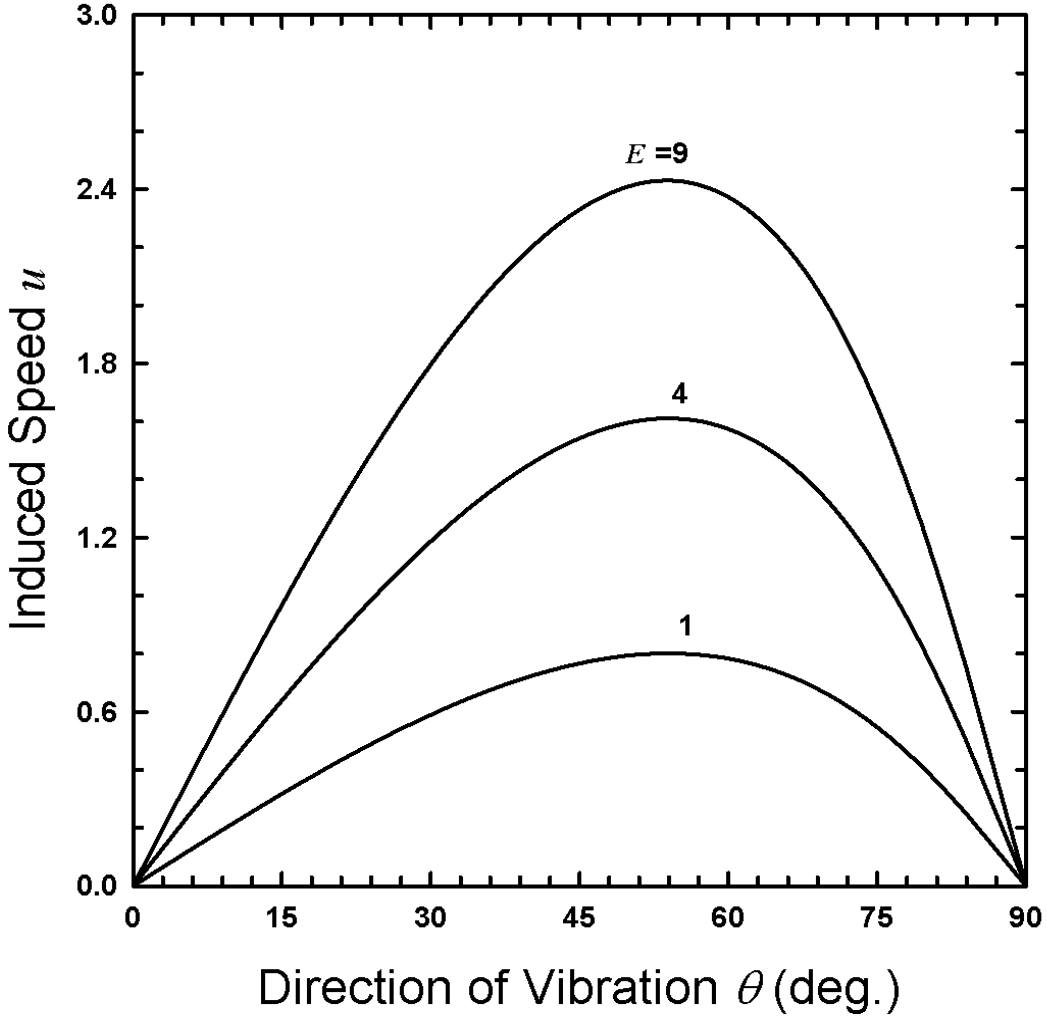

Figure 5.8: The variations of u with θ for 3 different cases E=9, 4 and 1, when ϕ=0, ξ_{nt}=90°, α=90° and $\Delta_\alpha = \Delta_t$ =.22.

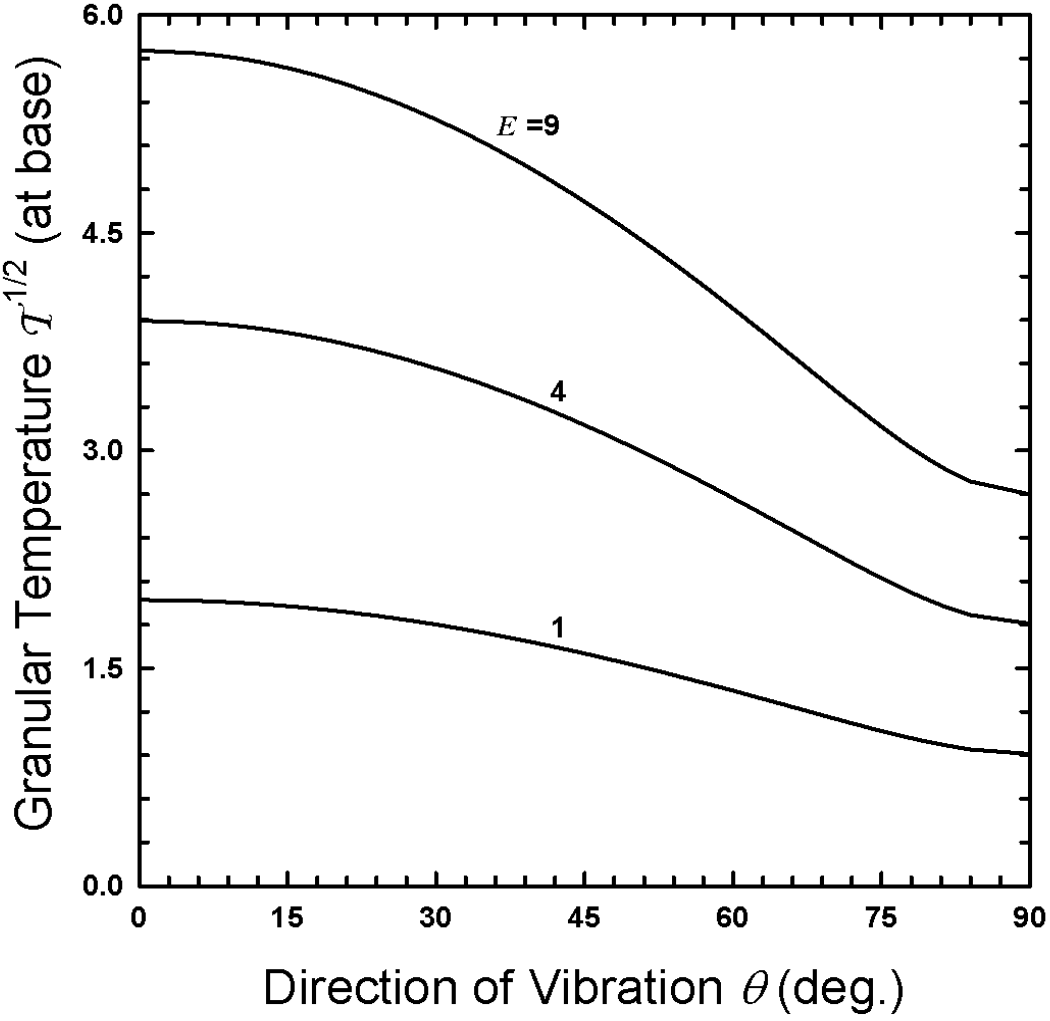

Figure 5.9: The variations of $\mathcal{T}^{1/2}$ at z=0, with θ for 3 different cases E=9, 4 and 1, when ϕ=0, ξ_{nt}=90°, α=90° and $\Delta_\alpha = \Delta_t$ =.22.

Figures 5.10 and 5.11 show the effect of changing the direction of tangential vibration ϕ on the mean motion of the assembly, i.e., the induced speed and direction of flow, for 4 different cases $\xi_{n\tau}$=0, 45°, 75° and 90°. Here, θ=54.74° (V_n^2=1), ξ_{nt}=0, and E=4, α=90° and $\Delta_\alpha = \Delta_t$=.22. When $\xi_{nt} = \xi_{n\tau}$=0, as the direction of tangential vibration changes, the orientation of square array with respect to vibration changes, and there is a slight change in the induced speed, u, and, the direction of motion, η, closely matches the direction of tangential vibration, ϕ. As the phase difference $\xi_{n\tau}$ increases from zero with ξ_{nt} fixed at zero, the difference between vibrations in $t-$ and $\tau-$directions increases, with vibrations in $t-$direction more effective than vibrations in $\tau-$direction, and hence u decreases as the tangential vibrations are more and more in $\tau-$direction, i.e., as ϕ increases from 0 to 90°. For the same reason, in this case, the direction of motion, η, lags with respect to the direction of tangential vibration, ϕ. Finally, when $\xi_{n\tau}$=90°, u decreases to zero as ϕ becomes 90°, and no slip is induced in $\tau-$direction, i.e., η=0.

Figures 5.12 and 5.13 show the effect of changing array angle α on the mean motion of assembly, for θ=45° (V_n^2=1.5), ϕ=0 ($V_\tau^2 = 0$), ξ_{nt}=0 and $\Delta_\alpha = \Delta_t$=.22 and for three different cases, E=1, 4 and 9. For fixed and equal array spacings, as α decreases from 90°, the boundary bumps get closer to each other and boundary becomes smoother in $\tau-$direction and rougher in $t-$direction. As the direction of tangential vibrations is t, with decreasing α, the induced speeds increase slightly. When α is 0, 60° and 90°, the array is symmetric in $t-$ and $\tau-$directions and the direction of motion is perfectly in $t-$direction, i.e., η=0. For other values of α, due to the un-symmetry of

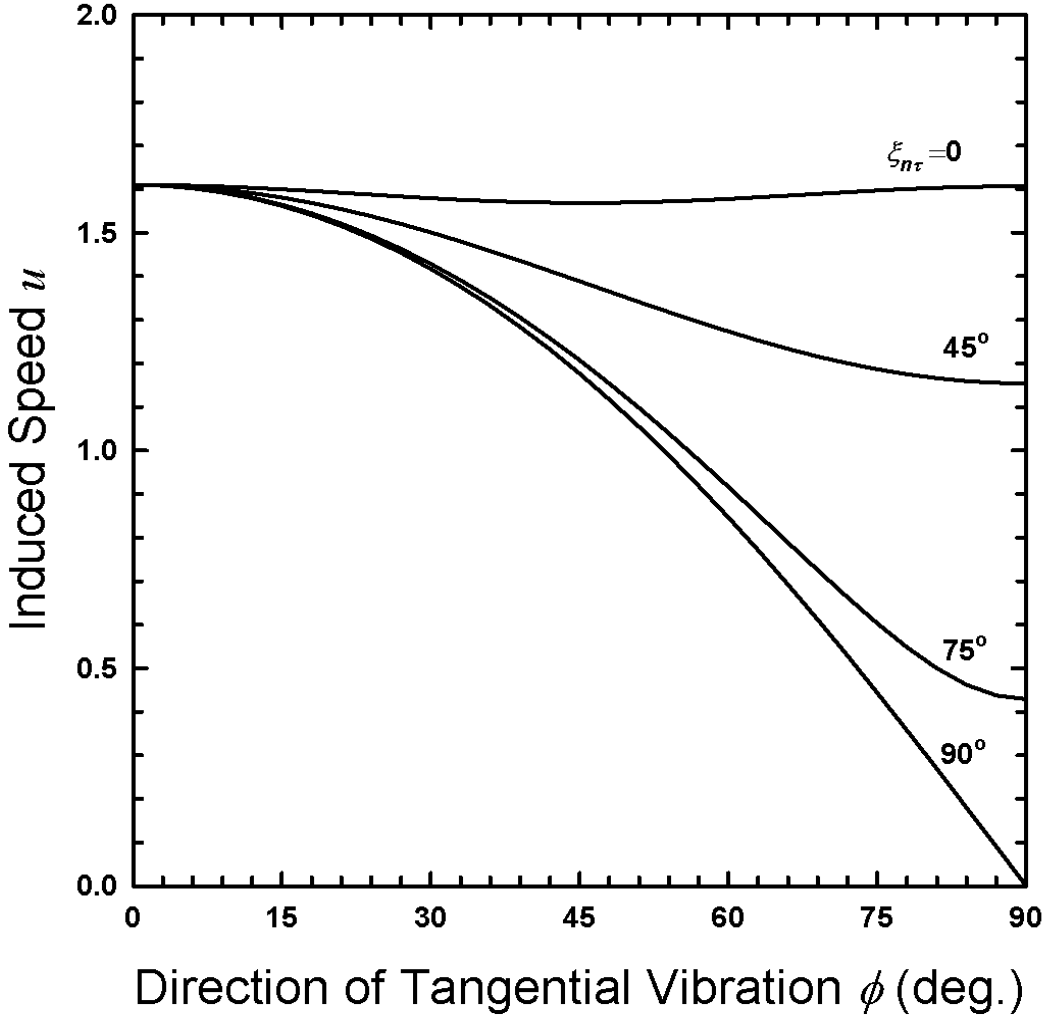

Figure 5.10: The variations of u with ϕ for 4 different cases $\xi_{n\tau}$=0, 45°, 75° and 90°. Here, θ=54.74°, ξ_{nt}=0, and E=4, α=90° and $\Delta_\alpha = \Delta_t$=.22.

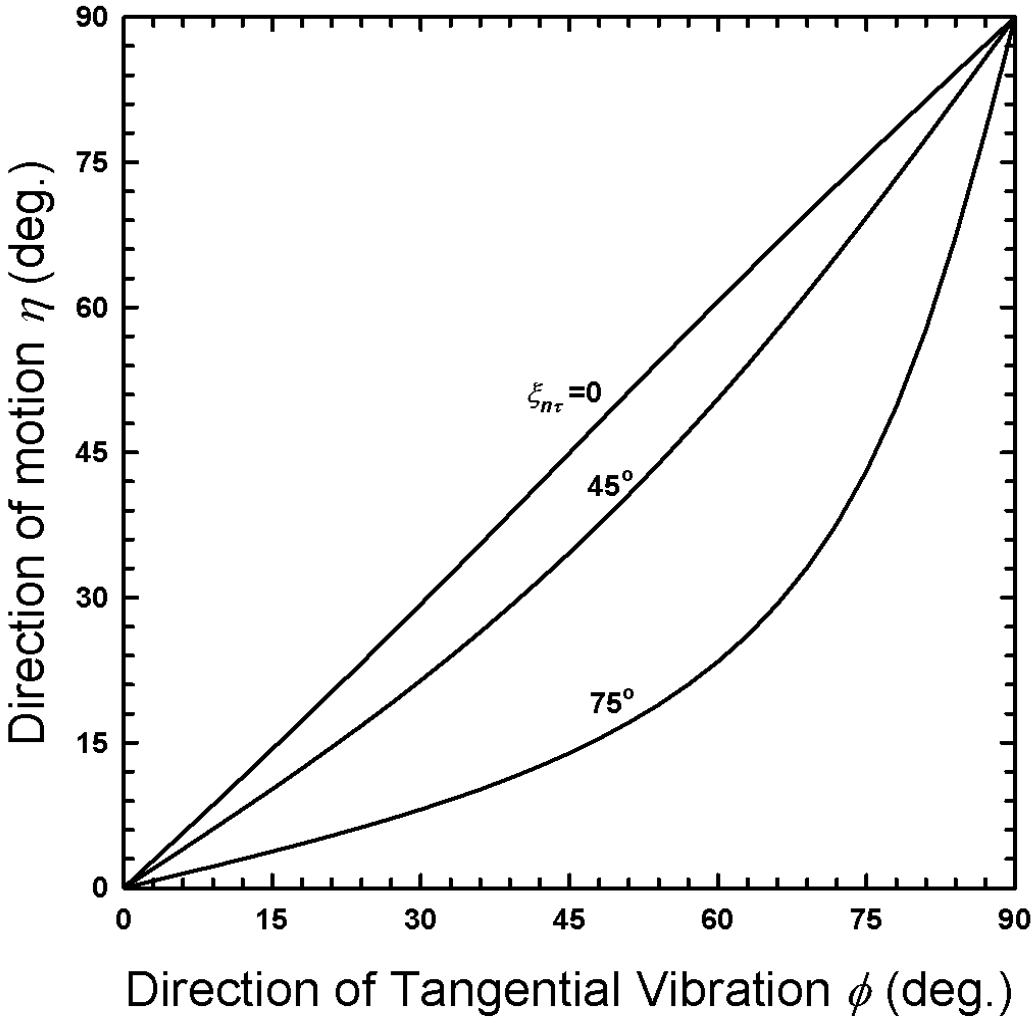

Figure 5.11: The variations of η with ϕ for 4 different cases $\xi_{n\tau}$=0, 45°, 75° and 90°. Here, θ=54.74°, ξ_{nt}=0, and E=4, α=90° and $\Delta_\alpha = \Delta_t$=.22

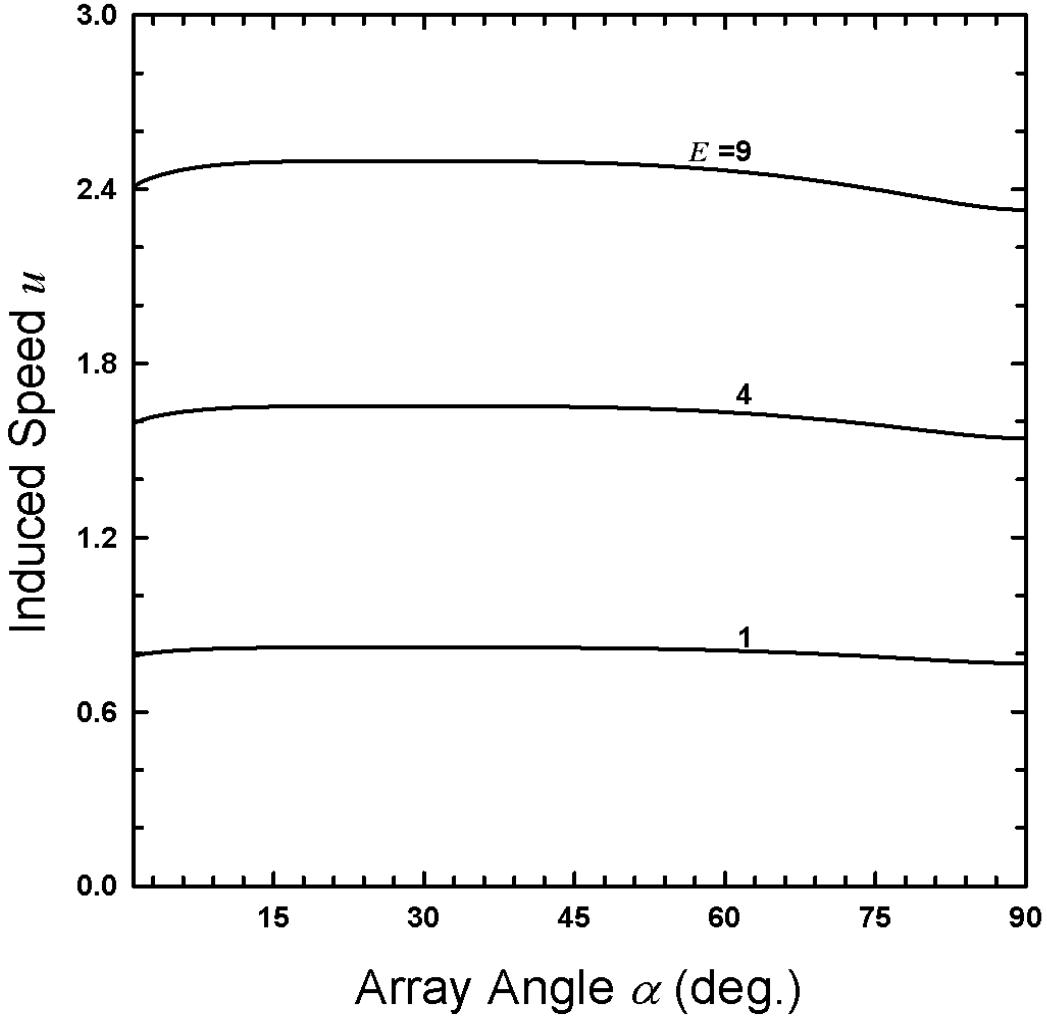

Figure 5.12: The variations of u with α for 3 different cases E=9, 4 and 1 for θ=45°, ϕ=0, ξ_{nt}=0 and $\Delta_\alpha = \Delta_t$=22.

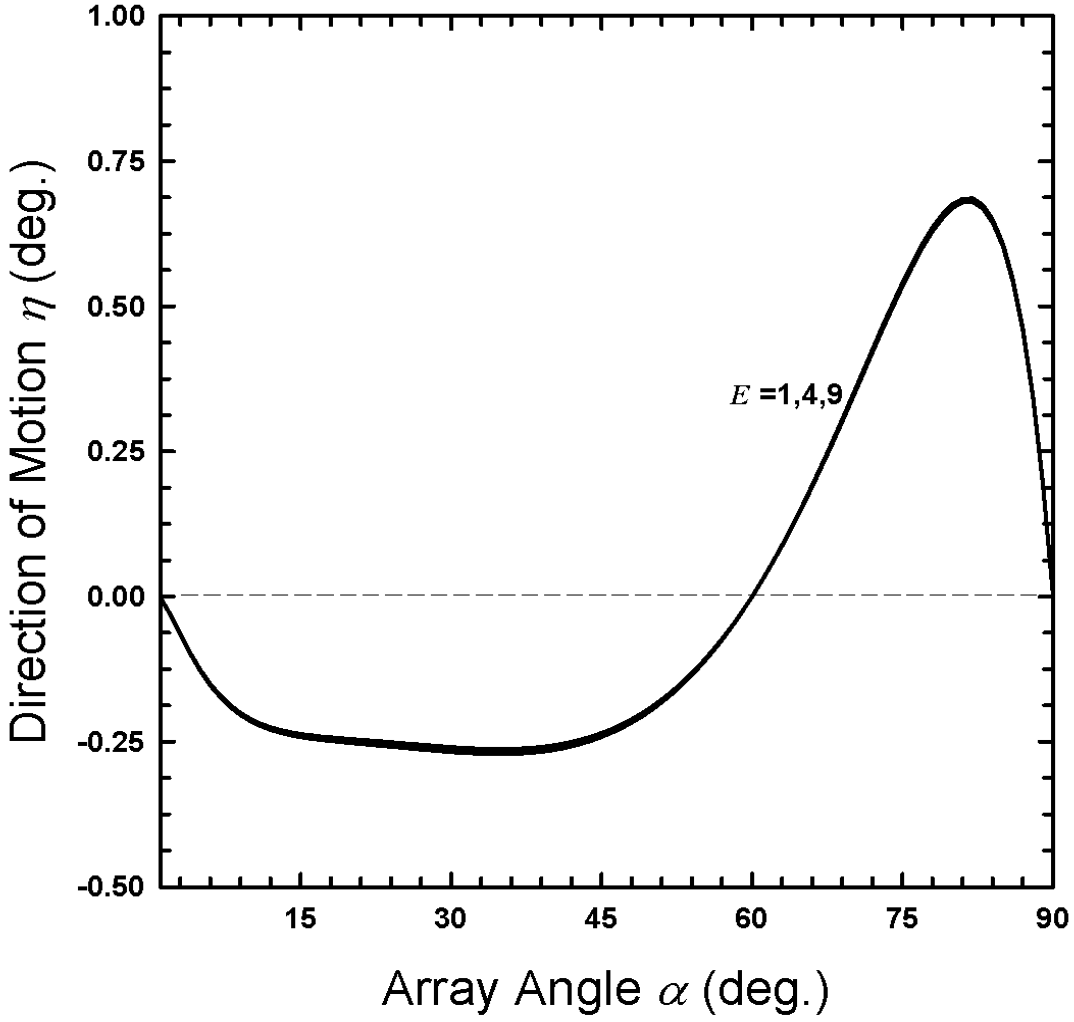

Figure 5.13: The variations of η with α for 3 different cases E=9, 4 and 1 for θ=45°, ϕ=0, ξ_{nt}=0 and $\Delta_\alpha = \Delta_t$ =22.

the array, vibrations in $t-$direction induce a very small motion in $\tau-$direction and hence η is not zero.

CHAPTER 6

Thermalization and Mean motion in Anisotropic Assemblies

In this chapter, we study the effects of anisotropic boundary vibrations on granular assemblies that are anisotropic. Unlike the isotropic assemblies, these assemblies could have very different temperatures in different directions, at least near the vibrating boundary. Also, unlike the isotropic flows, the mean motion induced is not uniform. Here, we examine the dependence of both the thermalized state and the induced mean motion on a variety of factors including the total amount of vibrational energy, its distribution, restitution coefficients, mass hold-ups, bumpiness of the boundary and particle size relative to boundary bumps.

We are concerned with unconfined flows compressed by gravity and driven by horizontal boundaries that vibrate anisotropically. We take the characteristic velocity a equal to $\sqrt{\sigma g}$ and locate the origin of coordinate system at the boundary such that z varies from 0 at the boundary to h at the free surface. As in the previous chapter, we take $G(\nu) = \nu/(1-\nu/\nu_m)^{5\nu_m/2}$. In these flows, shear stresses S_{nt} and $S_{n\tau}$ are constant throughout the assembly. Since they vanish at the free surface, they must vanish everywhere in the flow. But the boundaries may transmit tangential momentum to the assemblies which therefore may experience mean motion.

For prescribed values of m_t, e, e_w, r, E, θ, ϕ, ξ_{nt}, $\xi_{n\tau}$ and α, Δ_t, Δ_α, equations (4.2), (4.4), (4.5), (4.7), (4.8), (4.9), (4.10), (4.11), (4.12), (4.19), (4.20), (4.21), (4.22), (4.23) and (4.24) and, boundary conditions (4.25), (4.29), (4.35) through (4.41) and (4.44) through (4.49) determine ν, w, $\hat{\kappa}_{22}$, $\hat{\kappa}_{33}$, κ_{12}, κ_{23}, κ_{13}, u_t, u_τ, q_{ii}, $\hat{q}_{22}$, $\hat{q}_{33}$,

q_{12}, q_{23} and q_{13}. To obtain solutions, 15 non-linear *O.D.E.*s must be solved simultaneously subject to the 15 non-linear boundary conditions. This system of non-linear *O.D.E.*s subjected to non-linear *B.C.*s is solved numerically. The numerical procedure is slightly complicated and is described, in concise notation, in the following section.

6.1 Numerical Procedure for a System of Non-Linear *O.D.E.*s and Boundary Conditions

Consider a boundary value problem in N variables, y_1, y_2,.... and y_N which depend only on the spatial coordinate x. Let the N Ordinary Differential Equations (*O.D.E.*s) which describe this dependence be given by:

$$\dot{y}_i = f_i(y_1, y_2, ..., y_N, x) \qquad i = 1,2,...., N, \tag{6.1}$$

where, f_1, f_2,...., f_N represent non-linear functions of y_1, y_2,.... , y_N and x. These N *O.D.E.*s are subjected to N non-linear boundary conditions. Let K of these N boundary conditions be specified at the spatial location $x = x_1$ and the remaining (N-K) boundary conditions are specified at the location $x = x_2$. Let the K boundary conditions at $x = x_1$ be described as:

$$b_i[y_1(x_1), y_2(x_1), ..., y_N(x_1)] = 0 \qquad i = 1,2,...., K, \tag{6.2}$$

and the (N-K) boundary conditions at $x = x_2$ be described as:

$$B_i[y_1(x_2), y_2(x_2), ..., y_N(x_2)] = 0 \qquad i = K+1, K+2, ..., N, \tag{6.3}$$

where, $b_1, b_2, ..., b_K$ and B_{K+1}, B_{K+2},...., B_N represent non-linear functions of y_1, y_2,.... and y_N.

Let $y=[y_1,y_2,.....,y_N]^T$ be the column vector of unknowns, $f=[f_1,f_2,.....,f_N]^T$ be the column vector of functions of these unknowns, $b=[b_1,b_2,....,b_K]^T$ be the column vector of boundary conditions at $x=x_1$ and $B=[B_{K+1},B_{K+2},....,B_N]^T$ be the column vector of boundary conditions at $x=x_2$. Then, $\dot{y}=f$ represents the N *O.D.E.*s in vector form. Solution to this system of *O.D.E.*s can be obtained by solving the numerical scheme $\dot{y}^{n+1}=f^n+J^n\left(y^{n+1}-y^n\right)$, subjected to appropriate boundary conditions, where y^i and f^i denote the numerical evaluation of column vectors y and f at the i^{th} iteration in the numerical scheme and J is the Jacobian with entries J_{ij} that are defined as $J_{ij}=\dfrac{\partial f_i}{\partial y_j}$. In the discussion that follows, superscripts denote iteration in numerical scheme. The boundary conditions at $x=x_1$ can be written in numerical form as

$$\left[\left.\frac{\partial b}{\partial y}\right|_{x_1}\right]^n\left[y^{n+1}(x_1)-y^n(x_1)\right]=-b^n, \tag{6.4}$$

and the boundary conditions at $x=x_2$ can be written as

$$\left[\left.\frac{\partial B}{\partial y}\right|_{x_2}\right]^n\left[y^{n+1}(x_2)-y^n(x_2)\right]=-B^n, \tag{6.5}$$

where $\left[\dfrac{\partial b}{\partial y}\right]$ is a $K\times N$ matrix with entries $\dfrac{\partial b_i}{\partial y_j}$ and $\left[\dfrac{\partial B}{\partial y}\right]$ is a (N-K)$\times N$ matrix with entries $\dfrac{\partial B_i}{\partial y_j}$, where *i* represents row and *j* represents column of the entry.

Let $y=Y_0+Y\cdot C$ be the solution of $\dot{y}=f$, where $C=[C_1,C_2,....,C_N]^T$ is a column vector of constants and, Y and Y_0 are sets of variables where

$Y_0 = [Y_{01}, Y_{02}, ..., Y_{0N}]^T$ and Y is an $N \times N$ matrix with elements Y_{ij} in the i^{th} *row* and j^{th} column. This solution must satisfy $\dot{y} = f$. Let Y be the solution of homogenous system of *O.D.E.*s given by $\dot{Y}^{n+1} = J^n Y^{n+1}$ subjected to inhomogenous boundary conditions $Y(x_1) = [I]$ and, Y_0 is the solution of inhomogenous system of *O.D.E.*s given by $\dot{Y}_0^{n+1} = J^n Y_0^{n+1} - J^n y^n + f^n$ subjected to homogenous boundary conditions $Y_0(x_1) = 0$. Once we solve for Y and Y_0, C can be obtained by using the boundary conditions of the original problem specified at $x = x_1$ and $x = x_2$. The following system of N linear simultaneous equations gives solution of C.

$$\begin{bmatrix} \left[\frac{\partial b}{\partial y}\Big|_{x_1}\right]^n [Y(x_1)]^{n+1} \\ \left[\frac{\partial B}{\partial y}\Big|_{x_2}\right]^n [Y(x_2)]^{n+1} \end{bmatrix} [C]^{n+1} = \begin{bmatrix} \left[\frac{\partial b}{\partial y}\Big|_{x_1}\right]^n [y(x_1)]^n \\ \left[\frac{\partial B}{\partial y}\Big|_{x_2}\right]^n [y(x_2)]^n \end{bmatrix} - \begin{bmatrix} [b]^n \\ [B]^n \end{bmatrix} - \begin{bmatrix} \left[\frac{\partial b}{\partial y}\Big|_{x_1}\right]^n [Y_0(x_1)]^{n+1} \\ \left[\frac{\partial B}{\partial y}\Big|_{x_2}\right]^n [Y_0(x_2)]^{n+1} \end{bmatrix} \tag{6.6}$$

If the spatial domain between $x = x_1$ and $x = x_2$ is discretized into *r* parts, then the numerical scheme is converged if at any particular iteration, at each of the *r*+1 discretized points in space,

$$\frac{|y^{n+1} - y^n|}{|y^{n+1}|} < \varepsilon \tag{6.7}$$

where ε is prescribed tolerance value, usually taken as 1e-3.

When length of the spatial domain x is large, assumed solutions Y and Y_0 grow exponentially creating precision problems for calculation of actual solutions *y*. To obtain solutions in such cases, we proceed as following. In each single iteration the domain is divided into multiple sub-domains *twice*, first with smaller number of divisions and then

with larger and, once with even number of divisions and once with odd. Having smaller divisions first and larger later helps the scheme to converge faster, but whether it is even number of divisions first or odd is not important. We make even divisions first and odd later.

If, for example, we divide the domain into n+1 sub-divisions, we will need 2n new sets of boundary conditions. For the sub-domains including $x = x_1$ and $x = x_2$ points, we use boundary conditions specified in the original problem at $x = x_1$ and $x = x_2$. Now we need boundary conditions for all intermediate boundaries of sub-domains.

When a good guess is inputted to this numerical scheme, the guess is first divided in the same even number of sub-domains as in the numerical scheme. Values of variables at the sub-domain boundaries in the guess are used as boundary conditions for the remaining intermediate boundaries. There is certain flexibility as to values of which variables to specify at the intermediate boundary. We give preference to "primary" variables for that purpose. With this guess, such a numerical scheme would generate a solution that would match the guess at the sub-domain boundaries but will differ slightly between the boundaries. Now this solution is used as guess and the domain is divided into odd number of sub-domains so that none of the *intermediate* boundary location is repeated in this new division. Boundary conditions are specified for the intermediate boundaries, just as described above and again solution is obtained. This is considered as end of one iteration. Now this solution is used as guess for next iteration and iterations continue until solution converges. To generate a starting good guess for such a scheme,

first, a solution is obtained for reasonable domain size keeping other parameters the same.

6.2 Results and Discussion

In this section, we present results that describe the details of thermalized states and mean motion induced by boundary vibrations. This section is divided into three parts. In the first part, we take a closer look at velocity distribution functions. The second and third parts discuss results about non-driven assemblies and driven flows respectively.

6.2.1 Velocity Distribution Functions

In Chapter 2, we discussed about individual particle velocity distribution functions and derived expressions (2.88), (2.89) and (2.90) for $P(C_1)$, $P(C_2)$ and $P(C_3)$. We could not plot the probability distribution because we did not have values of mean fields which are solutions to boundary value problem. Now that we can solve boundary value problems, these distributions can be obtained. To relate to the $\boldsymbol{n}-\boldsymbol{t}-\boldsymbol{\tau}$ coordinate system, we use notations C_t, C_τ and C_n instead of C_1, C_2 and C_3 respectively.

Consider now the predictions of anisotropic theory at an interior point in the flow, z=3, for a case of entirely normal vibrations θ=0, (V_n^2=3), m_t=5, e=e_w=.9, r=1, E=4, $\xi_{nt}=\xi_{n\tau}$=90°, α=90° and $\Delta_t=\Delta_\alpha$=.22. The solution for mean fields in this case, at z=3, is ν=.317, $\mathcal{T}$=2.86, $\hat{\kappa}_{11}$=-.108, $\hat{\kappa}_{22}$=-.108, $\hat{\kappa}_{33}$=.216 and $\frac{d\mathcal{T}}{dz}$=-1.832 and $\mathcal{T}=\mathcal{T}(z)$. Figure 6.1 shows the velocity distribution function $(\sigma g)^{1/2}\,P(C_n)$ by solid curve and the

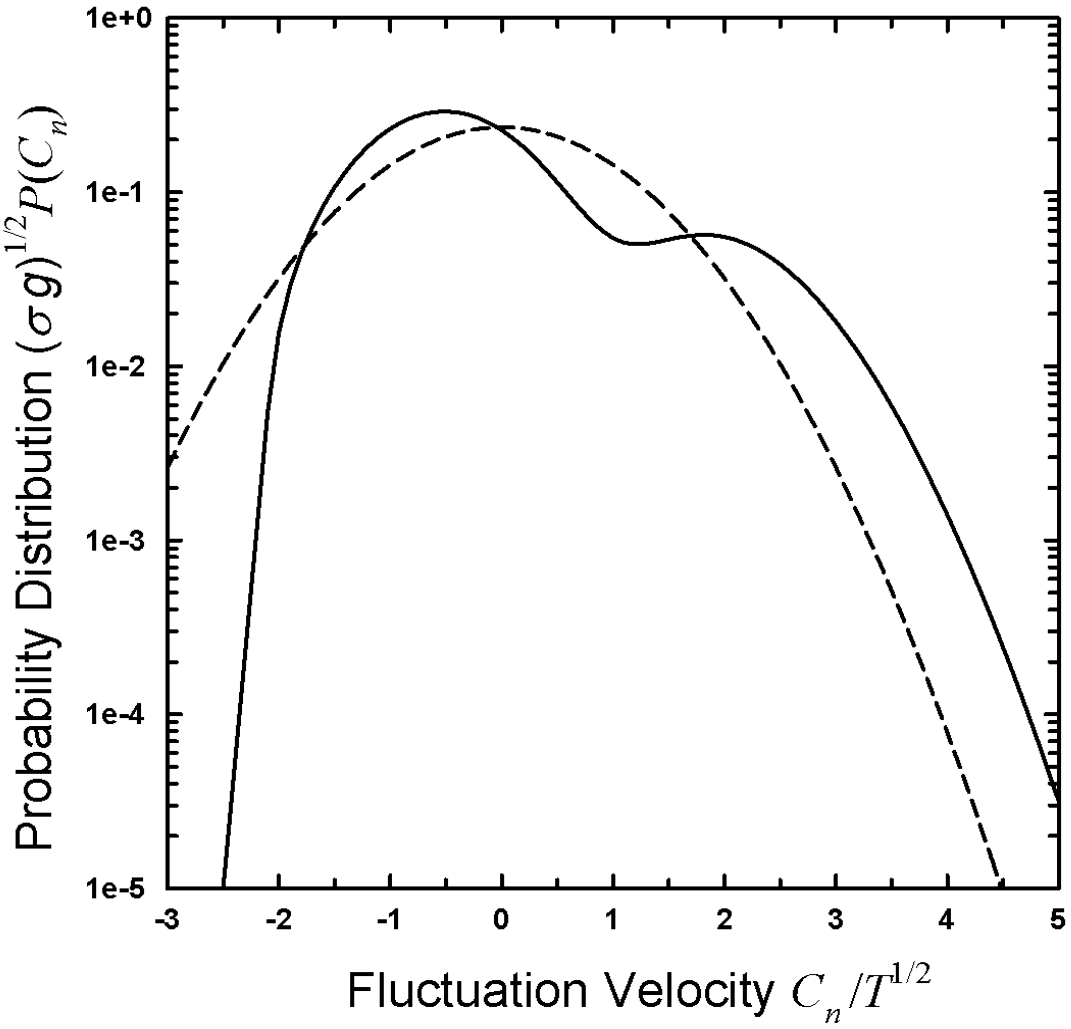

Figure 6.1 : The variation of probability $(\sigma g)^{1/2}P(C_n)$ (shown by solid curve) with $C_n/T^{1/2}$, at z=3, when θ=0, (V_n^2=3), m_t=5, e=e_w=.9, r=1, E=4, ξ_{nt} = $\xi_{n\tau}$ =90°, α =90° and Δ_t = Δ_α =.22. Also shown by dashed curve is the Gaussian profile.

Gaussian distribution (i.e., Maxwellian distribution) by dashed curve. As seen, $(\sigma g)^{1/2} P(C_n)$ strongly deviates from Gaussian distribution profile and has its peak in the negative velocity region. This is because the boundary vibrates entirely in $n-$direction and direction of gravity is opposite to that. Due to dominance of vibrations, large positive velocities are more probable than large negative velocities, resulting in departure from the symmetric Gaussian distribution. Figure 6.2 shows experimental measurements of Blair and Kudrolli (2003) for distribution function of velocity in the direction of vibration in a quasi 2-D case. We do not intend a direct comparison here, as the boundary value problem of Blair and Kudrolli is different from ours. They almost do not have gravity in the problem, but they have an upper boundary which has similar effect as gravity on the motion of particles. So, the external effects acting are more or less similar. We only want to see if the distribution profile predicted by our theory is a realistic one. As can be seen, the experimental measurements of Blair and Kudrolli have a very similar form as the distribution function predicted by our theory. Figure 6.3 shows predictions of our theory for probability distribution $(\sigma g)^{1/2} P(C_t)$ for tangential motion of particles in $t-$direction, for the same parameter values as used for Figure 6.1. For tangential fluctuations, the velocity distribution is similar to Gaussian as no other external effect like gravity influences them. $(\sigma g)^{1/2} P(C_\tau)$ is exactly same as $(\sigma g)^{1/2} P(C_t)$ as there is symmetry of array and vibration in $t-$ and $\tau-$directions. Figures 6.4 shows experimental measurements by Blair and Kudrolli (2003) for distribution functions of velocity in the direction perpendicular to direction of vibration. Again, we see that the theory predicts the form of distribution correctly.

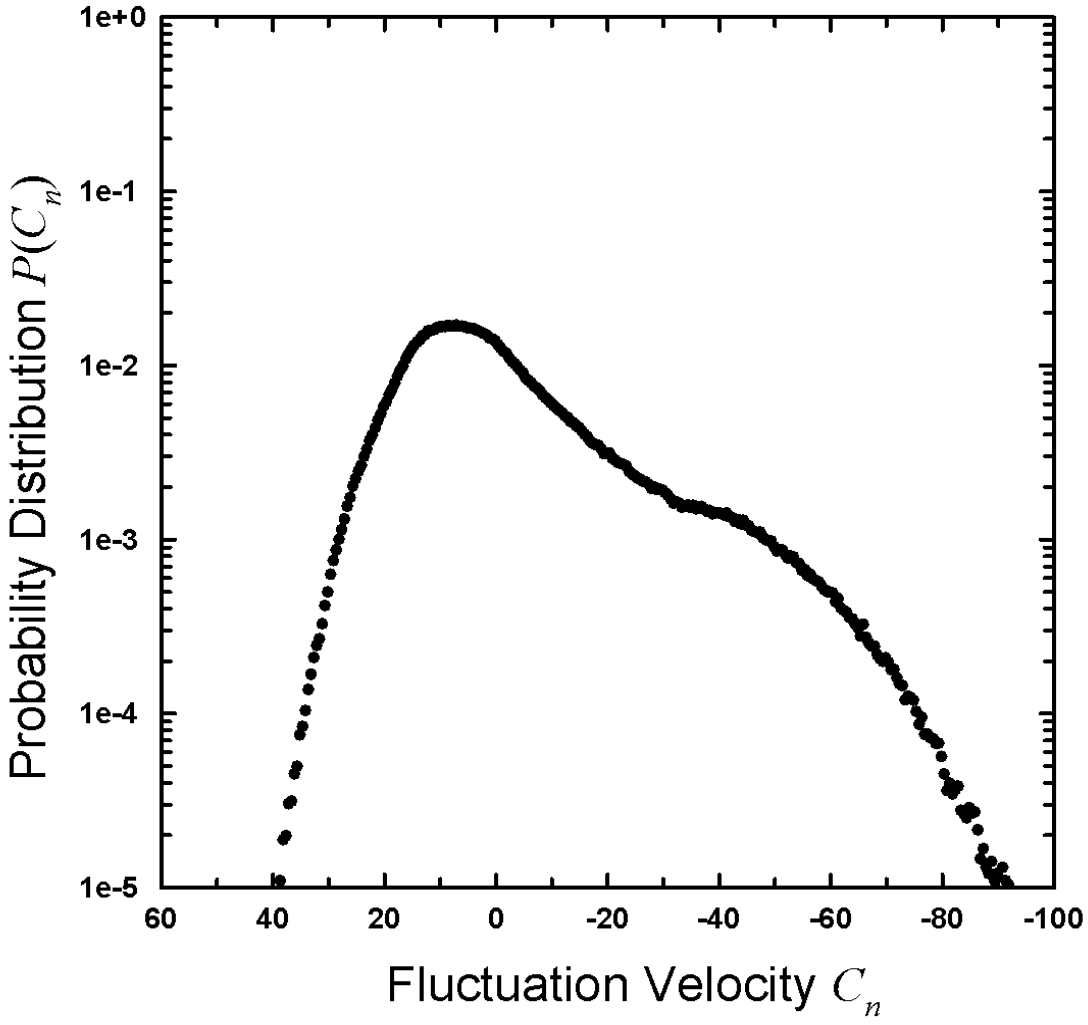

Figure 6.2 : Variation of probability $P(C_n)$ (shown by solid dots) with C_n, as measured experimentally by Blair and Kudrolli (2003).

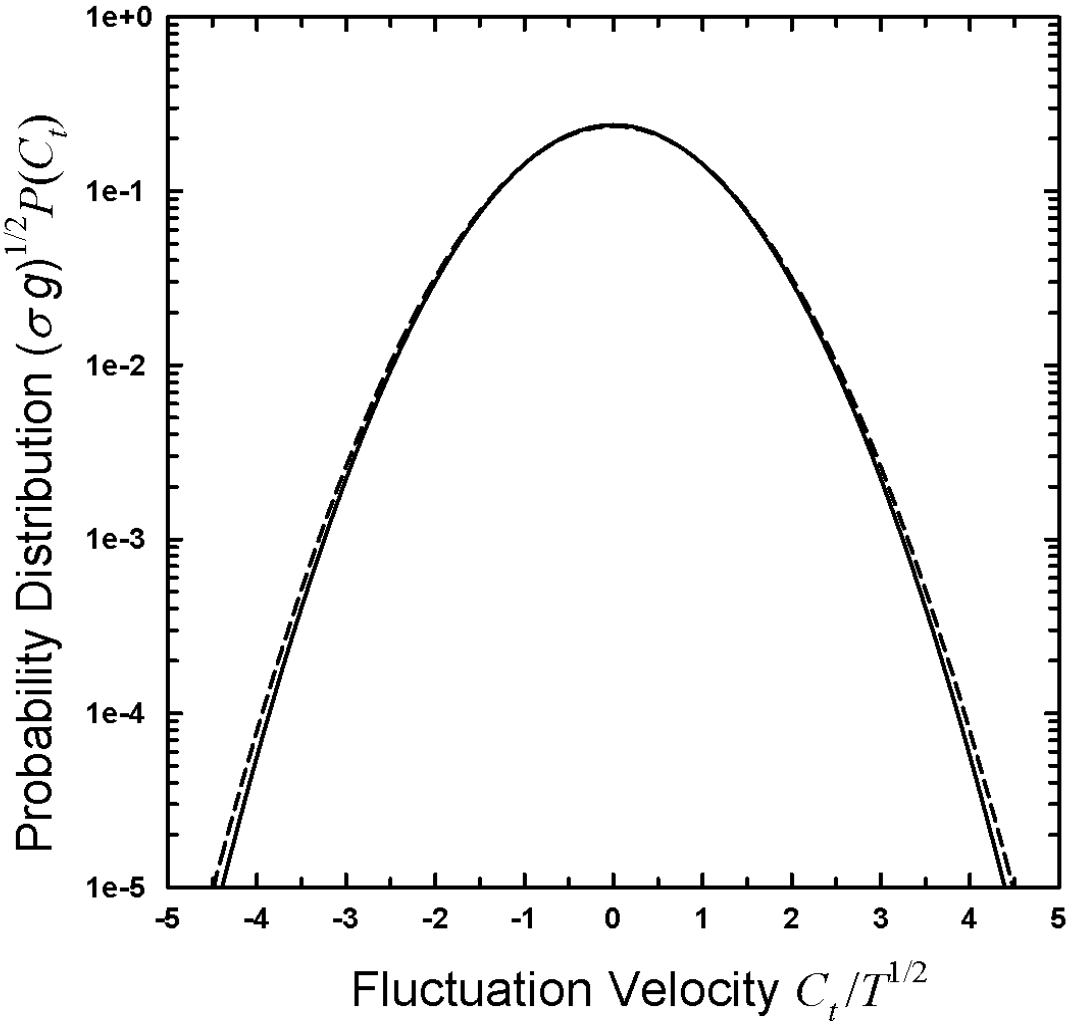

Figure 6.3 : The variation of probability $(\sigma g)^{1/2}P(C_t)$ (as shown by solid curve) with $C_t/T^{1/2}$, at z=3, when θ=0, (V_n^2=3), m_t=5, e=e_w=.9, r=1, E=4, ξ_{nt} = $\xi_{n\tau}$ =90°, α =90° and Δ_t = Δ_α =.22. Also shown by dashed curve is the Gaussian profile.

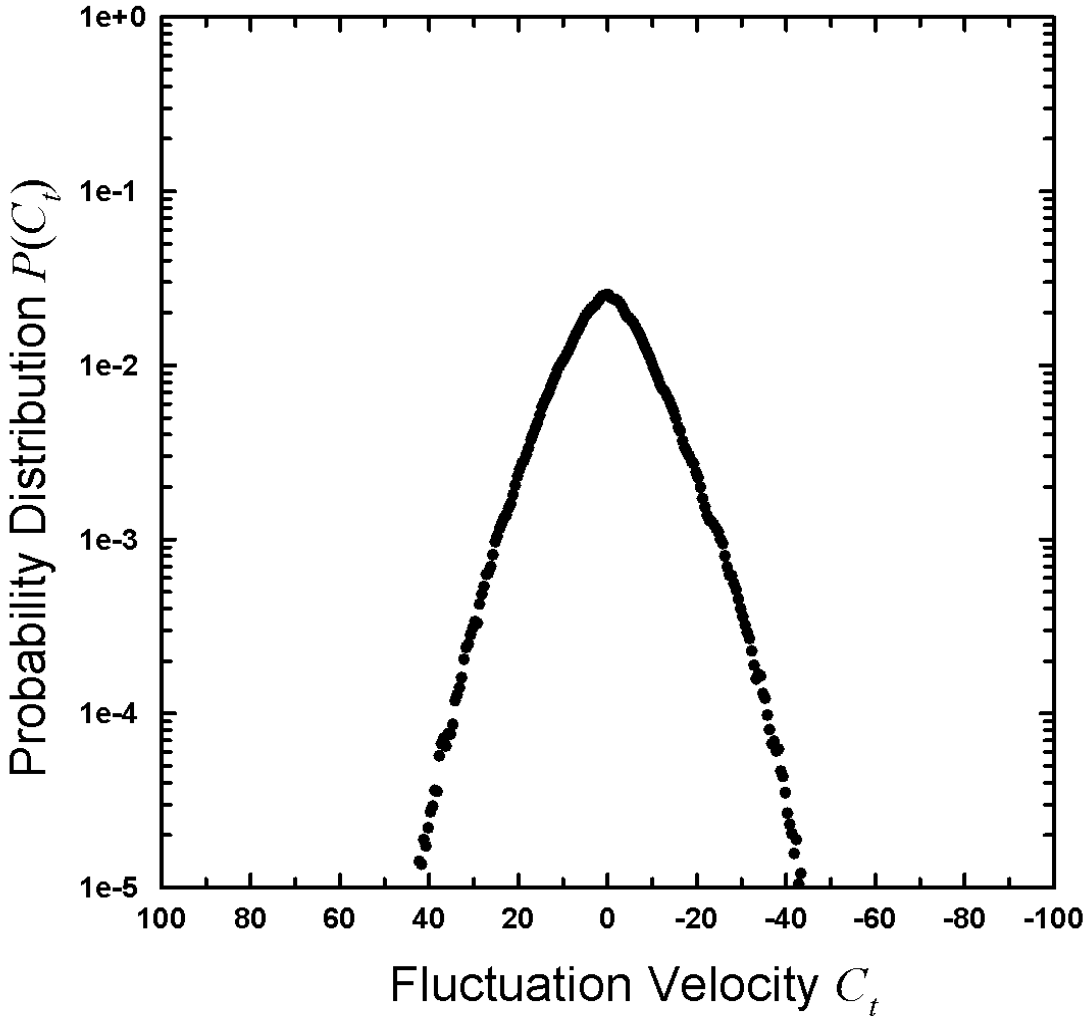

Figure 6.4 : Variation of probability $P(C_t)$ (shown by solid dots) with C_t, as measured experimentally by Blair and Kudrolli (2003).

6.2.2 Non-Driven Assemblies

Now, lets focus on the variations of mean fields. In case of non-driven assemblies where no mean motion is induced, the vibrations in both $t-$ and $\tau-$directions are 90° out of phase with respect to vibrations in $n-$direction. In case of driven flows, at least one of the $t-$ and $\tau-$directional vibrations is not 90° out of phase with respect to vibrations in $n-$direction. For non-driven assemblies, first we look at the profiles of granular temperature, solid volume fraction and different individual temperatures, and then study the dependence of thermalized state on many factors such as the total amount of vibrational energy, its distribution, restitution coefficients, mass hold-up, bumpiness of the boundary, etc. For driven flows, our primary focus is on the induced mean motion and in that part, we first look at the profiles of mean velocity and then study the dependence of induced motion on the above mentioned factors. Lets look at the non-driven assemblies.

In Figure 6.5, we show the profiles of granular temperature $\mathcal{T}^{1/2}(z)$ and solid volume fraction $\nu(z)$ for θ=0, 35.26°, 54.74° and 90° (V_n^2=3, 2, 1 and 0), when ϕ=0 ($V_\tau^2=0$), m_t=5, $e=e_w$=.9, r=1, E=4, $\xi_{nt}=\xi_{n\tau}$=90°, α=90° and $\Delta_t=\Delta_\alpha$=.22. As θ increases from 0, vibrational energy gets distributed more and more in tangential $t-$direction. As a result, the boundary becomes less effective in thermalizing the assembly and the flows become less thermalized, shallower and more dense. Figures 6.6, 6.7 and 6.8 show the details of anisotropic state of the assembly, i.e., the profiles of individual temperatures $\mathcal{T}_n^{1/2}(z)$, $\mathcal{T}_t^{1/2}(z)$ and $\mathcal{T}_\tau^{1/2}(z)$, for θ=0, 35.26°, 54.74° and 90° (V_n^2=3, 2, 1 and 0), and for above set of parameters. It can be seen that as θ increases,

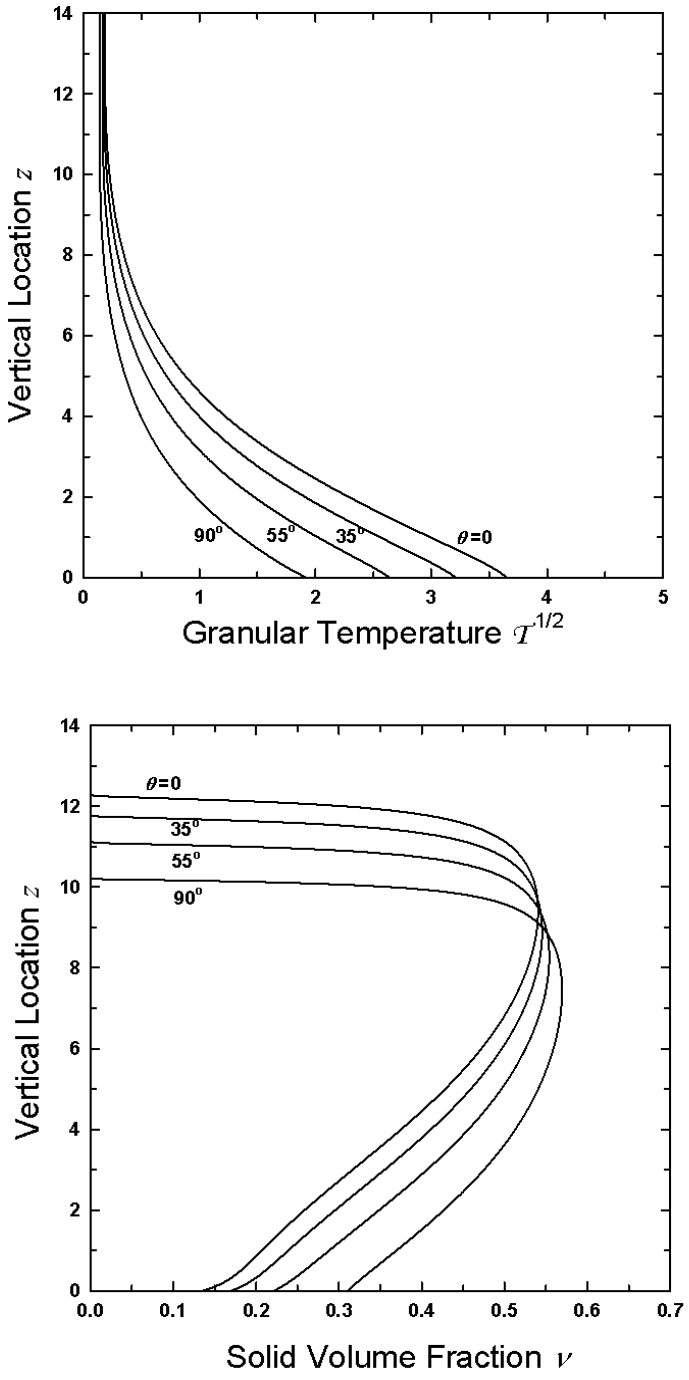

Figure 6.5: The variations of $\mathcal{T}^{1/2}(z)$ and $\nu(z)$ with z, for θ=0, 35.26°, 54.74° and 90°, when ϕ=0, m_t=5, e=e_w=.9, r=1, E=4, ξ_{nt} = $\xi_{n\tau}$ =90°, α =90° and Δ_t = Δ_α =.22.

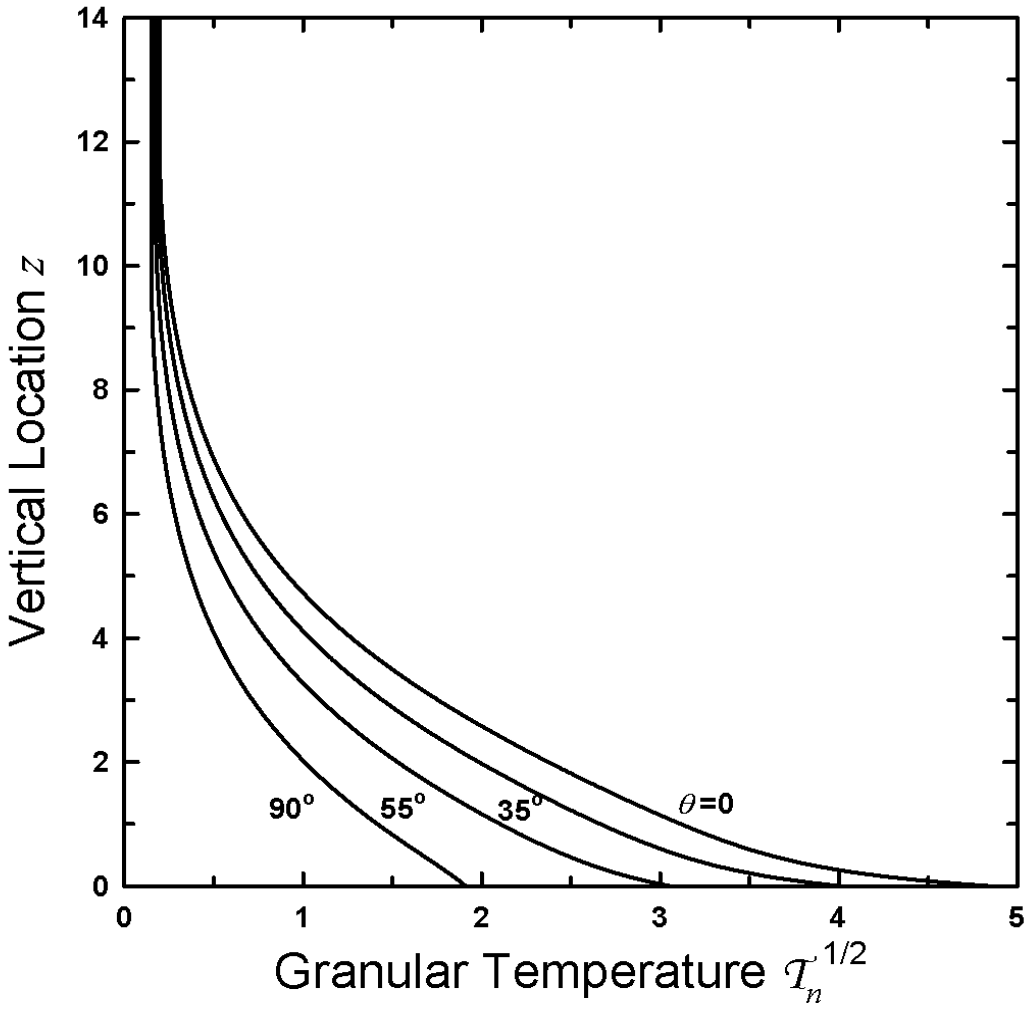

Figure 6.6: The variations of $\mathcal{T}_n^{1/2}(z)$ with z, for θ=0, 35.26°, 54.74° and 90°, (V_n^2=3, 2, 1 and 0) when ϕ=0 (V_τ^2=0), m_t=5, e=e_w=.9, r=1, E=4, ξ_{nt} = $\xi_{n\tau}$ =90°, α =90° and Δ_t = Δ_α =.22.

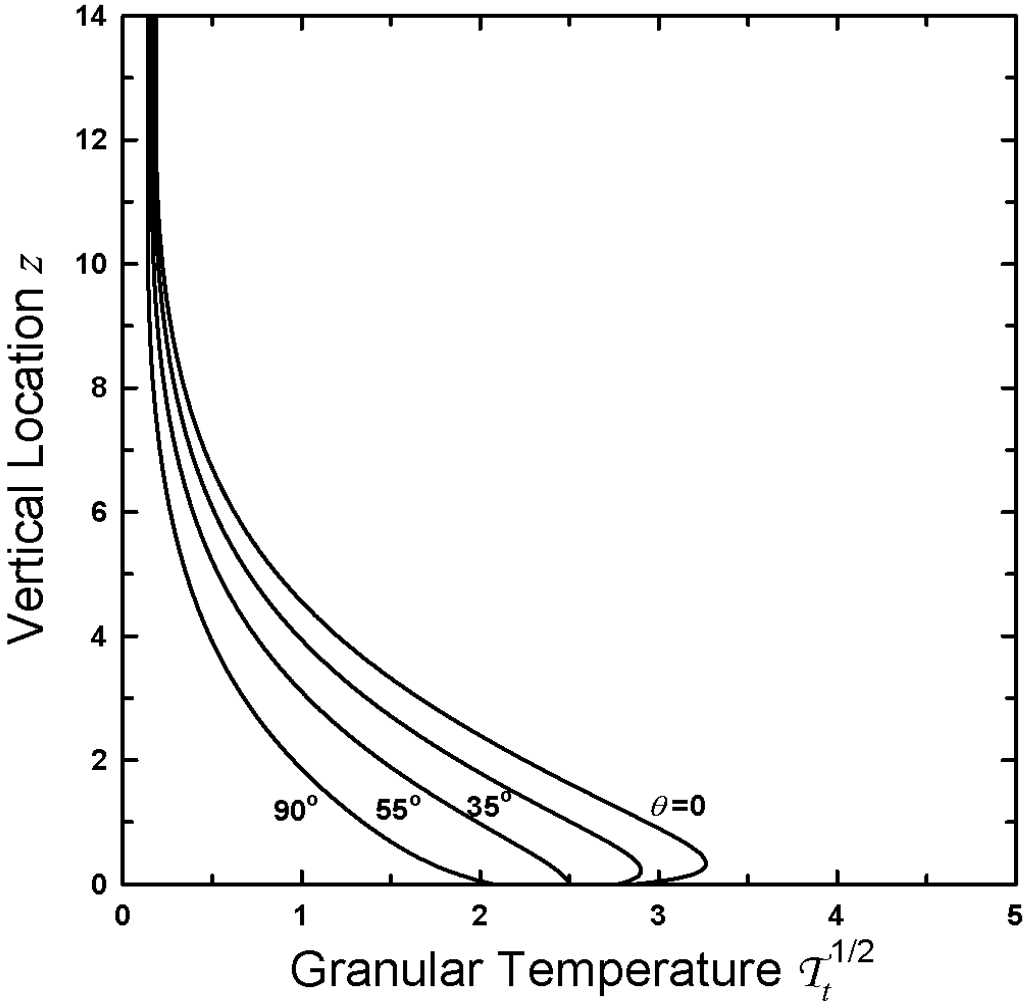

Figure 6.7: The variations of $\mathcal{T}_t^{1/2}(z)$ with z, for θ=0, 35.26°, 54.74° (V_n^2=3, 2, 1 and 0) and 90°, when ϕ=0 (V_τ^2=0), m_t=5, e=e_w=.9, r=1, E=4, ξ_{nt} = $\xi_{n\tau}$ =90°, α =90° and Δ_t = Δ_α =.22.

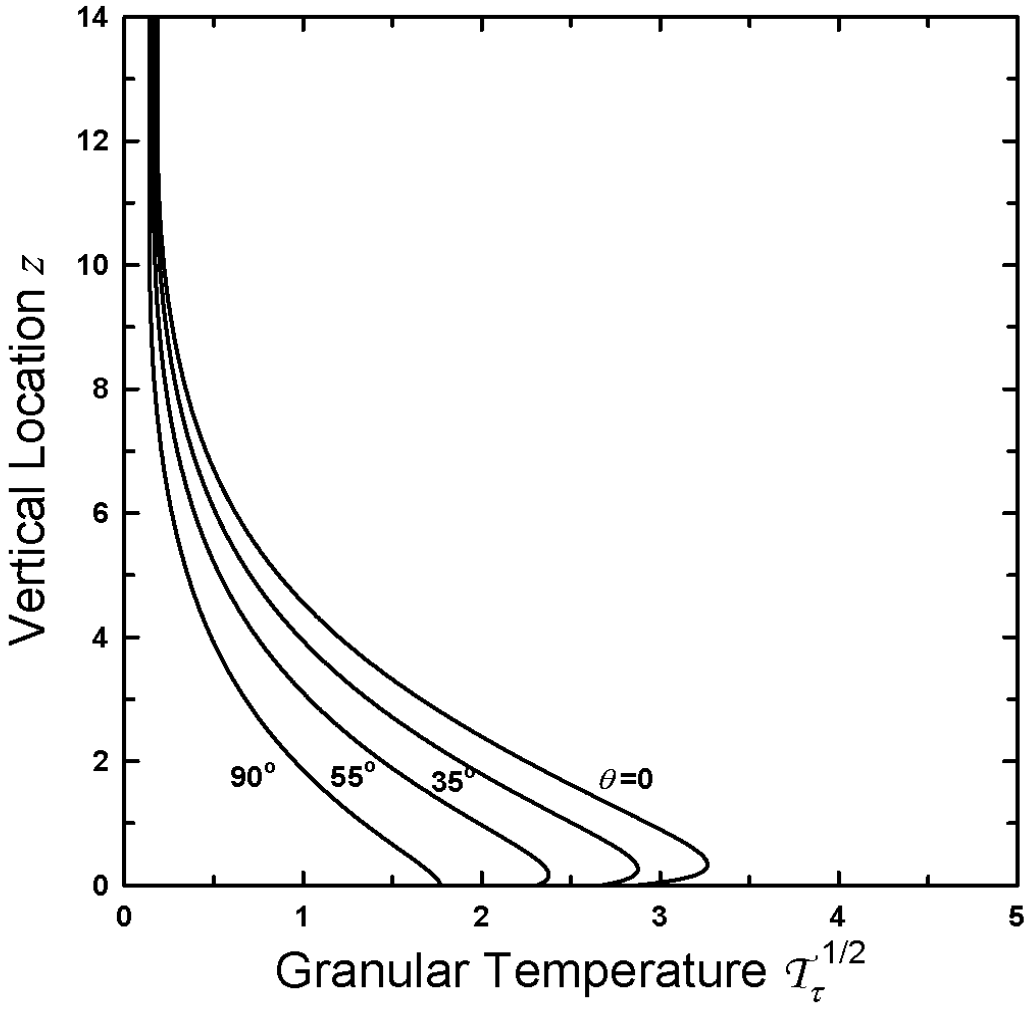

Figure 6.8: The variations of $\mathcal{T}_\tau^{1/2}(z)$ with z, for θ=0, 35.26°, 54.74° and 90°, (V_n^2=3, 2, 1 and 0) when ϕ=0 (V_τ^2=0), m_t=5, e=e_w=.9, r=1, E=4, ξ_{nt} = $\xi_{n\tau}$ =90°, α =90° and Δ_t = Δ_α =.22.

vibrations have decreasing normal component and all the temperatures decrease. The normal temperature $\mathcal{T}_n(z)$ always monotonically decreases away from the boundary, but the tangential temperatures $\mathcal{T}_t(z)$ and $\mathcal{T}_\tau(z)$, don't always do so. For values of θ far from 90°, for a small region near the boundary, $\mathcal{T}_t(z)$ and $\mathcal{T}_\tau(z)$ first increase and then start decreasing, resulting in hook-like curves. This phenomenon becomes more pronounced as θ gets closer to 0. At least near the boundary, values of the individual temperatures are very different. The difference between the individual temperatures reduces far from the boundary, and at the free surface even though the temperatures don't equalize, the difference between them is negligible. From the profiles of individual temperatures, we notice that the temperature at the boundary (at the base) provides a good measure of excitation of assembly. Hence it can be used to describe how excited the assembly is.

Figures 6.9, 6.10, 6.11 and 6.12 show the dependence of anisotropy and thermalized state on the angle of vibration θ, for the same set of parameters as above. Figure 6.9 shows variation of temperature $\mathcal{T}$ and individual temperatures $\mathcal{T}_n$, $\mathcal{T}_t$ and $\mathcal{T}_\tau$, at the base $z=0$, with θ. When θ=0, $\mathcal{T}_n$ is maximum and, $\mathcal{T}_t$ and $\mathcal{T}_\tau$ are equal to each other. As θ increases from 0, thermalization of the assembly decreases as indicated by the isotropic measure $\mathcal{T}$, and hence each of $\mathcal{T}_n$, $\mathcal{T}_t$ and $\mathcal{T}_\tau$ decrease. In addition to that, since with increasing θ more energy is supplied in $\boldsymbol{t}-$direction, difference between $\mathcal{T}_n$ and $\mathcal{T}_t$ reduces with increasing θ. However until θ=75°, $\mathcal{T}_n$ remains the largest temperature. This shows that the assembly has a preferential direction of excitation, which is the normal direction. Eventually $\mathcal{T}_t$ becomes larger than $\mathcal{T}_n$ and since, no

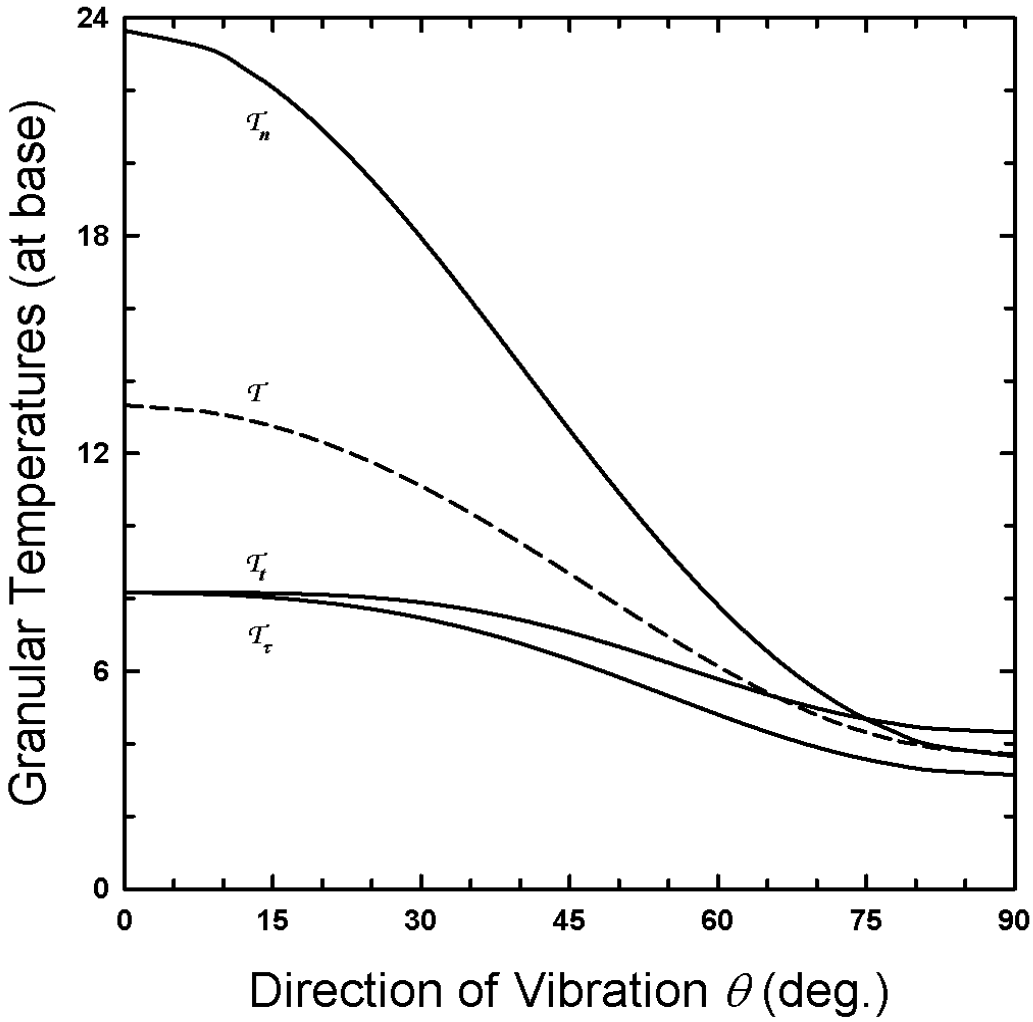

Figure 6.9: The variations of $\mathcal{T}$ (shown by dashed curve) and, $\mathcal{T}_n$, $\mathcal{T}_t$ and $\mathcal{T}_\tau$ (shown by solid curves), at z=0, with θ, when ϕ=0 (V_τ^2=0), m_i=5, e=e_w=.9, r=1, E=4, ξ_{nt} = $\xi_{n\tau}$ =90°, α =90° and Δ_t = Δ_α =.22.

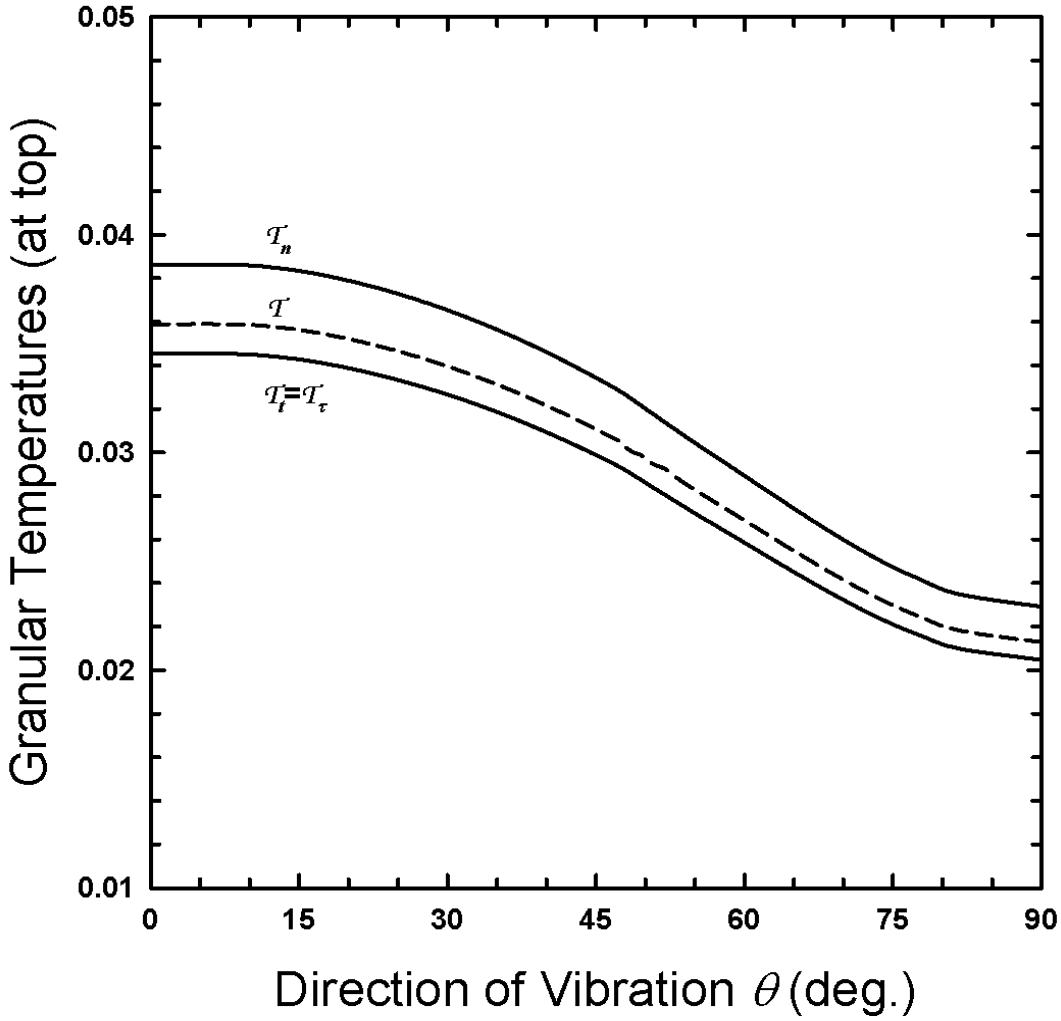

Figure 6.10: The variations of $\mathcal{T}$ (shown by dashed curve) and, $\mathcal{T}_n$, $\mathcal{T}_t$ and $\mathcal{T}_\tau$ (shown by solid curves), at $z=h$, with θ, when $\phi=0$ ($V_\tau^2=0$), $m_t=5$, $e=e_w=.9$, $r=1$, $E=4$, $\xi_{nt}=\xi_{n\tau}=90°$, $\alpha=90°$ and $\Delta_t=\Delta_\alpha=.22$.

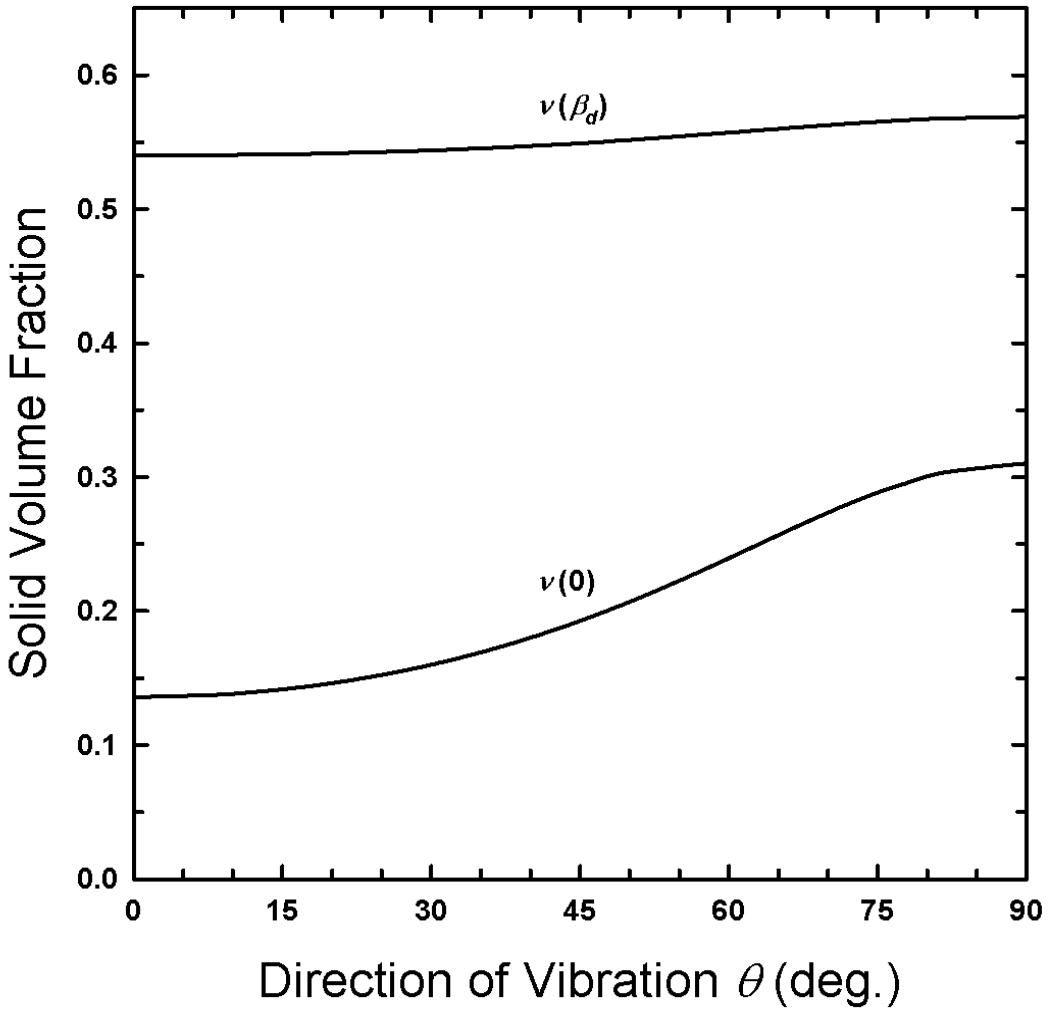

Figure 6.11: The variations of $\nu(\beta_d)$ and $\nu(0)$, with θ, when ϕ=0 (V_τ^2=0), m_t=5, e=e_w=.9, r=1, E=4, ξ_{nt} =$\xi_{n\tau}$ =90°, α =90° and Δ_t =Δ_α =.22.

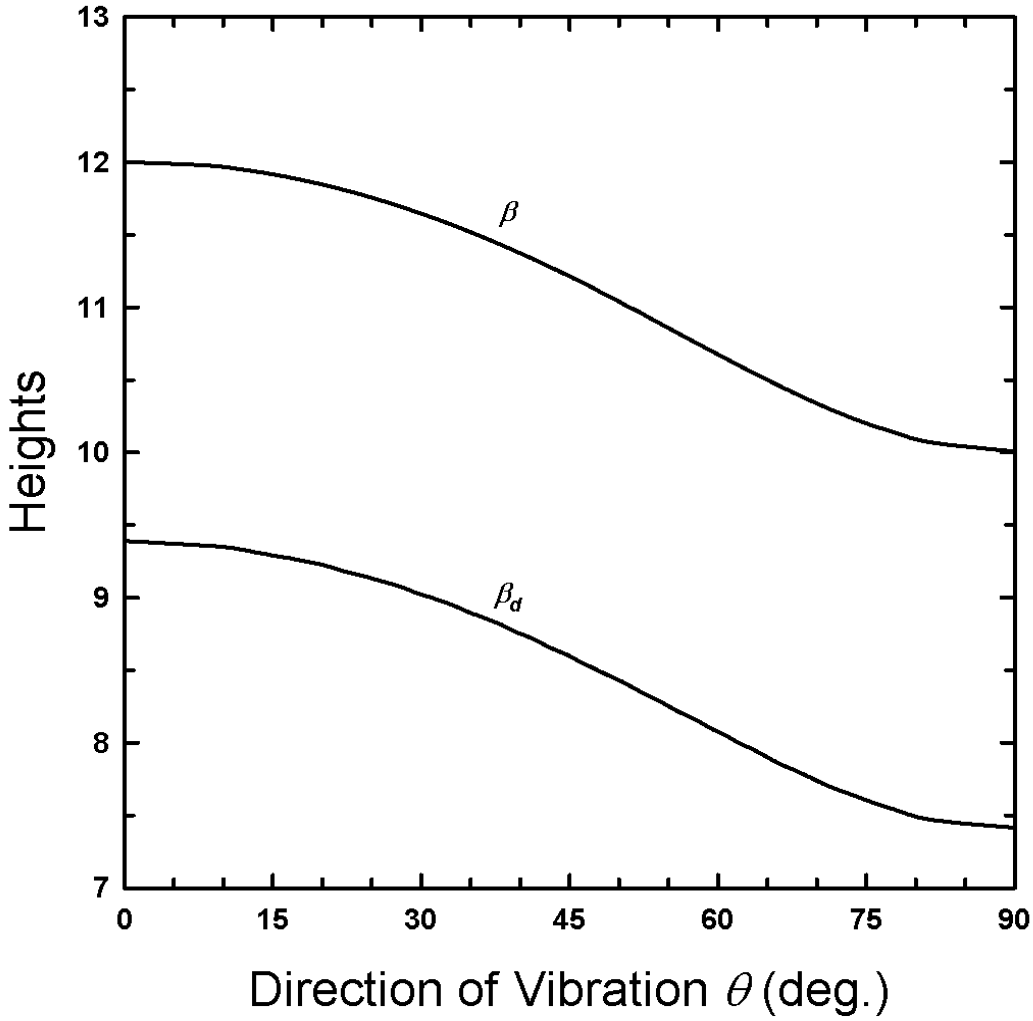

Figure 6.12: The variations of β and β_d, with θ, when ϕ=0 (V_τ^2=0), m_t=5, e=e_w=.9, r=1, E=4, ξ_{nt} =$\xi_{n\tau}$ =90°, α =90° and Δ_t =Δ_α =.22.

vibrational energy is supplied in $\tau-$direction, $\mathcal{T}_\tau$ remains smallest for all values of θ. So, at least near the boundary, we see that the flows can be very anisotropic. Also, we see that the anisotropy is largest when the vibrations are in normal direction and under such circumstances the individual temperatures differ significantly from their mean value $\mathcal{T}(z)$ which therefore can not adequately represent the excited state. Figure 6.10 shows the variation of temperature $\mathcal{T}$ and individual temperatures $\mathcal{T}_n$, $\mathcal{T}_t$ and $\mathcal{T}_\tau$, at the top $z=h$, with θ. As expected, all the temperatures decrease as θ increases. We see that at the free surface, far away from the boundary, the difference between the temperatures reduces. The two tangential temperatures are very nearly equal to each other, however the normal temperature $\mathcal{T}_n$ is still about 10% larger than them. Figure 6.11 and 6.12 shows variation of solid volume fraction at the base $\nu(0)$ and the maximum value of solid volume fraction inside the flow $\nu(\beta_d)$, and the variation of flow height β below which 99% of the total mass-holdup m_t is contained, and β_d which is the height at which the assembly is most dense, with θ. With increasing θ, the flows become less excited and hence more dense and more shallow. Figures 6.9 through 6.12 clearly demonstrate the importance of θ in influencing thermalization of assembly.

In Figure 6.13, we show variation of temperature $\mathcal{T}$ and individual temperatures $\mathcal{T}_n$, $\mathcal{T}_t$ and $\mathcal{T}_\tau$, at the base $z=0$, with the direction of tangential vibration ϕ, when θ=90° (V_n^2=0), m_t=5, $e=e_w$=.9, r=1, E=4, $\xi_{nt}=\xi_{n\tau}$=90°, α=90° and $\Delta_t=\Delta_\alpha$=.22. In this case, when ϕ=0, the vibrations are entirely in $t-$direction. As a result, $\mathcal{T}_t$ is the largest temperature and $\mathcal{T}_n$ is larger than $\mathcal{T}_\tau$, when ϕ=0. As ϕ increases, vibrations have increasing $\tau-$component and hence, $\mathcal{T}_t$ reduces while $\mathcal{T}_\tau$ increases. Also with increasing

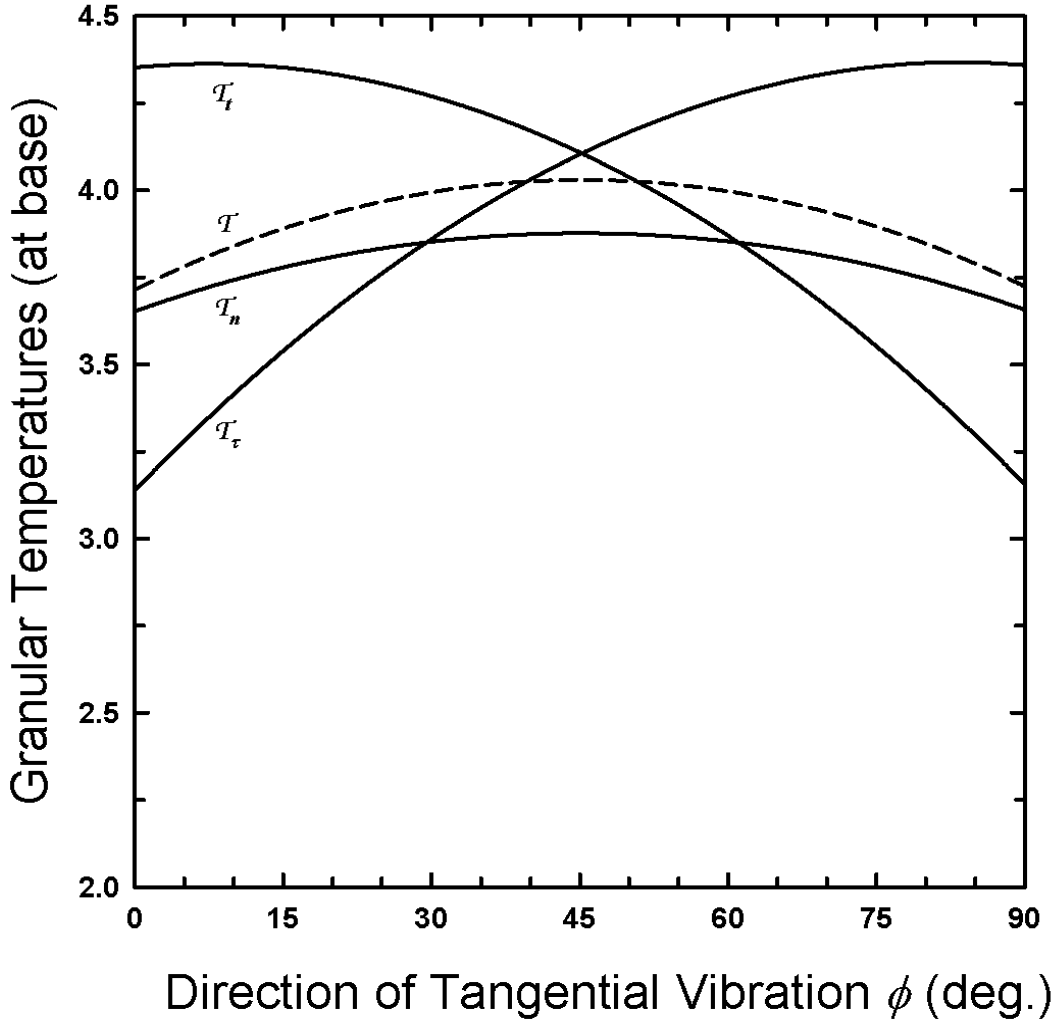

Figure 6.13: The variations of $\mathcal{T}$ (shown by dashed curve) and, $\mathcal{T}_n$, $\mathcal{T}_t$ and $\mathcal{T}_\tau$ (shown by solid curves), at z=0, with ϕ, when θ=90° (V_n^2=0), m_t=5, e=e_w=.9, r=1, E=4, ξ_{nt} = $\xi_{n\tau}$ =90°, α =90° and Δ_t = Δ_α =.22.

ϕ, the orientation of the bumps with respect to boundary vibrations also changes and hence initially $\mathcal{T}_n$ increases with increasing ϕ. When ϕ=45°, vibrations have equal $t-$ and $\tau-$components, and $\mathcal{T}_t$ and $\mathcal{T}_\tau$ become equal to each other. As ϕ increases beyond 45°, vibrations have larger $\tau-$component than $t-$component and $\mathcal{T}_\tau$ is the largest temperature. The variations are *symmetric* about ϕ=45° due to symmetry of array. Figure 6.14 shows the variation of temperature $\mathcal{T}$ and individual temperatures $\mathcal{T}_n$, $\mathcal{T}_t$ and $\mathcal{T}_\tau$, at the base $z=0$, with the direction of tangential vibration ϕ, when Δ_t=.22, Δ_α=.11, α=90°, θ=90° (V_n^2=0), m_t=5, $e=e_w$=.9, r=1, E=4 and $\xi_{nt}=\xi_{n\tau}$=90°. Now, the array is no longer *symmetric* with respect to ϕ=45°. When ϕ=0, $\mathcal{T}_t$ is the largest temperature. As ϕ increases, vibrations have increasing $\tau-$component and hence, $\mathcal{T}_t$ reduces while $\mathcal{T}_\tau$ increases. When ϕ=45°, even though vibration has equal $t-$ and $\tau-$components, since the array spacing in $t-$ and $\tau-$directions, Δ_t and Δ_α, are not the same, $\mathcal{T}_t$ and $\mathcal{T}_\tau$ are not equal at ϕ=45° and $\mathcal{T}_t$ is greater than $\mathcal{T}_\tau$ as Δ_t is greater than Δ_α. As ϕ increases beyond 45°, vibrations have larger $\tau-$component than $t-$component and eventually $\mathcal{T}_\tau$ becomes larger than $\mathcal{T}_t$, but $\mathcal{T}_n$ is the largest temperature when ϕ=90°. Figures 6.13 and 6.14 together demonstrate the importance of both, the direction of tangential vibration ϕ and pattern of boundary bumps, in influencing the thermalization of assembly.

Figure 6.15 further investigates the effect of array spacing on thermalization. In this figure, we show the variation of temperature $\mathcal{T}$ and individual temperatures $\mathcal{T}_n$, $\mathcal{T}_t$

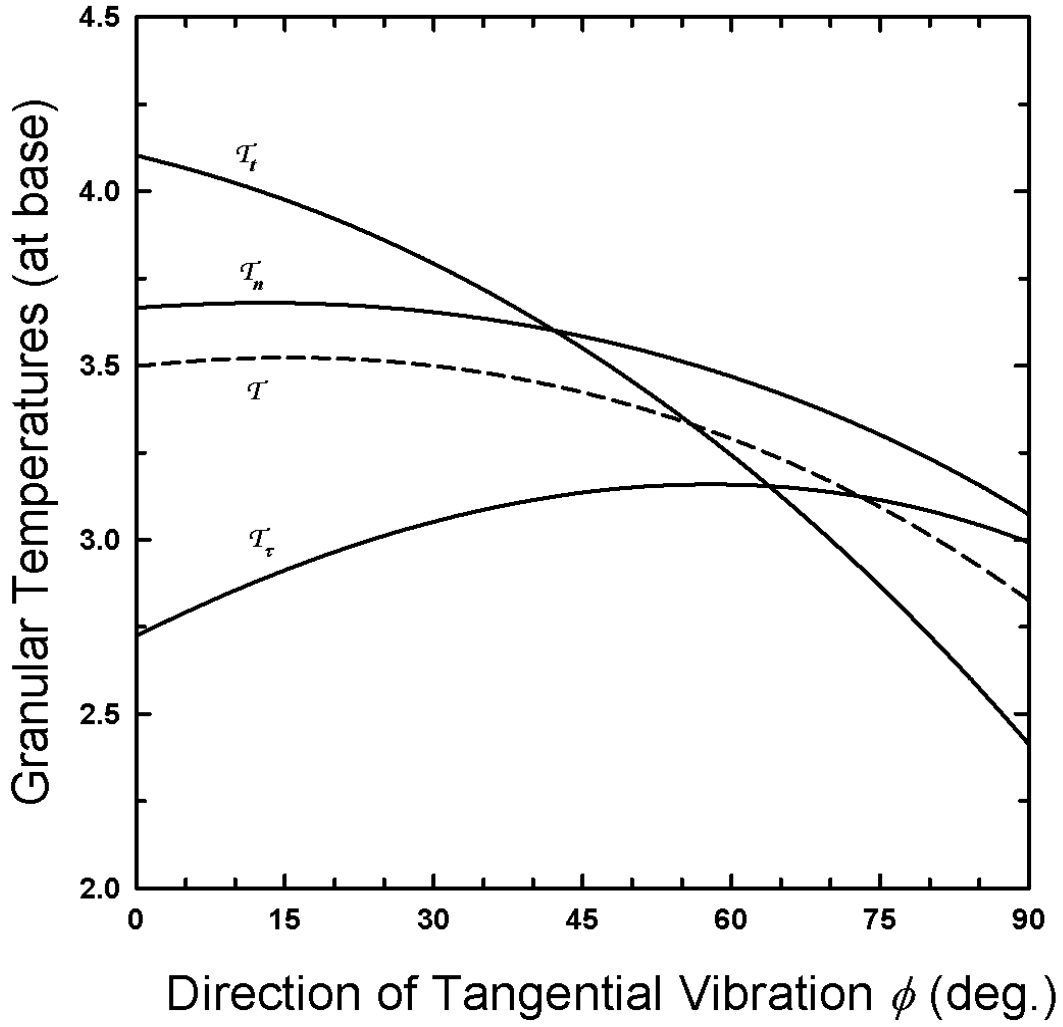

Figure 6.14: The variations of $\mathcal{T}$ (shown by dashed curve) and, $\mathcal{T}_n$, $\mathcal{T}_t$ and $\mathcal{T}_\tau$ (shown by solid curves), at z=0, with ϕ, when θ=90° (V_n^2=0), m_t=5, e=e_w=.9, r=1, E=4, ξ_{nt} = $\xi_{n\tau}$ =90°, α =90°, Δ_t =.22 and Δ_α =.11.

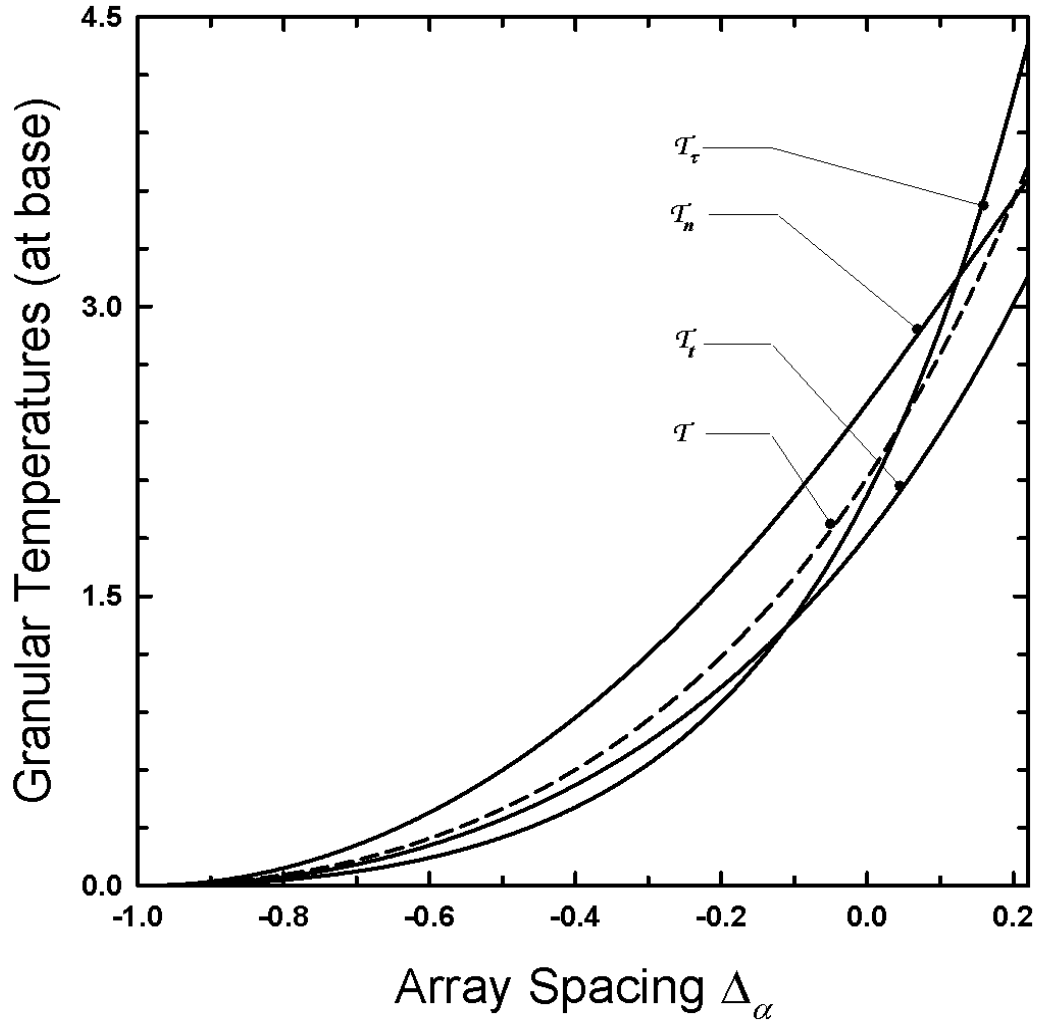

Figure 6.15: The variations of $\mathcal{T}$ (shown by dashed curve) and, $\mathcal{T}_n$, $\mathcal{T}_t$ and $\mathcal{T}_\tau$ (shown by solid curves), at z=0, with Δ_α, when θ=90°, ϕ=90° (V_τ^2=3), m_t=5, e=e_w=.9, r=1, E=4, ξ_{nt} = $\xi_{n\tau}$ =90°, α =90° and Δ_t =.22.

and $\mathcal{T}_\tau$, at the base $z=0$, with array spacing Δ_α, when θ=90° (V_n^2=0), ϕ=90° (V_t^2=0), m_t=5, $e=e_w$=.9, r=1, E=4, $\xi_{nt}=\xi_{n\tau}$=90°, α=90° and Δ_t=.22. When Δ_α=-1 and α=90°, the boundary essentially has humps parallel to $\tau-$direction. Also, since θ=90° and ϕ=90°, the vibrations are entirely in $\tau-$direction, and hence when Δ_α=-1, all the temperatures have zero values, i.e., the assembly is not even least excited and is undergoing motion as *one solid mass*. As Δ_α increases, the humps change to more bumpy arrays and all the temperatures increase. Initially, until the hump-effect is strong, $\mathcal{T}_\tau$ is smaller than $\mathcal{T}_t$ and as the arrays become sufficiently bumpy, $\mathcal{T}_\tau$ becomes larger than $\mathcal{T}_t$. Figures 6.16 and 6.17 show variations of solid volume fractions $\nu(0)$ and $\nu(\beta_d)$, and flow heights β and β_d, with Δ_α. With increasing Δ_α, the flows become more excited and hence less dense and deeper.

In Figure 6.18, we investigate the effect of array angle on the thermalization of the assembly. Here, we show the variation of temperature $\mathcal{T}$ and individual temperatures $\mathcal{T}_n$, $\mathcal{T}_t$ and $\mathcal{T}_\tau$, at the base $z=0$, with array angle α, when θ=90° (V_n^2=0), ϕ=90° (V_t^2=0), m_t=5, $e=e_w$=.9, r=1, E=4, $\xi_{nt}=\xi_{n\tau}$=90° and $\Delta_t=\Delta_\alpha$=.22. With equal spacing $\Delta_t=\Delta_\alpha$, when α=0, the boundary essentially has humps parallel to $\tau-$direction. Also, since θ=90° and ϕ=90°, the vibrations are entirely in $\tau-$direction, and hence when α=0, all the temperatures have zero values. As α increases, the humps change to a more bumpy boundary and all the temperatures increase. Initially, when the effect of humps is still dominating, $\mathcal{T}_\tau$ is smaller than $\mathcal{T}_t$ and as the arrays become sufficiently bumpy, $\mathcal{T}_\tau$ becomes larger than $\mathcal{T}_t$. Figures 6.19 and 6.20 show the variations with α of

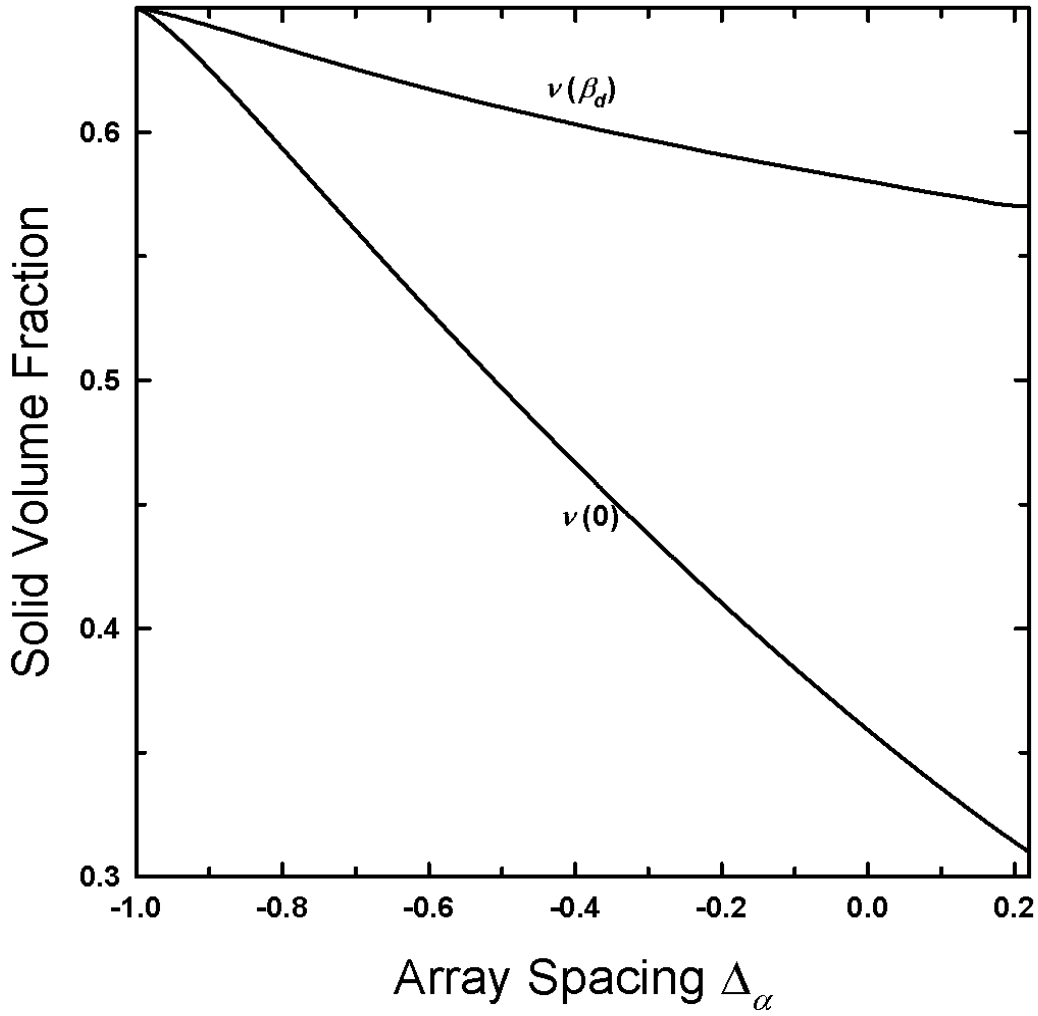

Figure 6.16: The variations of $\nu(\beta_d)$ and $\nu(0)$, with Δ_α, when θ=90°, ϕ=90° (V_τ^2=3), m_t=5, e=e_w=.9, r=1, E=4, ξ_{nt}=$\xi_{n\tau}$=90°, α=90° and Δ_t=.22.

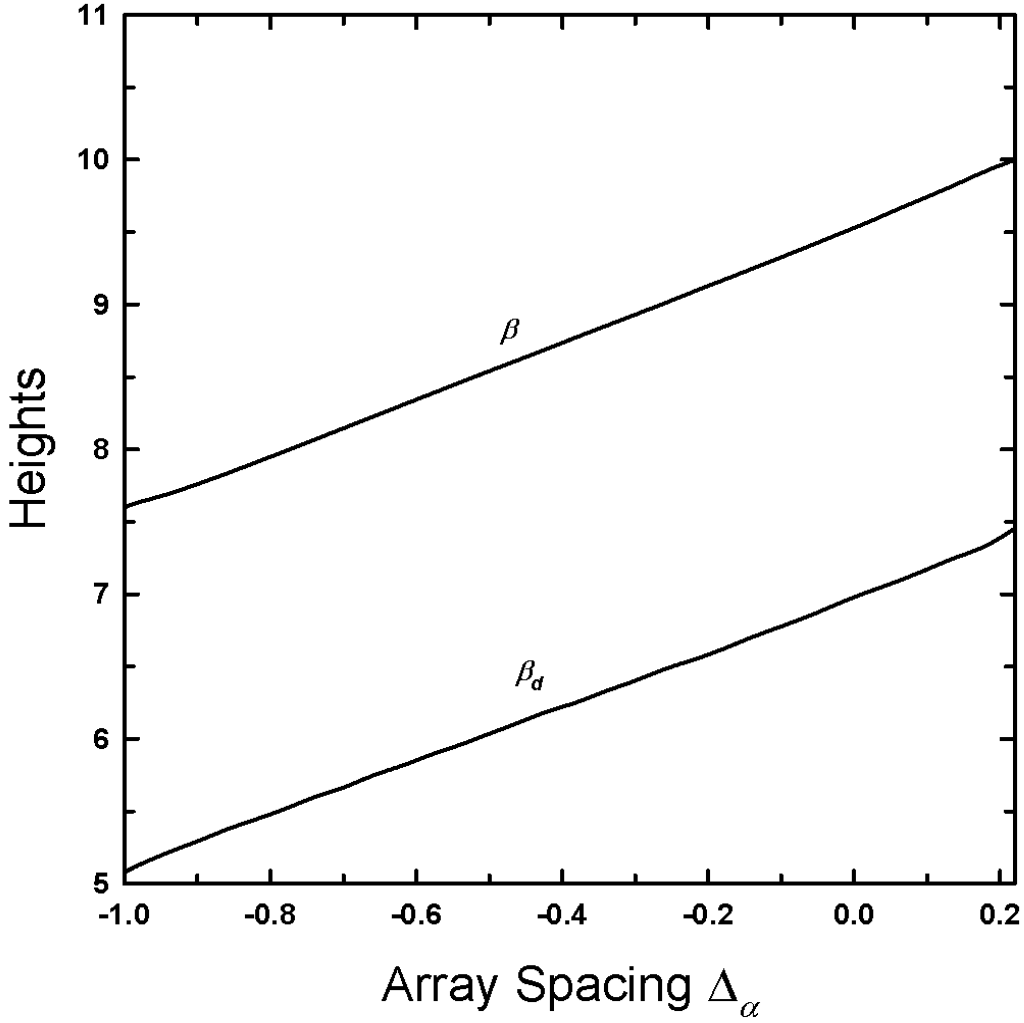

Figure 6.17: The variations of β and β_d, with Δ_α, when θ=90°, ϕ=90° (V_τ^2=3), m_t=5, e=e_w=.9, r=1, E=4, $\xi_{nt} = \xi_{n\tau}$ =90°, α =90° and Δ_t =.22.

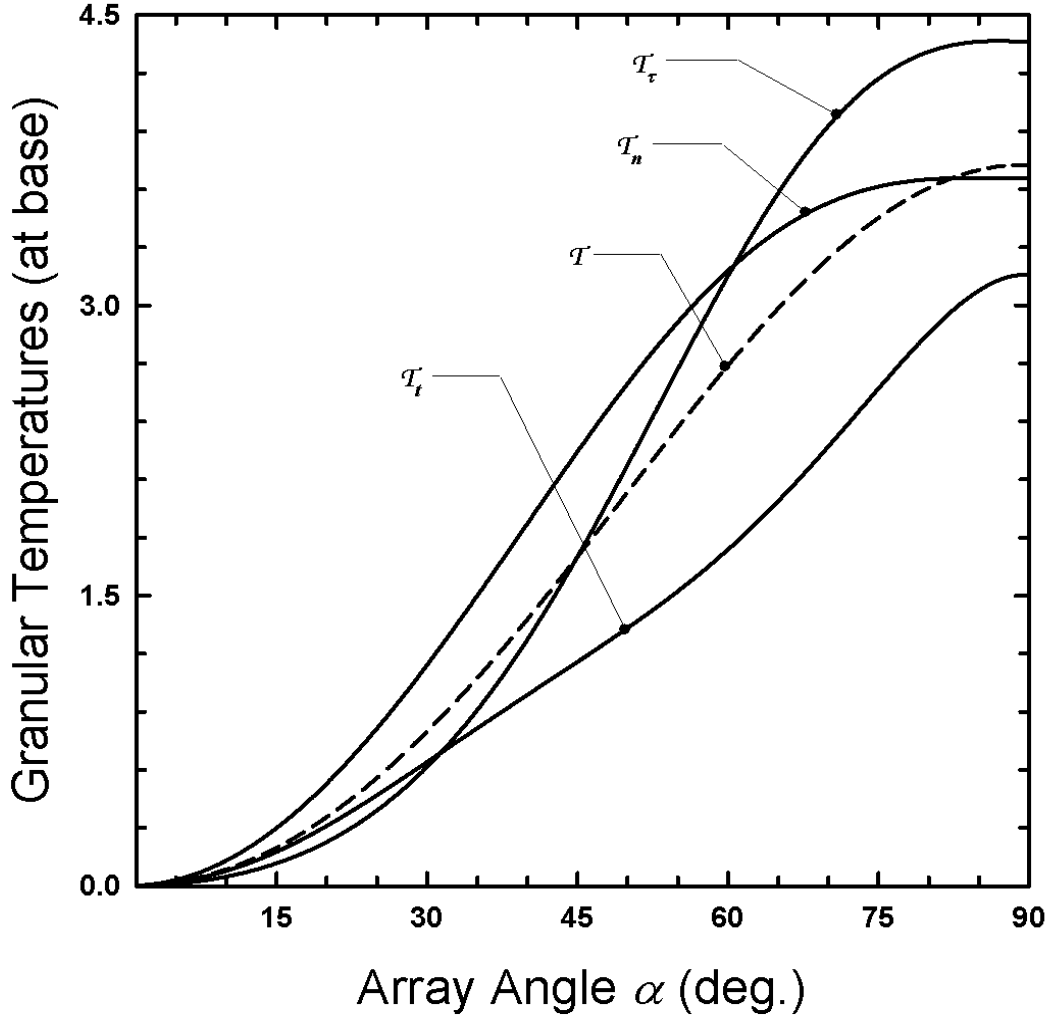

Figure 6.18: The variations of $\mathcal{T}$ (shown by dashed curve) and, $\mathcal{T}_n$, $\mathcal{T}_t$ and $\mathcal{T}_\tau$ (shown by solid curves), at z=0, with α when θ=90°, ϕ=90° (V_τ^2=3), m_t=5, e=e_w=.9, r=1, E=4, ξ_{nt} = $\xi_{n\tau}$ =90° and Δ_t = Δ_α =.22.

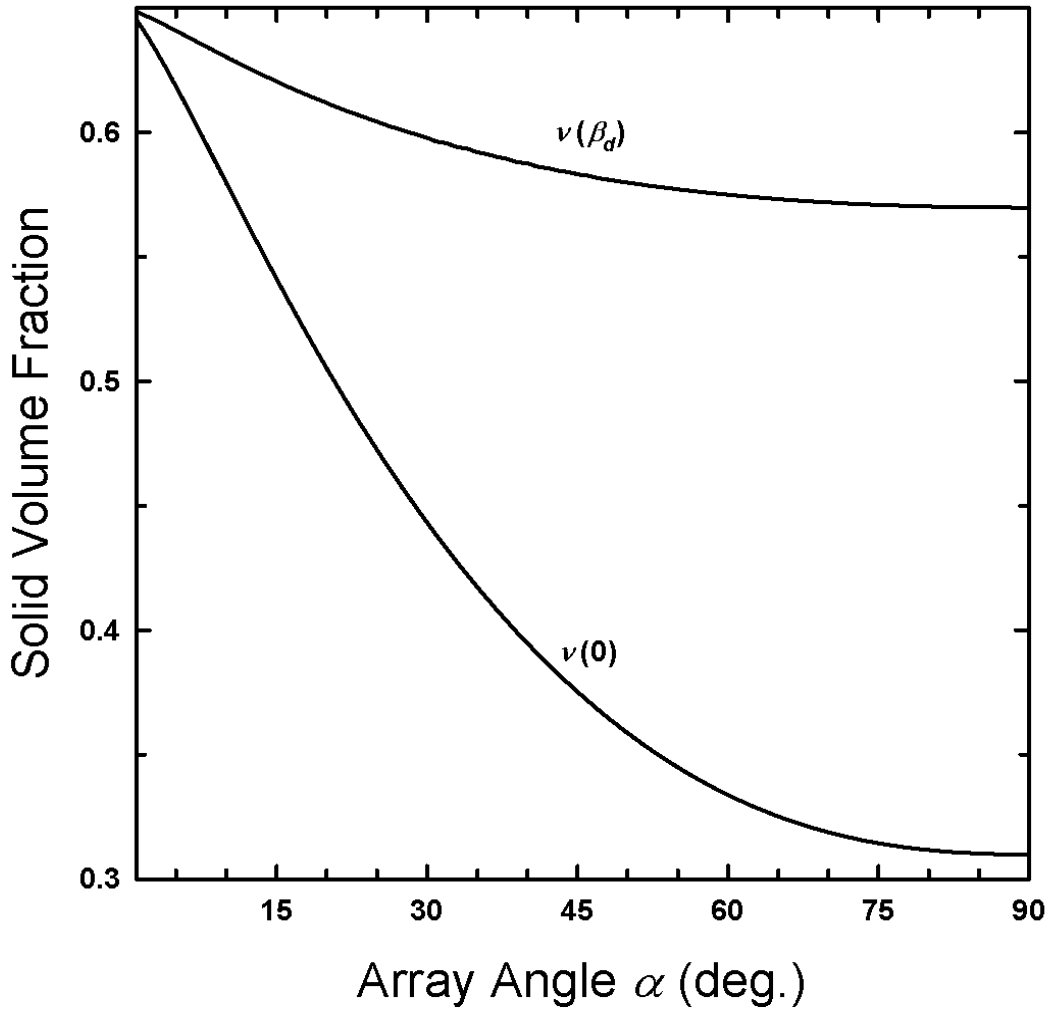

Figure 6.19: The variations of $\nu(\beta_d)$ and $\nu(0)$, with α when θ=90°, ϕ=90° (V_τ^2=3), m_t=5, e=e_w=.9, r=1, E=4, ξ_{nt} = $\xi_{n\tau}$ =90° and Δ_t = Δ_α =.22.

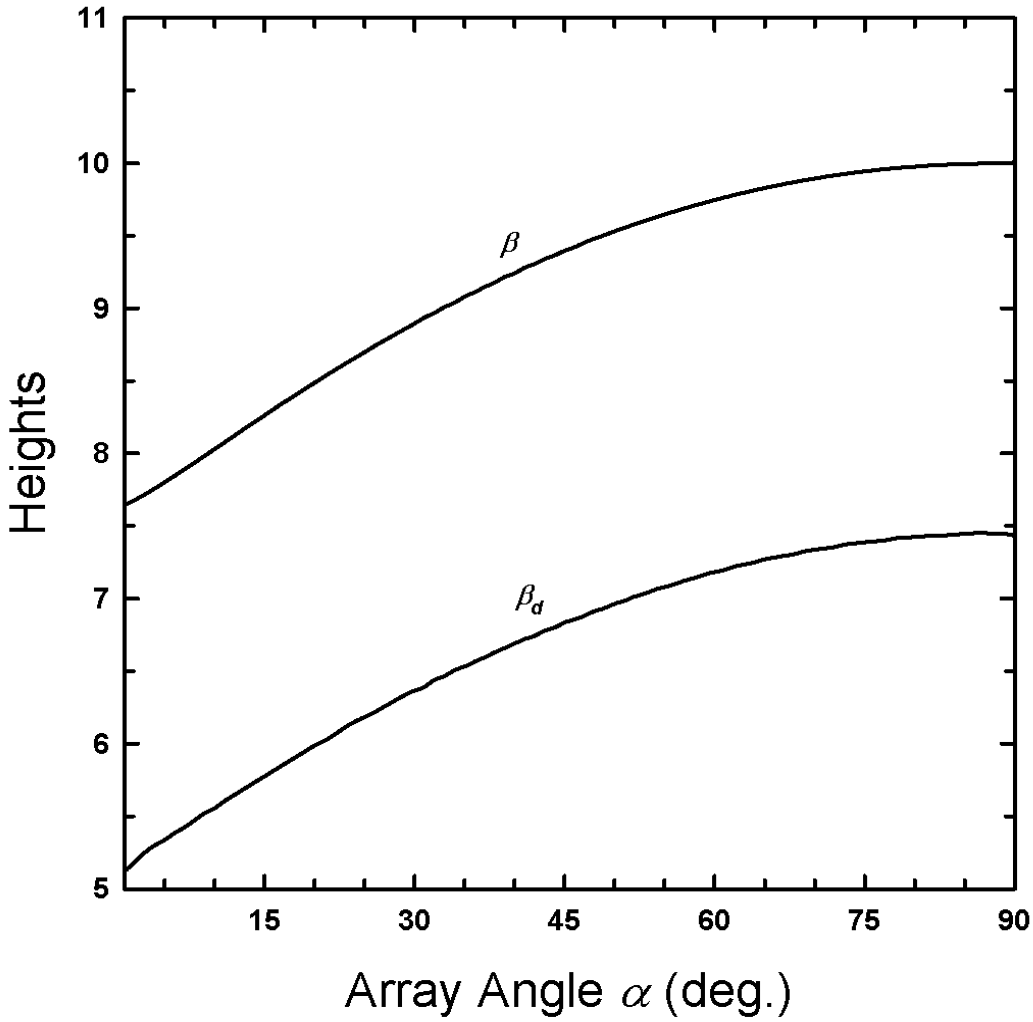

Figure 6.20: The variations of β and β_d, with α when θ=90°, ϕ=90° (V_τ^2=3), m_t=5, e=e_w=.9, r=1, E=4, $\xi_{nt} = \xi_{n\tau}$ =90° and $\Delta_t = \Delta_\alpha$ =.22.

flow heights, β and β_d, and solid volume fractions $\nu(0)$ and $\nu(\beta_d)$, for the above set of parameters. As α increases, the flow becomes more thermalized and hence flow heights increase and solid volume fractions decrease.

Next, we show the effect of total boundary energy E on thermalization of the assembly. In Figure 6.21, we plot variation of temperature $\mathcal{T}$ and individual temperatures $\mathcal{T}_n$, $\mathcal{T}_t$ and $\mathcal{T}_\tau$, at the base $z=0$, with total boundary energy E, when θ=54.74° (V_n^2=1), ϕ=0 ($V_\tau^2=0$), m_t=5, $e=e_w$=.9, r=1, $\xi_{nt}=\xi_{n\tau}$=90° and α=90°, $\Delta_t=\Delta_\alpha$=.22. When E=0, no energy is supplied to the assembly and as a result, no excitation is produced in the flow and all temperatures are zero. With increasing E, initially all temperatures increase because of increased thermalization. Since the vibrations of boundary are only in $\boldsymbol{n}-$ and $\boldsymbol{t}-$ directions, with increasing E, $\mathcal{T}_n$ and $\mathcal{T}_t$ increase. However, temperature $\mathcal{T}_\tau$ is influenced by two competing effects. With increasing E, even though the total energy input to the assembly increases, the solid volume fraction near the base substantially decreases which reduces the number of collisions. So, $\mathcal{T}_\tau$ initially increases, due to increasing energy input and then decreases due to reducing number of collisions near the boundary. Figures 6.22 and 6.23 show the variations with E of solid volume fractions $\nu(0)$ and $\nu(\beta_d)$, and flow heights, β and β_d, for the above set of parameters. As E increases, the flow becomes more thermalized and hence less dense and more deep.

In Figure 6.24, we show the profiles of granular temperature $\mathcal{T}^{1/2}(z)$ and solid volume fraction $\nu(z)$ for m_t=2.5, 5, 10 and 20, when θ=0 (V_n^2=3), $e=e_w$=.9, r=1, E=4,

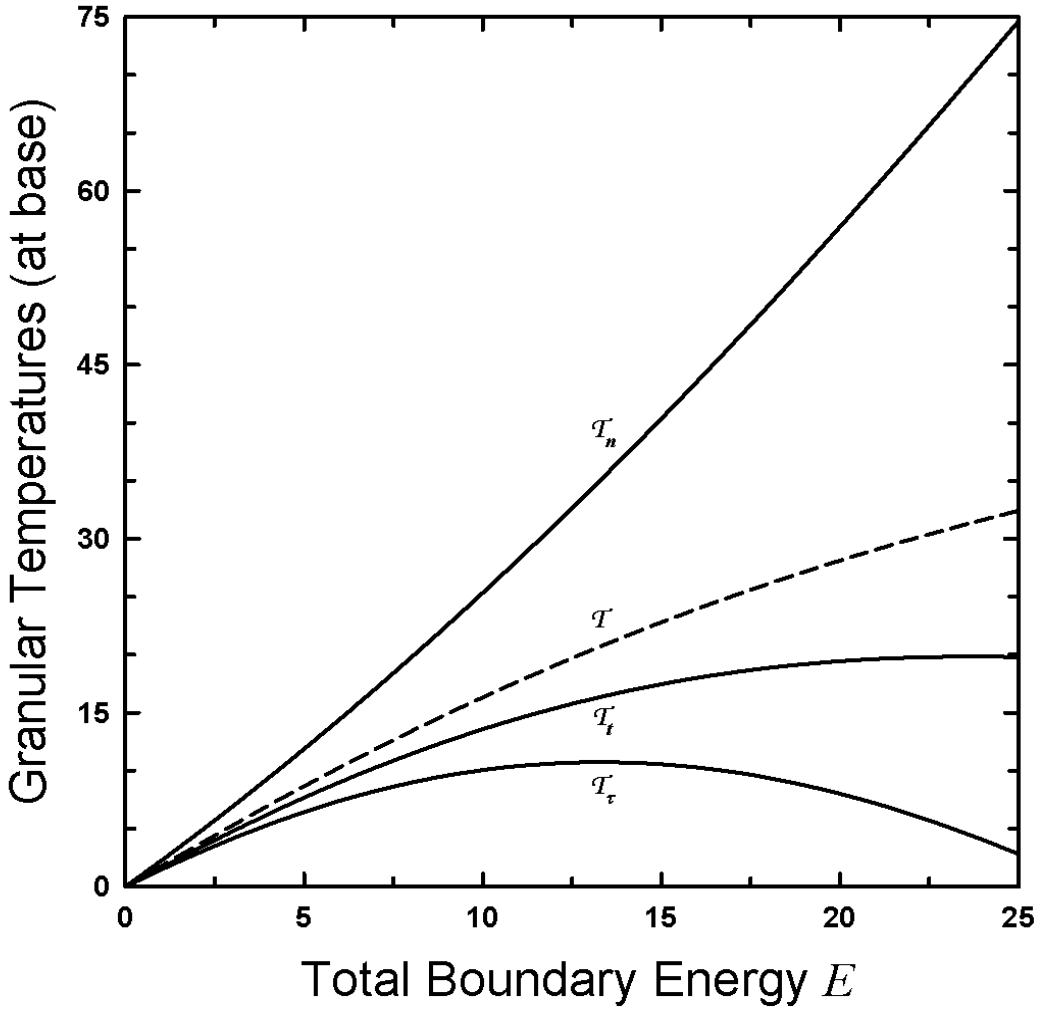

Figure 6.21: The variations of $\mathcal{T}$ (shown by dashed curve) and, $\mathcal{T}_n$, $\mathcal{T}_t$ and $\mathcal{T}_\tau$ (shown by solid curves), at z=0, with E, when θ=54.74°, ϕ=0 (V_n^2=1, V_t^2=2), m_t=5, e=e_w=.9, r=1, ξ_{nt} = $\xi_{n\tau}$ =90°, α =90° and Δ_t = Δ_α =.22.

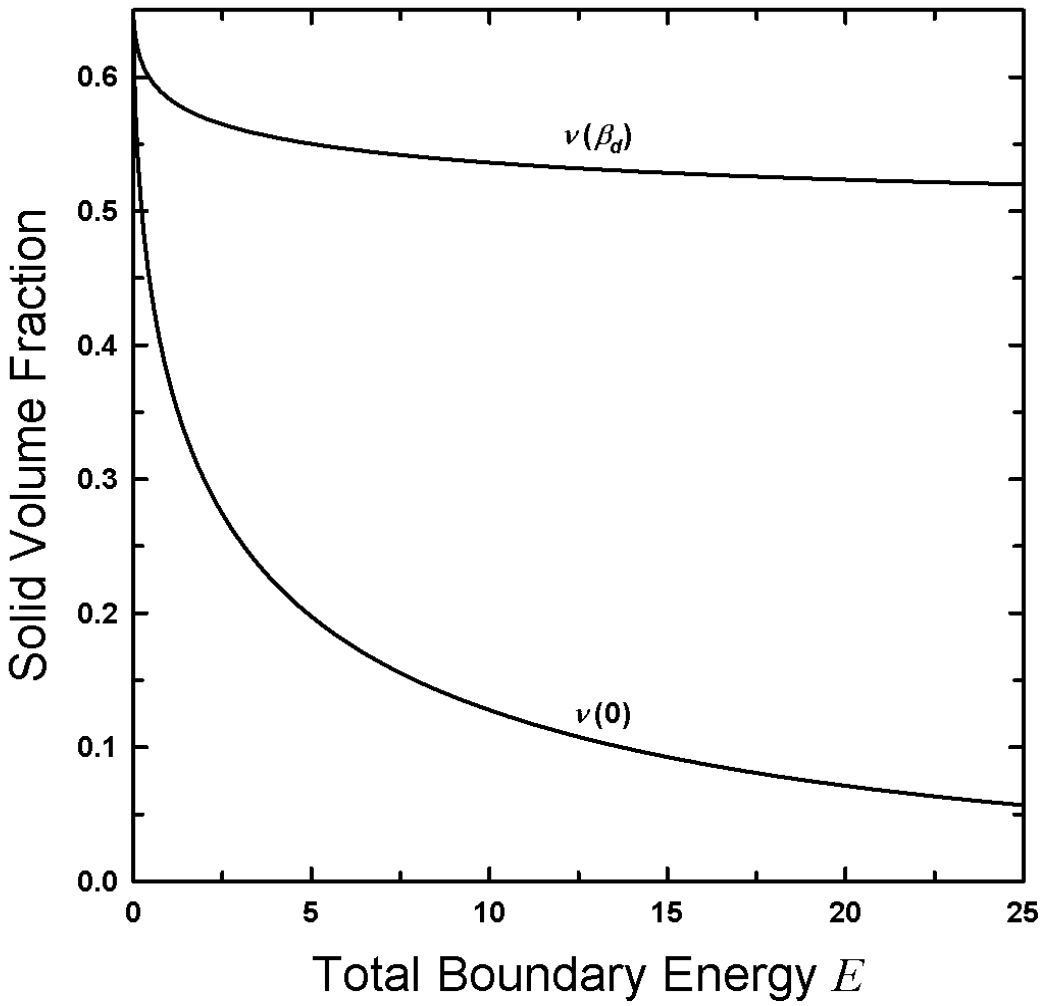

Figure 6.22: The variations of $\nu(\beta_d)$ and $\nu(0)$, with E, when θ=54.74°, ϕ=0 (V_n^2=1, V_t^2=2), m_t=5, e=e_w=.9, r=1, ξ_{nt} = $\xi_{n\tau}$ =90°, α =90° and Δ_t = Δ_α =.22.

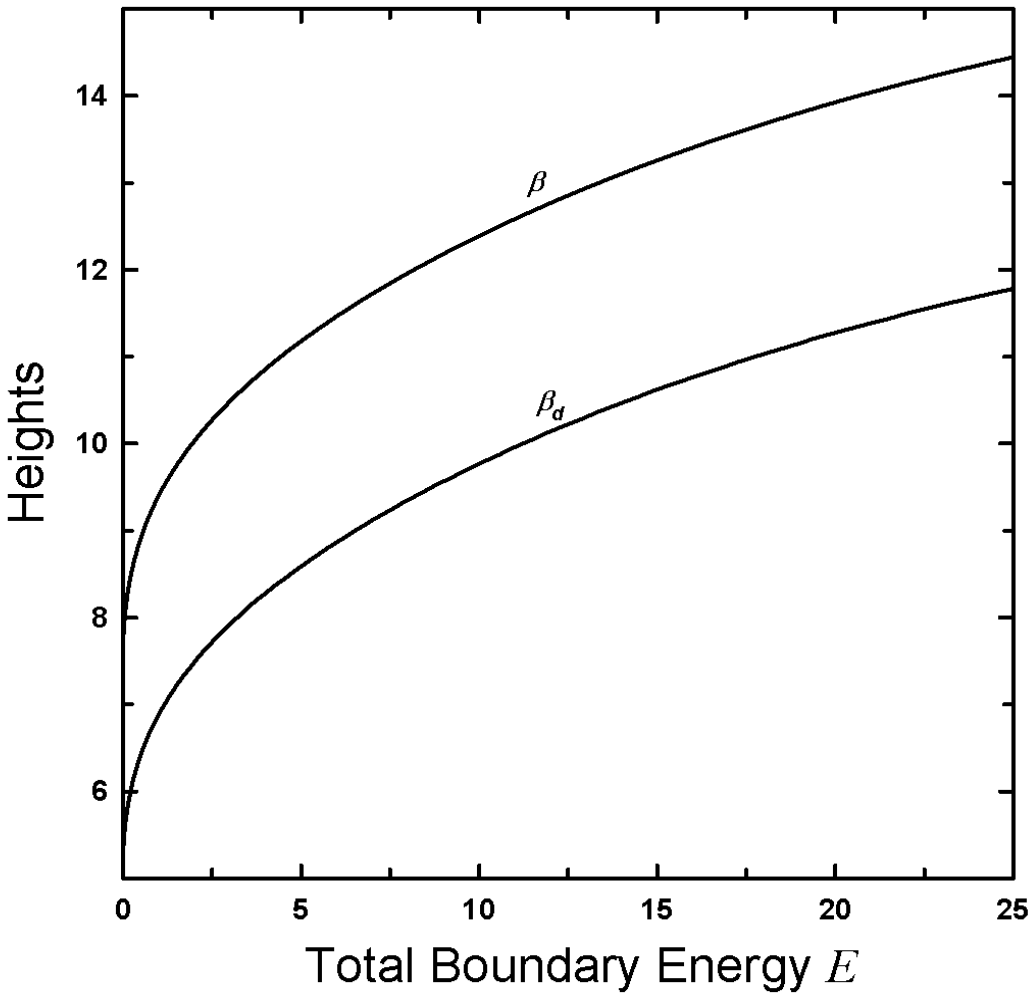

Figure 6.23: The variations of β and β_d with E, when θ=54.74°, ϕ=0 (V_n^2=1, V_t^2=2), m_t=5, e=e_w=.9, r=1, ξ_{nt} = $\xi_{n\tau}$ =90°, α =90° and Δ_t = Δ_α =.22.

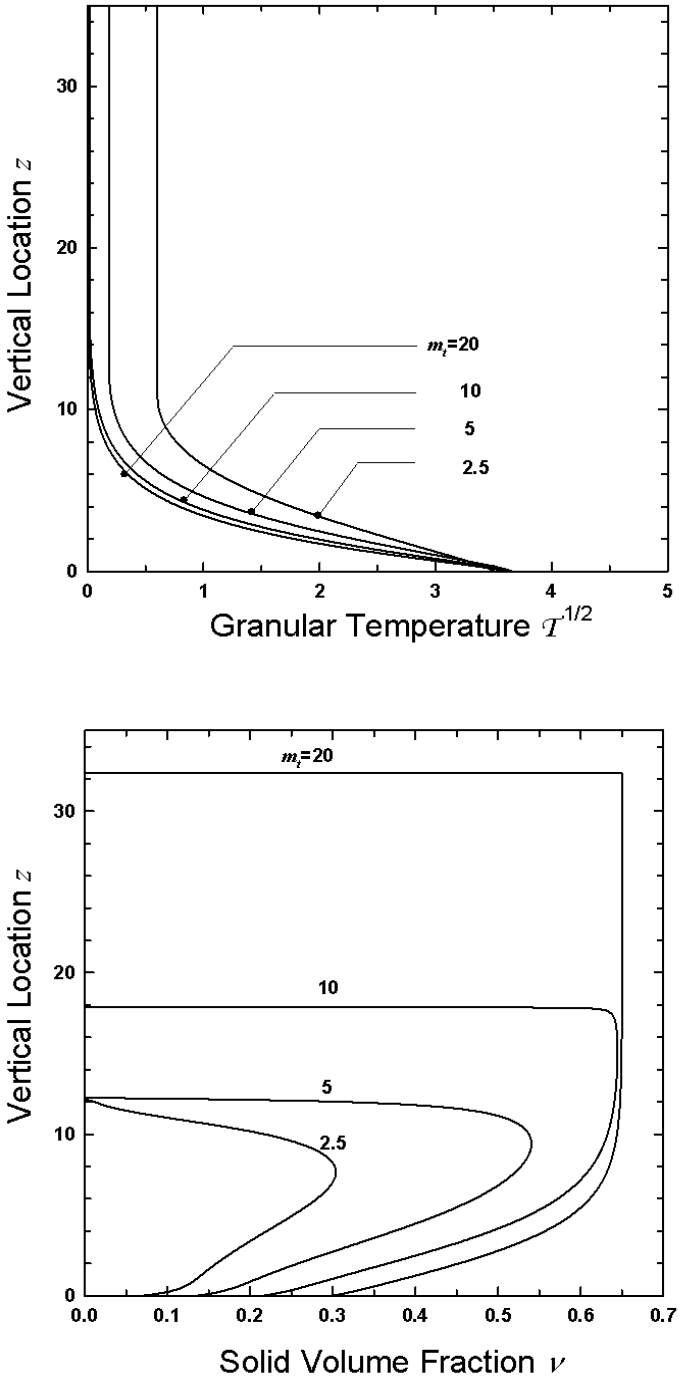

Figure 6.24: The variations of $\mathcal{T}^{1/2}(z)$ and $\nu(z)$ with z, for m_t=2.5, 5, 10 and 20, when θ=0 (V_n^2=3), e=e_w=.9, r=1, E=4, ξ_{nt} = $\xi_{n\tau}$ =90°, α =90° and Δ_t = Δ_α =.22.

$\xi_{nt} = \xi_{n\tau}$ =90°, α =90° and $\Delta_t = \Delta_\alpha$ =.22. For fixed amount of total boundary energy E, as m_t increases, the same amount of energy has to energize more mass. As a result, with increasing m_t, excitation of the assembly reduces. Particularly when m_t =20, the solid volume fraction profile shows that only the bottom portion of the assembly is excited and about top 3/4th of the assembly is experiencing no thermalization. Figures 6.25 and 6.26 show the details of anisotropic state of the assembly, i.e., the profiles of individual temperatures $\mathcal{T}_n^{1/2}(z)$ and $\mathcal{T}_t^{1/2}(z) = \mathcal{T}_\tau^{1/2}(z)$ when m_t =2.5, 5, 10 and 20, for above set of parameters. It can be seen that at least near the boundary, the individual temperatures differ from their mean value $\mathcal{T}$. The normal temperature $\mathcal{T}_n(z)$ is always larger than the tangential temperatures $\mathcal{T}_t(z) = \mathcal{T}_\tau(z)$. Also, profiles of tangential temperatures show *hooks* near the base.

Figures 6.27, 6.28, and 6.29 show the dependence of anisotropy and thermalized state on the mass hold-up m_t, for the same set of parameters as above. Figure 6.27 shows variation of temperature $\mathcal{T}$ and individual temperatures $\mathcal{T}_n$, $\mathcal{T}_t$ and $\mathcal{T}_\tau$, at the base $z = 0$, with m_t. As m_t increases, increasing portion of assembly near the top becomes stagnant and as a result $\mathcal{T}_n$ reduces. Because with increasing m_t, the solid volume fraction near the boundary also increases, number of collisions increase. So, with increasing m_t, $\mathcal{T}_t = \mathcal{T}_\tau$ increase. Figures 6.28 and 6.29 show the variations with m_t of flow heights, β and β_d, and solid volume fractions $\nu(0)$ and $\nu(\beta_d)$, for the above set of parameters. As m_t increases, the flow becomes more dense and hence $\nu(0)$ and $\nu(\beta_d)$ increase. Also, with increasing mass hold-up, the heights β and β_d increase.

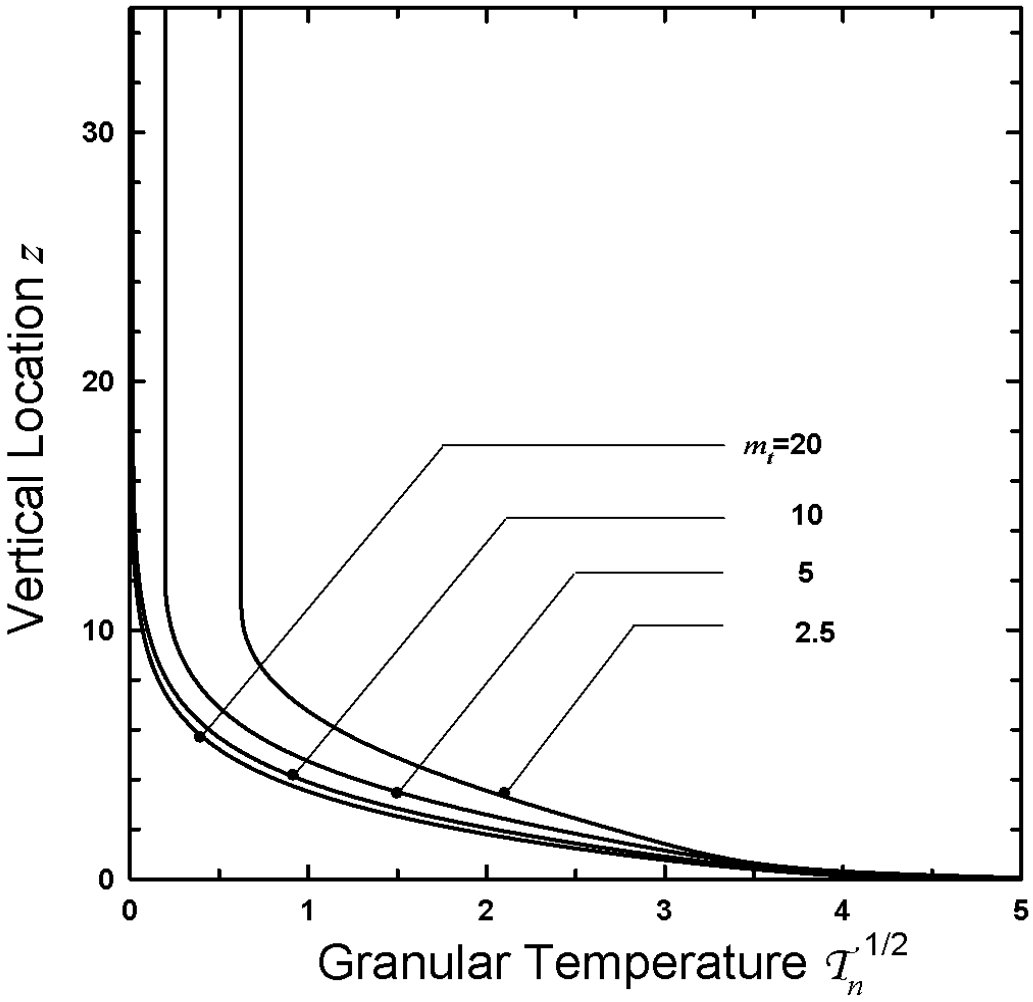

Figure 6.25: The variations of $\mathcal{T}_n^{1/2}(z)$ with z, for m_t=2.5, 5, 10 and 20, when θ=0 (V_n^2=3), e=e_w=.9, r=1, E=4, ξ_{nt} = $\xi_{n\tau}$ =90°, α =90° and Δ_t = Δ_α =.22.

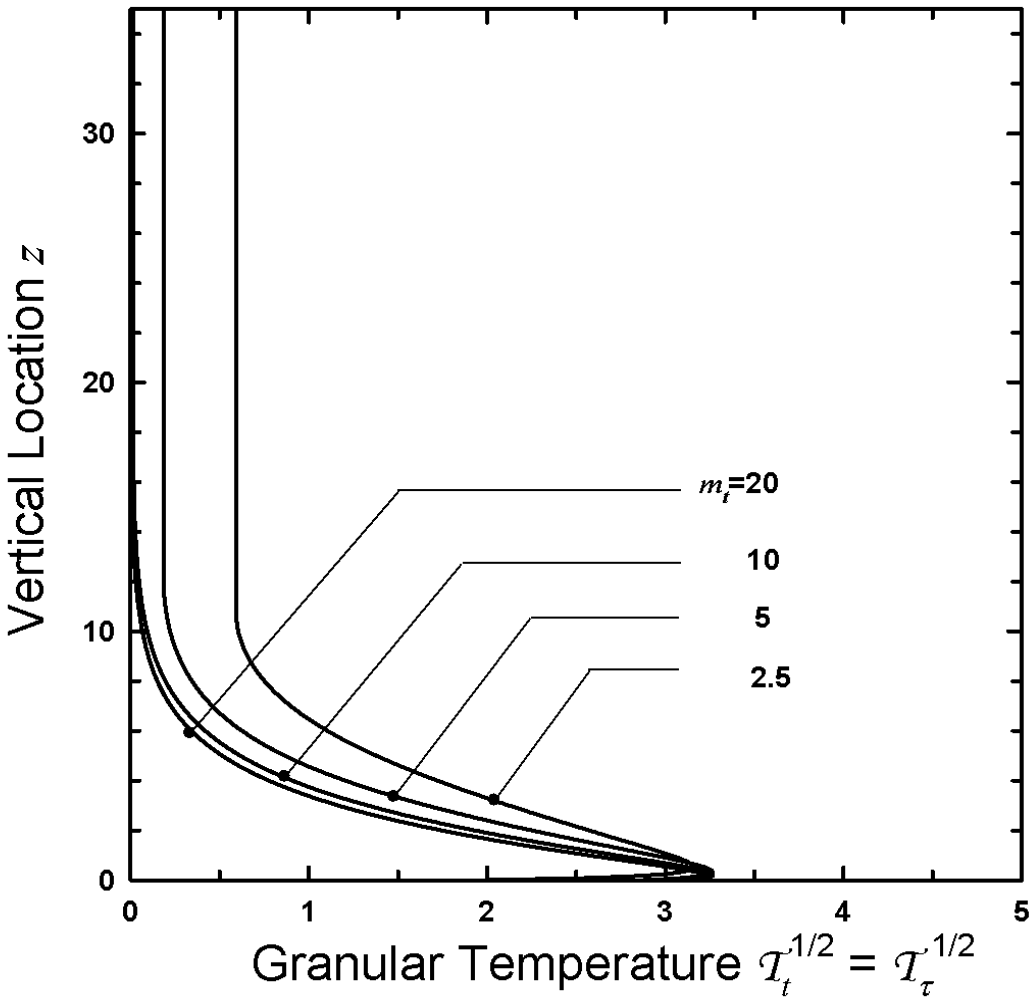

Figure 6.26: The variations of $\mathcal{T}_t^{1/2}(z) = \mathcal{T}_\tau^{1/2}(z)$ with z, for m_t=2.5, 5, 10 and 20, when θ=0 (V_n^2=3), e=e_w=.9, r=1, E=4, $\xi_{nt} = \xi_{n\tau}$ =90°, α =90° and $\Delta_t = \Delta_\alpha$ =.22.

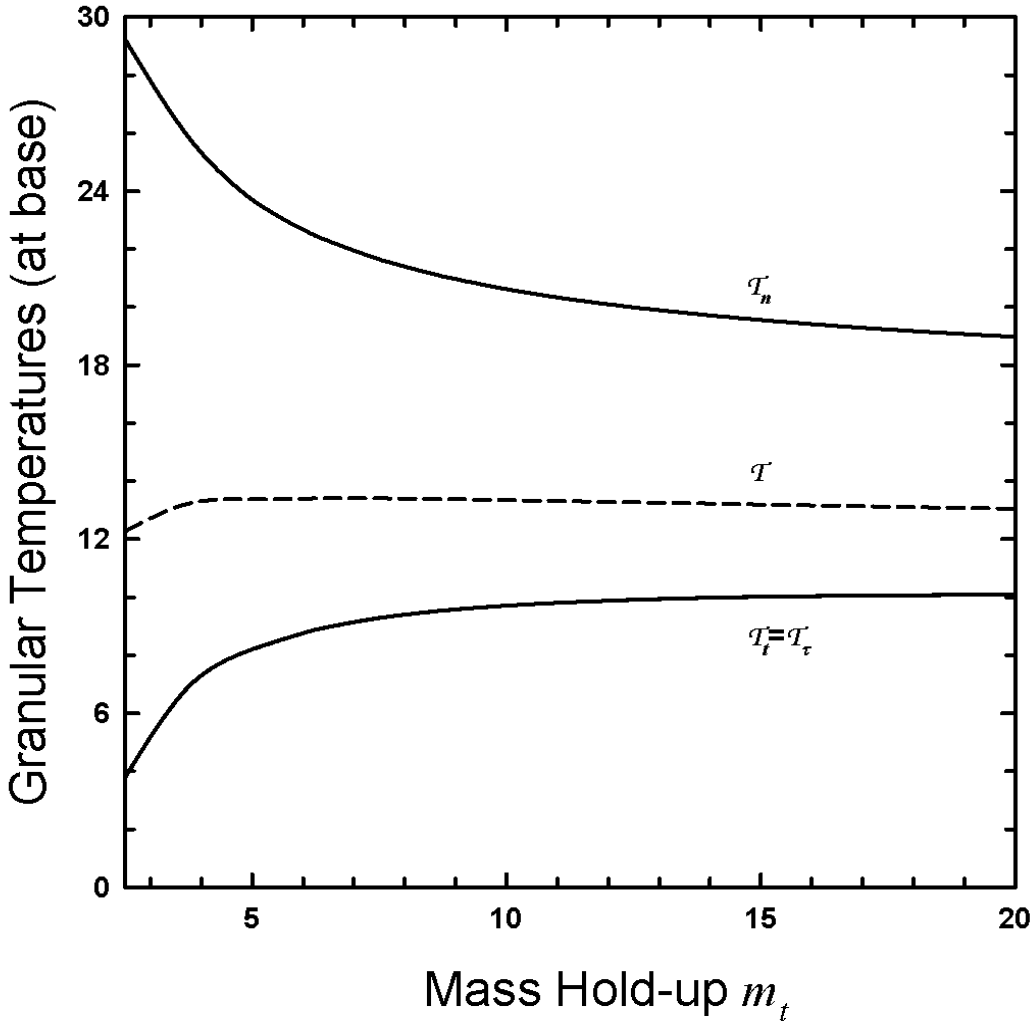

Figure 6.27: The variations of $\mathcal{T}$ (shown by dashed curve) and, $\mathcal{T}_n$, $\mathcal{T}_t$ and $\mathcal{T}_\tau$ (shown by solid curves), at z=0, with m_t, when θ=0 (V_n^2=3), e=e_w=.9, r=1, E=4, ξ_{nt} =$\xi_{n\tau}$ =90°, α =90° and Δ_t =Δ_α =.22.

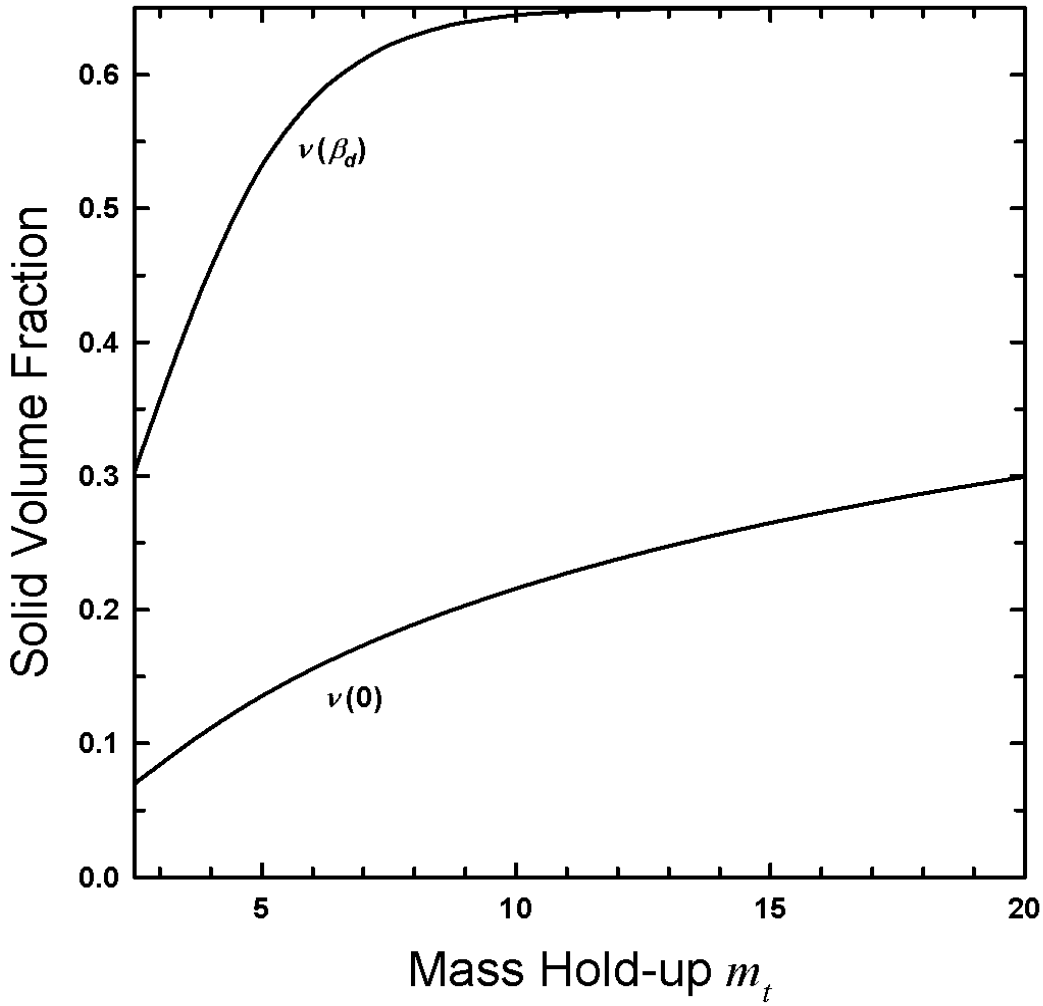

Figure 6.28: The variations of $\nu(\beta_d)$ and $\nu(0)$, with m_t, when θ=0 (V_n^2=3), e=e_w=.9, r=1, E=4, ξ_{nt} = $\xi_{n\tau}$ =90°, α =90° and Δ_t = Δ_α =.22.

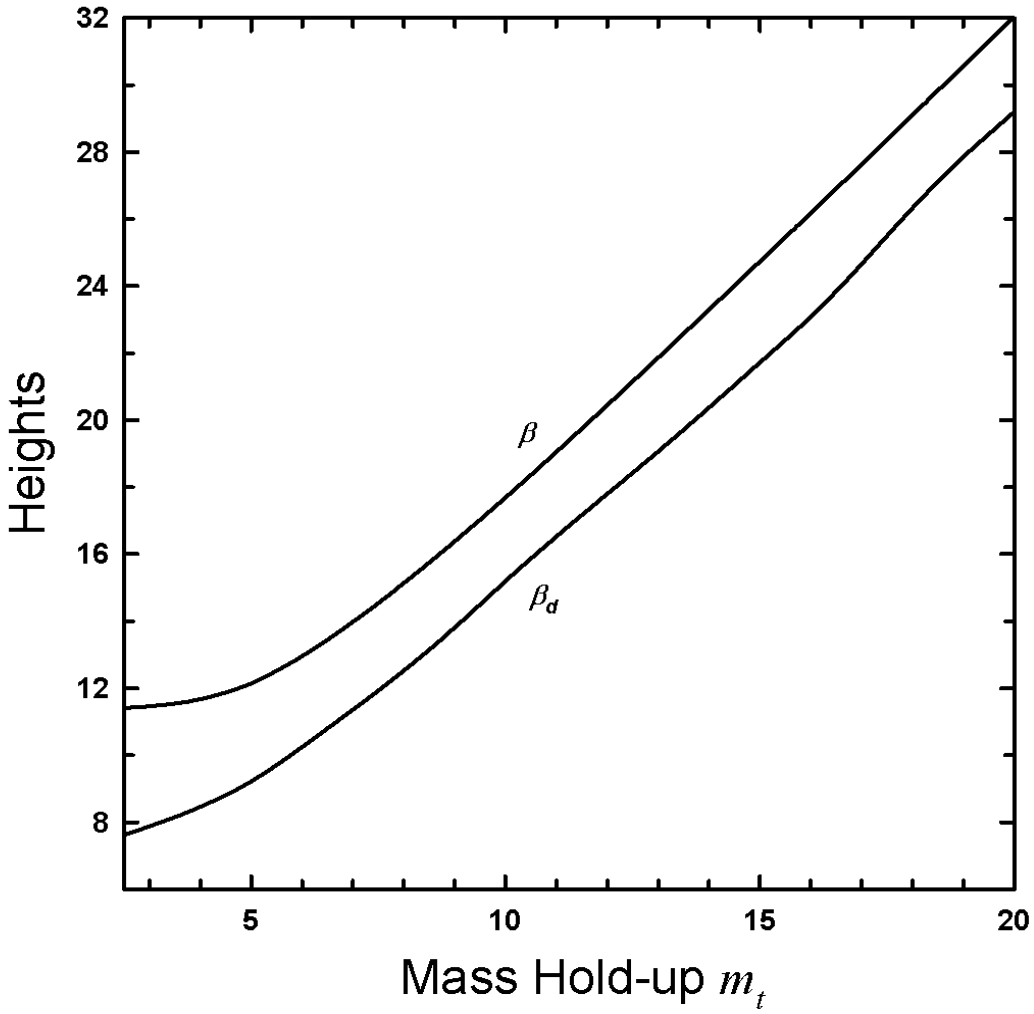

Figure 6.29: The variations of β and β_d with m_t, when θ=0 (V_n^2=3), e=e_w=.9, r=1, E=4, ξ_{nt} = $\xi_{n\tau}$ =90°, α =90° and Δ_t = Δ_α =.22.

In Figure 6.30, we show the profiles of granular temperature $\mathcal{T}^{1/2}(z)$ and solid volume fraction $\nu(z)$ for $e=e_w$=.9, .8, .7 and .6, when θ=0 (V_n^2=3), m_t=5, r=1, E=4, $\xi_{nt}=\xi_{n\tau}$=90°, α=90° and $\Delta_t=\Delta_\alpha$=.22. As the coefficients of restitution $e=e_w$ decrease from .9, the collisions become more inelastic and hence more energy is dissipated making the flows less thermalized, shallower and more dense. Figures 6.31, and 6.32 show the details of anisotropic state of the assembly, i.e., the profiles of individual temperatures $\mathcal{T}_n^{1/2}(z)$ and $\mathcal{T}_t^{1/2}(z)=\mathcal{T}_\tau^{1/2}(z)$ for $e=e_w$=.9, .8, .7 and .6, for above set of parameters. It can be seen that at least near the boundary, the individual temperatures differ from their mean value $\mathcal{T}$ and the assembly is far from isotropic. The normal temperature $\mathcal{T}_n(z)$ is always larger than the tangential temperatures $\mathcal{T}_t(z)=\mathcal{T}_\tau(z)$. Also, profiles of tangential temperatures show pronounced *hooks* near the base.

Figures 6.33, 6.34 and 6.35 show the dependence of anisotropy and thermalized state on the restitution coefficients $e=e_w$, for the same set of parameters as above. Figure 6.33 shows variation of temperature $\mathcal{T}$ and individual temperatures $\mathcal{T}_n$, $\mathcal{T}_t$ and $\mathcal{T}_\tau$, at the base $z=0$, with $e=e_w$. As $e=e_w$ increases, less energy is dissipated in collisions and all temperatures increase. Figures 6.34 and 6.35 show the variations with $e=e_w$ of flow heights, β and β_d, and solid volume fractions $\nu(0)$ and $\nu(\beta_d)$, for the above set of parameters. As $e=e_w$ increases, the assembly becomes more thermalized and hence $\nu(0)$ and $\nu(\beta_d)$ decrease. Also, with increasing $e=e_w$, the heights β and β_d increase.

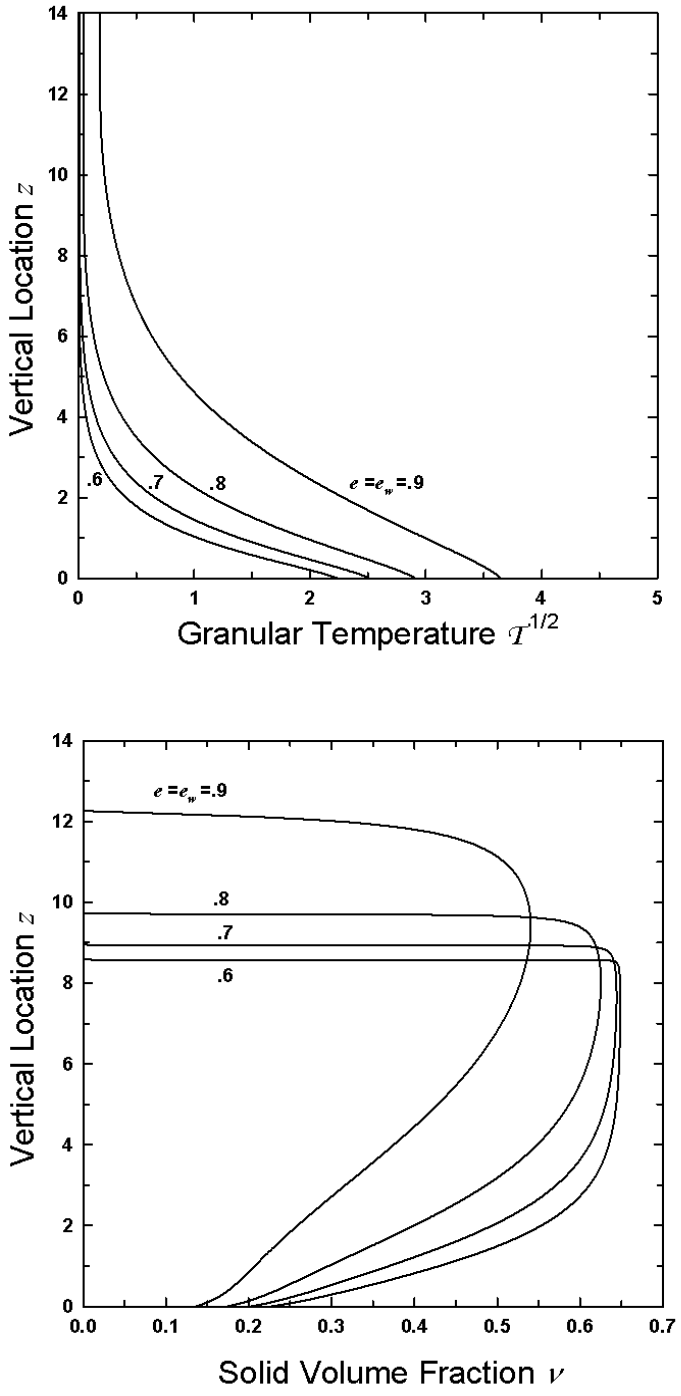

Figure 6.30: The variations of $\mathcal{T}^{1/2}(z)$ and $\nu(z)$ with z, for e=e_w=.6, .7, .8 and .9, when θ=0 (V_n^2=3), m_t=5, r=1, E=4, $\xi_{nt}=\xi_{n\tau}$=90°, α=90° and $\Delta_t=\Delta_\alpha$=.22.

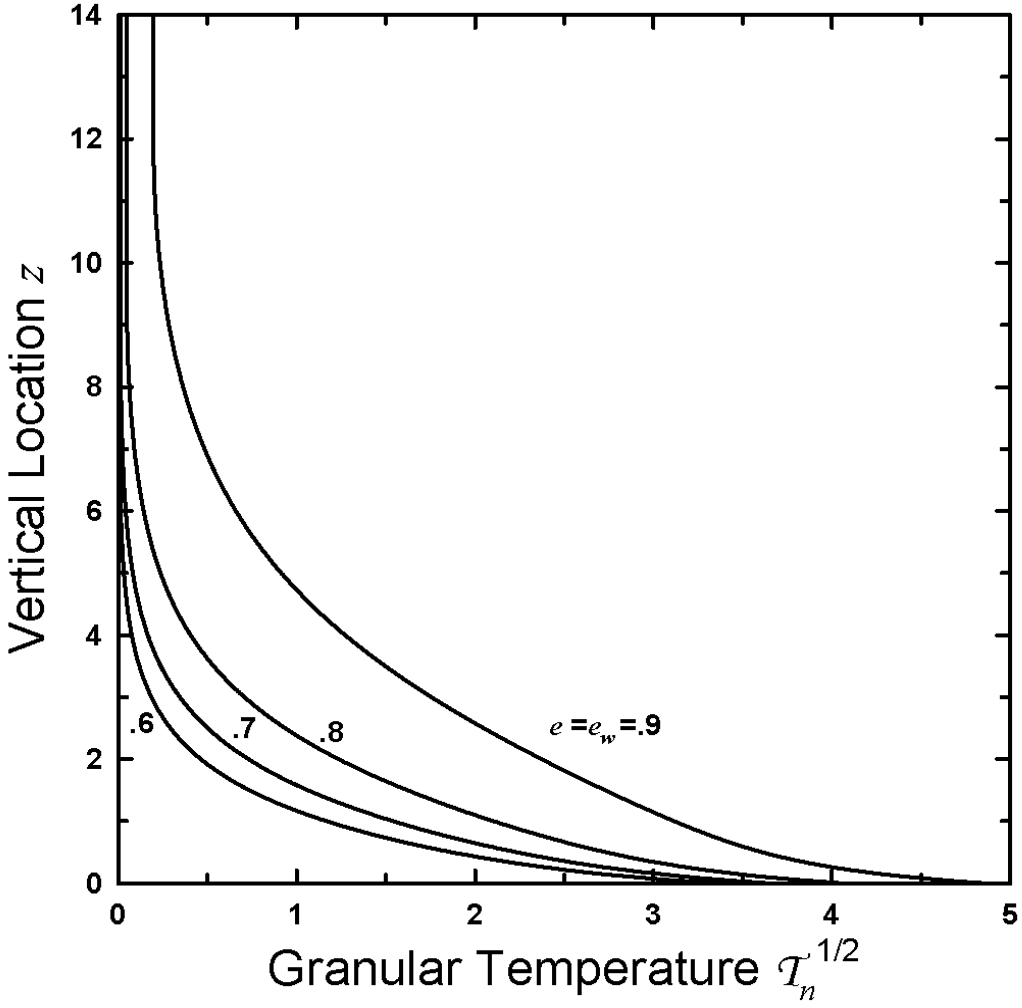

Figure 6.31: The variations of $\mathcal{T}_n^{1/2}(z)$ with z, for $e=e_w=.6$, .7, .8 and .9, when $\theta=0$ ($V_n^2=3$), $m_t=5$, $r=1$, $E=4$, $\xi_{nt}=\xi_{n\tau}=90°$, $\alpha=90°$ and $\Delta_t=\Delta_\alpha=.22$.

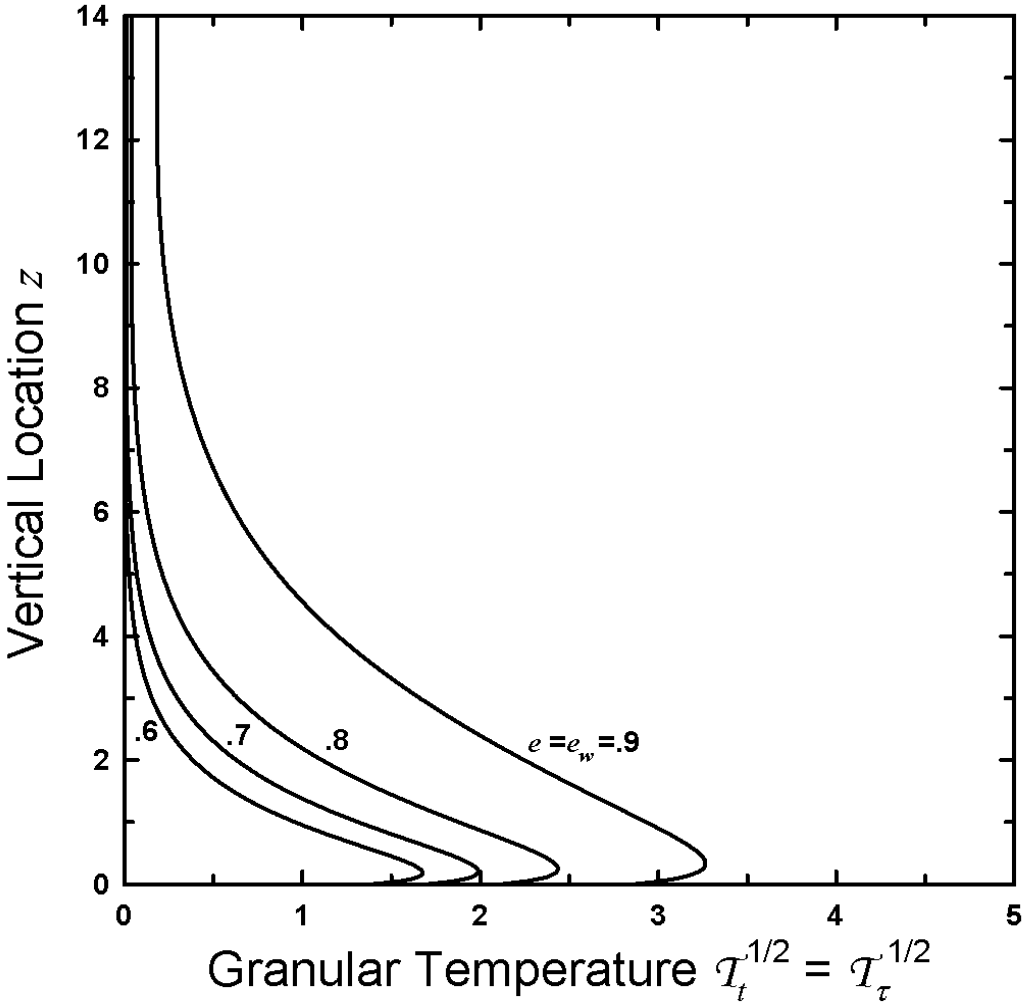

Figure 6.32: The variations of $\mathcal{T}_t^{1/2}(z) = \mathcal{T}_\tau^{1/2}(z)$ with z, for $e=e_w=.6$, .7, .8 and .9, when $\theta=0$ ($V_n^2=3$), $m_t=5$, $r=1$, $E=4$, $\xi_{nt} = \xi_{n\tau} = 90°$, $\alpha = 90°$ and $\Delta_t = \Delta_\alpha = .22$.

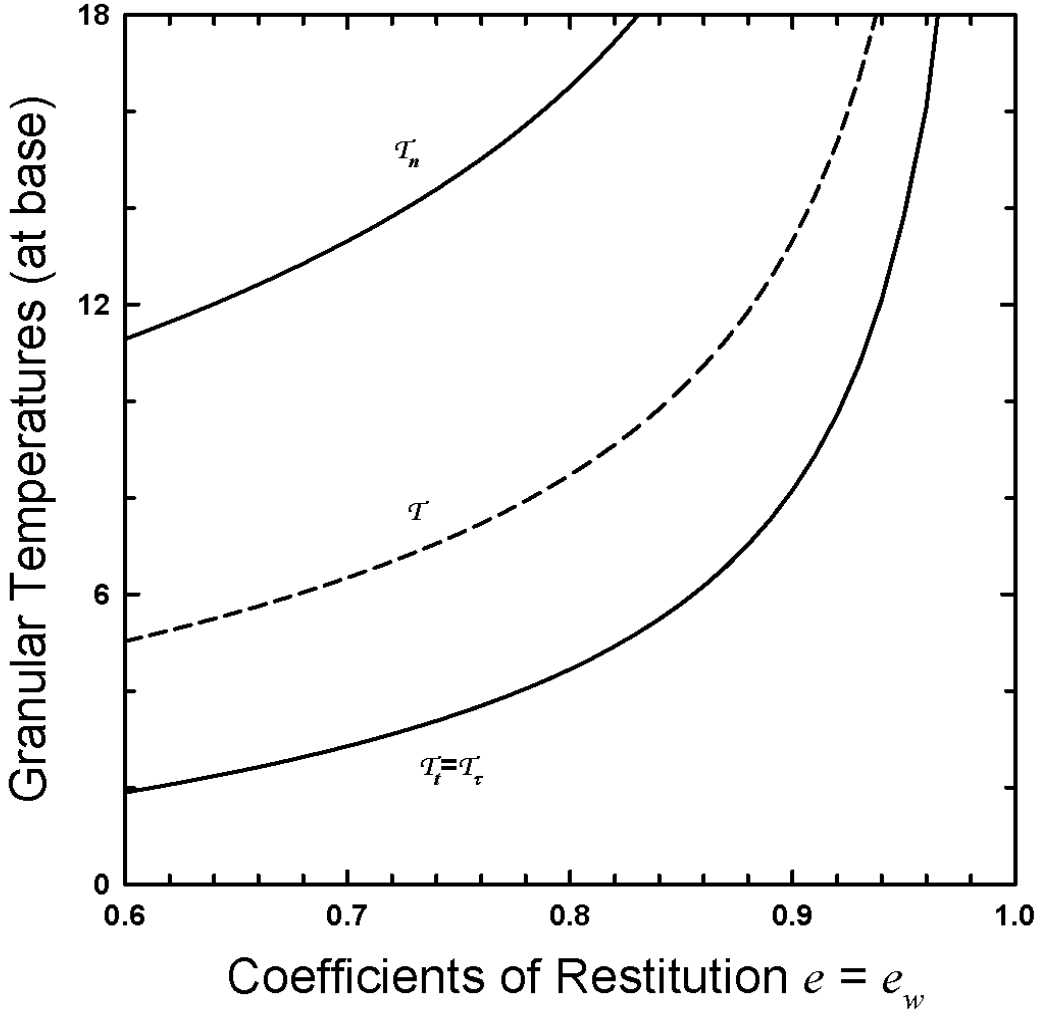

Figure 6.33: The variations of $\mathcal{T}$ (shown by dashed curve) and, $\mathcal{T}_n$, $\mathcal{T}_t$ and $\mathcal{T}_\tau$ (shown by solid curves), at z=0, with e=e_w, when θ=0 (V_n^2=3), m_t=5, r=1, E=4, ξ_{nt} =$\xi_{n\tau}$ =90°, α =90° and Δ_t =Δ_α =.22.

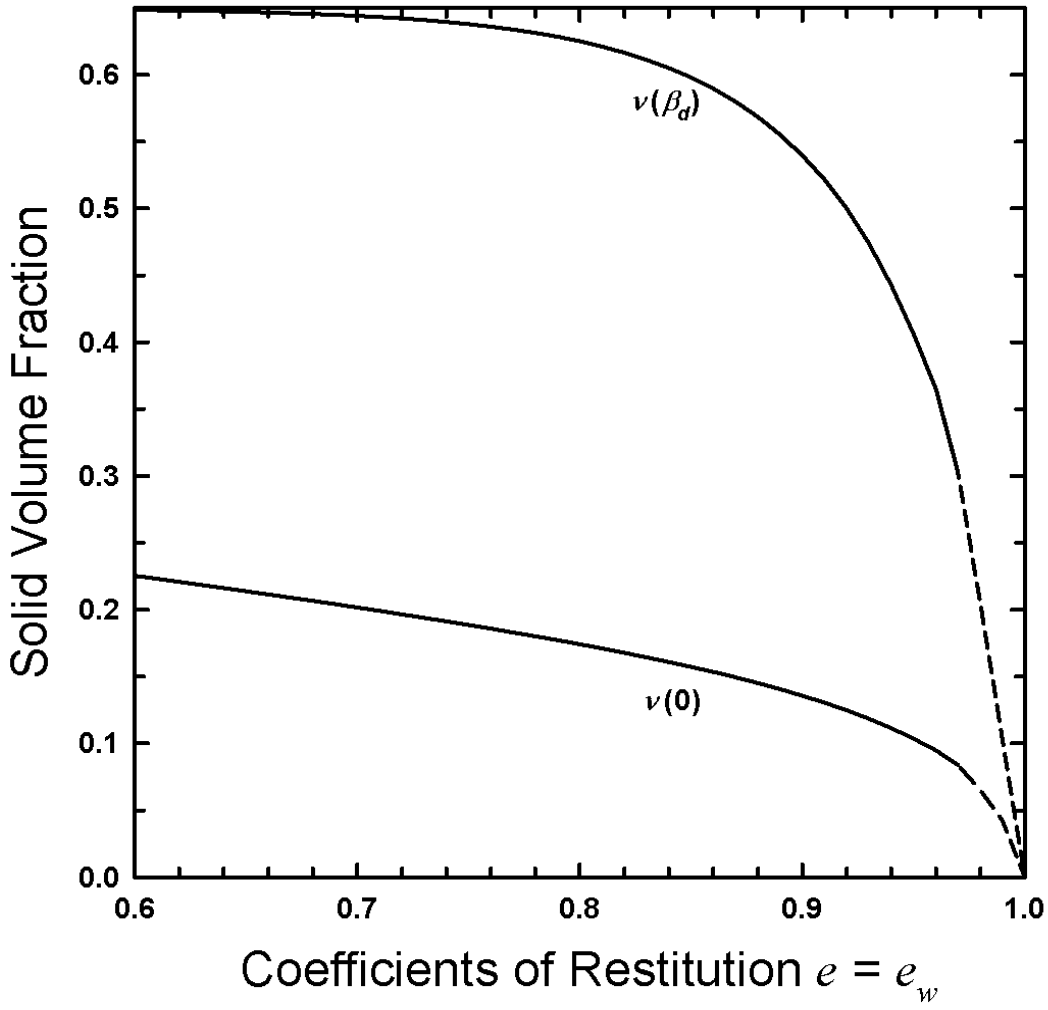

Figure 6.34: The variations of $\nu(\beta_d)$ and $\nu(0)$, with $e=e_w$, when $\theta=0$ ($V_n^2=3$), $m_t=5$, $r=1$, $E=4$, $\xi_{nt}=\xi_{n\tau}=90°$, $\alpha=90°$ and $\Delta_t=\Delta_\alpha=.22$.

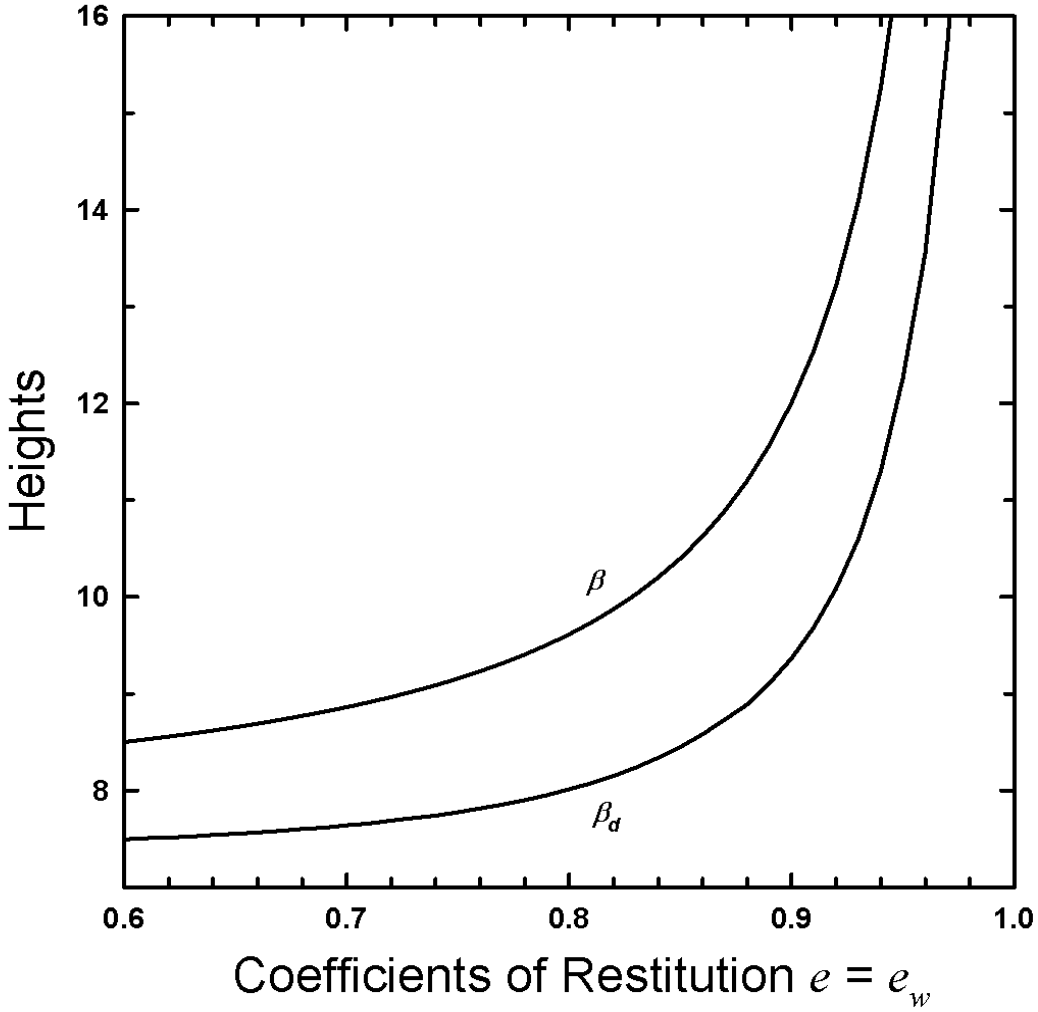

Figure 6.35: The variations of β and β_d with $e=e_w$, when $\theta=0$ ($V_n^2=3$), $m_t=5$, $r=1$, $E=4$, $\xi_{nt}=\xi_{n\tau}=90°$, $\alpha=90°$ and $\Delta_t=\Delta_\alpha=.22$.

6.2.3 Driven Assemblies

So far, we have seen results concerning non-driven assemblies with focus on thermalization. Now in the second part of this section, we look at driven flows. Here, unlike non-driven assemblies, at least one of the $\boldsymbol{t}-$ and $\boldsymbol{\tau}-$directional vibration is **not** 90° out of phase with respect to vibrations in $\boldsymbol{n}-$direction and hence, mean motion is induced. In this part of the section, our focus is going to be on the induced mean motion, i.e., the induced mean velocity and the mass flow rate per unit boundary area. We will show some profiles of mean velocity and then variations of its basal and top values and mass flow rate with the concerned parameter. Effects on thermalization, of most of the factors presented in this part, have already been studied in the previous part of this section. So, thermalization results for such cases will not be presented in this part.

In Figure 6.36, we show the profiles of induced velocity $u_t(z)$ for θ=15°, 30°, 45°, 60° and 75° (V_n^2=2.8, 2.25, 1.5, .75 and .2), when ϕ=0 ($V_\tau^2 = 0$), m_t=5, $e = e_w$=.9, r=1, E=4, ξ_{nt}=0, $\xi_{n\tau}$=90°, α=90° and $\Delta_t = \Delta_\alpha$=.22. We see that the induced velocity $u_t(z)$ is not uniform. It is maximum at the base and reduces for a short distance away from the boundary and is then practically constant. So, the induced mean motion can be concisely described by using two values, the value of u_t at the base, $u_t(0)$, which actually is the slip, and its value at the top, $u_t(h)$. Figure 6.37 shows the dependence of induced mean motion, i.e., the mass flow rate and $u_t(0)$ and $u_t(h)$, on θ, for the above set of parameters. When θ=0 the boundary vibrates only in $\boldsymbol{n}-$direction, and when θ=90° and ϕ=0 the boundary vibrates only in $\boldsymbol{t}-$direction. Hence, in these cases, no mean motion is induced. As θ increases from 0, mean motion is induced. With

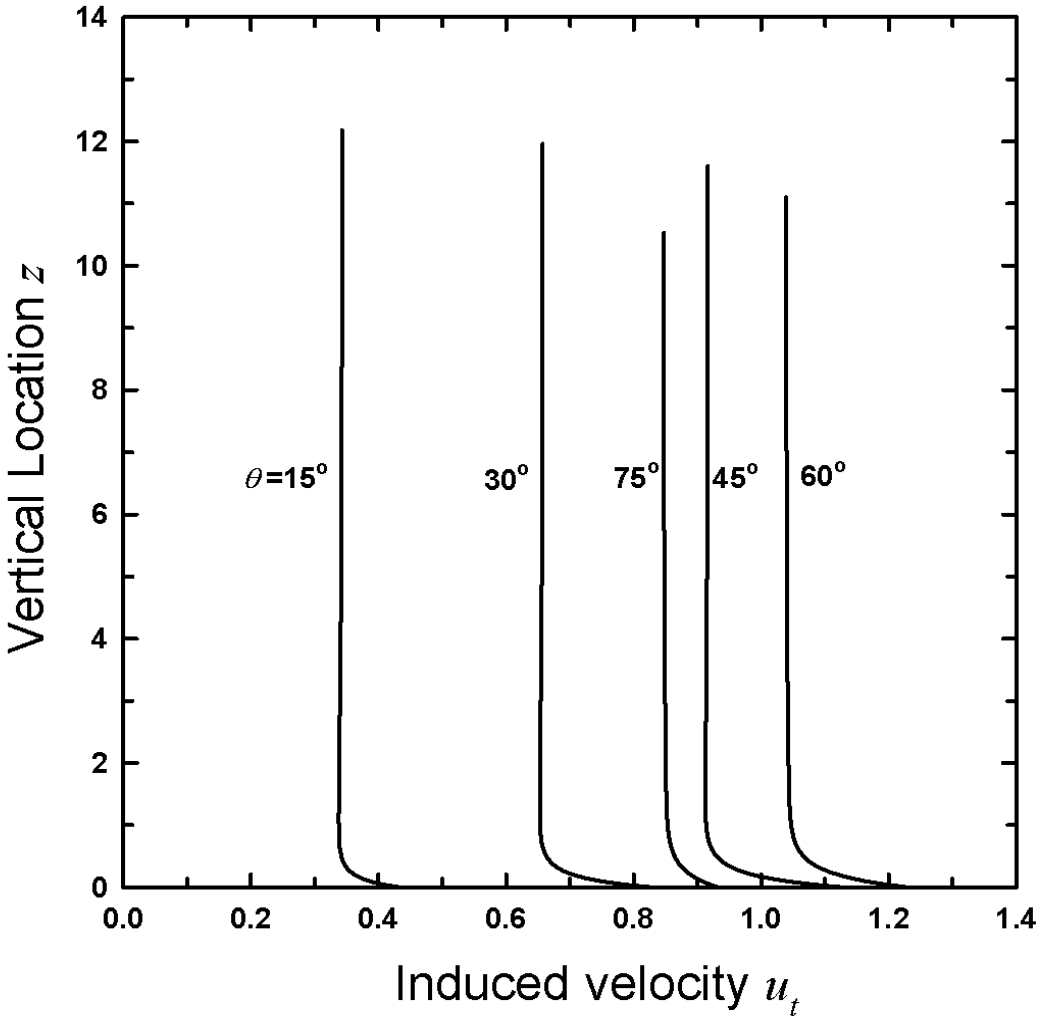

Figure 6.36: The variations of $u_t(z)$ with z, for θ=15°, 30°, 45°, 60° and 75° (V_n^2=2.8, 2.25, 1.5, .75 and .2), when ϕ=0 (V_τ^2=0), m_t=5, e=e_w=.9, r=1, E=4, ξ_{nt}=0, $\xi_{n\tau}$=90°, α=90° and $\Delta_t = \Delta_\alpha$=.22.

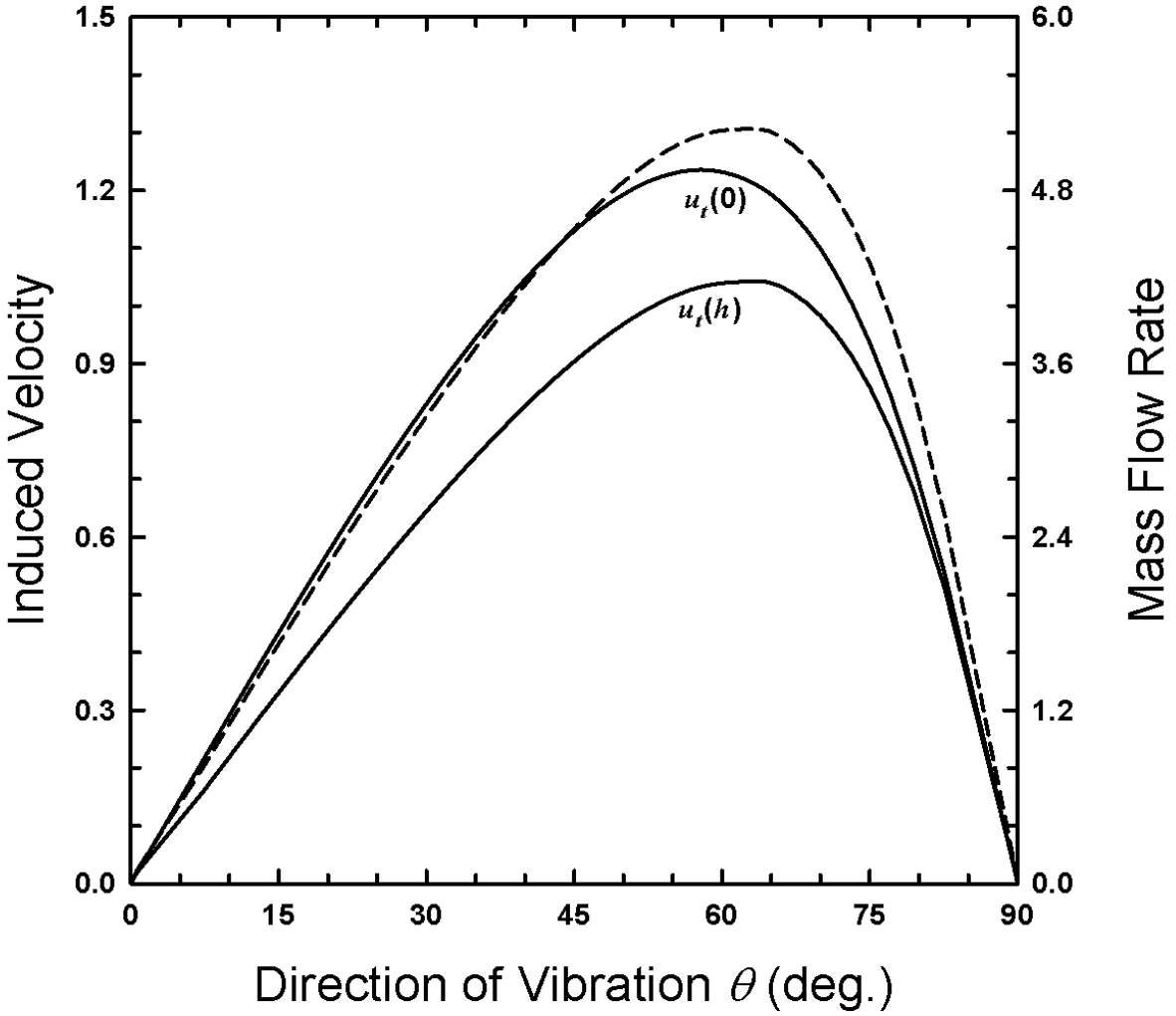

Figure 6.37: The variations of $u_t\,(0)$ and $u_t\,(h)$ (shown by solid curves) and mass flow rate (shown by dashed curve), with θ, when ϕ=0 (V_τ^2=0), m_t=5, e=e_w=.9, r=1, E=4, ξ_{nt} =0, $\xi_{n\tau}$ =90°, α =90° and Δ_t =Δ_α =.22.

increasing θ, first $u_t(0)$ and $u_t(h)$ increases, with the difference between them increasing as well. After reaching optimum values, both, $u_t(0)$ and $u_t(h)$, decrease to 0, when θ=90°. As a result, the mass flow rate initially increases from 0 as θ increases, reaches an optimum value at around θ=65° and then decreases to zero as θ=90°. So, there is an optimum value of θ, for which maximum mass flow rate is obtained. This angle depends on the set of parameters. Figure 6.38 explores the dependence of optimum value of θ on the array spacing Δ_t, when ϕ=0 ($V_\tau^2 = 0$), m_t=5, $e = e_w$=.9, r=1, E=4, ξ_{nt}=0, $\xi_{n\tau}$=90°, α=90° and Δ_α=.22. As Δ_t increases from -1 to its maximum value of .22, the optimum θ decreases significantly from almost 90° to 60°. This implies that as the boundary gets more bumpy, in order to achieve more mass flow rate, more $n-$component of vibration should be added.

Figure 6.39 shows the dependence of induced mean motion, i.e., the mass flow rate and $u_t(0)$ and $u_t(h)$, on the phase difference between vibrations in $\boldsymbol{n}-$ and $\boldsymbol{t}-$directions ξ_{nt}, when θ=60° (V_n^2=2.25), ϕ=0 ($V_\tau^2 = 0$), m_t=5, $e = e_w$=.9, r=1, E=4, $\xi_{n\tau}$=90°, α=90° and $\Delta_t = \Delta_\alpha$=.22. When ξ_{nt}=0, the vibrations in $\boldsymbol{n}-$ and $\boldsymbol{t}-$directions are in phase and we get maximum $u_t(0)$ and $u_t(h)$. As ξ_{nt} increases from 0, the vibrations go more and more out of phase and the induced velocity decreases down to zero when ξ_{nt}=90°. As a result, maximum mass flow rate is obtained when ξ_{nt}=0 and mass flow rate decreases to 0 as ξ_{nt} increases to 90°. Here, we also show the details of thermalization of the flow. Figure 6.40 shows variation of temperature $\mathcal{T}$ and individual temperatures $\mathcal{T}_n$, $\mathcal{T}_t$ and $\mathcal{T}_\tau$, at the base $z = 0$, with ξ_{nt}, for the above set of parameters.

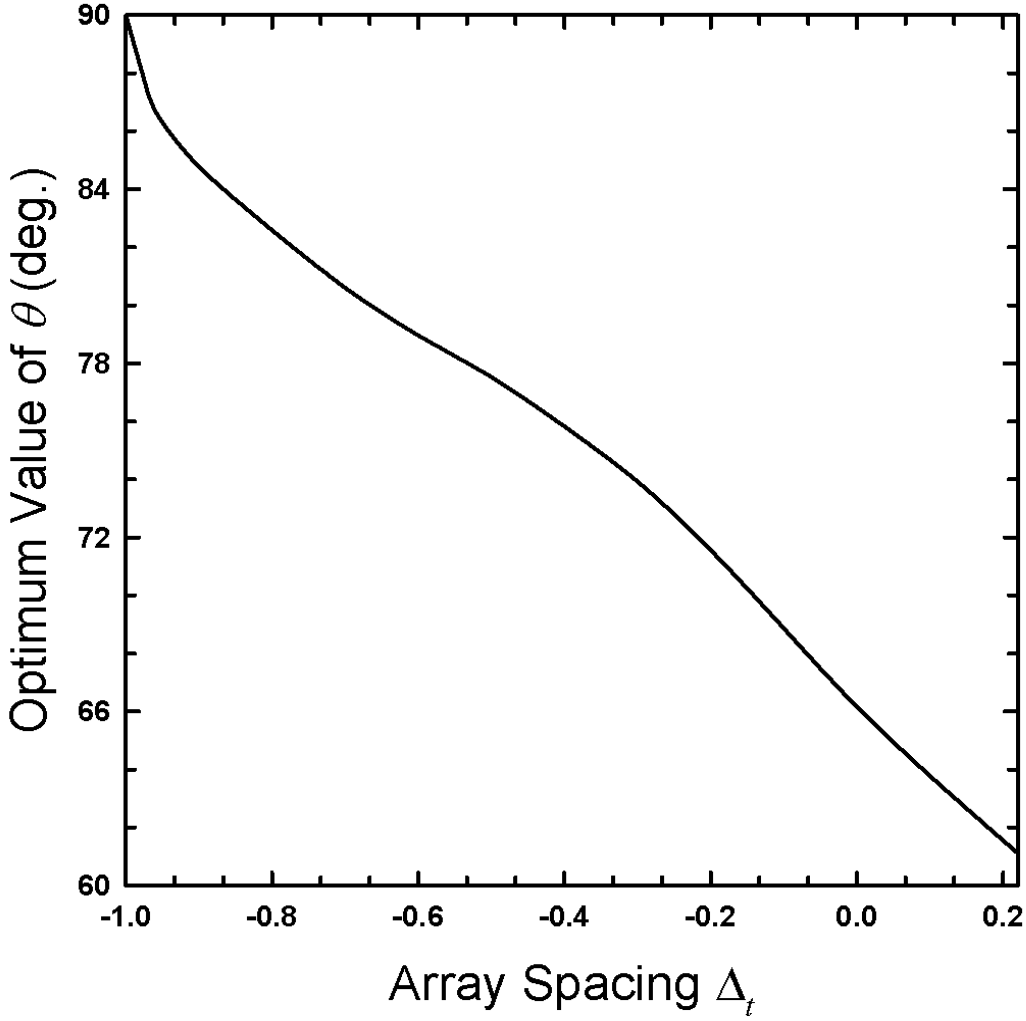

Figure 6.38: The variations of optimum value of θ with Δ_t, when ϕ=0 (V_τ^2=0), m_t=5, e=e_w=.9, r=1, E=4, ξ_{nt} =0, $\xi_{n\tau}$ =90°, α =90° and Δ_α =.22.

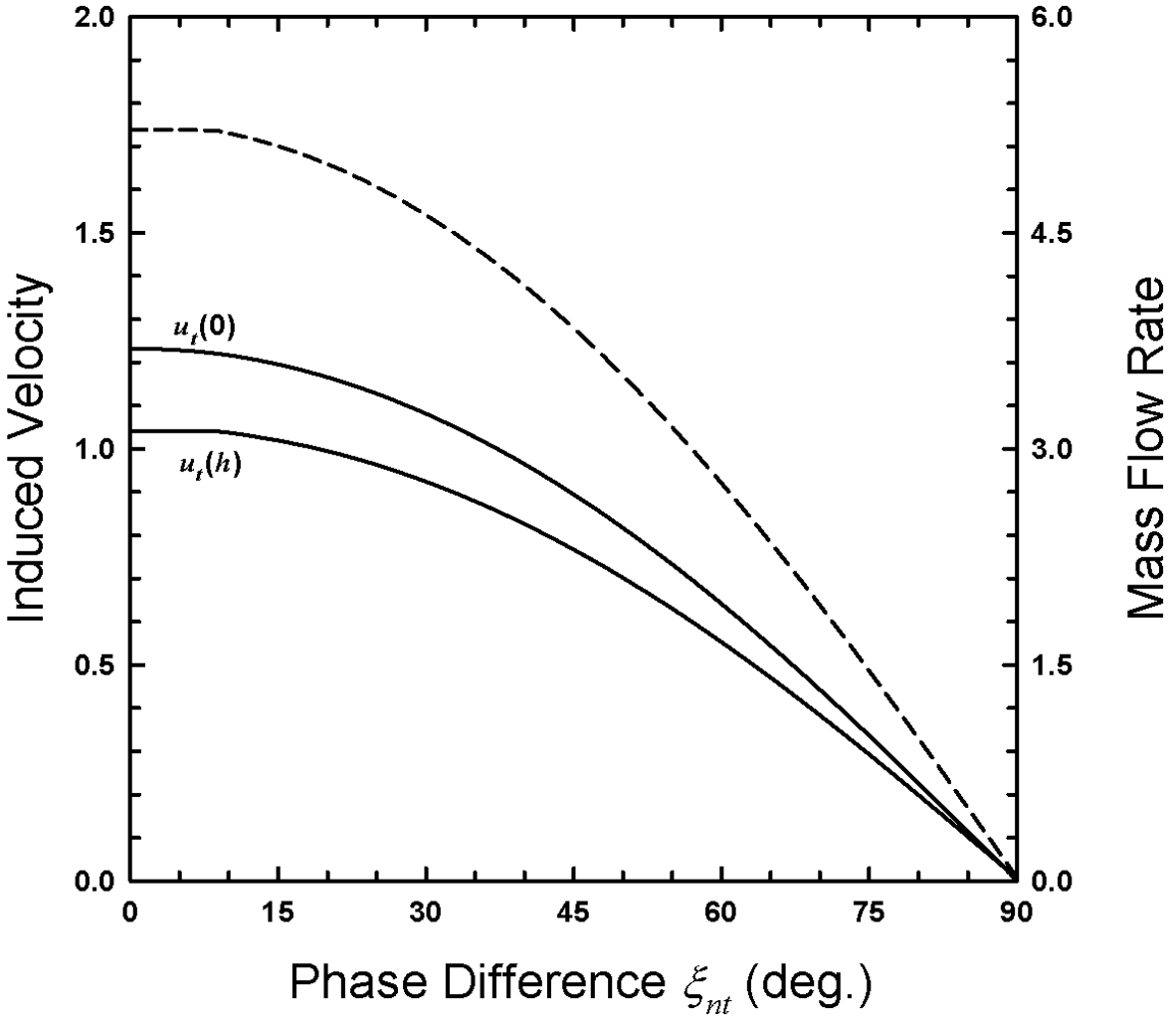

Figure 6.39: The variations of $u_t(0)$ and $u_t(h)$ (shown by solid curves) and mass flow rate (shown by dashed curve), with ξ_{nt}, when θ=60°, ϕ=0 (V_n^2=.75, V_t^2=2.25), m_t=5, e=e_w=.9, r=1, E=4, $\xi_{n\tau}$=90°, α=90° and $\Delta_t = \Delta_\alpha$=.22.

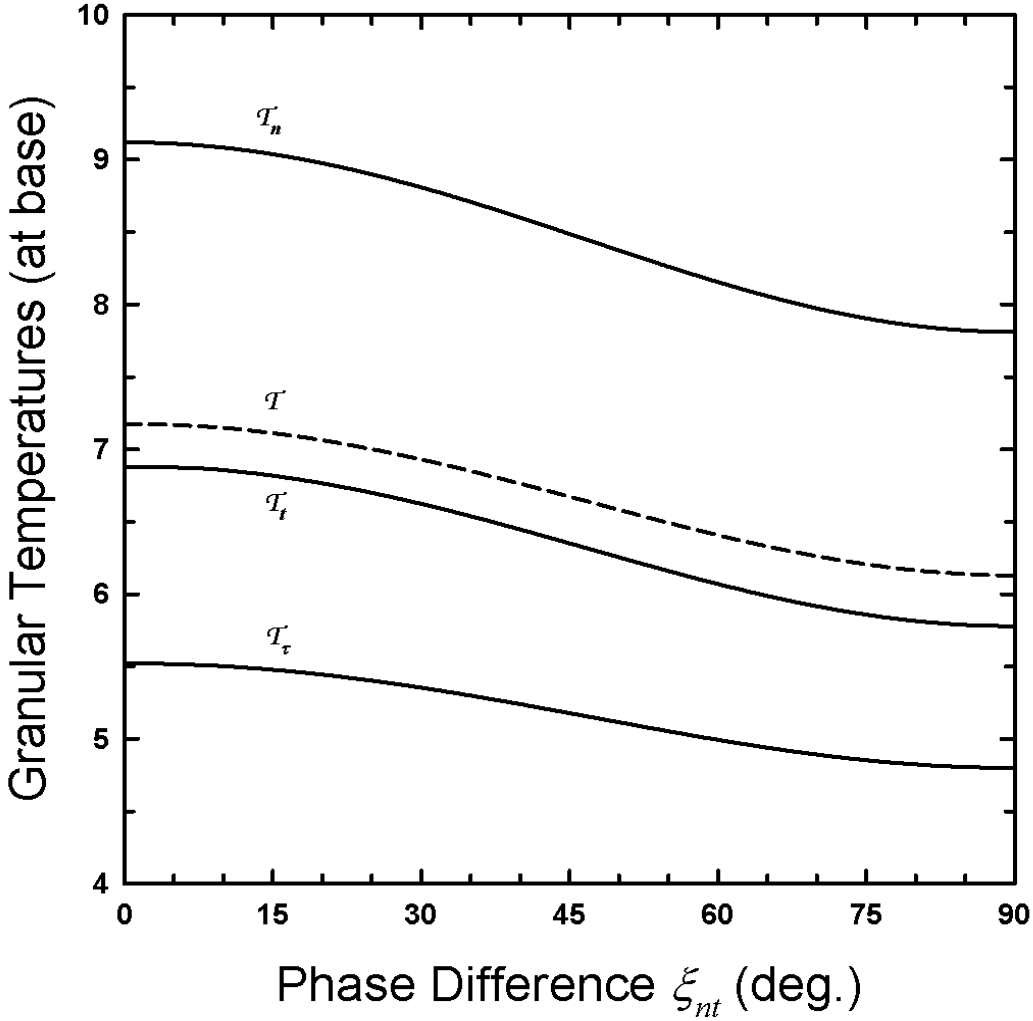

Figure 6.40: The variations of $\mathcal{T}$ (shown by dashed curve) and, $\mathcal{T}_n$, $\mathcal{T}_t$ and $\mathcal{T}_\tau$ (shown by solid curves), at z =0, with ξ_{nt}, when θ=60°, ϕ=0 (V_n^2=.75, V_t^2=2.25), m_t=5, e=e_w=.9, r=1, E=4, $\xi_{n\tau}$ =90°, α =90° and Δ_t = Δ_α =.22.

When ξ_{nt}=0, the vibrations in $\boldsymbol{n}-$ and $\boldsymbol{t}-$directions are in phase and hence all the temperatures are at their maximums. As ξ_{nt} increases from 0, the vibrations go out of phase, which decreases the temperatures. However, the decrease is not substantial. As a result, the flow heights, β and β_d, and solid volume fractions, $\nu(0)$ and $\nu(\beta_d)$ also change slightly. In this case, with increasing ξ_{nt}, β decreases from 10.88 to 10.67 while β_d decreases from 8.30 to 8.10, whereas $\nu(0)$ increases from .22 to .24 and $\nu(\beta_d)$ increases from .55 to .56.

Next, we look at the effect of bumpiness of the boundary which is controlled by array spacing and array angle. Figure 6.41 shows the effect of changing array spacing Δ_α on the induced mean motion when, Δ_t=.22, α=90°, θ=54.74° (V_n^2=1), ϕ=90° ($V_t^2=0$), m_t=5, $e=e_w$=.9, r=1, E=4, ξ_{nt}=90° and $\xi_{n\tau}$=0. As the array spacing Δ_α decreases from its maximum value .22 to -1 where the boundary essentially has humps parallel to $\boldsymbol{\tau}-$direction, the induced slip velocity $u_\tau(0)$ and $u_\tau(h)$, and hence the mass flow rate decrease towards zero. Figures 6.42 and 6.43 show the effect of changing array angle α on the induced mean motion when, $\Delta_t=\Delta_\alpha$=.22, θ=54.74° (V_n^2=1), ϕ=90° ($V_t^2=0$), m_t=5, $e=e_w$=.9, r=1, E=4, ξ_{nt}=90° and $\xi_{n\tau}$=0. Figure 6.42 shows that as α decreases from 90° to 0, because the boundary is becoming more hump-like, $u_\tau(0)$ and $u_\tau(h)$, and hence the mass flow rate in $\boldsymbol{\tau}-$direction decrease towards zero. Figure 6.43 shows that as α decreases from 90° to 0, small amount of mean motion is also induced in $\boldsymbol{t}-$direction. Particularly when α=0, 60° and 90°, the array is symmetric and in those cases, no mean motion is induced in $\boldsymbol{t}-$direction.

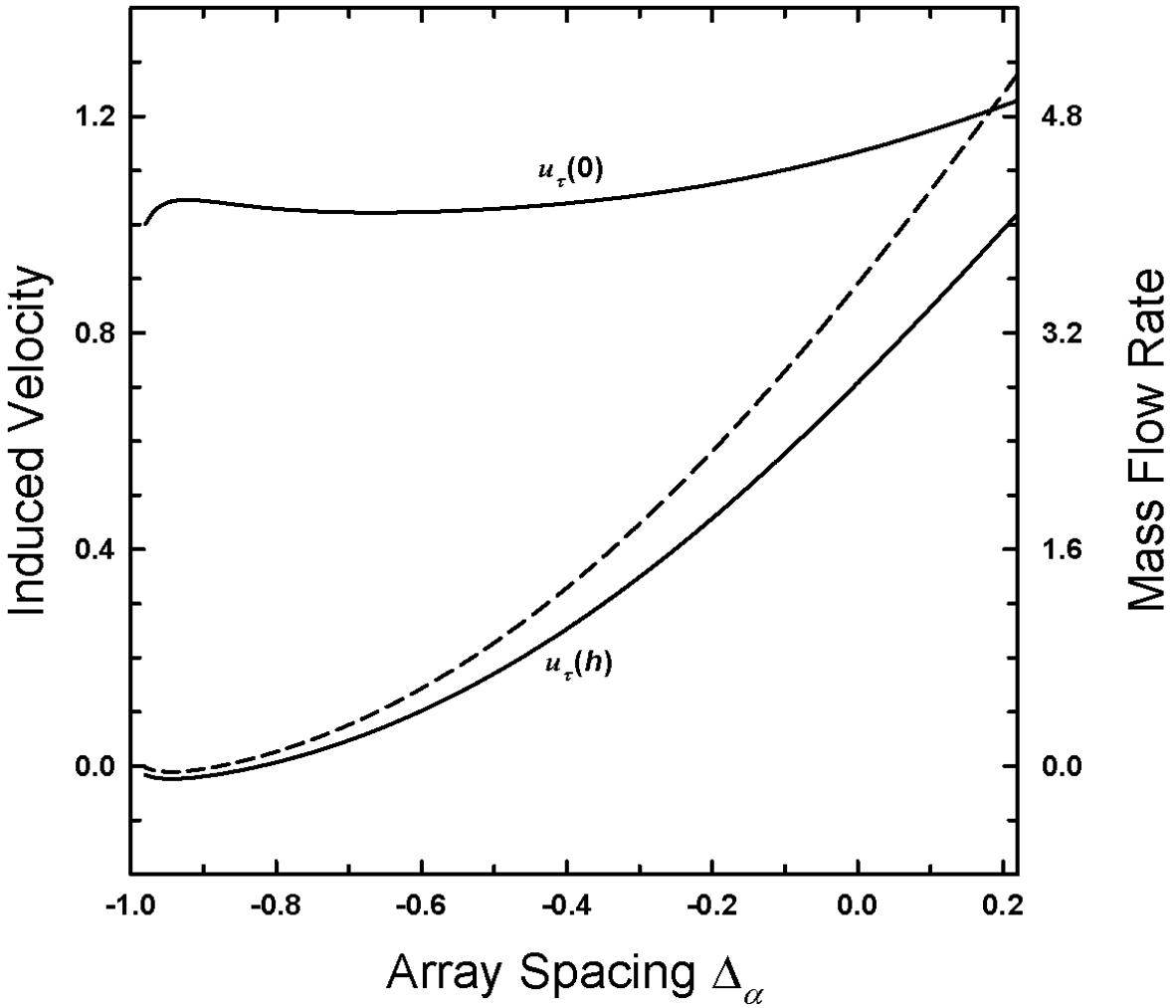

Figure 6.41: The variations of $u_\tau(0)$ and $u_\tau(h)$ (shown by solid curves) and mass flow rate (shown by dashed curve), with Δ_α, when θ=54.74°, ϕ=90° (V_n^2=1, V_τ^2=2), m_t=5, e=e_w=.9, r=1, E=4, ξ_{nt}=90°, $\xi_{n\tau}$=0, α=90° and Δ_t=.22.

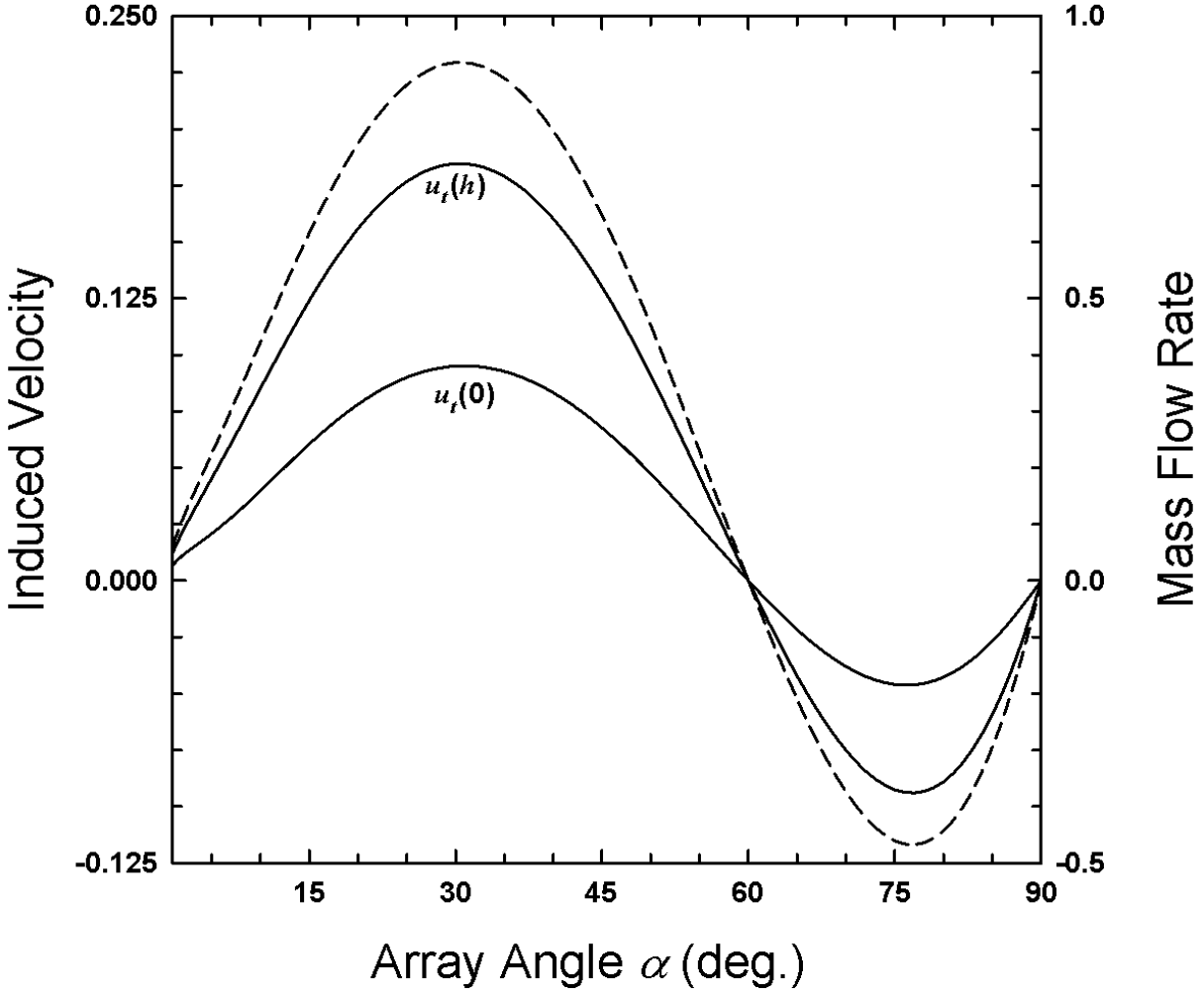

Figure 6.42: The variations of $u_t(0)$, $u_t(h)$ (shown by solid curves) and mass flow rate (shown by dashed curve), with α, when θ=54.74°, ϕ==90° (V_n^2=1, V_τ^2=2), m_t=5, e=e_w=.9, r=1, E=4, ξ_{nt} =90°, $\xi_{n\tau}$ =0 and Δ_t =Δ_α =.22.

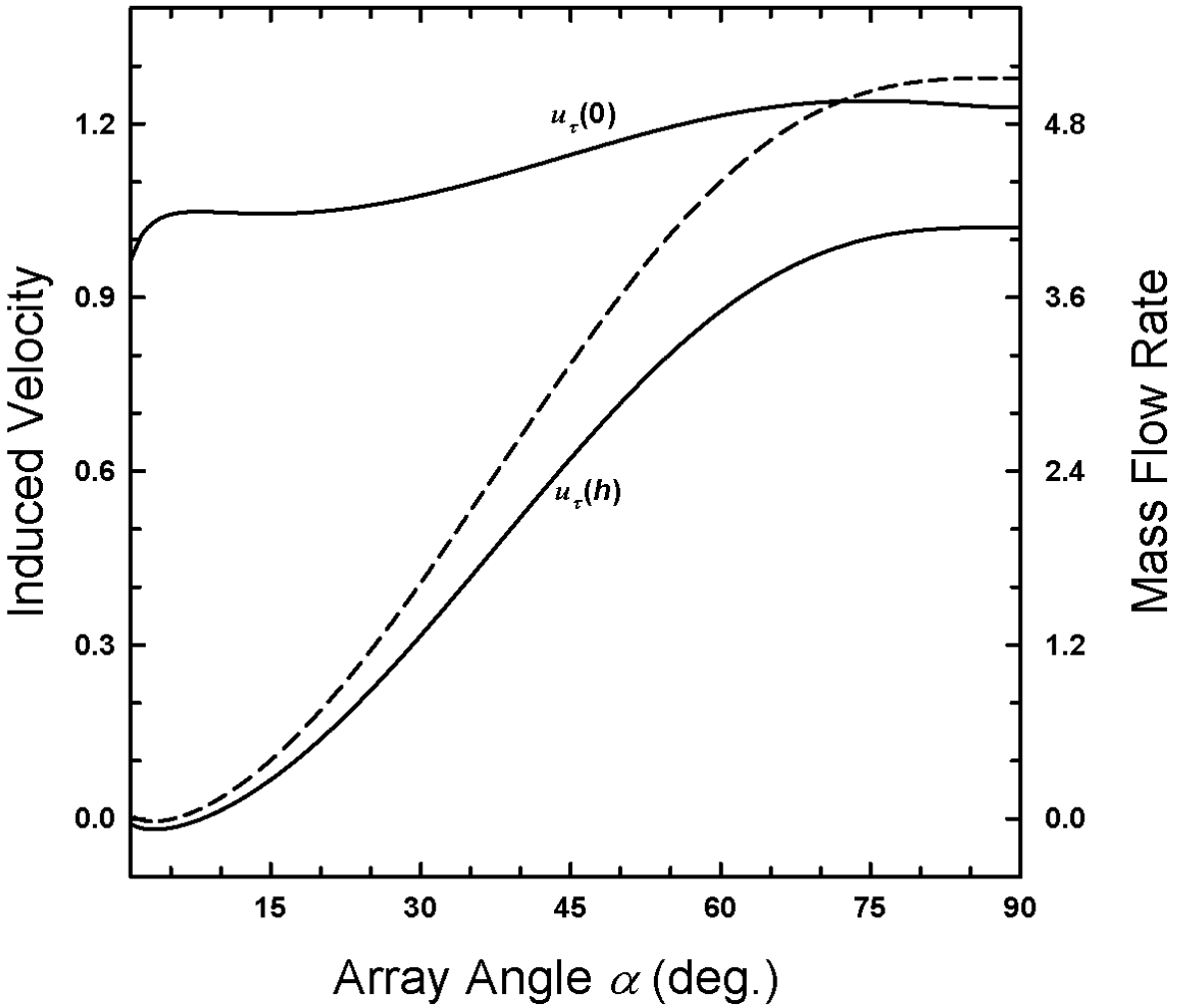

Figure 6.43: The variations of $u_\tau(0)$ and $u_\tau(h)$ (shown by solid curves) and mass flow rate (shown by dashed curve), with α, when θ=54.74°, ϕ==90° (V_n^2=1, V_τ^2=2), m_t=5, e=e_w=.9, r=1, E=4, ξ_{nt} =90°, $\xi_{n\tau}$ =0 and Δ_t =Δ_α =.22.

Figure 6.44 shows the variation of induced mean motion with the total boundary energy E, when θ=54.74° (V_n^2=1), ϕ=0 ($V_\tau^2 = 0$), m_t=5, $e = e_w$=.9, r=1, ξ_{nt}=0, $\xi_{n\tau}$=90°, α=90° and $\Delta_t = \Delta_\alpha$=.22. As expected, with increasing total boundary energy E, $u_t(0)$ and $u_t(h)$ increase which increases the mass flow rate.

As mentioned in Chapter 1, 'Review of Previous Work' section, researchers have reported interesting results about the induced mean motion, particularly about the sign of the velocity gradient. In Figure 6.45 we show the profiles of induced velocity $u_t(z)$ for ratio of radii r=.5, .75, 1, 1.5 and 2, when m_t=5, $e = e_w$=.9, E=4, θ=79.48° (V_n^2=.1), ϕ=0 ($V_\tau^2 = 0$), ξ_{nt}=0, $\xi_{n\tau}$=90°, α=90° and $\Delta_t = \Delta_\alpha$=-.15. We see that as r decreases from 2, the velocity gradient starts reducing and finally changes sign when r=.5. Figure 6.46 shows the variation of induced mean motion, i.e., the mass flow rate and, $u_t(0)$ and $u_t(h)$, with r, for the above set of parameters. With decreasing r, the size of flow particles becomes smaller than the size of bumps on the boundary and competing effects determine the sign of the velocity gradient. As r decreases, slip velocity decreases but the velocity gradient reduces, increasing the top velocity. Near r=.5, the two velocities cross over indicating changed sign of velocity gradient. Figure 6.47 shows the variation of temperature $\mathcal{T}$ and individual temperatures $\mathcal{T}_n$, $\mathcal{T}_t$ and $\mathcal{T}_\tau$, at the base $z = 0$, with r for the above set of parameters. As r decreases from 2, size of flow particles reduces which excites them and hence all temperatures increase with decreasing r. Figures 6.48 and 6.49 show the variations with r of flow heights, β and β_d, and solid volume fractions $\nu(0)$ and $\nu(\beta_d)$, for the above set of parameters. Since with decreasing r

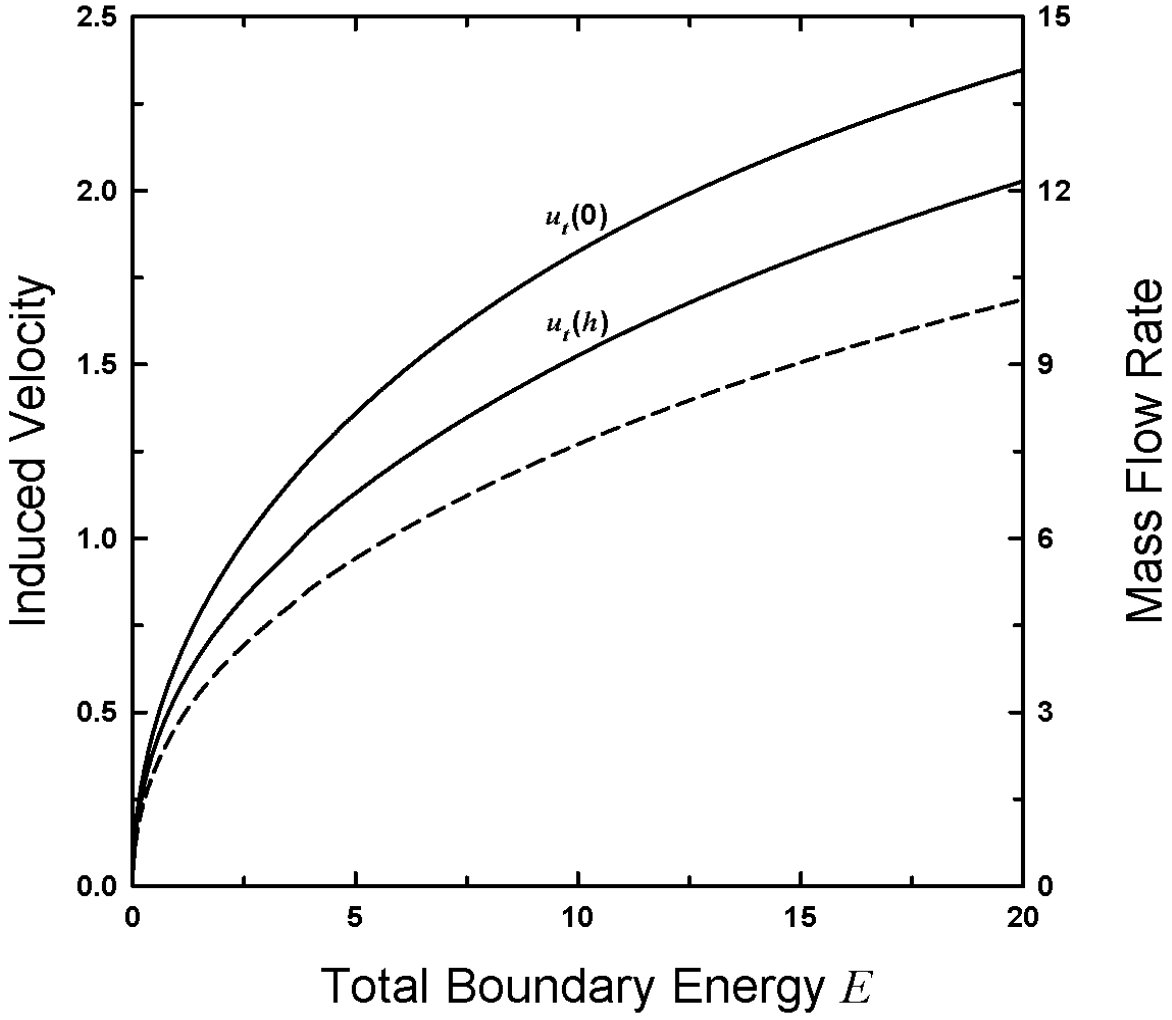

Figure 6.44: The variations of $u_t(0)$ and $u_t(h)$ (shown by solid curves) and mass flow rate (shown by dashed curve), with E, when θ=54.74°, ϕ=0 (V_n^2=1, V_t^2=2), m_t=5, e=e_w=.9, r=1, ξ_{nt} = $\xi_{n\tau}$ =90°, α =90° and Δ_t = Δ_α =.22.

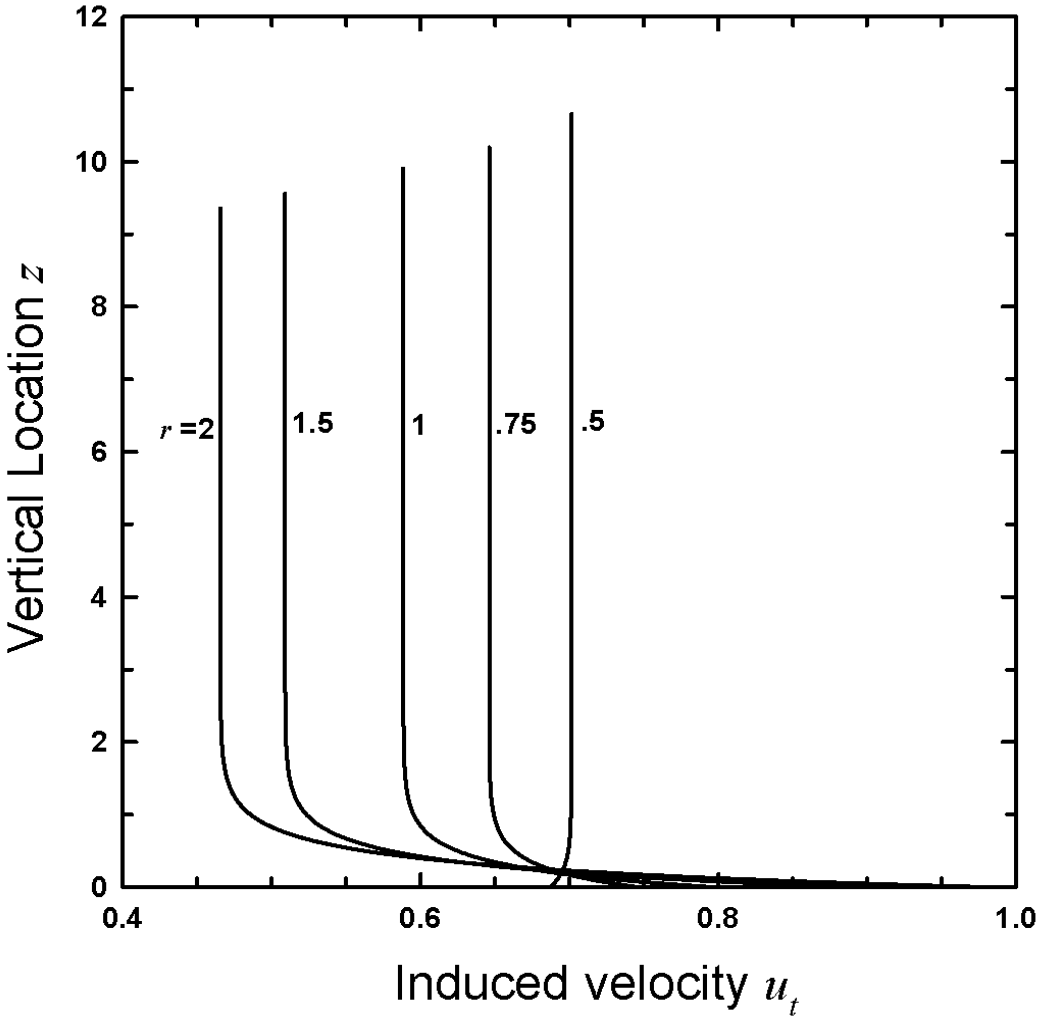

Figure 6.45: The variations of $u_t(z)$ with z, for r=.5, .75, 1, 1.5 and 2, for θ=79.48°, ϕ=0 (V_n^2=.1, V_t^2=2.9), m_t=5, e=e_w=.9, E=4, ξ_{nt}=0, $\xi_{n\tau}$=90°, α=90° and Δ_t=Δ_α=-.15.

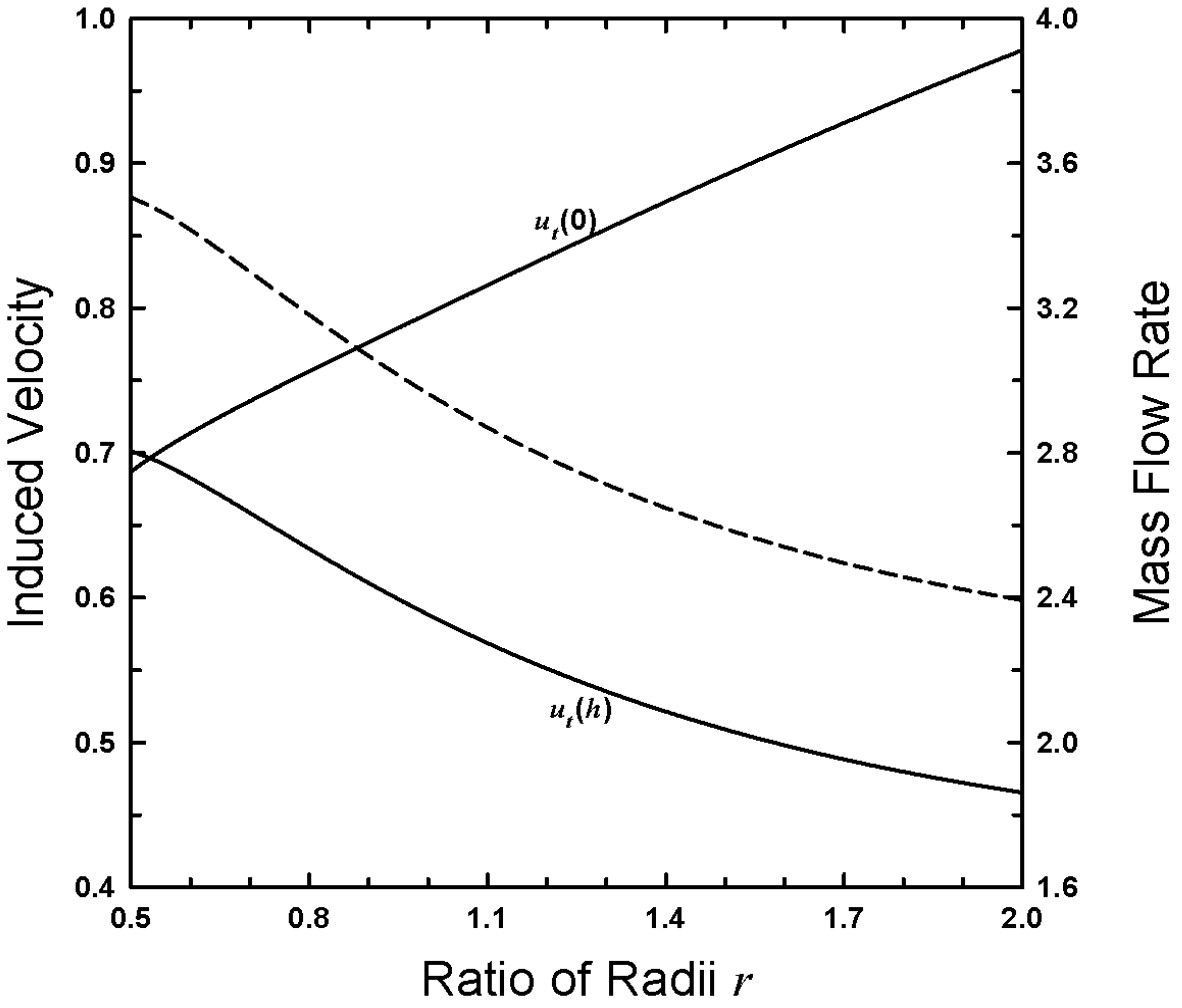

Figure 6.46: The variations of $u_t(0)$ and $u_t(h)$ (shown by solid curves) and mass flow rate (shown by dashed curve), with r, for θ=79.48°, ϕ=0 (V_n^2=.1, V_t^2=2.9), m_t=5, e=e_w=.9, E=4, ξ_{nt}=0, $\xi_{n\tau}$=90°, α=90° and Δ_t=Δ_α=-.15.

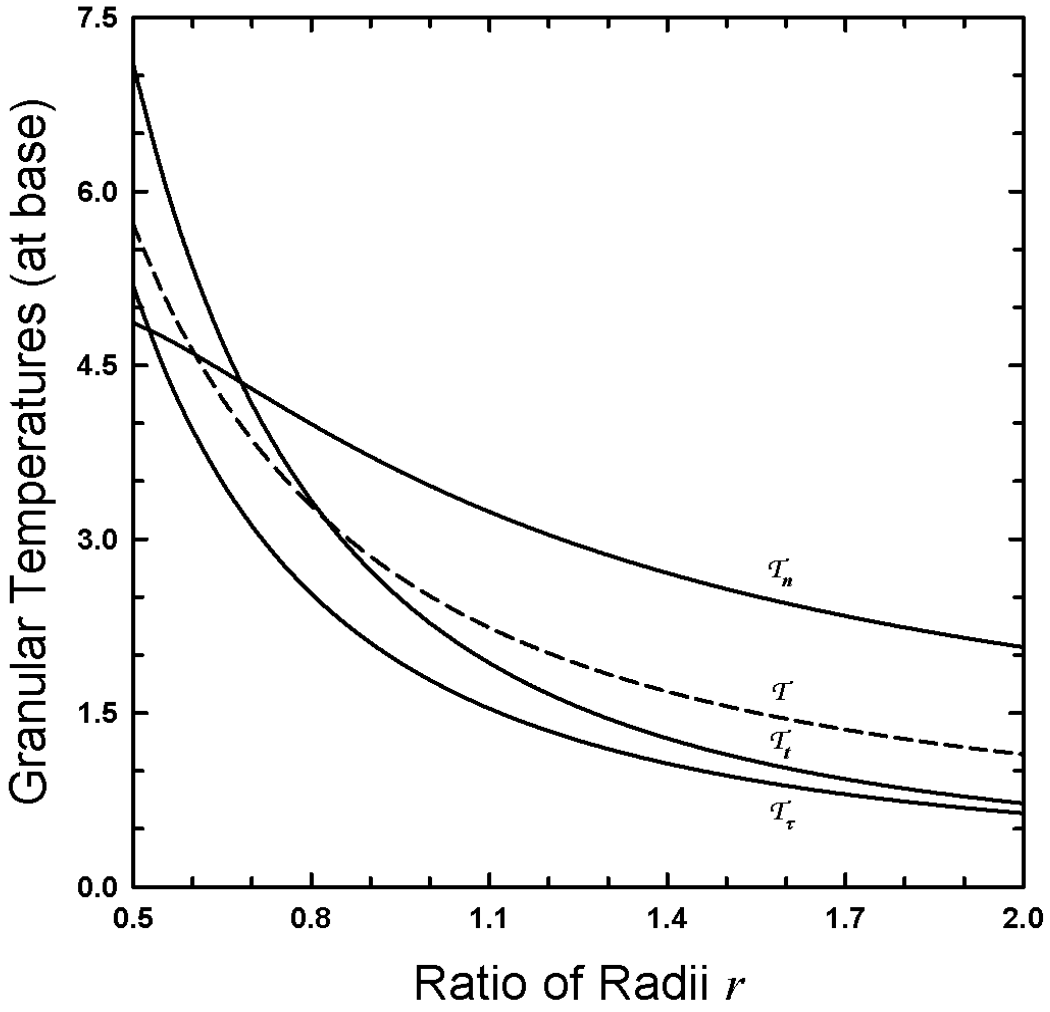

Figure 6.47: The variations of $\mathcal{T}$ (shown by dashed curve) and, $\mathcal{T}_n$, $\mathcal{T}_t$ and $\mathcal{T}_\tau$ (shown by solid curves), at z=0, with r, for θ=79.48°, ϕ=0 (V_n^2=.1, V_t^2=2.9), m_t=5, e=e_w=.9, E=4, ξ_{nt}=0, $\xi_{n\tau}$=90°, α=90° and Δ_t=Δ_α=-.15.

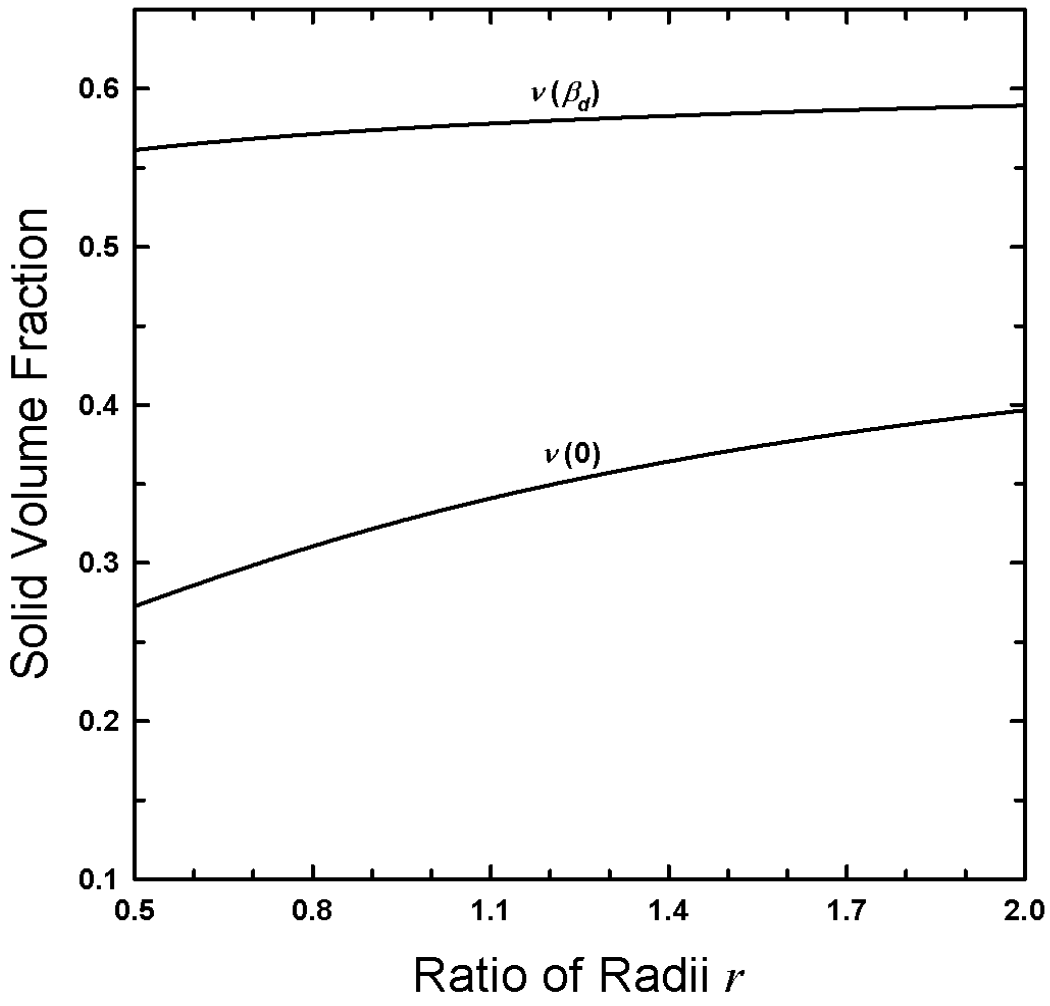

Figure 6.48: The variations of $\nu(\beta_d)$ and $\nu(0)$, with r, for θ=79.48°, ϕ=0 (V_n^2=.1, V_t^2=2.9), m_t=5, e=e_w=.9, E=4, ξ_{nt}=0, $\xi_{n\tau}$=90°, α=90° and Δ_t=Δ_α=-.15.

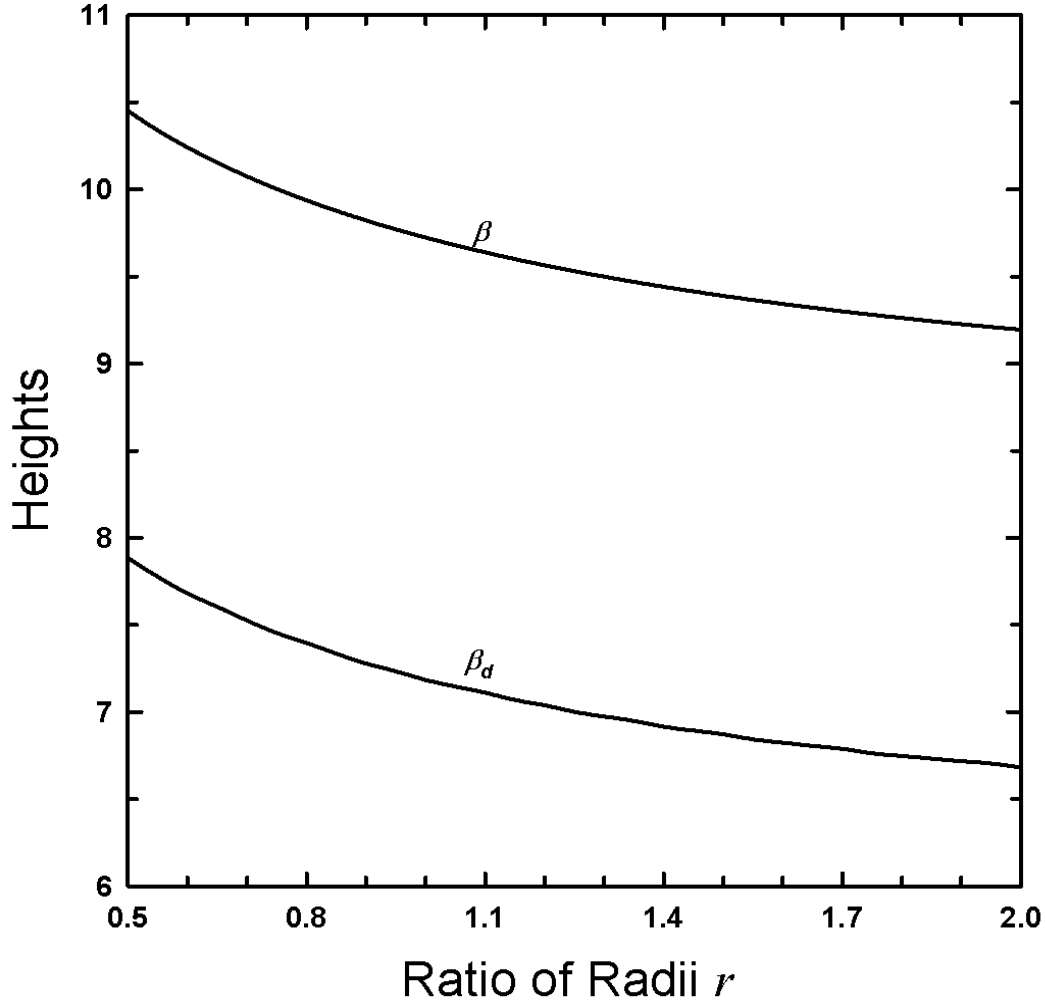

Figure 6.49: The variations of β and β_d, with r, for θ=79.48°, ϕ=0 (V_n^2=.1, V_t^2=2.9), m_t=5, e=e_w=.9, E=4, ξ_{nt}=0, $\xi_{n\tau}$=90°, α=90° and Δ_t=Δ_α=-.15.

thermalization increases, flows become less dense and $\nu(0)$ and $\nu(\beta_d)$ decrease, and the heights β and β_d, increase.

Figure 6.50 shows the profiles of induced velocity $u_t(z)$ for $e=e_w$=.6, .7, .8 and .9, when m_t=5, r=1, E=4, θ=54.74° (V_n^2=1), ϕ=0 ($V_\tau^2=0$), ξ_{nt}=0, $\xi_{n\tau}$=90°, α=90° and $\Delta_t=\Delta_\alpha$=.22. As $e=e_w$ decreases, the velocity gradients don't completely vanish even away from the boundary. Figure 6.51 shows the dependence of induced mean motion, i.e., the mass flow rate and, $u_t(0)$ and $u_t(h)$, on $e=e_w$, for the above set of parameters. As $e=e_w$ increases from 0.6, the flow becomes more thermalized and the particle fluctuations increase. As a result of this increased *disorder* the mean motion reduces with increasing $e=e_w$. Figure 6.52 shows the dependence of induced mean motion with respect to variation of just e_w. As e_w increases from 0.6 to 1, as expected, the induced motion decreases but the effect is reduced compared to Figure 6.51, as value of e is fixed e=.9.

Finally, we look at the effect of the mass hold-up m_t. Figure 6.53 shows the profiles of induced velocity $u_t(z)$ for m_t=2.5, 5, 10 and 20, when $e=e_w$=.9, r=1, E=4, θ=54.74° (V_n^2=1), ϕ=0 ($V_\tau^2=0$), ξ_{nt}=0, $\xi_{n\tau}$=90°, α=90° and $\Delta_t=\Delta_\alpha$=.22. As m_t increases, the velocity gradients don't vanish even away from the boundary. Figure 6.54 shows the dependence of induced mean motion, i.e., the mass flow rate and $u_t(0)$ and $u_t(h)$, on m_t, for the above set of parameters. As m_t increases from 2.5, the flow becomes less thermalized and as a result of this decreased *disorder* $u_t(0)$ and $u_t(h)$

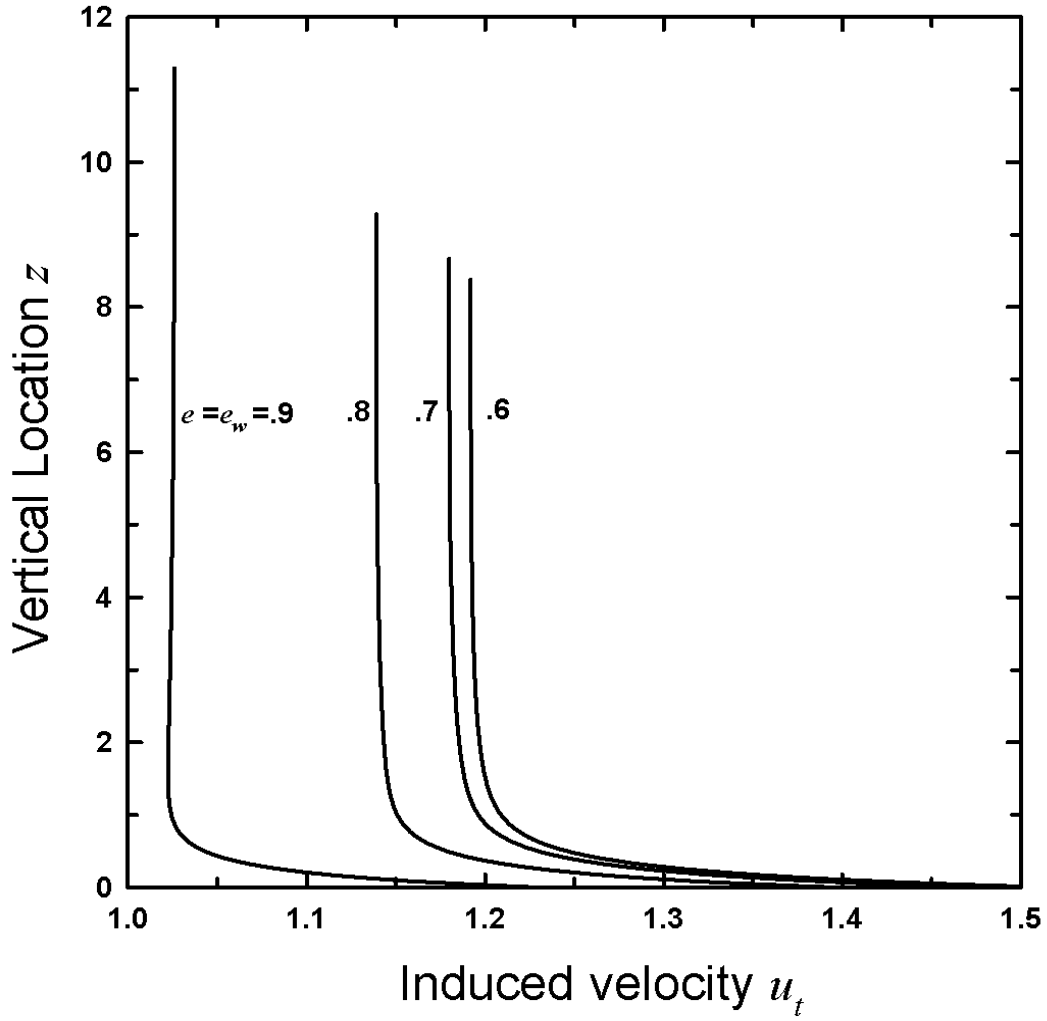

Figure 6.50: The variations of $u_t(z)$, with z, for e=e_w=.6, .7, .8 and .9, when θ=54.74°, ϕ=0 (V_n^2=1, V_t^2=2), m_t=5, r=1, E=4, ξ_{nt}=0, $\xi_{n\tau}$=90°, α=90° and $\Delta_t = \Delta_\alpha$=.22.

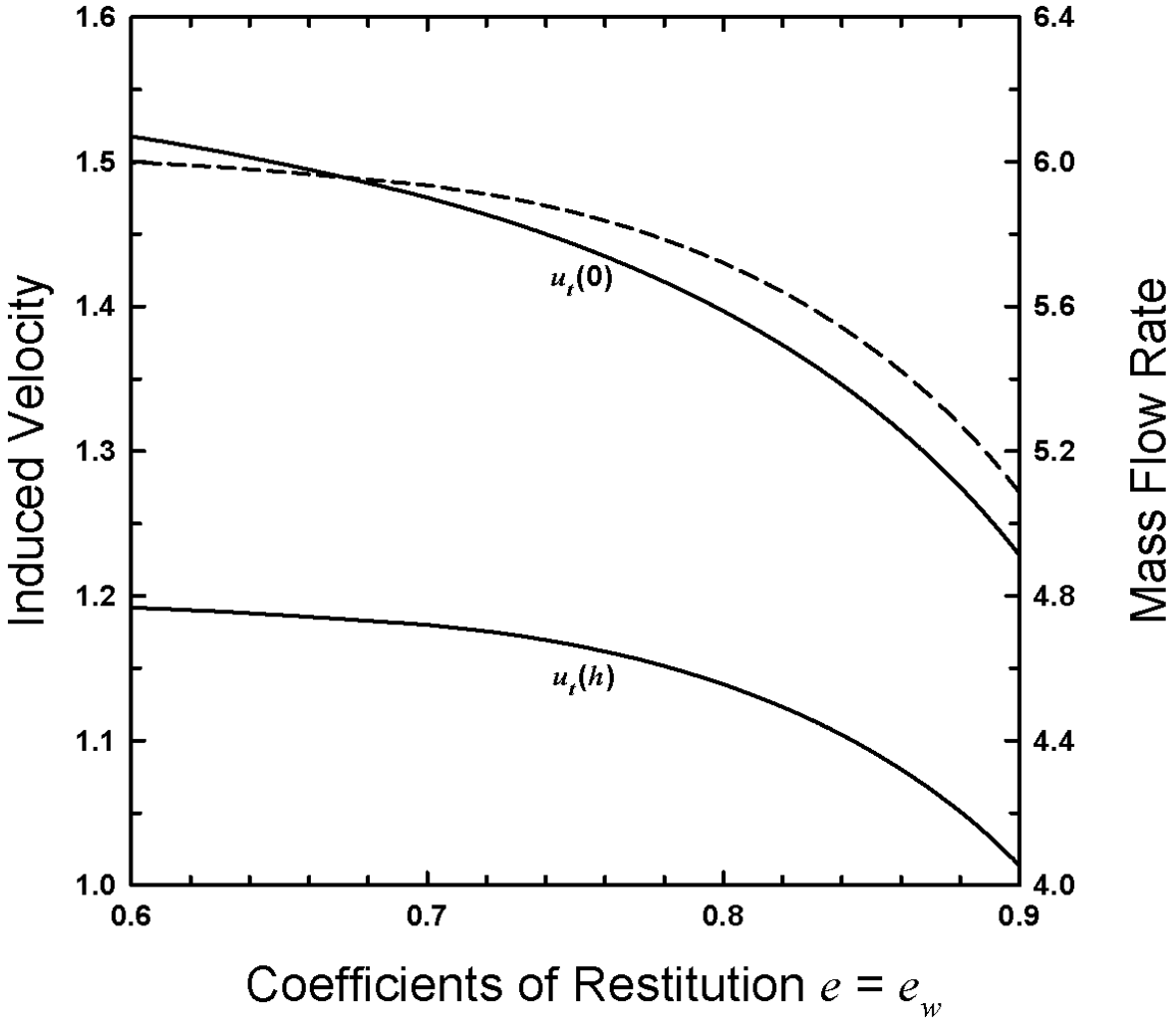

Figure 6.51: The variations of $u_t(0)$ and $u_t(h)$ (shown by solid curves) and mass flow rate (shown by dashed curve), with $e=e_w$ when $\theta=54.74°$, $\phi=0$ ($V_n^2=1$, $V_t^2=2$), $m_t=5$, $r=1$, $E=4$, $\xi_{nt}=0$, $\xi_{n\tau}=90°$, $\alpha=90°$ and $\Delta_t=\Delta_\alpha=.22$.

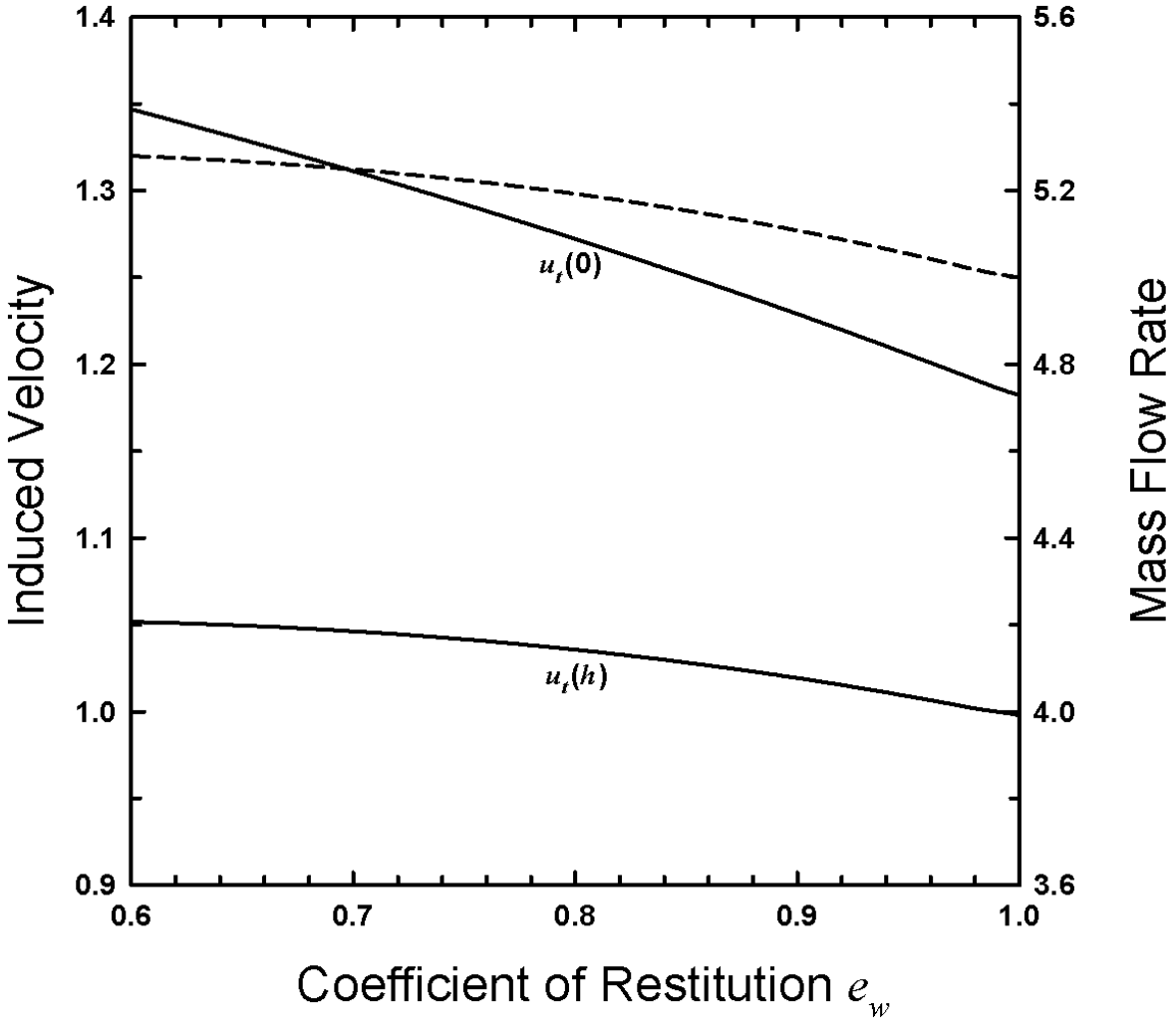

Figure 6.52: The variations of $u_t(0)$ and $u_t(h)$ (shown by solid curves) and mass flow rate (shown by dashed curve), with e_w, when θ=54.74°, ϕ=0 (V_n^2=1, V_t^2=2), m_t=5, , r=1, E=4, e=.9, ξ_{nt}=0, $\xi_{n\tau}$=90°, α=90° and $\Delta_t = \Delta_\alpha$=.22.

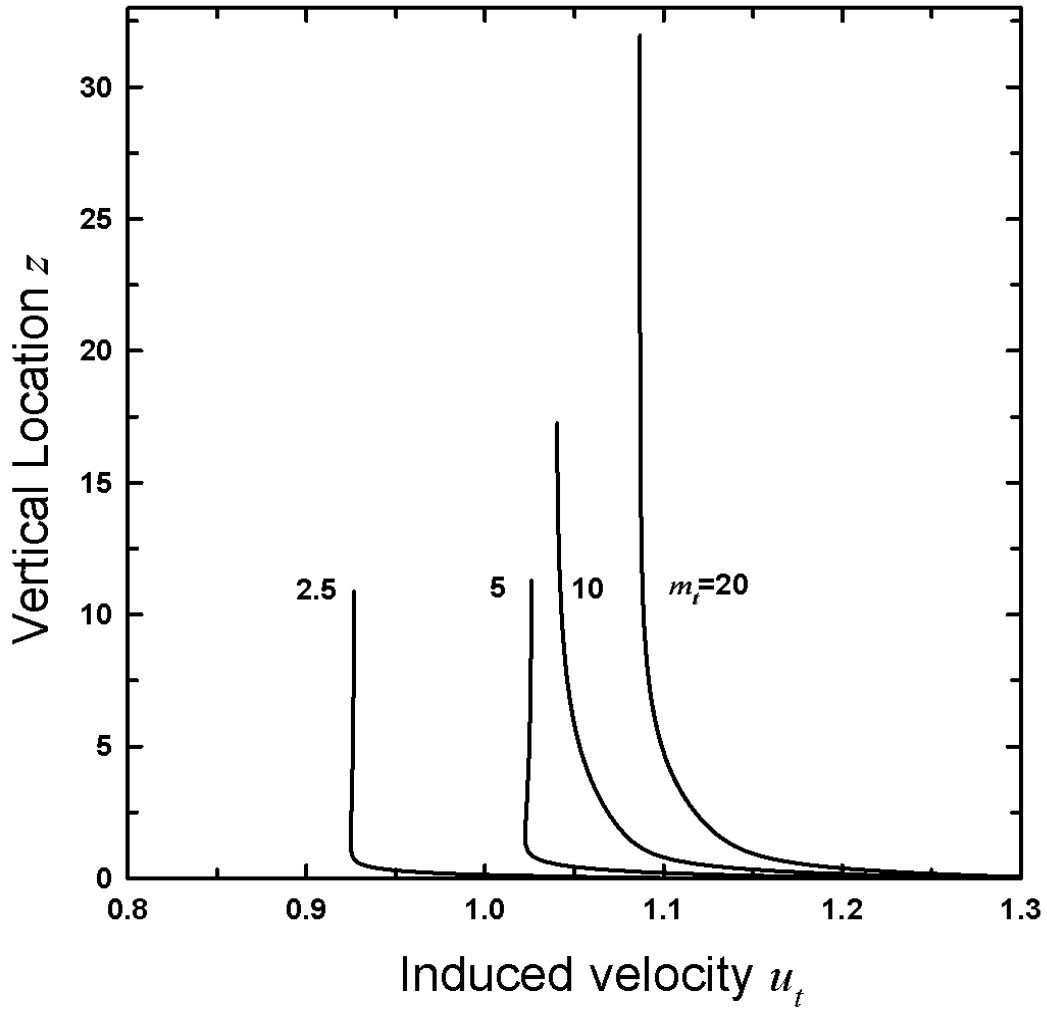

Figure 6.53: The variations of $u_t(z)$ with z, for m_t=2.5, 5, 10 and 20, when θ=54.74°, ϕ=0 (V_n^2=1, V_t^2=2), =5, e=e_w=.9, r=1, E=4, ξ_{nt}=0, $\xi_{n\tau}$=90°, α=90° and Δ_t=Δ_α=.22.

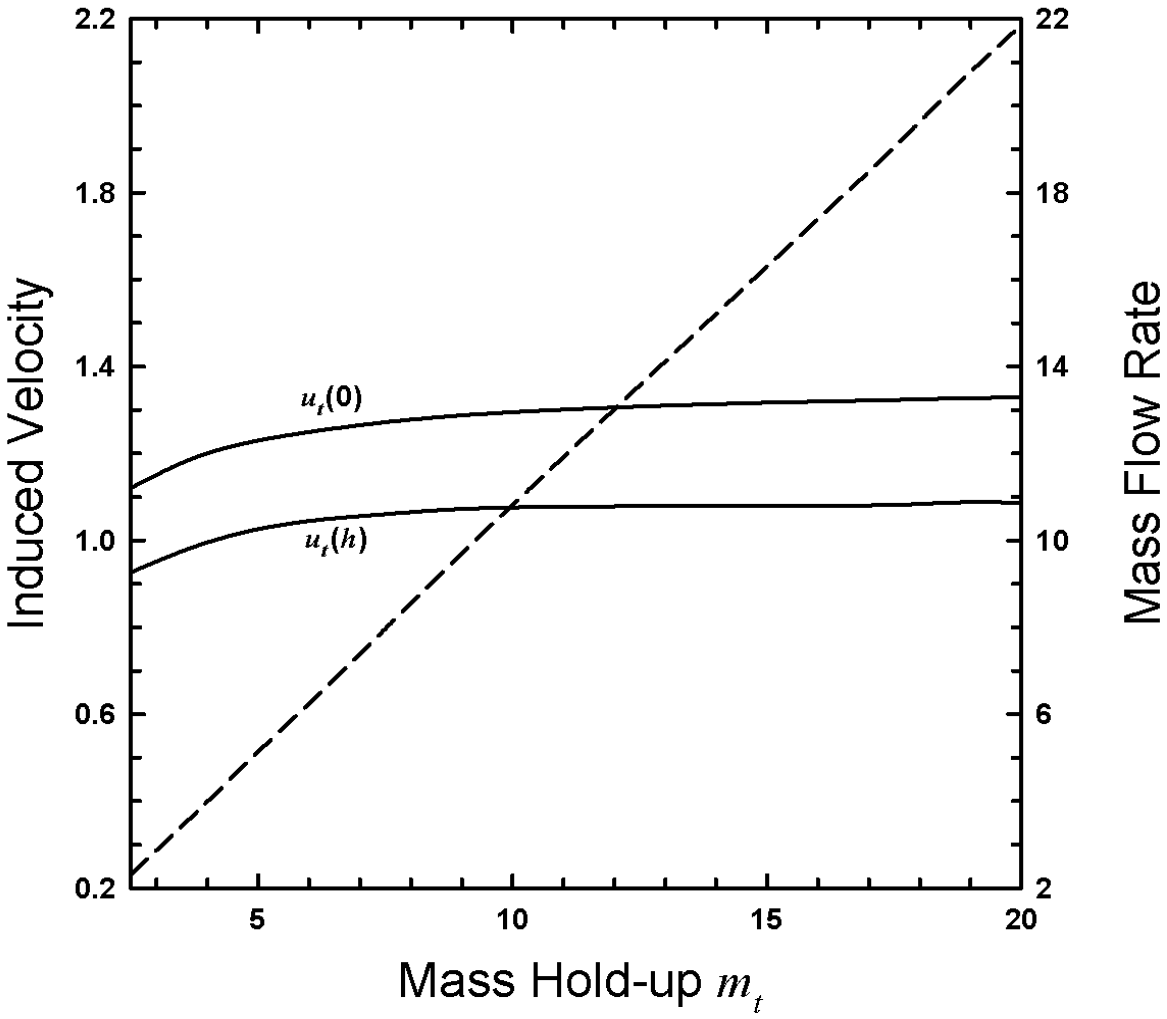

Figure 6.54: The variations of $u_t(0)$ and $u_t(h)$ (shown by solid curves) and mass flow rate (shown by dashed curve), with m_t, when θ=54.74°, ϕ=0 (V_n^2=1, V_t^2=2), =5, e=e_w=.9, r=1, E=4, ξ_{nt}=0, $\xi_{n\tau}$=90°, α=90° and $\Delta_t = \Delta_\alpha$=.22.

increase with increasing m_t. Because of this and also because m_t itself is increasing, the mass flow rate increases with increasing m_t.

CHAPTER 7

Conclusions

We have employed statistical averaging techniques to derive constitutive theory for rapid, dense flows of identical, smooth, inelastic spheres. Also, we derived boundary conditions for bumpy boundaries undergoing random vibrations, using statistical averaging. The constitutive theory and boundary conditions are consistent with the assumptions used to derive the theory of Jenkins and Richman (1985 a). The constitutive theory allows the flow temperatures to be anisotropic and is not limited to dilute or nearly elastic flows. Hence, it can be used to describe many types of flows. The boundary conditions ensure the balance of momentum and full second moment at vibrating boundaries. The bumpiness of the boundary can be changed to model a variety of conditions from smooth to highly bumpy boundaries. Since the boundary conditions include the effects of slip and velocity gradients and apply to boundaries that do and do not vibrate, the boundary conditions may be employed to study a wide variety of boundary effects.

We applied the balance equations and constitutive theory to spatially uniform flows to study decay of diagonal components of second moment. When the particles are elastic, the relaxation times are short. As inelasticity increases, the relaxation times increase, as expected. We also found that non-zero value of off-diagonal component of second moment can induce small diagonal components over time.

For simple and homogenous shearing of granular materials, we applied the balance equations for mass, momentum, and second moment, as well as the constitutive relations for pressure tensor and source of second moment to a steady, homogeneous,

rectilinear shear flow. In this flow, the solid fraction, the velocity gradient and the second moment are uniform throughout. As the density of such flows increases, the temperature drops down. Most importantly, we see that the normal stresses in the three directions are not equal to each other and differ significantly. This has also been seen in experimental and simulation results.

The constitutive theory was applied to steady, fully-developed, free surface flows that are parallel to the boundary to solve two different boundary value problems. In the first boundary value problem, particles are nearly elastic and granular temperature was isotropic. In this case, we only needed to use mass, momentum and energy conservation inside the flow. Also, at the vibrating boundary, we only needed momentum and energy balance boundary conditions. For such flows, shear stresses vanished everywhere and induced mean velocity was uniform. In the second boundary value problem, particles were inelastic and granular temperatures were anisotropic. In this case, the velocity was not uniform but shear stresses vanished everywhere. Here, we needed to use the mass, momentum and full second moment balance laws and boundary conditions.

We studied the effect of bumpiness of boundary, total vibrational energy, distribution of the total vibrational energy, phase differences, mass hold-ups over bed, dissipative character of boundary and particles and size effects of bumps on both thermalization and induced mean motion of the assembly. We also looked at profiles of individual temperatures and solid volume fraction and induced mean motion for different cases. Particularly, we noted that the normal boundary vibration was the best way to thermalize the assembly. Also, we saw that, at least near the vibrating boundary the flows can be very anisotropic. We showed that the direction of tangential boundary

vibration and bumpiness of boundary can significantly affect the thermalized state and induced mean motion. Furthermore, we saw that no mean motion is induced when off-diagonal components of second moment of boundary fluctuations are zero.

The boundary conditions derived are capable of describing more complicated cases than those considered here. Of particular interest is vibrationally enhanced shear flows. The study of these flows is one possible extension of this work. Another possible extension could be *confined* flows induced by vibrations of boundaries. One could also look at *inclined* flows enhanced by boundary vibrations and it could demonstrate the possibility of uphill flows.

REFERENCES

Ackermann, N.L., Shen, H.T., (1978). Flow of granular material as a two-component system. Proc. of U.S.- Japan Seminar on mechanics of granular materials (ed. *Cowin, Satake*), 258-265.

Ackermann, N.L., Shen, H.T., (1982). Stresses in rapidly sheared fluid-solid mixtures. ASCE Journal of Engineering Mechanics, 108, 95-113.

Ahn, H., Brennen, C.E., Sabersky, R.H., (1991). Measurements of velocity, velocity fluctuations, density and stresses in chute flows of granular materials. Journal of Applied Mechanics, 58, 792-803.

Arthur, J.R.F., Menzies, B.K., (1972). Inherent anisotropy in a sand. Geotechnique, 22, 1, 115-128.

Bagnold, R.A., (1954). Experiments on a gravity-free dispersion of large solid spheres in a Newtonian fluid under shear. Proc. Royal Society of London, A 255, 49-63.

Baldassarri, A., Marconi, U.M.B., Puglisi, A., Vulpiani, A., (2001). Driven granular gases with gravity. Physical Review E, 64, 113011-1130113.

Behringer, R.P., (2002). Granular materials: taking the temperature. Nature, 415, 6872, 594-595.

Blair, D.L., Kudrolli, A., (2001). Velocity correlations in dense granular gases. Physical Review E, 64, 5, 0503011-0503014.

Blair, D.L., Kudrolli, A., (2003 a). Collision statistics of driven granular materials. Physical Review E, 67, 4, 413011-4130112.

Blair, D.L., Kudrolli, A., (2003 b). Clustering transitions in vibro-fluidized magnetized granular materials. Physical Review E, 67, 213021-213024.

Blair, D.L., Neicu, T., Kudrolli, A., (2003). Vortices in vibrated granular rods. Physical Review E, 67, 313031-313036.

Blair, D.L., Kudrolli, A., (2004). Magnetized granular materials. The Physics of granular media, (*eds. H. Hinrichsen and D.E. Wolf*), Wiley-VCH publishers, 281-296.

Blinowski, A., (1978). On the dynamic flow of granular media. Archives of Mechanics, 30, 1, 27-34.

Bose, M., Kumaran, V., (2004). Velocity distribution for a two-dimensional sheared granular flow. Physical Review E, 69, 6, 613011-6130116.

Campbell, C.S., Brennen, C.E., (1984). Computer simulations of granular shear flows. Journal of Fluid Mechanics, 151, 167-188.

Campbell, C.S., (1989). The stress tensor for simple shear flows of granular material. Journal of Fluid Mechanics, 203, 449-473.

Campbell, C.S., (1993). Boundary interactions for two dimensional granular shear flows. Journal of Fluid Mechanics, 247, 137-156.

Campbell, C.S., (1994). Impulse strengths in rapid granular shear flows. Acta Mechanica, 104, 65-90.

Campbell, C.S., (2002). Granular shear flows at the elastic limit. Journal of Fluid Mechanics, 465, 261-291.

Campbell, C.S., (2005). Stress-controlled elastic granular shear flows. Journal of Fluid Mechanics, 539, 273-297.

Changfu Y., Hailiang Z., Yi C., Haiying Q., Xuchang X., (2004). Experimental investigation of interparticle collision rate in particulate flow. International Journal of Multiphase Flow, 30, 9, 1121-1138.

Chehata, D., Zenit, R.; Wassgren, C.R., (2003). Dense granular flow around an immersed cylinder. Physics of Fluids, 15, 6, 1622-1631.

Clement, E., Luding, S., Blumen, A., Rajchenbach, J., Duran, J., (1993). Fluidization, condensation and clusterization of a vibrating column of beads. International Journal of Modern Physics, B 7, 1807-1827.

Cordero, P., Risso, D., Soto, R., (2005). Steady quasi-homogeneous granular gas state. Physica A, 356, 1, 54-60.

Corwin, E.I., Jaeger, H.M., Nagel, S.R., (2005). Structural signature of jamming in granular media. Nature, 435, 7045, 1075-1078.

Cowin, S.C., (1974). A theory for the flow of granular materials. Powder Technology, 9, 61-69.

Cowin, S.C., (1978). Microstructural continuum models for granular materials. Proc. of U.S.- Japan Seminar on mechanics of granular materials (ed. *Cowin, Satake*), 162-170.

Daniels, K.E., Behringer, R.P., (2006). Characterization of a freezing/melting transition in a vibrated and sheared granular medium. Journal of Statistical Mechanics: Theory and Experiment, 7, P07018, 1-12.

Derenyi, I., Tegzes, P., Vicsek, T., (1998). Collective transport in locally asymmetric periodic structures. Chaos, 8, 3, 657-664.

Douady S., Fauve, S., Larouche, C., (1989). Subharmonic instabilities and defects in a granular layer under vertical vibrations. Europhysics Letters, 8, 621-627.

Drake, T.G., (1991). Granular flow: physical experiments and their implications for microstructural theories. Journal of Fluid Mechanics, 225, 121-152.

Ehrichs, E.E., Jaeger, H.M., Karczmar, G.S., Knight, J.B., Kupermann, V.Y., (1995). Granular convection observed by magnetic resonance imaging. Science, 267, 1632-1634.

El hor, H., Linz, S.J., Grochowski, R., Walzel, P., Kruelle, C.A., Rouijja, M., Gotzendorfer, A., Rehberg, I., (2005). Model for transport of granular matter on vibratory conveyors. Powders and Grains, Stuttgart, (ed. *Garcia-Rojo, Hermann, MacNamara*), 1191-1194.

Evesque, P., Rajchenbach, J., (1989). Instability in a sand heap. Physical Review Letters, 62, 44-46.

Farkas, Z., Tegzes, P., Vukics, A., Vicsek, T., (1999). Transitions in the horizontal transport of vertically vibrated granular layers. Physical Review E, 60, 6, 7022-7031.

Forterre, Y., Pouliquen, O., (2001). Longitudinal vortices in granular flows. Physical Review Letters, 86, 26, 5886-5889.

Forterre, Y., Pouliquen, O., (2002). Stability analysis of rapid granular chute flows: formation of longitudinal vortices. Journal of Fluid Mechanics, 467, 361-387.

Gallas, J.A.C., Herrmann, H.J., Sokolowski, S., (1992). Two-dimensional powder transport on a vibrating belt. Journal of Physics II France, 2, 1389-1400.

Galvin, J.E., Dahl, S.R., Hrenya, C.M., (2005). On the role of non-equipartition in the dynamics of rapidly flowing granular mixtures. Journal of Fluid Mechanics, 528, 10, 207-232.

Goldshtein, A., Shapiro, M., Moldavsky, L., Fichman, M., (1995). Mechanics of collisional motion of granular materials II: Wave propagation through vibrofluidized granular layers. Journal of Fluid Mechanics, 297, 349-382.

Goodman, M.A., Cowin, S.C., (1971). Two problems in the gravity flow of granular materials. Journal of Fluid Mechanics, 45, 2, 321-339.

Grad H., (1949). On the kinetic theory of rarified gases. Communications of Pure and Applied Mathematics, 2, 331-407.

Grochowski, R., Walzel, P., Rouijja, M., Kruelle, C.A., Rehberg, I., (2004). Reversing granular flow on a vibratory conveyor. Applied Physics Letters, 84, 6, 1019-1021.

Haff, P.K., (1983). Grain flow as a fluid-mechanical phenomenon. Journal of fluid mechanics, 134, 401-430.

Hanes, D.M., Inman, D.L., (1985). Observations of rapidly flowing granular-fluid materials. Journal of Fluid Mechanics, 150, 357-380.

Hanes, D.M., Walton, O.R., (2000). Simulations and physical measurements of glass spheres flowing down a bumpy incline. Powder Technology, 109, 133-144.

Hartley, R.R., Behringer, R.P., (2003). Logarithmic rate dependence of force networks in sheared granular materials. Nature, 421, 6926, 928-931.

Hopkins, M.A., Shen, H.H., (1992). A Monte Carlo solution for rapidly shearing granular flows based on the kinetic theory of dense gases. Journal of Fluid Mechanics, 244, 477-491.

Howell, D., Behringer, R.P., Veje, C., (1999). Stress fluctuations in a 2D granular Couette experiment: a continuous transition. Physical Review Letters, 82, 26, 5241-5244.

Hsiau, S.S., Hunt, M.L., (1993). Shear induced particle diffusion and longitudinal velocity fluctuations in a granular flow mixing layer. Journal of Fluid Mechanics, 251, 299-313.

Hsiau, S.S., Lu L.S., (2005). Mixing in vibrated granular beds with the effect of electrostatic force. Powder Technology, 160, 3, 170-179.

Huang, K., Miano, G., Zhang, P., Yun, Y., Wei, R., (2006). Shock wave propagation in vibrofluidized granular materials. Physical Review E, 73, 4, 413021-413026.

Hunt, M.L., (1997). Discrete element simulations for granular material flows: effective thermal conductivity and self-diffusivity. International Journal of Heat and Mass Transfer, 40, 13, 3059-3068.

Jenkins, J.T., Cowin, S.C., (1979). Theories for flowing granular materials. Mechanics Applied to the Transport of Bulk Materials (ed. *S. Cowin*) ASME AMD-31, 79-89.

Jenkins, J.T., Savage, S.B., (1981). The mean stress resulting from interparticle collisions in a rapid granular shear flow. Continuum Models of Discrete Systems 4 (ed. Brulin and Hsieh), 365-371.

Jenkins, J.T., Savage, S.B., (1983). A theory for the rapid flow of identical, smooth, nearly elastic, spherical particles. Journal of Fluid Mechanics, 130, 187-202.

Jenkins, J.T., Richman, M.W., (1985 a). Grad's 13-moment system for a dense gas of inelastic spheres. Archive for Rational Mechanics and Analysis, 87, 4, 355-377.

Jenkins, J.T., Richman, M.W., (1985 b). Kinetic theory for plane flows of a dense gas of identical, rough, inelastic, circular disks. Physics of Fluids, 28, 12, 3485-3494.

Jenkins, J.T., Richman, M.W., (1986). Boundary conditions for plane flows of smooth, nearly elastic, circular disks. Journal of Fluid Mechanics, 171, 53-69.

Jenkins, J.T., Richman, M.W., (1988). Plane simple shear of smooth, inelastic circular discs: the anisotropy of the second moment in the dilute and dense limits. Journal of Fluid Mechanics, 192, 313-328.

Jenkins, J.T., Askari, E., (1991). Boundary conditions for rapid granular flows: phase interfaces. Journal of Fluid mechanics, 223, 497-508.

Jenkins, J.T., (1992). Boundary conditions for rapid granular flow: flat, frictional walls. Journal of Applied Mechanics, 59, 1, 120-127.

Jenkins, J.T., Hanes, D.M., (1993). The balance of momentum and energy at an interface between colliding and freely flying grains in a rapid granular flow. Physics of Fluids A, 5, 3, 781-783.

Jenkins, J.T., Louge, M.Y., (1997). On the flux of fluctuation energy in a collisional grain flow at a flat, frictional wall. Physics of Fluids, 9, 10, 2485-2490.

Jenkins, J.T., La Ragione, L., (2001). Particle spin in anisotropic granular materials. International Journal of Solids and Structures, 38, 1063-1069.

Jenkins, J.T., Agnolin, I., La Ragione, L., (2006). A continuum theory for a random array of identical, elastic, frictional disks. Mechanics of Materials. 38, 687-701.

Karion, A., Hunt, M.L., (2000). Wall stresses in granular Couette flows of mono-sized particles and binary mixtures. Powder Technology, 109, 1, 145-163.

Khain, E., Meerson, B., (2006). Shear-induced crystallization of a dense rapid granular flow: Hydrodynamics beyond the melting point. Physical Review E, 73, 6, 613011-613016.

Kudrolli, A., Henry, J., (2000). Non-Gaussian velocity distributions in excited granular matter in the absence of clustering. Physical Review E, 62, 2, 1489-1492.

Kumaran, V., (1998 a). Kinetic theory for a vibro-fluidized bed. Journal of Fluid Mechanics, 364, 163-185.

Kumaran, V., (1998 b). Temperature of a granular material 'fluidized' by external vibrations. Physical Review E, 57, 5, 5660-5664.

Kumaran, V., (2006). The constitutive relation for the granular flow of rough particles, and its application to the flow down an inclined plane. Journal of Fluid Mechanics, 561, 1-42.

Lan, Y., Rosato, A.D., (1995). Macroscopic behavior of vibrating beds of smooth inelastic spheres. Physics of Fluids, 7, 8, 1818-1831.

Lan, Y., Rosato, A.D., (1997). Macroscopic Convection related phenomena in granular dynamics simulations of vibrated beds. Physics of Fluids, 9, 12, 3615-3630.

Levanon, M., Rapaport, D.C., (2001). Stratified horizontal flow in vertically vibrated granular layers. Physical Review E, 64, 113041-113044.

Liu, C., Nagel, S.R., (1994). Sound and vibration in granular materials. Journal of Physics for Condensed Matter, 6, A433-436.

Liu. J., Rosato, A.D., (2003). Dynamic behavior of an intruder in a granular Couette flow. Proceedings of the Material Research Society Symposium, Vol.759, 103-108.

Liu. J., Rosato, A.D., (2005). General features of granular Couette flow and intruder dynamics. Journal of Physics: Condensed Matter, 17, 24, 2609-2622.

Luding, S., Clement, E., Blumen, A., Rajchenbach, J., Duran, J., (1994). Studies of columns of beads under external vibrations. Physical Review E, 49, 1634-1646.

Lun, C.K.K., Savage, S.B., Jeffrey, D.J., Chepurniy, N., (1984). Kinetic theories for granular flow: inelastic particles in Couette flow and slightly inelastic particles in a general flowfield. Journal of Fluid Mechanics, 140, 223-256.

Majmudar, T.S., Behringer, R.P., (2005). Contact force measurements and stress-induced anisotropy in granular materials. Nature, 435, 7045, 1079-1082.

Makse, H.A., Kurchan, J., (2002). Testing the thermodynamic approach to granular matter with a numerical model of a decisive experiment. Nature, 415, 6872, 614-617.

Mandl G., Fernadez, L.R., (1970). Fully developed plastic shear flow of granular materials. Geotechnique, 20, 3, 277-307.

Martin, R.E., (1993). The effects of boundary vibration on steady, fully developed, granular flows. M. S. thesis, Worcester Polytechnic Institute, Worcester, MA.

Massoudi, M., Anand, N.K., (2004). A theoretical study of heat transfer to flowing granular materials. International Journal of Applied Mechanics and Engineering, 9, 2, 383-398.

Massoudi, M., (2006). On the heat flux vector for flowing granular materials - Part I: Effective thermal conductivity and background. Mathematical Methods in the Applied Sciences, 29, 13, 1585-1598.

Mayor, P., D'anna, G., Barrat, A., Loreto, V., (2005). Observing Brownian motion and measuring temperatures in vibration-fluidized granular matter. New Journal of Physics, 7, 1, 1-8.

McTigue, D.F., (1978). A model for stresses in shear flow of granular material. Proc. of U.S.- Japan Seminar on mechanics of granular materials, 1978 (ed. *Cowin, Satake*), 266-271

Montanero, J.M., Garzo, V., (2002). Rheological properties in a low-density granular mixture. Physica A, 310, 1, 17-38.

Montanero, J.M., Garzo, V., (2003). Energy nonequipartition in a sheared granular mixture. Molecular Simulation, 29, 357-362.

Muite, B.K., Hunt, M.L., Joseph, G.G., (2004). The effects of a counter-current interstitial flow on a discharging hourglass. Physics of Fluids, 16, 9, 3415-3425.

Natarajan, V.V.R., Hunt, M.L., Taylor, E.D., (1996). Local measurements of velocity fluctuations and diffusion coefficients for a granular material flow. Journal of Fluid Mechanics, 304, 1-25.

Nowak, S., Samadani, A., Kudrolli, A., (2005). Maximum angle of stability of a wet granular pile. Nature Physics, 1, 50-52.

Ogawa, S., (1978). Multi-temperature theory of granular materials. Proc. of U.S.-Japan Seminar on mechanics of granular materials, 1978 (ed. *Cowin, Satake*), 208-217.

Ogawa, S., Umemura, A., Oshima N., (1980). On the equations of fully fluidized granular materials. Journal of Applied Mathematics and Physics, 31, 483-493.

Pak, H.K., Behringer, R.P., (1993). Surface waves in vertically vibrated granular materials. Physical Review Letters, 71, 12, 1832-1835.

Peidong, Y., Behringer, R.P., ((2005). Granular friction: a slider experiment. Chaos, 15, 4, 411021-411027.

Pohlman, N.A., Severson, B.L., Ottino, J.M., Lueptow, R.M., (2006). Surface roughness effects in granular matter: influence on angle of repose and the absence of segregation. Physical Review E, 73, 3, 313041-313049.

Poschel, T., (1993). Granular Material flowing down an inclined chute: a molecular dynamics simulation. Journal of Physics II, France, 3, 27-40.

Potapov, A.V., Campbell, C.S., (1996). Computer simulations of hopper flow. Physics of Fluids, 8, 11, 2884-2894.

Reif, F., (1965). Fundamentals of statistical mechanics and thermal physics. McGraw-Hill, New York.

Reynolds, O., (1885). On the dilatancy of media composed of rigid particles in contact. Philosophical Magazine Journal of Science, 5, 20, 469-481.

Richman, M.W., (1984). Constitutive models for rapidly deforming granular materials. Ph.D. Dissertation. Cornell University, Ithaca, NY.

Richman, M.W., (1988). Boundary conditions based upon a modified Maxwellian velocity distribution for flows of identical, smooth, nearly elastic spheres. Acta Mechanica, 75, 227-240.

Richman, M.W., Chou, C.S., (1988). Boundary effects on granular shear flows of smooth disks. Journal of Applied Mathematics and Physics (ZAMP), 39, 6, 885-901.

Richman, M.W., (1989). The source of second moment in dilute granular flows of highly inelastic spheres. Journal of Rheology, 33, 1293-1306.

Richman, M.W., Chou, C.S., (1989). A theory for grain-size reduction in granular flows of spheres. Journal of Applied Mathematics and Physics (ZAMP), 40, 6, 883-898.

Richman, M.W., Marciniec, R.P., (1990). Gravity-driven granular flows of smooth, inelastic spheres down bumpy inclines. Journal of Applied Mechanics, 57, 4, 1036-1043.

Richman, M.W., (1992). Boundary conditions for granular flows at randomly fluctuating bumpy boundaries. Mechanics of Materials, 16, 205-210.

Richman, M.W., Martin, R.E., (1992). The effects of anisotropic boundary vibrations on confined, thermalized, granular assemblies. Proc. of the 9th ASCE engineering conference (ed. *Lutes, Niedzwedki*), 900-903.

Richman, M.W., Martin, R.E., (1993). Confined granular flows induced by identical, parallel, vibrating boundaries. Proc. of symposium on developments in Non-Newtonian flows, ASME winter annual meeting.

Richman, M.W., Wang, L., (1995). Granular flows through vibrating surfaces with holes. SES 32nd Annual Technical Meeting, Oct. 1995.

Richman, M.W., Wang, L., (1996). Thermalized states of granular materials flowing through vibrating sieves. ASCE Engineering Mechanics Conference, May. 1996.

Rosato, A.D., Kim, H., (1994). Particle dynamics calculations of wall stresses and slip velocities for Couette flow of smooth inelastic spheres. Continuum Mechanics and Thermodynamics, 6, 1, 1-20.

Rosato, A.D., Yacoub D., (1994). Microstructure evolution in compacted granular beds. Powder Technology, 109, 1, 255-261.

Rosato, A.D., Blackmore, D.L., Zhang, N., Lan, Y.D., (2002). A perspective on vibration-induced size segregation of granular materials. Chemical Engineering Science, 57, 2, 265-275.

Sadjapour, M., Campbell, C.S., (1999). Granular chute flow regimes: mass flowrates, flowrate limits and clogging. Advanced Powder Technology, 10, 2, 175-185.

Samadani, A., Kudrolli, A., (2000). Segregation transitions in wet granular matter, Physical Review Letters, 85, 5102-5105.

Samadani, A., Kudrolli, A., (2001). Angle of repose and segregation of cohesive granular matter. Physical Review E, 64, 513011-513019.

Santos, A., Garzo, V., Dufty, J.W., (2004). Inherent rheology of a granular fluid in uniform shear flow. Physical Review E, 69, 6, 613031-06130310.

Savage, S.B., (1978). Some studies of the flow of cohesionless granular materials. Zeitschrift fur Angewandte Mathematik und Mechanik, 58, 7, T313-T315.

Savage S.B., (1979). Gravity flow of cohesionless granular materials in chutes and channels. Journal of Fluid Mechanics, 92, 53-96.

Savage, S.B., Jeffrey, D.J., (1981). The stress tensor in a granular flow at high shear rates. Journal of Fluid Mechanics, 110, 255–272.

Savage, S.B., McKeown, S., (1983). Shear stresses developed during rapid shear of concentrated suspensions of large spherical particles between concentric cylinders. Journal of Fluid Mechanics, 127, 453-472.

Savage, S.B., Sayed, M., (1984). Stresses developed by dry cohesionless granular materials sheared in an annular shear cell. Journal of Fluid Mechanics, 142, 391-430.

Silbert, L.E., Ertas, D., Grest, G.S.; Halsey, T.C., Levine, D., (2002). Analogies between granular jamming and the liquid-glass transition. Physical Review E, 65, 5, 513071-513076.

Strumendo, M., Canu, P., (2002). Method of moments for the dilute granular flow of inelastic spheres. Physical Review E, 66, 4, 413041-413048.

Studt, T. (1995). For materials researchers, it's back to the sandbox. (granular materials). R & D, July 1995.

Toyama, S., (1970). The flow of granular materials in moving beds. Powder Technology, 4, 214-220.

Walton, O.R., Broun, R.L., (1986 a). Stress calculations for assemblies of inelastic spheres in uniform shear. Acta Mechanica, 63, 73-86.

Walton, O.R., Broun, R.L., (1986 b). Viscosity and temperature calculations for shearing assemblies of inelastic, frictional discs. Journal of Rheology, 30, 949-980.

Walton, O.R., (1989). Numerical simulations of homogenous shear flows of hard spheres. Personal Communications.

Wambaugh, J.F., Reichhardt, C., Olson, C.J., (2002). Ratchet-induced segregation and transport of nonspherical grains. Physical Review E, 65, 313081-313087.

Warr, S., Jacques, G.T.H.; Huntley, J.M., (1994). Tracking the translational and rotational motion of granular particles: Use of high-speed photography and image processing. Powder Technology, 81, 1, 41-56.

Warr, S., Huntley, J.M.; Jacques, G.T.H., (1995). Fluidization of a two-dimensional granular system: experimental study and scaling behavior. Physical Review E, 52, 5, 5583-5595.

Wassgren, C.R., Hunt, M.L., Freese, P.J., Palamara, J., Brennen, C.E., (2002). Effects of vertical vibration on hopper flows of granular material. Physics of Fluids, 14, 10, 3439-3448.

Wildman, R.D., Parker, D.J., (2002). Coexistence of two granular temperatures in binary vibrofluidized beds. Physical Review Letters, 88, 6, 643011-643014.

Xu, N., O'Hern, C.S., Kondic, L., (2005). Stabilization of nonlinear velocity profiles in athermal systems undergoing planar shear flow. Physical Review E, 72, 4, 415041-4150410.

Yoon, D.K., Jenkins, J.T., (2005). Kinetic theory for identical, frictional, nearly elastic disks. Physics of Fluids, 17, 8, 833011-8330110.

Zenit, R., Hunt, M.L., Brennen, C.E., (1997). Collisional particle pressure measurements in solid-liquid flows. Journal of Fluid Mechanics, 353, 261-283.

Zhang, N., Rosato, A.D., (2004). Analysis of instantaneous dynamic states of vibrated granular materials. Mechanics Research Communications, 31, 5, 525-544.

Zheng, X.M., Hill, J.M., (1996). Molecular dynamics modeling of granular chute flow: density and velocity profiles. Powder Technology, 86, 219-227.

Zheng, X.M., Hill, J.M., (1998). Molecular dynamics simulation of granular flows: slip along rough inclined planes. Computational Mechanics, 22, 160-166.